BULGARIAN CHEMICAL COMMUNICATIONS

2026 Volume 58 / Number 2

Journal of the Chemical Institutes
of the Bulgarian Academy of Sciences
and of the Union of Chemists in Bulgaria

Bulgarian Chemical Communications, Volume 58, Issue 2 (pp. 129-135) 2026 DOI: 10.34049/bcc.58.2.5722

Electrode shape modification for efficient dye removal using electrocoagulation

S. M. Al-Mahmoud

Department of Chemistry, College of Education for Women, Tikrit University, Tikrit, 34001, Iraq

Received: October 07, 2025; Revised: December 05, 2025

The electrode configuration can strongly influence the electrocoagulation removal performance. This study aimed to introduce a new aluminum-based curved plate (AlCP) electrode to improve the electrocoagulation process as a treatment method for Eriochrome black T-contaminated water. Different factors influencing the electrocoagulation process, such as coagulation time, applied voltage, initial dye concentration, electrode distance, and operating temperature, were investigated. The superior removal efficiency of 97% was acquired at 105 min removal time, 30 V applied voltage, 1 cm electrode distance, 80 mg/L initial EBT concentration, and 318 K operating temperature. The findings emphasize that the removal efficiency of EBT dye increased with increasing coagulation time, applied voltage, initial dye concentration, and operating temperature, and it decreased with increasing the distance between electrodes. The kinetic investigation revealed that the pseudo-second order adsorption model properly described the removal process. In addition, the comparison between the new curved plate electrodes and the conventional flat plate electrodes under the same operating conditions revealed that the maximum removal efficiency of 97% was obtained for the new aluminum-based curved plate (AlCP) electrodes compared to 90% for the conventional flat plate electrodes. This higher removal efficiency is due to the curved structure of the electrodes, which helps to improve flow hydrodynamics and mass transfer, thus reducing the removal time.

Keywords: Electrocoagulation, Curved electrode, Electrode modification, Eriochrome black T.

INTRODUCTION

Aquatic systems are exposed to numerous activities, caused by human beings, that alter their intrinsic nature. One of these primary activities is the disposal of colored materials, resulting from industrial processes, into water bodies [1]. Dyes are organic compounds that have a negative influence on aquatic organisms due to their durability, toxicity, and low biodegradability [2, 3]. Eriochrome black T (EBT) is an anionic azo dye that is exceedingly utilized in the textile industry [4]. It was recently reported that prolonged exposure to EBT can cause carcinogenic and toxic effects to the aquatic environment [5]. Therefore, eliminating EBT from contaminated water before discharging to water bodies is substantial.

Among the major methods used for dye treatment in wastewater, electrocoagulation (EC) can be considered a promising technique for water treatment due to its unique properties, such as operation simplicity, process efficiency, and various contaminants removal ability [6, 7]. However, some limitations hinder its wide spread, such as sludge production, energy consumption, and electrode corrosion [8, 9].

Electrocoagulation merges the advantages of coagulation, flotation, sedimentation, and electrochemical oxidation processes [10]. Its working principle is based on the formation of a coagulant as a result of the current flows through the metal electrodes flooded in the sample solution [11]. The metal cations produced from the surface of the anode electrode (Eq. 1) associate with the hydroxyl ions released from the water reduction at the cathode electrode (Eq. 2), to form metal hydroxides (Eq. 3) [12]. The reactions occurring on the aluminum electrodes are as follows [10–12]:

$$Al_{(s)} \longrightarrow Al^{3+}_{(aq)} + 3\,e^- \qquad (at\ the\ anode) \qquad (1)$$

$$3\,H_2O_{(l)} + 3\,e^- \longrightarrow \frac{3}{2}\,H_{2(g)} + 3\,OH^-_{(aq)} \qquad (at\ the\ cathode) \qquad (2)$$

The hydroxyl formation through the EC process is:

$$Al^{3+}_{(aq)} + 3\,OH^-_{(aq)} \longrightarrow Al(OH)_{3(s)} \qquad (3)$$

$Al(OH)_3$ has a large surface area, which is of great benefit in the rapid adsorption of dissolved compounds and trapping of colloidal particles [16]. It works as a coagulant to destabilize the polluting particles and leads to the formation of larger particles that are easier to separate and remove from the water through sedimentation or by flotation to the surface with hydrogen gas bubbles liberated at the cathode [17].

Recent studies by Mohan *et al.* concluded that the maximum removal efficiency about 98% of Congo

---

* To whom all correspondence should be sent:
Email: *s_almahmoud@tu.edu.iq*

red [18], and 99% of EBT [19] was achieved using copper electrodes in an electrocoagulation process. The investigation of Kalivel *et al.* [20] disclosed that aluminum electrodes are preferable to copper electrodes in removing Red BFL dye. Bendaia *et al.* [21] showed 95% removal efficiency of Acid red 14 using planar aluminum electrodes. Yazdandoust *et al.* [22] applied planar aluminum electrodes for the elimination of Direct red 80 from polluted water, and only 89.3% of the dye removal was achieved with the assistance of Moringa oleifera seed extract.

The hydrodynamics and the mass transport in major electrocoagulation cells that use normal planar plate electrodes are not very efficient [23]. The planar plate electrodes can act as a barrier disturbing the flow dynamics that can reduce the degree of homogenization in the solution [24]. Also, the generated gas bubbles can act as an electrical shield of the electrode nucleation sites that significantly affect the current distribution and the electrolyte conductivity [25]. Therefore, to overcome these obstacles, some literature reported the use of an alternative strategy based on improving the electrode design, such as a perforated plate electrode [26], rotating electrode [27], rotating cylindrical electrode [28], folded plate electrode [29], cubic electrodes [30], spiral electrode [31], which can enhance mixing efficiency and mass transport rates and thus promote uniform current distribution [32, 33].

The novelty of this paper consists of using two Al-based parallel curved plate (AlCP) electrodes in the electrocoagulation technique to remove EBT from a synthetic aqueous solution. The influence of electrode shape, treatment time, electrode distance, applied voltage, process temperature, and initial dye concentration was examined in terms of EBT removal from aqueous media.

EXPERIMENTAL

Eriochrome black T (EBT) of analytical grade was obtained from Fluka and used as received without any treatment. Its chemical formula is $C_{20}H_{12}N_3NaO_7S$, m. wt. 463.381 g/mol, and its λ_{max} is about 530 nm [34].

The electrocoagulation experiments were performed in a 250-mL cylindrical cell. The experimental setup of the electrocoagulation process is illustrated in Fig. 1. The experiments were carried out using a DC power supply (Dazheng, 0-30 V, China), 8-tube centrifuge (Gallenkamp, England), and ultraviolet-visible spectroscopy (UV-1800, Shimadzu, Japan). The experiments were conducted using 200 mL of a dye solution prepared by dissolving EBT in distilled water to obtain the desired EBT concentration.

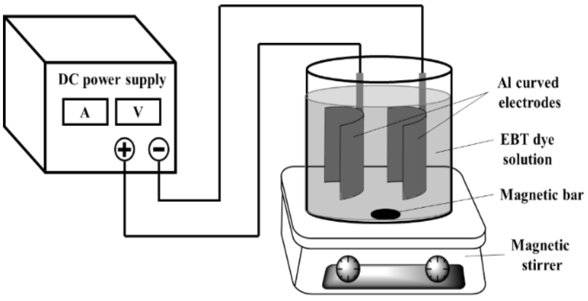

Fig. 1. Schematic experimental setup of the electrocoagulation system.

A pair of aluminum-based parallel curved plate (AlCP) electrodes (Fig. 2a) with dimensions of 4 cm length, 5 cm width, and 0.6 cm thickness, with an effective surface area of 20 cm^2, was immersed in the dye solution in the cylindrical cell. The electrodes were connected through a copper wire to a DC power supply. For comparison, a pair of aluminum-based flat plate (AlFP) electrodes (Fig. 2b) with the same dimensions was also utilized. The electrocoagulation cell before and after the removal process is presented in Figs. 2c and 2d, respectively.

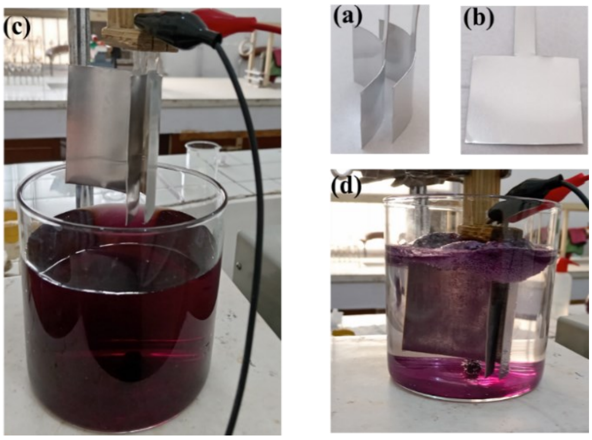

Fig. 2. AlCP electrode (a), AlFP electrode (b), the cylindrical cell before (c) and after (d) electrocoagulation.

The effect of different factors on the EBT removal efficiency by the electrocoagulation process was tested. Each experiment was performed by varying one factor and keeping the others constant to obtain the optimal removal circumstances. These factors are removal time (15, 30, 45, 60, 75, 90, 105, and 120 min), applied voltage (10, 20, 30 V), electrode distance (1, 2, 3 cm), temperature (298, 308, 318 K), and initial EBT concentration (20, 40, 60, 60, and 80 mg/L). The solutions were separated at 3000 rpm in an 8-tube centrifuge to obtain a clear residual EBT dye supernatant whose absorbance was measured by ultraviolet-visible spectroscopy at 530 nm.

The values of the removal efficiency (% Removal) and adsorption capacity (q_e) were estimated using Eqs. 4 and 5, respectively [18].

$$\% \, Removal = \frac{A_0 - A_t}{A_0} \times 100 \quad (4)$$

$$q_e = \frac{(C_0 - C_e)V}{m} \quad (5)$$

where A_0 is the solution absorbance before electrocoagulation and A_t is the solution absorbance after electrocoagulation, C_0 and C_e represent the initial concentration and the equilibrium concentration (mg/L), respectively, V is the volume of the dye solution (L), and m is the amount of electrode consumption (g).

The energy consumption (C_{energy}) and electrode consumption ($C_{electrode}$) depending on Faraday's law, were calculated using Eqs. 6 and 7, respectively [17, 19].

$$C_{energy} = U\,I\,t \quad (6)$$

$$C_{electrode} = \frac{M\,I\,t}{n\,F} \quad (7)$$

where U is the applied voltage (V), I is the electric current (A), t is the electrolysis time (s), M is the aluminum molar mass (26.98 g/mol), n is the number of transferred electrons, and F is Faraday constant (96487 C/mol).

The kinetic study of the AlCP electrodes was performed by applying two kinetic models, the pseudo-first order (Eq. 8) and the pseudo-second order (Eq. 9) [18],

$$\ln(q_e - q_t) = \ln q_e - k_1 t \quad (8)$$

$$\frac{t}{q_t} = \frac{1}{k_2\,q_e^2} + \frac{t}{q_e} \quad (9)$$

where q_e and q_t represent the adsorption capacity at equilibrium and at time (t), respectively, k_1 and k_2 are the pseudo-first and the pseudo-second order rate constants.

RESULTS AND DISCUSSION

The influence of electrocoagulation time on the removal of EBT dye from aqueous media using AlCP electrodes was investigated using removal time intervals (15, 30, 45, 60, 75, 90, 105, and 120 min), applied voltage 30 V, electrode distance 1 cm, temperature 298 K, and initial EBT concentration 20 mg/L. Fig. 3 shows that a lower removal efficiency of about 68% occurs at the beginning of the electrocoagulation process. Increasing the process time increases the removal efficiency to achieve its maximum value of about 97% in about 105 min. In addition, as the electrolysis time increases from 15 to 105 min, the energy consumption rises from 0.225 kWh to 1.575 kWh, along with electrode consumption from 0.0025 g to 0.0176 g. This can be explained by considering that increasing the removal time will increase the release of Al^{3+} ions at the anode (Eq. 1) and of hydroxyl ions at the cathode (Eq. 2), which can lead to the production of an additional amount of aluminum hydroxide that promotes the adsorption of more dye molecules. Moreover, the improved mixing and hydrodynamic flow provided by the AlCP electrodes can create more opportunities for interaction to occur between the produced coagulant and the dye particles, thereby improving the contaminant removal efficiency during the electrocoagulation process. Hashim *et al.* [26] explained that the treatment time exerts an important effect on the removal efficiency and reported that increasing the electrolysis time from 5 to 30 min using aluminum baffle-plate electrodes can enhance the removal efficiency of *Escherichia coli* by 60%. Hawari *et al.* [35] reported that about 19.6% of the total organic carbon removal was achieved in 5 min using symmetrical aluminum electrodes compared to 67.7% in 60 min, and they claimed that changing the electrode configuration by introducing asymmetrical aluminum electrodes can enhance the removal efficiency to 87.7%.

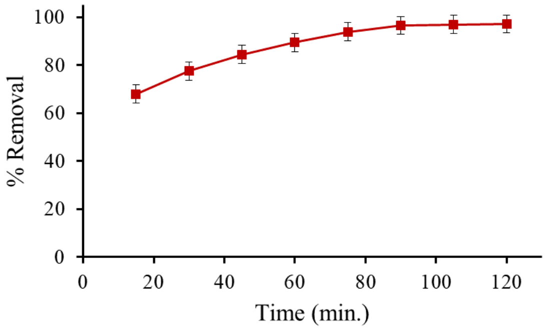

Fig. 3. EBT removal with time using AlCP electrodes

The operation potential is a crucial factor that has an essential impact on the electrocoagulation process. Fig. 4 displays the EBT dye removal using AlCP electrodes at various applied voltages (10, 20, and 30 V), electrode distance 1 cm, temperature 298 K, and initial EBT concentration of 20 mg/L. It shows that increasing the applied voltages from 10 V to 30 V increases the removal efficiency from 72% to 97%. This proves that the higher the potential, the greater is the electrocoagulation efficiency. Gasmi *et al.* [17] reported that better removal efficiency can be achieved at a higher voltage. Increasing the potential leads to an increase in the electric current flowing through the cell. According to Faraday's law (Eq. 7), the amount of dissolved material from the electrodes is proportional to the amount of current flowing through them. Therefore, increasing the electric voltage contributes to the dissolution of the aluminum electrodes, which leads to the release of larger quantities of Al^{3+} ions that react with water to form aluminum hydroxide flocs which have a high capacity to absorb and clump dye molecules [14]. In addition, increasing the electrical voltage also contributes to the generation of larger quantities of hydrogen gas bubbles at the cathode, resulting from the decomposition of water, which in turn contributes to raising pollutant particles to the surface *via* electroflotation [36].

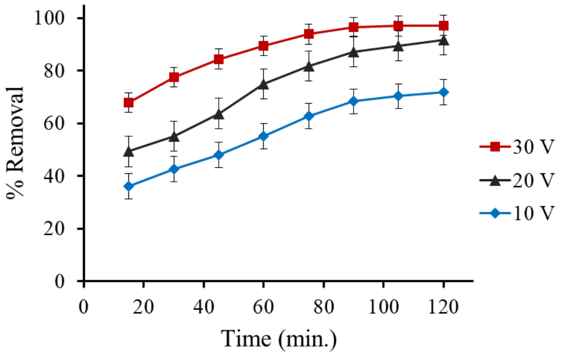

Fig. 4. EBT removal with time at different voltages using AlCP electrodes.

The effect of the distance between the electrodes was also studied using three electrode distances (1, 2, and 3 cm), applied voltage 30 V, temperature 298 K, and initial EBT concentration of 20 mg/L. It can be seen from Fig. 5 that the highest removal efficiency of 97% is achieved using 1 cm distance. Increasing the distance between the electrodes to 3 cm lowers the removal efficiency to about 84%. Also, a decrease in the electrode consumption from 0.0176 g to 0.0058 g occurs as the electrode distance increases from 1 cm to 3 cm. This is due to the increase in the solution resistance and thus decrease of electrical conductivity that reduces the generation of coagulant particles and hydrogen bubbles necessary for dye removal. Mohan *et al.* [18] reported that inter-electrode distance plays a critical role in the removal process, and the removal efficiency was enhanced by about 9% on decreasing the electrode distance from 3 cm to 0.5 cm.

The operating temperature has a key role in the electrocoagulation performance. This study examined different temperatures (298, 308, 318 K), using 30 V applied voltage, electrode distance 1 cm, and initial EBT concentration of 20 mg/L.

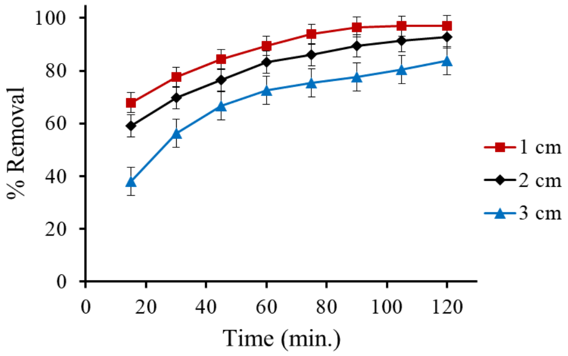

Fig. 5. EBT removal with time at different electrode distances using AlCP electrodes.

At the early stages of the electrocoagulation process, the removal efficiency is affected by the changes in the temperature, significantly increasing with increasing temperature, as shown in Figure 6. However, there is no considerable effect after 100 min since the electrocoagulation process has reached the final stage. It is well-known that raising the operating temperature usually increases the electrocoagulation efficiency [37]. Increasing the temperature would enhance the solution conductivity and ionic mobility as a result of the reduction in the solution resistance and viscosity [24], allowing a higher current flow that would accelerate the electrochemical reactions at the electrodes and thus facilitate coagulant generation. Mohan *et al.* [19] explained that raising the temperature can enhance the ionic mobility as a result of the increase in the kinetic energy of each molecule, and removal efficiency can be enhanced by 29% through raising the temperature from 313 K to 348 K. Al-Raad *et al.* [27] reported that about 4% of the removal efficiency was obtained by increasing the temperature from 298 K to 318 K.

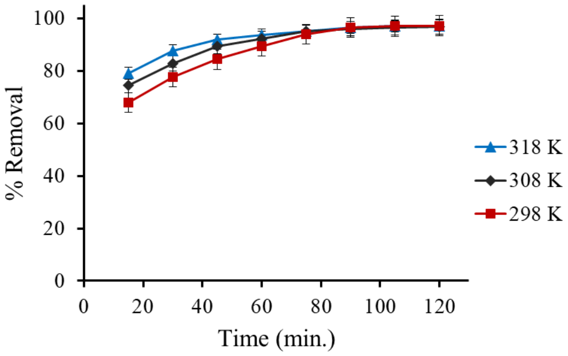

Fig. 6. EBT removal with time at different temperatures using AlCP electrodes.

The influence of initial EBT concentration on the removal efficiency of the electrocoagulation process utilizing AlCP electrodes was also investigated using initial EBT concentrations of 20, 40, 60, 60, and 80 mg/L, applied voltage 30 V, electrode distance 1 cm, and temperature of 298 K. A clear difference in the removal efficiency can be noticed at the beginning of the removal process, as illustrated in Fig. 7. As the initial EBT concentration rises from 20 mg/L to 80 mg/L, the removal efficiency increases from 68% to 96%. At higher dye concentration, there will be more dye molecules in the solution. This increases the probability of collision and interaction with the generated aluminum hydroxide coagulants. As a result, it enhances the aggregation and floc formation. Moreover, many dyes are charged, and a higher concentration increases the ionic strength of the solution, which helps neutralize charges more effectively and promotes coagulation/flocculation, thereby enhancing the efficient removal of the dye. On the other hand, the removal efficiencies are almost identical after 100 min at all concentrations used, which can be attributed to the electrocoagulation process being close to reaching the final stage. Bazrafshan *et al.* [38] attributed the significant reduction in removal efficiency at lower initial concentration to the dilute solution theory. The diffusion layer formed around the electrode in a dilute solution causes a slower reaction rate, while the diffusion layer in the concentrated solution has no impact on the rate of migration of metal ions to the surface of the electrode. Kausleya *et al.* [39] reported that only 70% reduction was achieved at a lower initial TOC concentration, while 91% drop was obtained for a higher initial TOC concentration. They explained that a higher initial concentration can increase the collision rate between the pollutant molecules and with the produced coagulants that reduces the pollutant content in the solution.

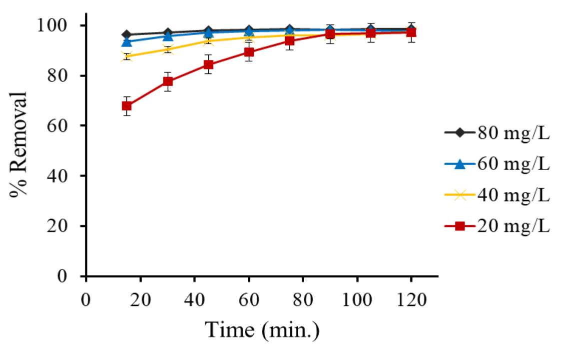

Fig. 7. EBT removal with time at different initial EBT concentrations using AlCP electrodes.

The kinetic study of the AlCP electrodes was carried out by applying the pseudo-first order (Eq. 8) and the pseudo-second order (Eq. 9) adsorption models to the data obtained from the removal time experiment under the optimized conditions. Fig. 8 shows the plots of these two models, and their calculated parameters are presented in Table 1. It can be clearly seen that the highest correlation coefficient of 0.99 was achieved by the pseudo-second order adsorption model compared to 0.88 for the pseudo-first order adsorption model. Also, the theoretical adsorption capacity of the pseudo-second order adsorption model is the closest value to the experimental adsorption capacity. These findings prove that the kinetic study results are more consistent with the pseudo-second order adsorption model, which confirms a chemical adsorption of EBT dye molecules on the aluminum surface.

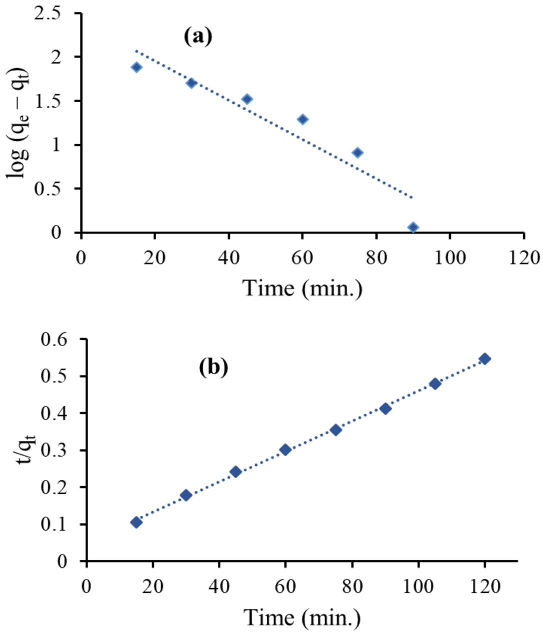

Fig. 8. Kinetic plots of (a) pseudo-first order, (b) pseudo-second order adsorption models.

Table 1. Kinetic parameters calculated for the removal process.

Kinetic model	Kinetic parameter	Value
	q_e exp. (mg. g^{-1})	219.1
Pseudo-first order	q_e calc. (mg. g^{-1}) k_1 (min^{-1}) R^2	250.8 0.051 0.88
Pseudo-second order	q_e calc. (mg. g^{-1}) k_2 (g. mg^{-1} min^{-1}) R^2	243.9 0.0003 0.99

A comparison between the traditional aluminum-based flat plate (AlFP) electrodes and the new shaped aluminum-based curved plate (AlCP) electrodes was made using removal time intervals of 15, 30, 45, 60, 75, 90, 105, and 120 min, under optimal conditions of applied voltage 30 V, electrode distance 1 cm, temperature 298 K, and initial EBT concentration of 20 mg/L. Figure 9 shows that both AlFP and AlCP electrodes attained a reasonable removal efficiency of approximately 68% at the start of the elimination process. As the treatment time increases, the removal efficiency gradually increases for both electrodes. However, the AlCP electrodes perform better and provide more effective removal, attaining 97% at 105 min compared to 86% of conventional AlFP electrodes. This finding can be explained by the fact that conventional AlFP electrodes can act as a barrier, disturbing the flow circulation and hindering the hydrodynamics of the flow, which reduces their performance [24, 40]. Zafar *et al.* [41] reported that using planar aluminum electrodes can eliminate about 81% and 82% of methylene blue and methyl orange, respectively. Soliman *et al.* [42] made a modification to the electrocoagulation reactor to treat ammonia-contaminated wastewater, and only 76.3% of the removal efficiency was due to the stacked aluminum disc electrode. Jafari *et al.* [31] stated that mixing is the major drawback that affects the removal efficiency in a conventional electrocoagulation reactor and the electrode configuration can play a substantial role in the electrocoagulation process. They reported that the mass transfer between the electrodes using spiral electrode configuration is anticipated to increase the removal efficiency.

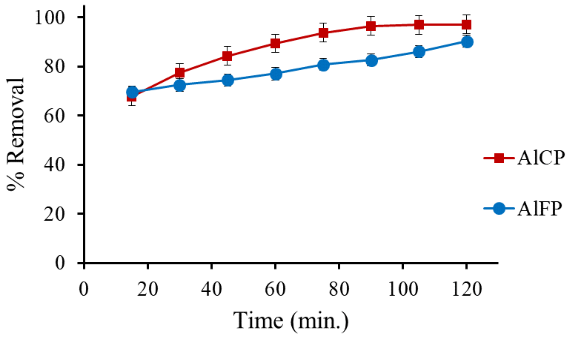

Fig. 9. EBT removal with time using AlFP and AlCP electrodes.

The new AlCP electrode can better promote the hydrodynamic flow. Its curved configuration, expected to enhance mixing and mass transfer, allows for rapid homogeneity of the solution and provides more opportunities for interaction to occur between coagulant flocs and EBT particles, thereby decreasing treatment time. This leads to improved contaminant removal efficiency of the electrocoagulation process compared to conventional aluminum-based flat plate electrodes (AlFP).

CONCLUSIONS

This research aims to introduce aluminum-based curved plate electrodes in the electrocoagulation technique for enhancing the removal of EBT from aqueous media. The main factors influencing the electrocoagulation process were examined, including treatment time, applied voltage, initial EBT concentration, electrode distance, and operating temperature. The optimal removal efficiency of 97% was obtained at optimized parameters: 105 min removal time, 30 V applied voltage, 1 cm electrode distance, 80 mg/L initial EBT concentration, and 318 K operating temperature. The results confirm that the EBT dye removal efficiency increases with increasing coagulation time, applied voltage, initial dye concentration, and operating temperature, and it decreases with increasing the inter-electrode distance. The pseudo-second order adsorption model provides a better fit to the experimental data of the removal process. A comparison was made between the new curved plate electrodes and the traditional flat plate electrodes under the optimized operating conditions. Efficient removal of EBT from aqueous solution was accomplished by the new aluminum-based curved plate (AlCP) electrodes, which can be attributed to their curved shape that promotes mixing and mass transfer, allowing for rapid homogeneity of the solution to take place, which increases the removal efficiency of the electrocoagulation process. These findings emphasize that the new aluminum-based curved plate (AlCP) electrodes can be adopted in the electrocoagulation technology.

Acknowledgement: *The author thanks the Department of Chemistry, College of Education for Women, Tikrit University, for supporting this research.*

REFERENCES

1. H. B. Rahmoun, M. Boumediene, A. N. Ghenim, E. F. da Silva, J. Labrincha, *Environments,* **12**, 1 (2025).
2. I. A. W. Khalaf, S. M. Al-Mahmoud, *Macromol. Symp.*, **414**, 2400223 (2025).
3. S. M. Al-Mahmoud, *Eurasian Chem. J.*, **27**, 219 (2025).
4. W. Boumya, M. Khnifira, A. Machrouhi, M. Abdennouri, M. Sadiq, M. Achak, G. Serdaroğlu, S. Kaya, S. Şimşek, N. Barka, *J. Mol. Liq.*, **331**, 115706 (2021).
5. S. Karishma, V. C. Deivayanai, P. Thamarai, A. Saravanan, P. R. Yaashikaa, *Sustain. Chem. Environ.*, **7**, 100143 (2024).

6. M. Kobya, P. I. Omwene, S. M. Sarabi, S. Yildirim, Z. Ukundimana, *Process Saf. Environ. Prot.*, **152**, 188 (2021).
7. P. V. Nidheesh, Ö. Gökkuş, *Chemosphere*, **310**, 2021 (2023).
8. A. A. Moneer, N. M. El-Mallah, M. M. El-Sadaawy, M. Khedawy, M. S. H. Ramadan, *Desalin. Water Treat.*, **256**, 300 (2022).
9. J. T. Jose, K. L. Priya, S. Chellappan, S. Sreelekshmi, A. Remesh, V. Venkidesh, A. J. Krishna, A. Pugazhendhi, S. Selvam, V. Baiju, M. S. Indu, *Environ. Res.*, **252**, 118759 (2024).
10. M. Mousazadeh, E. K. Niaragh, M. Usman, S. U. Khan, M. A. Sandoval, Z. Al-Qodah, Z. Bin Khalid, V. Gilhotra, M. M. Emamjomeh, *Environ. Sci. Pollut. Res.*, **28**, 43143 (2021).
11. B. Biswas, S. Goel, *Chemosphere*, **302**, 134709 (2022).
12. A. Gasmi, N. Elboughdiri, D. Ghernaout, A. Hannachi, *Desalin. Water Treat.*, **271**, 74 (2022).
13. M. M. Emamjomeh, S. Kakavand, H. A. Jamali, S. M. Alizadeh, M. Safdari, S. E. S. Mousavi, K. S. Hashim, M. Mousazadeh, *Desalin. Water Treat.*, **205**, 161 (2020).
14. B. K. Zaied, M. Rashid, M. Nasrullah, A. W. Zularisam, D. Pant, L. Singh, *Sci. Total Environ.*, **726**, 138095 (2020).
15. H. Liu, Y. Wu, M. Li, H. Ma, M. Li, K. Zhu, Jian zhang, G. Chen, Z. Wang, S. Wang, *Chemosphere*, **268**, 128851 (2021).
16. N. Ungureanu, V. Vlăduț, G. Paraschiv, *Water (Switzerland)*, **3**, 206 (2019).
17. A. Gasmi, S. Ibrahimi, N. Elboughdiri, M. A. Tekaya, D. Ghernaout, A. Hannachi, A. Mesloub, B. Ayadi, L. Kolsi, *ACS Omega*, **7**, 22456 (2022).
18. S. Mohan, P. Sharath, B. M. Nagabhushana, Chikkahanumantharayappa, C. Shivakumara, *Indian J. Chem.*, **61**, 1054 (2022).
19. S. Mohan, B. M. Nagabhushana, Chikkahanumantharayappa, C. Shivakumara, *Asian J. Sci. Appl. Technol.*, **10**, 5 (2021).
20. P. Kalivel, J. C. Jisson, S. Kavitha, J. Bhagavathsingh, J. Palanichamy, M. M. Stephen, J. J. David, *Int. J. Environ. Anal. Chem.*, **103**, 5619 (2021).
21. M. Bendaia, S. Hazourli, A. Aitbara, N. Merzoug, *Sep. Sci. Technol.*, **56**, 2087 (2020).
22. M. Yazdandoust, M. H. Ehrampoush, A. Dalvand, *Int. J. Environ. Anal. Chem.*, **104**, 2485 (2022).
23. A. A. Márquez, O. Coreño, J. L. Nava, *J. Electroanal. Chem.*, **911**, 116223 (2022).
24. S. Adamović, R. Milošević, M. Prica, *Desalin. Water Treat.*, **321**, 100982 (2025).
25. A. D. Villalobos-Lara, T. Pérez, A. R. Uribe, J. A. Alfaro-Ayala, J. D. J. Ramírez-Minguela, J. I. Minchaca-Mojica, *J. Electroanal. Chem.*, **858**, 113807 (2020).
26. K. S. Hashim, P. Kot, S. L. Zubaidi, R. Alwash, R. Al Khaddar, A. Shaw, D. Al-Jumeily, M. H. Aljefery, *J. Water Process Eng.*, **33**, 101079 (2020).
27. A. A. Al-Raad, M. M. Hanafiah, A. S. Naje, M. A. Ajeel, *Environ. Pollut.*, **265**, 115049 (2020).
28. A. D. Villalobos-Lara, F. Álvarez, Z. Gamiño-Arroyo, R. Navarro, J. M. Peralta-Hernández, R. Fuentes, T. Pérez, *Chemosphere*, **264**, 128491 (2021).
29. Z. Wu, J. Dong, Y. Yao, Y. Yang, F. Wei, *Environ. Technol. Innov.*, **22**, 101448 (2021).
30. F. Y. AlJaberi, Z. A. Hawaas, *MethodsX*, **10**, 101951 (2023).
31. E. Jafari, M. R. Malayeri, H. Brückner, T. Weimer, P. Krebs, *J. Environ. Manage.*, **347**, 119085 (2023).
32. P. V. Nidheesh, A. A. Oladipo, N. G. Yasri, A. R. Laiju, V. R. S. Cheela, A. Thiam, Y. G. Asfaha, S. Kanmani, E. (Ted) P. L. Roberts, *Process Saf. Environ. Prot.*, **166**, 600 (2022).
33. M. Bajpai, I. Seidu, E. Gengec, *J. Water Process Eng.*, **77**, 108637 (2025).
34. E. D. Luna, M. Daniel, G. de Flores, D. A. D. Genuino, C. M. Futalan, M. Wan, *J. Taiwan Inst. Chem. Eng.*, **44**, 646 (2013).
35. A. H. Hawari, A. M. Alkhatib, M. A. Hafiz, P. Das, *Environ. Sci. Pollut. Res.* **27**, 23888 (2020).
36. N. Muhammad Niza, N. Abdul Razak, M. S. Yusoff, M. A. A. Mohd Zainuri, M. I. Emmanuel, A. Mohamed Hussen Shadi, M. H. Mohd Hanif, M. A. Kamaruddin, *Sep. Purif. Technol.*, **258**, 118089 (2021).
37. S. Boinpally, A. Kolla, J. Kainthola, R. Kodali, J. Vemuri, *Water Cycle*, **4**, 26 (2023).
38. E. Bazrafshan, K. A. Ownagh, A. H. Mahvi, *E-Journal Chem.,* **9**, 2297 (2012).
39. S. B. Kausley, C. P. Malhotra, A. B. Pandit, *J. Water Process Eng.,* **16**, 149 (2017).
40. J. N. Hakizimana, B. Gourich, M. Chafi, Y. Stiriba, C. Vial, P. Drogui, J. Naja, *Desalination*, **404**, 1 (2017).
41. A. M. Zafar, A. Naeem, M. A. Minhas, M. J. Hasan, S. Rafique, A. Ikhlaq, *Total Environ. Adv.*, **9**, 200087 (2024).
42. M. S. Soliman, I. M. Awaad, S. A. Nosier, M. Hussein, M. H. Abdel-Aziz, M. A. El-Naggar, *Results Eng.*, **28**, 107819 (2025).

Bulgarian Chemical Communications, Volume 58, Issue 2 (pp. 136-142) 2026 DOI: 10.34049/bcc.58.2.5726

Zn-doped $SrBi_2O_4$ nanopowders prepared by sol-gel method and their photocatalytic properties

H. N. E. Rabiaa[1], H. Benhebal[1*], O. Sebbah[2], S. Kadi[3], S. Lellou[3], A. Farcy[4], J. G. Mahy[4], S. D. Lambert[4]

[1]*Department of Chemistry, Faculty of Matter Sciences, University of Tiaret, Tiaret 14000, Algeria*
[2]*Synthesis and Catalysis Laboratory, University of Tiaret, Tiaret 14000, Algeria*
[3]*Biodiversity, Health and Valorization of Biological Resources Laboratory, Department of Biology, University of Tiaret, Tiaret 14000, Algeria*
[4]*Department of Chemical Engineering–Nanomaterials, Catalysis and Electrochemistry, B6a, University of Liège, 4000 Liège, Belgium*

Received: October 18, 2025; Revised: February 07, 2026

The aim of this work is to synthesize photocatalysts usable in the decomposition processes of organic pollutants under visible irradiation. In this context, pure and zinc-doped $SrBi_2O_4$ spinel oxide powders were synthesized by sol-gel process. Physical and chemical properties of the calcination nanoproducts were characterized by XRD, FTIR spectroscopy, BET surface area and SEM. Congo red was selected as a model dye to evaluate the photocatalytic activity of the materials. The formation of spinel structure was confirmed by XRD and infrared spectroscopy. The nanometric size of the crystallites undergoes a decrease following the incorporation of zinc ions. On the other hand, all powders display very low specific surfaces between 0.1429 and 0.3549 m^2/g. Low zinc doping in this case (1-3%) was favorable to boost the activity of $SrBi_2O_4$ which gave an 84% degradation of the dye after 3 hours of irradiation.

Keywords: $SrBi_2O_4$, doping, sol-gel, photocatalysis, Congo red

INTRODUCTION

Water, a precious natural resource, is without competition the essence of life, so meeting human needs for drinking water has become one of the main concerns around the world. However, many countries are now facing an imminent drinking water supply crisis due to excessive consumption and high contamination of surface water [1]. Wastewater loaded with toxic molecules such as dyes constitutes one of the main sources of water pollution [2]. Due to the diversity and complexity of dye structures, most physical, biological and chemical treatments used for water purification remain ineffective and are limited only to the transfer of contamination from one phase to another [3]. Oxidation reactions of organic pollutants by heterogeneous photocatalysis carried out in aqueous media with dispersions of inorganic photocatalysts under light irradiation have widely become an effective approach for water treatment [4]. However, the application of photocatalytic processes is primarily conditioned by the choice of the material used as a photocatalyst. While some semiconductors such as titanium dioxide, zinc oxide and others have been widely studied, their use has been limited only to ultraviolet radiation, which further reduces the profitability of such treatment. Following the efforts deployed in the field of nanotechnology, new photocatalysts sensitive to visible light have emerged. Among these materials there are spinel oxides of structure AB_2O_4 of which A and B are metal cations of valences +2 and +3, respectively [5, 6]. Bismuth-based spinels MBi_2O_4 have recently received great attention as promising candidates for the removal of organic pollutants by visible light photocatalysis due to their low band gap energies [7, 8]. Only a few reports have been published on the use of $SrBi_2O_4$ as a photocatalyst under visible light for the photodegradation of dyes. According to Shtarev and Serpone's review [9], only three works have been devoted to the study of the $SrBi_2O_4$ system [10-12]. The objective of the present study is to develop pure and zinc-doped $SrBi_2O_4$ nanoparticles and to evaluate their photocatalytic activity for the degradation of dyes in aqueous solution. The sol-gel method was used for the synthesis of pure and Zn-doped $SrBi_2O_4$ photocatalysts. Physical and chemical properties of the calcined nanoproducts were characterized by X-ray diffraction (XRD), Fourier transform infrared spectroscopy (FTIR), specific surface area measurement (BET), and scanning electron microscopy (SEM). Congo red (CR) was chosen as a model dye to evaluate the photocatalytic activity of the materials.

---

* To whom all correspondence should be sent:
Email*: benhebal@univ-tiaret.dz*

EXPERIMENTAL

Materials

Strontium nitrate [$Sr(NO_3)_2$], bismuth nitrate pentahydrate [$Bi(NO_3)_3.5H_2O$], zinc nitrate tetrahydrate [$Zn(NO_3)_2.4H_2O$] and citric acid $C_6H_8O_7$ were used as starting materials without prior treatment.

- *Synthesis of Zn-doped $SrBi_2O_4$ photocatalysts.* Zn-doped $SrBi_2O_4$ photocatalysts were synthesized by a facile sol–gel citrate method (Fig. 1). Distilled water was used as solvent throughout all synthesis steps. The stoichiometric amounts of strontium nitrate and bismuth nitrate pentahydrate at a molar ratio of 1:2 were dissolved in distilled water. To this mixture, citric acid solution was added. The pH was adjusted by ammonium hydroxide solution. The solution was stirred and then the appropriate amount of zinc nitrate (1, 3 and 5 wt %) was added to the mixture, followed by vigorous stirring at 80 °C. The obtained dry gels were further ground and calcined at 600 °C for 4 h. The as-synthesized products with various Zn contents (0, 1, 3 and 5 wt%) were labelled as SB, ZSB(1%), ZSB(3%) and ZSB(5%), respectively.

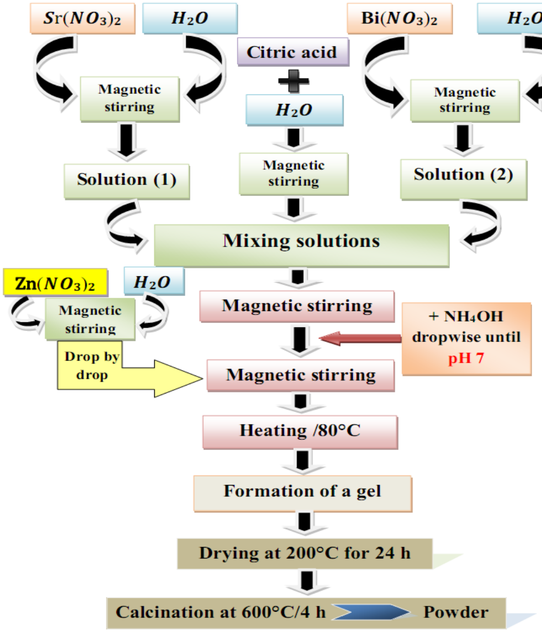

Figure 1. Diagram of the synthesis protocol of pure and Zn-doped $SrBi_2O_4$ by sol-gel process.

- *Materials characterization.* X-ray diffraction (XRD) was used for the structural studies of the undoped and zinc-doped $SrBi_2O_4$ nanoparticles using Rigaku Miniflex 600 diffractometer through CuKα radiation (0.154056 nm). The data were collected within the range of 0°–80° with a step size of 0.02°. The surface morphology of the nano-particles was studied by scanning electron microscopy (SEM) images using a Tescan Bruker model. Fourier transform infrared spectroscopy analysis has been performed on a Shimadzu FTIR-8400 spectrometer using KBr pellet technique in the range of 4000–400 cm^{-1}. ASAP 2420 multi-sampler volumetric device was used to determine nitrogen adsorption–desorption isotherms of the powder samples.

- *Photocatalytic experiments.* The tests of materials' photocatalytic activities were performed by the degradation of Congo red ($300 \leq \lambda \leq 550$ nm) under visible light irradiation in a laboratory-mounted device (Fig. 2). The visible light source used was a white lamp LED of 12 Watt (1.4 10^5 lm/m^2) positioned perpendicularly above the suspension at a distance of 8 cm. Briefly, 0.5 g of the as-synthesized photocatalysts was dispersed in 500 mL of aqueous CR solution (7 mg/L) with pH of the suspension (~6.0) at room temperature. Before lighting the lamp, the mixture was stirred in the dark for 30 min to properly disperse the photocatalyst nanoparticles and ensure adsorption-dissociation equilibrium. During the reaction, volumes were withdrawn from the solution at regular time intervals, filtered and then analyzed by UV-Vis spectrophotometry.

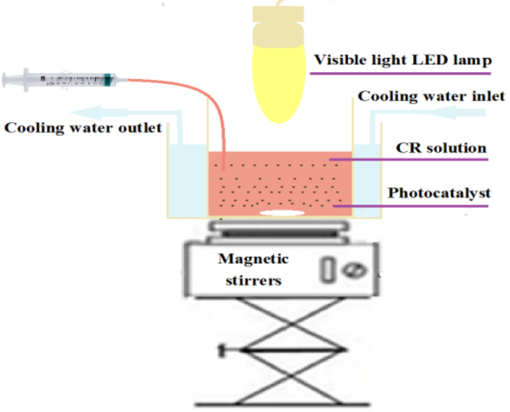

Figure 2. Schematic diagram of the photocatalytic device.

RESULTS AND DISCUSSION

Characterization

X-ray diffraction is a non-destructive characterization technique that does not damage the crystal structure of the solid sample. It allows understanding of atomic and molecular arrangements and identification of crystalline phases in the sample. X-ray diffraction spectra of the prepared samples were collected using a Rigaku miniflex 600 X-ray diffractometer with a Cu-Kα line (λ=1.5406 Å). The measurement was started after the analysis conditions such as scanning speed (2°/min) and 2θ interval (0°-80°) were set on the instrument. The diffractograms presented in Figure 3 clearly show the presence of reflections (211), (220), (002), (310), (112), (202), (411), (420), (213) and (332) belonging to $SrBi_2O_4$ [13]. Some peaks indexed to the monoclinic phase of Bi_2O_3 were identified. Additionally, low-intensity reflections related to the crystalline phase of zinc oxide were observed in the doped samples.

The crystallographic properties of the phase formed in the prepared samples were estimated from the most intense peak at 2θ = 27.50°. The Debye-Scherrer equation was used to estimate crystallite size as follows [14]:

$$D = \frac{0{,}9\lambda}{\beta \mathrm{Cos}(\theta)} \qquad (1)$$

where λ is the wavelength of the radiation used in Cu Kα (0.15406 nm), β is the full width at half maximum (in rad) of the peak and θ is the angle at the position of the maximum peak (in rad).

Microstrain was calculated by the Williamson-Hall method [15]:

$$\varepsilon = \frac{\beta}{4tan\theta} \qquad (2)$$

The dislocation density is affected by the change in the average crystallite size and consequently by the doping rate. The relationship between the average crystallite size and the dislocation density is expressed by the equation:

$$\delta = \frac{1}{D^2} \qquad (3)$$

The results of the calculations of the average crystallite size (D), microstress (ε) and dislocation density (δ) are grouped in Table 1. The values thus obtained indicate that the particle size of $SrBi_2O_4$ decreases with increasing Zn concentration. This shows that the nanoparticles of the doped samples are less agglomerated than those of the undoped sample. The microstrain values increase with increasing Zn content due to the effect of the nanoparticle size on the overall stress of the materials. The number of dislocation lines per unit area inside the materials increases with decreasing crystallite size [16].

Table 1. Average grain size (D), mean microstrain (ε) and dislocation density (δ) of the photocatalysts.

	SB	SBZ (1%)	SBZ (3%)	SBZ (5%)
D (nm)	43.24	28.52	27.43	27.44
ε	0.00337	0.00514	0.00533	0.00531
δ	0.000534	0.00122	0.00132	0.00132

The FTIR spectra of the prepared samples (Fig. 4) show that (i) these samples have a spinel structure through the appearance of two main characteristic absorption bands around 507 cm^{-1} and 435 cm^{-1} according to the Waldron hypothesis [17]. The vibrations of the tetrahedral stretching were recorded at a higher wavenumber than those of the octahedral stretching, because the A-O bond in the tetrahedral site is shorter than the B-O bond in the octahedral site [18]. (ii) Zinc substitution caused an increase in the intensity of the absorption peak at 507 cm^{-1} which can be attributed to an incorporation of zinc ions into the tetrahedral site (preferred site of Zn^{2+} ions). The FTIR spectra of all doped samples exhibit the same characteristic peaks as that of the undoped oxide, illustrating the similar nature of the chemical bonds. The interaction between the incorporated zinc ions and the native strontium ions can be inferred from the change in intensity of the FTIR spectra and the slight shift of the peaks to either side, depending on the doping level corresponding to the M-O bond [19]. Finally, the band at about 1435 cm^{-1} in the undoped spectrum corresponds to the absorption characteristics of carbonate ions (CO_3^{2-}) on the sample surface [20].

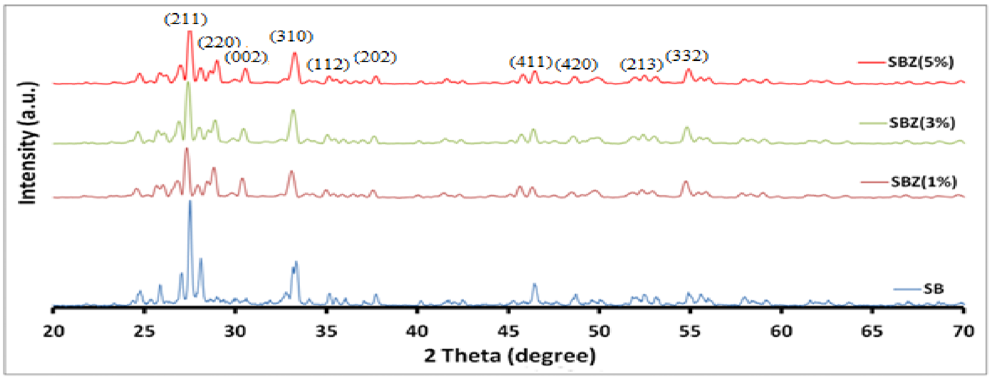

Figure 3. XRD patterns of pure and Zn-doped $SrBi_2O_4$ nanoparticles.

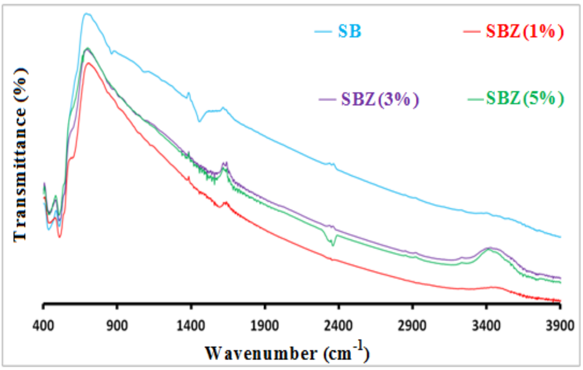

Figure 4. FTIR spectra of the photocatalysts.

The SEM study, whose micrographs are shown in Figure 5, was carried out on pure and Zn-doped $SrBi_2O_4$. The microstructures show an irregular distribution of agglomerated grains throughout the samples. Apparently, the particle size gradually decreases with increasing dopant concentration.

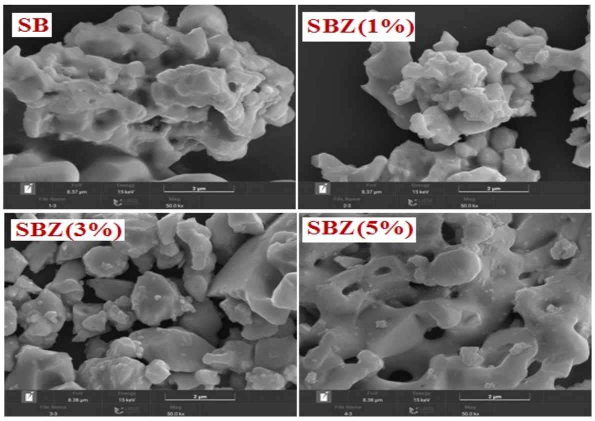

Figure 5. SEM micrographs of pure and doped $SrBi_2O_4$.

The Brunauer-Emmett-Teller (BET) adsorption-desorption isotherms for pure $SrBi_2O_4$ and Zn-doped $SrBi_2O_4$ samples synthesized through the sol–gel method are displayed in Figure 6. The textural properties of the synthesized samples are depicted in Table 2. The isotherms shown in Figure 6 are almost of the same shape and can be classified as type III according to the Brunauer-Deming-Deming-Teller (BDDT) classification, typical of macroporous materials [21, 22]. All powders display very low specific surfaces between 0.1429 and 0.3549 $m^2\ g^{-1}$. These results are in excellent agreement with the value cited by Shtarev *et al.* (0.13 $m^2\ g^{-1}$) [9]. According to calculations using the Barrett-Joyner-Halenda (BJH) method (Table 2), the synthesized photocatalysts have pore volume ranging from 8.2 12^{-4} cc/g to 12.8 10^{-4} cc/g and size ranging from 12.58 nm to 22.70 nm.

Table 2. Textural properties of pure and Zn-doped $SrBi_2O_4$.

	SB	SBZ (1%)	SBZ (3%)	SBZ (5%)
Surface area (m^2/g)	0.3549	0.1429	0.2508	0.3173
Pore size (nm)	12.58	17.68	16.28	22.70
Pore volume (cm^3/g)	0.00121	0.00082	0.00097	0.00128

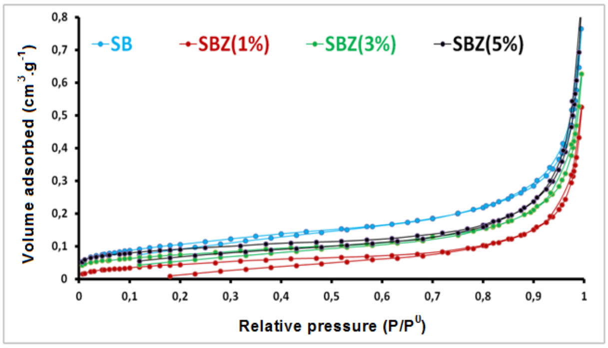

Figure 6. BET analysis of the fabricated photocatalysts.

- *Photocatalytic activity.* Both undoped and zinc-doped materials showed promising photocatalytic degradation of Congo red dye. This degradation was found to be a function of the reaction time as shown in Figure 7, where the initial strong absorption peak visible around 498 nm gradually decreased with time. However, in the case of 3% doped $SrBi_2O_4$, the CR degradation was 84% within 180 min of irradiation, which was comparatively better. The effect of Zn doping on the photocatalytic activity of the $SrBi_2O_4$ system can be explained by the ability of the Zn^{2+} ion to combine with hydroxyl ions to form the coordination ion $[Zn(OH)_4]^{2-}$, which further increases the hydroxyl content on the surface of the photocatalyst and consequently increases the amount of adsorbed dye [23]. Furthermore, at a doping concentration of 3%, impurity energy levels form within the band gap of $SrBi_2O_4$, leading to its narrowing and consequently increased light absorption. Simultaneously, the zinc dopant ions create shallow potential wells that trap electrons, thus promoting the separation of photogenerated electron-hole pairs and minimizing their recombination [24]. When the Zn^{2+} doping concentration increases (5%), the Fermi level shifts into the conduction band, resulting in a significant increase in the band gap due to the Burstein-Moss effect and, consequently, a decrease in visible light absorption [25]. In addition, excess zinc acts as a recombination center and covers the active sites on the surface of $SrBi_2O_4$, thus reducing the efficiency of charge separation [26].

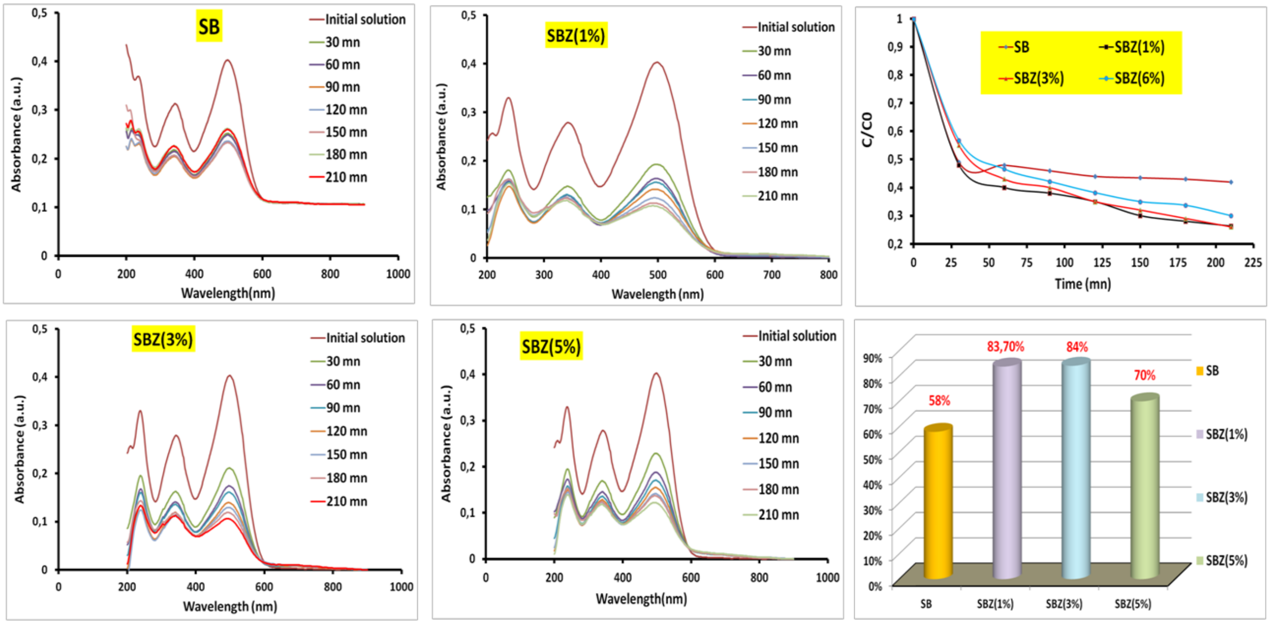

Figure 7. Degradation of CR dye: intensity change with irradiation time, C/C_0 *vs.* time plot.

Table 3. Comparison of the photocatalytic performance of Zn-doped $SrBi_2O_4$ under visible light (this work) with some photocatalysts reported in the literature.

S. no	Catalyst material	Pollutant	Time (min)	Degradation (%)	Ref.
1	Zn-doped NiO	Congo red	120	57	[30]
2	Zn-dopedTiO_2	Methylene blue	120	92.6	[31]
4	Zn-doped Nb_2O_5	Rhodamine B	180	90	[32]
5	Zn/Al-TiO_2	Congo red	120	81.24	[33]
6	$Zn_xCd_{0.8-x}Mn_{0.2}Al_{0.1}Fe_{1.9}O_4$	Congo red	80	93.12	[34]
7	$TiO_2.[ZnFe_2O_4]_{0.1}$	Congo red	300	90	[35]
8	Ag-$CuBi_2O_4$	Rhodamine B	60	91.7	[36]
9	$NaNbO_3/CuBi_2O_4$	Rhodamine B	90	75	[37]
10	$ZnO/NiBi_2O_4$	Malachite green	120	92.30	[38]
11	$Zn/SrBi_2O_4$	Congo red	210	84	This work

Few studies have examined the photocatalytic activity of $SrBi_2O_4$ under visible irradiation; however, spinel bismuth-based photocatalysts such as $ZnBi_2O_4$, $CuBi_2O_4$ and $NiBi_2O_4$ have been the subject of several studies. Telmani *et al.* (2019) reported that the total degradation of methylene blue (30 mg/L) at neutral pH was achieved in less than 2 h on a $NiBi_2O_4/ZnO$ heterojunction [27]. Nafees *et al.* (2022) obtained an ammonia removal rate of 96% using a $CuBi_2O_4$/PANI composite [28]. Nguyen *et al.* (2020) proposed the use of a hybrid photocatalyst (rGO/$ZnBi_2O_4$). Applied to the photodegradation of 2,4-dichlorophenoxyacetic acid, the catalyst showed better catalytic performance with more than 90% degradation [29].

The photocatalytic activity of the present photocatalysts under visible light was compared with that of some photocatalytic systems reported, and the results are presented in Table 3.

- *Kinetic analysis.* A simplified Langmuir–Hinshelwood (L–H) kinetic model (equation 4) was used to describe the photocatalytic degradation rate of CR by plotting the graph of $-\ln(C/C_0)$ *versus* time, t, (Figure 8(a)) [39].

$$-ln\frac{C}{C_0} = k_{app}t \qquad (4)$$

where C_0 and C are the concentrations of Congo red in solution at time 0 and t, respectively, and k_{app} is the apparent first-order reaction rate constant.

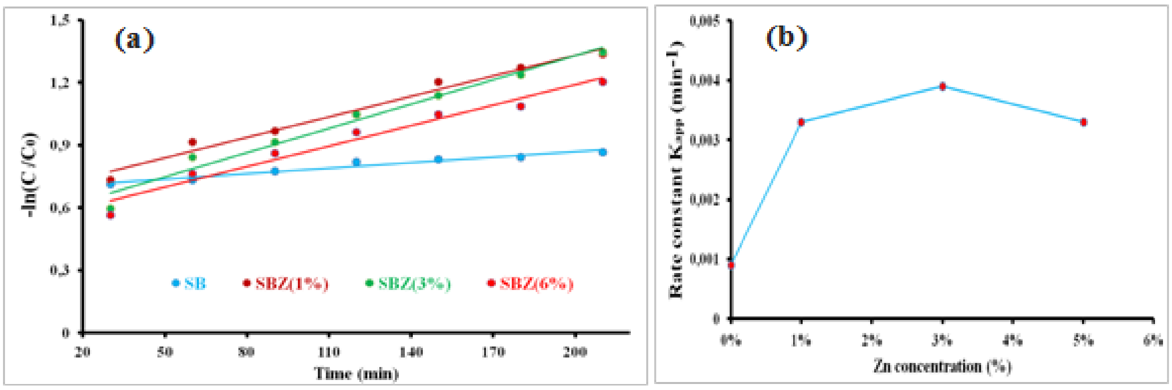

Figure 8. Pseudo-first-order kinetic curves (a) and reaction rate constant (k_{app}) (b) of the degradation of CR at diferent Zn contents.

The slopes of the curves, obtained by plotting -ln(C/C_0) as a function of time, were used to determine the rate constants (K_{app}) of the different photocatalysts. The graphical representation of the rate constants as a function of the Zn doping level (Fig. 8(b)) clearly confirms the effect of zinc doping on the photocatalytic activity of $SrBi_2O_4$. The highest degradation rate of Congo red was achieved at 3% Zn. The energy diagram and the suggested mechanism of the photocatalytic degradation of Congo red under visible light illumination are illustrated in Figure 9 and Eqs. (5) to (9):

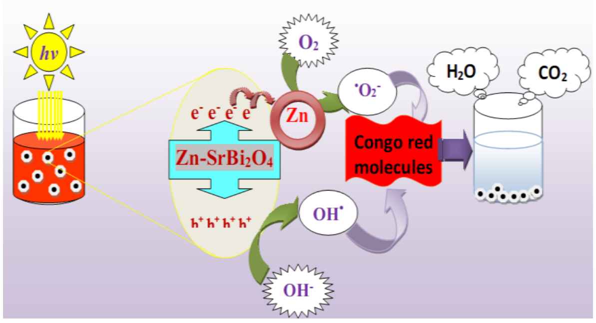

Figure 9. Schematic illustration of the photocatalytic degradation process of Congo red dye onto SBZ photocatalyst.

$$SrBi_2O_4 + hv \rightarrow SrBi_2O_4(e^-_{CB} + e^-_{VB}) \quad (5)$$

$$\begin{cases} e^-_{CB} + Zn^{2+} \rightarrow Zn^{1+} \\ Zn^{1+} + O_2 \rightarrow Zn^{2+} + O_2^{-\bullet} \end{cases} \quad (6)$$

$$e^-_{CB} + O_2 \rightarrow O_2^{-\bullet} \quad (7)$$

$$\begin{cases} h^+_{VB} + OH^- \rightarrow HO^\bullet \\ h^+_{VB} + H_2O \rightarrow H^+ + HO^\bullet \end{cases} \quad (8)$$

$$\begin{cases} O_2^{-\bullet} \\ HO^\bullet \end{cases} + CR \rightarrow \textit{degradation products}\ (CO_2 + H_2O + \bullet\bullet\bullet\bullet) \quad (9)$$

CONCLUSIONS

In this study, the photocatalytic degradation reaction of Congo red, one of the water pollutants, was carried out in the presence of pure and doped spinel photocatalysts. For this purpose, pure and zinc-doped $SrBi_2O_4$ catalysts at 1, 3 and 5% were prepared by sol-gel method. In the photocatalytic degradation reactions of Congo red under visible radiation, half-hour dark time, initial CR concentration of 7 mg/L, and catalyst amount of 1 g/L were considered as optimal reaction conditions, and all prepared catalysts were tested under these conditions.

A kinetic study of the reaction was carried out. The formation of spinel crystalline phases was confirmed by X-ray diffraction and infrared spectroscopy. Crystallographic calculations revealed a reduction in the average crystallite size and an increase in microstress and dislocation density with the increase in doping rate. All materials displayed a relatively good photocatalytic activity towards the Congo red dye with a clear superiority of the photocatalysts doped at 1 and 3% which gave degradation rates of 83.7 and 84%, respectively. These results showed the possibility to further improve the photocatalytic activity of the spinel $SrBi_2O_4$ (i) by optimizing the preparation conditions and the photocatalytic process (pH in particular) and (ii) by considering other dopants.

Acknowledgement: *We thank the Ministry of Higher Education and Scientific Research of Algeria for the financial assistance allocated to the research. The authors thank the Platform CARPORVISU from the University of Liège for the nitrogen adsorption-desorption measurements. S. D. Lambert thanks the "Fonds National de la Recherche Scientifique" for her position as Research Director. The authors thank the "Région Wallonne" for its financial contribution.*

REFERENCES

1. M. M. S. Mahbubul, Md H. Shakhawat, Md K. Rajaul, Fa U. Mohammad, H. Mahady, H K. Razib, *Environ. Sustain. Indic.,* **18,** 100247 (2023).
2. V.P. Dinesh, P. Biji, A. Anuradha, S.K. Dhara, M. A. Kamaruddin, K. Tyagi, R. Baldev, *RSC Adv.,* **4**, 58930 (2014).
3. M.D. Murcia, M. Gómez. E. Gómez, J.L. Gómez, N. Christofi, *Desalination,* **281**, 364 (2011).
4. E. Akbar, N. Simin, Y. Bahram, M. Alireza, V. Foroogh, N, Ramin, N. Shahrokh, *J. Chem. Technol. Biotechnol,* .**83**,1447 (2008).
5. W. Fei, Y. Hua, Z. Yunchuan, *Mater. Sci. Semicond. Process.,* **73**, 58 (2018).
6. H J. Zaid, H G. Bassim, H A. Saad, G. Athraa, A M. Taher, A M. Abrar, *Solar Energy*, **282**(1), 112988 (2024).
7. H.A. Enayatullah, S. Raja, A. Adeel, P. Junqing, *Colloids Surf. A: Physicochem. Eng. Asp.,* **684**, 1331855 (2024).
8. C. O. Olalekan, S. Lawrence, L Y. Tunde, C. O. Damian, *J. Water Process. Eng.,* **66**, 105890 (2024).
9. D.S. Shtarev, N. Serpone, *J. Photochem. Photobiol. C: Photochem*., **50**, 100501 (2022).
10. Z. Shan, Y. Xia, Y. Yang, H. Ding, *F. Mater. Lett.* **63**, 75 (2009).
11. X. Hu, C. Hu, J. Qu, *Appl. Catal., B Environ*., **69**, 17 (2006).
12. C. Hu, X. Hu, J. Guo, J. Qu, *Environ. Sci. Technol.*, **40**, 5508 (2006).
13. S. Rezaei, A. Gholizadeh, D. Kalhor, *J. Sol-Gel Sci. Technol.,* **115**, 1336 (2025).
14. B.D. Cullity, S.R. Stock, Elements of X-Ray Diffraction, Prentice Hall, 2001.
15. P. Rajeswari, S. Dhanuskodi, *Cryst. Res. Technol.,* **48**, 589 (2013).
16. E F. Abo Zeid, I A. Ibrahem, M A. Atif, A. A. M. Walied, *Results Phys.*, **12**, 562 (2019).
17. W. Qin, T. Nagase, Y. Umakoshi, J. A. Szpunar, *J. Phys. Condens. Matter.,* **19**, 236217 (2007).
18. D. Yu, Y. Yifu, S. Huixia, *Electrochim. Acta,* **56**, 9433 (2011).
19. A.N. Naveen, S. Selladurai, *Electrochim. Acta,* **125**, 404 (2014).
20. S. S. N. Clament, K. R. Thinesh, K. L. John, V J. Judith, *J. Alloys Compd.,* **509** (41), 9809 (2011).
21. H. Mittal, A. Al Alili, S. M. Alhassan, *Micropor. Mesopor. Mat.* **299**,110106 (2020).
22. H. Li, J. Lin, J. Wu, J. Wang, P. Wang, G. Kang, S. Huang, M. Fu, J. Wei, Z. Ding, J. Long, *Adv. Sci*, **12**, 2412082(2025).
23. X. Zhong-Lian, W. Xuan-Yi, T. He-Yun, P. Aprea, H. Shi-You, *Chin. J. Inorg. Chem.,* **37**, 1700 (2021).
24. Y. Chen, Z. Liu, Y. Yan, L. Liu., *Inorg. Chem. Commun*., **180**, 115123 (2025).
25. C.G. Jin, T. Yu, Z.F. Wu, F. Wang, M.Z. Wu, Y.Y. Wang, Y.M. Yu, L.J. Zhuge, X.M. Wu, *Appl. Phys. A.,* **106**, 961 (2012).
26. Y. Chen, Z. Liu, Y. Yan, L. Liu., *Inorg. Chem. Commun*., **180**, 115123 (2025).
27. K. Telmani, H. Lahmar, M. Benamira, L. Messaadia, M. Trari, *Optik,* **207**, 163762 (2020).
28. A. Nafees, A. Jerry, K. Zain, S. Suhail, C. Pablo, C. Frederic, *Heliyon,* **8**, e10210 (2022).
29. M T. Nguyen, N K. Dang, Q T. Nguyen, L. Yong, T K P. Nguyen, *Environ. Sci. Pollut. Res.*, **27**, 11127 (2020).
30. M. Keerthana, M. Ingle, T. Pushpa Malini, R. Sangavi, *Rasayan. J. Chem*., **15**,1646 (2022).
31. Y. Zou, T. Yu, X. Huang, Y. Li, L. Guo, H. Yan, J. Zhou, Y. Wang, *Mater. Res. Express*, **10**, 085005 (2023).
32. J. A. Oliveira, M. O. Reis, M. S. Pires, L.A.M. Ruotolo, T.C. Ramalho, C.R. Oliveira, L.C.T. Lacerda, F.G.E. Nogueira, *Mater. Phys. Chem*., **228**,160 (2019).
33. N. Yuliasari, A. Amri, R. Mohadi, E. Elfita, A. Lesbani, *Sci. Technol. Indones*.,**7**, 449 (2022).
34. M. Yasar, M. Ibrahim, M. Zeeshan, K. Javed, F. Noreen, *React. Kinet. Mech. Catal.,* **137**, 2807 (2024).
35. H. Narayan, H. Alem, *Int. J. Nanosci. Nanotechnol.,* **13**, 315 (2017).
36. F. Wang, H. Yang, Y. Zhang. *Mater. Sci. Semicond. Process.,* **73**, 58 (2018).
37. K. D. Rajan, P.P. Gotipamul, S. Khanna, S. Chidambaram, M. Rathinam, *Mater. Lett.*, **296**, 12990 (2021).
38. T. C. Esnawan, D. O. B. Apriandanu, R. M. Surya, H. Watarai, M. Ridwan, Y. Yulizar, *Mater. Lett.,* **365**, 136387 (2024).
39. Z. Z. Vasiljevic, M. P. Dojcinovic, J. D. Vujancevic, I. Jankovic-Castvan, M. Ognjanovic, N. B. Tadic, S. Stojadinovic, G. O. Brankovic, M. V. Nikolic, *R. Soc. Open Sci.,* **7**, 200708 (2020).

Bulgarian Chemical Communications, Volume 58, Issue 2 (pp. 143-153) 2026 *DOI: 10.34049/bcc.58.2.5733*

Unveiling mechanisms of action of isoquinoline alkaloids from *Hylomecon japonica* as promising inhibitors of breast cancer through computational modelling

H. D. Nguyen*

Faculty of Biology, Thai Nguyen University of Education, 24124 Thai Nguyen, Vietnam

Received: November 26, 2025; Revised: March 03, 2026

Breast cancer remains the leading cancer diagnosis and cause of cancer-related mortality in women, accounting for approximately 25% of new female cases and around 670,000 deaths globally in 2022. Isoquinoline alkaloids from *Hylomecon japonica* exhibit cytotoxicity against MCF-7 cells. However, their precise molecular mechanisms, particularly with respect to apoptosis regulators, remain unclear. The present study evaluated selected isoquinoline alkaloids from *H. japonica* as potential breast cancer therapeutics through multi-computational approaches targeting Bcl-2. CPD3 displayed superior docking affinity (-7.30 kcal/mol) compared to Tamoxifen (-7.13 kcal/mol), forming one hydrogen bond and seven van der Waals interactions. Molecular dynamics simulations spanning 100 ns confirmed the complex's stability, with an average RMSD of 0.20 nm, Rg of 1.45 nm, and 1.8 hydrogen bonds for CPD3-6GL8, compared to 0.19 nm RMSD and 1.2 bonds for Tamoxifen. MMGBSA calculations revealed a binding free energy of -20.31 ± 3.12 kcal/mol for CPD3, supported by strong van der Waals contributions. ADMET prediction suggested that CPD3 has favorable pharmacokinetic properties and lower predicted toxicity than Tamoxifen, despite remaining CYP inhibition and hERG II concerns. DFT computations revealed that CPD3 possessed EHOMO of -9.2815 eV, energy gap of 9.4325 eV, and electrophilicity index of 2.2095 eV. These findings establish CPD3 as a promising Bcl-2 inhibitor, warranting further experimental validation for the management of breast cancer.

Keywords: Anti-apoptosis; Bcl-2; Breast cancer; DFT; *Hylomecon japonica*; Isoquinoline alkaloids.

INTRODUCTION

Cancer challenges in 21st century include treatment resistance, managing long-term side effects of treatments. It becomes a growing global burden due to factors like environmental influences and aging of populations. Other significant challenges involve socioeconomic and cultural factors, maintaining a humanistic approach to patient care amidst technological advancement [1, 2]. Globally, breast cancer ranks as the most common cancer diagnosis and the top cause of cancer-related deaths among women. It represents roughly 25% of new female cancer cases worldwide and led to approximately 670,000 fatalities in 2022 [3]. Breast cancer originates from the uncontrolled growth and division of breast cells, leading to the formation of tumors that can spread to other parts of the body, a process known as metastasis [4]. Numerous chemotherapeutic agents have been discovered for breast cancer treatment, and they are generally used in combination to enhance effectiveness [5]. The B-cell lymphoma 2 (Bcl-2) protein is a promising research target because it is a key regulator of the intrinsic apoptotic pathway, allowing cancer cells to evade cell death [6, 7]. In breast cancer, the overexpression of Bcl-2 is paradoxically associated with a favorable prognosis. It is strongly correlated with characteristics of less aggressive tumors, such as positive estrogen receptor and progesterone receptor status, low tumor grade, and a low proliferation rate [8]. Thus, blocking anti-apoptotic Bcl-2 proteins can restore the natural cell death process and overcome resistance to traditional chemotherapy and radiation in many malignancies.

Isoquinoline alkaloids comprise a large family of natural products derived from the isoquinoline chemical structure, which is found in many plants and is used for various medicinal purposes [9]. These compounds can induce apoptosis in various cancer cells through mechanisms such as mitochondrial dysfunction, leading to the release of cytochrome c and the activation of caspases. They also induce other cell death mechanisms, such as autophagy and cell cycle arrest, making them a focus of cancer research [10]. Previous phytochemical studies on *Hylomecon japonica* have reported the isolation of numerous isoquinoline alkaloids, some of which exhibit cytotoxic activity against the MCF-7 breast cancer cell line [11]. Nevertheless, their underlying mechanisms, especially those involving major apoptosis regulators, remain poorly understood. This study employed multiple computational techniques to investigate the anti-breast cancer potential of selected isoquinoline alkaloids from *H. japonica* and clarify their mechanism of action.

---

* To whom all correspondence should be sent:
Email*: hungnd@tnue.edu.vn*

MATERIALS AND METHODS

Structural preparation of selected ligands

The ligands evaluated in the present study were selected from the isoquinoline alkaloids previously isolated from *Hylomecon japonica* [11]. Among the 26 alkaloids reported in that study, 6-methoxydihydrosanguinarine (CPD1), dihydrosanguinaline (CPD2), and 10-methoxyboconoline (CPD3) were prioritized for computational analysis because of their reported cytotoxic relevance and their representativeness within the identified isoquinoline scaffold class. These alkaloids have molecular formulas of $C_{21}H_{17}NO_5$, $C_{20}H_{15}NO_4$, and $C_{23}H_{23}NO_6$, respectively, with corresponding molecular weights of 363.1107, 333.1001, and 409.1525 g/mol. Tamoxifen, possessing a molecular formula of $C_{26}H_{29}NO$ and a molecular weight of 371.2249 g/mol, was chosen as the positive control (Figure 1).

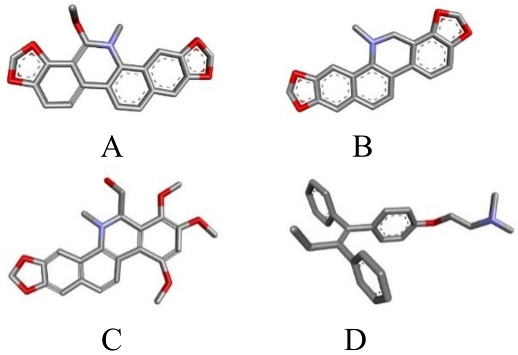

Figure 1. 3D Structures of selected ligands. (A) CPD1, (B) CPD2, (C) CPD3, (D) Tamoxifen

Molecular docking

Construction of the three-dimensional configurations for the selected ligands was performed in PDB format using Biovia Discovery Studio Visualizer, incorporating polar hydrogens, computing Gasteiger charges, and accounting for torsional bond flexibility. Acquisition of the Bcl-2 protein structure (PDB ID: 6GL8) occurred in PDB format from the RCSB Protein Data Bank [12]. Execution of ligand-protein docking utilized AutoDock Tools, employing a grid box comprising 60 points across each x, y, and z dimension at a spacing of 0.375 Å. Establishment of binding site coordinates for 6GL8 involved x = 9.866 Å, y = 0.590 Å, and z = 16.717 Å. Utilization of the Lamarckian genetic algorithm enabled the identification of conformations with minimal energy, thereby enhancing interaction stability. After docking, the highest-affinity conformation was assessed using Discovery Studio Client 2024, followed by comparison with Tamoxifen docking outcomes on the same protein to evaluate similar binding features [13].

Molecular dynamics simulation

Molecular dynamics simulations were executed to target the highest-affinity docked conformation in complex with the Bcl-2 protein (PDB ID: 6GL8) for a duration of 100 ns, using GROMACS version 2024.4 [14]. Optimization of the protein structure involved the addition of missing atoms and residues using Swiss-PdbViewer [15]. Generation of ligand force-field parameters relied on SwissParam [16]. Solvation of the protein-ligand complex occurred within a triclinic simulation box using the SPC water model supplemented with 0.15 M NaCl. Energy minimization, comprising 50,000 steps, achieved structural refinement and charge neutralization. Equilibration phases consisted of a 200 ps NVT ensemble, followed by a 200 ps NPT ensemble, both maintained at 300 K and 1 bar. Three independent production simulations, each spanning 100 ns, were performed with a 2 fs integration step, and coordinate trajectories were recorded every 10 ns. Analysis of simulation trajectories utilized Grace software to derive critical dynamical metrics, namely root mean square deviation (RMSD), root mean square fluctuation (RMSF), radius of gyration (Rg), number of hydrogen bonds (Hbonds), and solvent-accessible surface area (SASA). Evaluation of conformational stability across the simulated complexes was performed using UCSF Chimera version 1.13.3 *via* structural superposition [17].

Molecular mechanics generalized Born surface area (MMGBSA) analysis

Calculation of binding free energies for the CPD3-6GL8 and Tamoxifen-6GL8 complexes employed the gmx_MMPBSA package in conjunction with the charmm36 force field. Polar solvation energy components were derived from the generalized Born implicit solvent model, whereas non-polar terms originated from solvent-accessible surface area estimations. The extraction of data relied on molecular dynamics trajectories comprising 125 equally spaced frames, collected every 80 ps, across an 80 ns window (spanning 20 ns to 100 ns). Application of this ensemble-averaging protocol effectively delineated differences in ligand-protein interaction energetics, thereby elucidating relative binding affinities and complex stability throughout the simulation period [18].

Assay protocol for ADMET prediction

A concise evaluation of ADMET characteristics, encompassing absorption, distribution, metabolism, excretion, and toxicity, constitutes a fundamental step in early drug discovery because pharmacokinetic liabilities and potential safety risks can be recognized before advanced development stages. Such analysis contributes to lower attrition in subsequent phases and supports prioritization of molecules with favorable therapeutic prospects. For the present analysis, ADMET profiles of CPD3 and Tamoxifen were estimated with the pkCSM platform, a computational framework based on graph-derived molecular descriptors. Use of this platform enabled the prediction of major pharmacokinetic and toxicological parameters and allowed a systematic comparison of developability-related properties for the compounds examined.

Quantum chemistry computation using the Density Functional Theory (DFT) method

Optimization of molecular geometries for CPD3 and Tamoxifen utilized the ORCA quantum chemistry package version 6.1.0. Generation of initial coordinates occurred in Avogadro, whereas subsequent visualization of molecular orbitals and associated analyses employed IboView version 20211019 [19-21]. All density functional theory calculations employed the B3LYP functional in conjunction with the 6-31G(d,p) basis set to generate accurate electronic wave functions. From the fully optimized structures, extraction of key quantum-chemical descriptors proceeded, comprising energies of the highest occupied molecular orbital (HOMO) and the lowest unoccupied molecular orbital (LUMO), the HOMO-LUMO energy gap (ΔE), chemical potential (μ), electronegativity (χ), global hardness (η), softness (σ), and electrophilicity index (ω). Determination of these reactivity parameters was approximately based on Kohn-Sham HOMO/LUMO energies within conceptual DFT to characterize the electronic properties and chemical behavior of the investigated compounds [22, 23].

RESULTS AND DISCUSSION

Molecular docking analysis

Molecular docking is a computational technique in natural product research that predicts how a natural compound binds to a protein target, aiding in the screening of potential drugs and in understanding their mechanisms. This process allows researchers to virtually screen vast libraries of natural compounds to identify promising candidates for experimental validation, saving time and resources compared to traditional laboratory methods [24, 25]. Examination of docking affinities and intermolecular interactions was conducted for three selected ligands bound to the Bcl-2 protein (PDB ID: 6GL8), using Tamoxifen as a reference. Table 1 presents the residues that constitute the binding pocket and their contributions to the interaction profile between these ligands and 6GL8, focusing on non-covalent forces, including hydrogen bonds, van der Waals forces, and hydrophobic interactions between the protein and the ligands. Ligands CPD1-CPD3 demonstrated diverse engagement patterns with Bcl-2, a pivotal modulator of apoptotic pathways in oncogenic processes. CPD1 established 10 interactions in total, incorporating 2 hydrogen bonds (Gly145, Arg146), 4 van der Waals forces (Phe104, Asp111, Phe112, Leu137), and 4 hydrophobic interactions (Tyr108, Met115, Arg146, Ala149) (Figure 2A). Participating binding site residues comprised Phe104, Tyr108, Asp111, Phe112, Leu137, Gly145, Arg146, and Ala149, resulting in a binding energy of -6.65 kcal/mol for the CPD1-6GL8 complex. CPD2 registered 9 interactions: no hydrogen bonds, 6 van der Waals forces (Phe104, Tyr108, Asp111, Phe112, Gln118, Phe153), and 3 hydrophobic interactions (Met115, Leu119, Val133). Pocket residues involved Phe104, Tyr108, Asp111, Phe112, Gln118, and Phe153, achieving a binding energy of -6.38 kcal/mol, indicative of moderate stabilization.

Table 1. Interactions between docked ligands and protein 6GL8.

Docked ligands	Binding energy (kcal/mol)	Hydrogen bond interaction	Van der Waals interaction	Hydrophobic interaction
CPD1	-6.65	Gly145, Arg146	Phe104, Asp111, Phe112, Leu137	Tyr108, Met115, Arg146, Ala149
CPD2	-6.38	-	Phe104, Tyr108, Asp111, Phe112, Gln118, Phe153	Met115, Leu119, Val133
CPD3	-7.30	Ala149	Phe104, Asp111, Phe112, Gln118, Leu137, Glu152, Phe153	Tyr108, Met115, Leu119, Val133
Tamoxifen	-7.13	Glu136	Phe104, Tyr108, Glu114, Gln118, Thr132, Val133, Leu137, Glu152, Phe153	Asp111, Phe112, Met115, Ala149

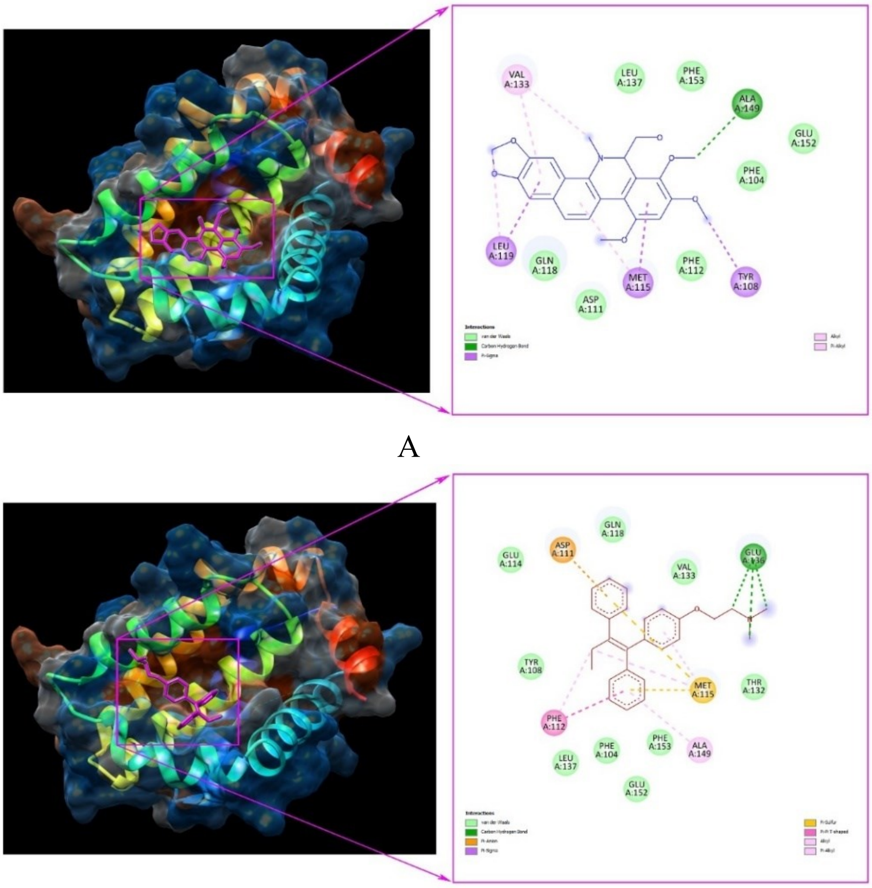

A

B

Figure 2. Molecular docking model and 2D diagram of CPD3 (A) and Tamoxifen (B) interaction with 6GL8 protein

CPD3 distinguished itself with 12 interactions: 1 hydrogen bond (Ala149), 7 van der Waals forces (Phe104, Asp111, Phe112, Gln118, Leu137, Glu152, Phe153), and 4 hydrophobic interactions (Tyr108, Met115, Leu119, Val133) (Figure 2A). Residues at the site included Phe104, Tyr108, Asp111, Phe112, Gln118, Leu137, Ala149, and Phe153, achieving the highest binding energy of -7.30 kcal/mol, indicating a robust attachment. For comparison, Tamoxifen generated 14 interactions, featuring 1 hydrogen bond (Glu136), 9 van der Waals forces (Phe104, Tyr108, Glu114, Gln118, Thr132, Val133, Leu137, Glu152, Phe153), and 4 hydrophobic interactions (Asp111, Phe112, Met115, Ala149) (Figure 2B). Binding site residues encompassed Phe104, Tyr108, Asp111, Phe112, Gln118, Leu137, Ala149, and Phe153, with an energy value of -7.13 kcal/mol. Although Tamoxifen displayed a reliable association, its comparatively less negative energy and interaction composition implied a diminished overall affinity relative to CPD3, which surpassed it in binding strength. These docking findings underscore an array of non-covalent modalities that underpin complex integrity, ranging from hydrogen bonds that enable precise atomic alignment with electronegative atoms to hydrophobic interactions that reduce aqueous exposure, thereby promoting condensed structures [26]. Van der Waals contributions provided nuanced enhancement *via* short-range interactions, augmenting the ensemble to optimize association kinetics [27]. Greater negativity in binding energy, meaning a more negative value, typically correlates with enhanced complex durability and stronger ligand sequestration at the receptor site [28].

Owing to its exceptional docking characteristics against 6GL8, characterized by an energy of -7.30 kcal/mol and 12 interactions, CPD3 surfaced as the prime contender for further molecular dynamics explorations. This superiority relative to counterparts, including CPD2 (-6.38 kcal/mol) and Tamoxifen (-7.13 kcal/mol), designates CPD3 for comprehensive evaluation of structural dynamics, energetic profiles, and amino acid involvements across temporal scales, employing Tamoxifen as a comparative reference in probing apoptosis regulation for therapeutic interventions in breast cancer.

Molecular dynamics simulation

Molecular dynamics simulation and docking are computational techniques used together in natural product research to identify and validate potential new drug candidates from natural sources. The combination of molecular docking and molecular dynamics simulation improves the accuracy and efficiency of drug discovery by helping to rank potential compounds before experimental testing [29]. Therefore, the evaluation systematically investigated RMSD, RMSF, Rg, Hbonds, and SASA metrics to determine the stability, flexibility, and solvent exposure of the CPD3-6GL8 and Tamoxifen-6GL8 complexes throughout the simulation. Consequently, the total energy and potential energy values for the CPD3-6GL8 complex were found to be -227,476 kJ/mol and -282,483 kJ/mol, respectively. For the Tamoxifen-6GL8 complex, the total energy and potential energy values were measured at -227,598 kJ/mol and -282,593 kJ/mol, respectively. The simulation system maintained equilibrium at a temperature of 300 K.

Elevated RMSD values signify substantial deviations from the baseline conformation, whereas diminished values denote preserved structural fidelity. Throughout the 100 ns trajectory, RMSD profiles for the CPD3-6GL8 and Tamoxifen-6GL8 assemblies exhibited discernible variations (Figure 3A). The CPD3-6GL8 assembly exhibited RMSD magnitudes predominantly ranging from 0.15 to 0.28 nm, with an approximate mean of 0.20 nm, indicating substantial structural stability and firm ligand anchorage within the 6GL8 pocket. Conversely, the Tamoxifen-6GL8 assembly exhibited oscillations between 0.15 and 0.25 nm, averaging approximately 0.19 nm, indicating moderate flexibility despite overall conformational resilience. Such disparities underscore a marginally enhanced equilibrium for the CPD3-6GL8 assembly compared to the Tamoxifen-6GL8 assembly, potentially attributable to optimized intermolecular interactions at the binding interface. In aggregate, the RMSD metrics indicate superior retention of the native architecture in the CPD3-6GL8 assembly compared with the Tamoxifen-6GL8 assembly over the simulation duration. Figure 3B displays RMSF profiles for the CPD3-6GL8 and Tamoxifen-6GL8 complexes over residues from approximately 1 to 2000, with magnitudes generally confined to the 0.05 to 0.25 nm interval. In the CPD3-6GL8 complex, deviations hover steadily around 0.1 nm throughout most of the polypeptide chain, indicating constrained flexibility and enhanced structural rigidity, likely due to stabilizing interactions at loci such as Phe104, Leu137, and Phe153.

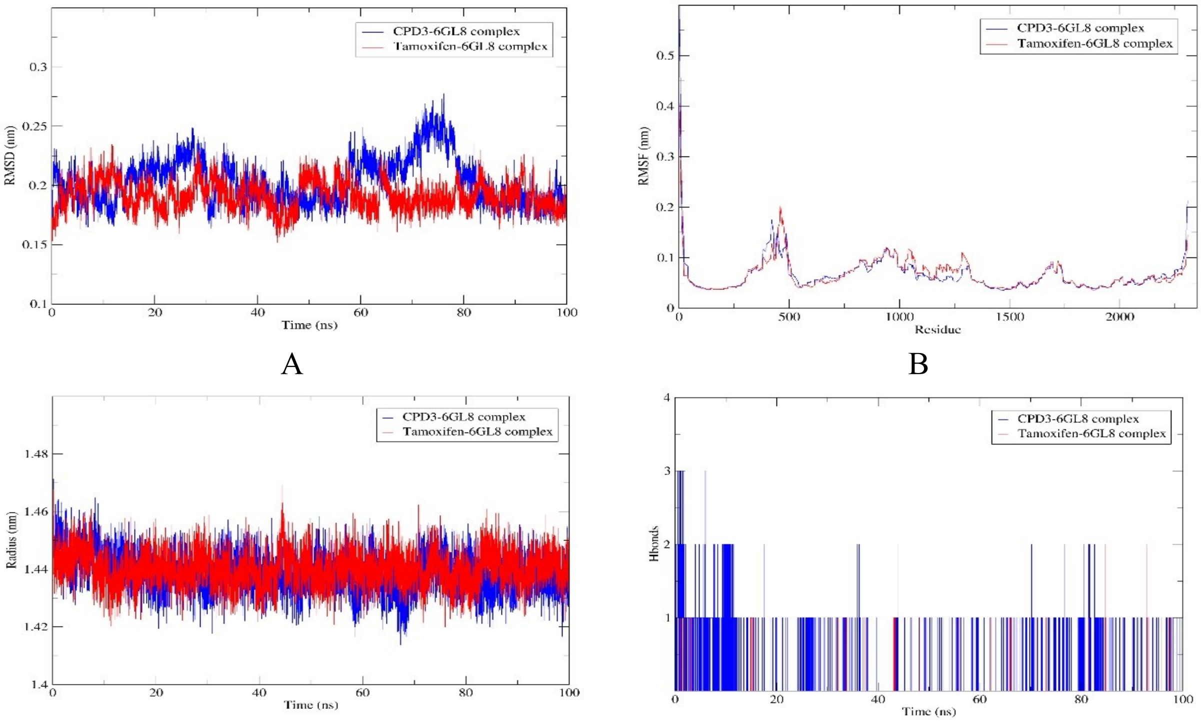

A B

C D

Figure 3. Results of MD simulation for the bindings of CPD3 (blue) and Tamoxifen (red) with 6GL8 protein. (A) RMSD, (B) RMSF, (C) Rg, (D) Hbonds, (E) SASA

The Tamoxifen-6GL8 complex exhibits an analogous pattern characterized by an average deviation of approximately 0.1 nm, accompanied by modest oscillations and correspondences, and indicating equivalent levels of conformational restraint. This congruence across both assemblies highlights the capacity of ligands to stabilize protein structure, thereby facilitating sustained interactions in functional domains. Figure 3C illustrates Rg trajectories for CPD3-6GL8 and Tamoxifen-6GL8 complexes throughout 100 ns, with both profiles exhibiting consistent fluctuations between 1.42 and 1.48 nm and an estimated average of 1.45 nm, signifying preservation of a tightly organized and compact configuration in the 6GL8 protein under ligand-bound conditions during the entire simulation period. Throughout the 100 ns duration, counts of hydrogen bonds within the CPD3-6GL8 complex varied between 1 and 3, in contrast to 0 and 2 bonds observed in the Tamoxifen-6GL8 complex (Figure 3D). These consistent associations indicate firm integration into the 6GL8 pocket for both configurations, although the CPD3-6GL8 complex generally maintained an average close to 1.8, surpassing the approximate 1.2 observed for Tamoxifen-6GL8. Such variation underscores CPD3's enhanced capacity to establish persistent connections with the protein. Evaluation of SASA profiles was performed for the CPD3-6GL8 and Tamoxifen-6GL8 complexes to assess changes in solvent exposure. Across the 100 ns timeframe, both demonstrated persistent variations, ranging roughly from 80 to 92 nm^2 with an estimated mean of 86 nm^2. These behaviors suggest minor adjustments in protein-solvent interactions in the presence of ligands, which may influence binding longevity. Equivalent extents and central values across the complexes denote equilibrated solvent interaction, signifying robust persistence at the 6GL8 binding domain despite differences in ligand attributes. A comprehensive appraisal of dynamical parameters elucidates the conformational equilibrium and associative characteristics in the CPD3-6GL8 and Tamoxifen-6GL8 complexes, highlighting the role of the 6GL8 protein in ligand coordination. Results indicate that the CPD3-6GL8 complex configuration exhibits slightly greater resilience compared to the Tamoxifen-6GL8 equivalent within the 6GL8 framework, positioning CPD3 as a promising candidate for further investigation. These observations validate CPD3's ability to maintain strong, lasting interactions with the 6GL8 protein.

Free binding energy (MMGBSA) analysis

Molecular mechanics with generalized Born surface area (MMGBSA) is a computational method used in natural product research to estimate the binding free energy of molecules and identify potential drug candidates. It combines molecular mechanics force fields with continuum solvation models, including generalized Born for polar solvents and surface area for non-polar solvation, to provide a fast and accurate method for predicting the binding affinity of a natural product or its derivative to a biological target. This approach can be complemented by techniques such as virtual screening and molecular dynamics simulations. This technique is widely used to understand the thermodynamics of a protein-ligand complex and identify key interactions that contribute to stable binding [38]. Estimation of binding free energies for the complexes employed the MMGBSA methodology with gmx_MMPBSA and the CHARMM36 force field. Selection of frames from molecular dynamics trajectories spanning 80 ns facilitated this computation. For both instances, calculation of binding free energy (ΔG_bind) adhered to ΔG_bind = G_complex - (G_receptor + G_ligand), where G_receptor denotes the energy of the free receptor, and G_ligand represents the energy of the unbound ligand. Alternatively, expression as ΔG_bind = ΔH - TΔS was observed, with ΔH encompassing enthalpic contributions and -TΔS capturing entropic penalties during association. Exclusion of entropy contributions provided a relative energy indicator suitable for affinity comparisons across similar systems. The focus of this evaluation was the 80 ns segment, with 125 frames extracted at 80 ps intervals (ranging from 20 ns to 100 ns). The implementation of this protocol yielded averaged energies that captured the temporal progression of associations, providing insights into compound potency and resilience in modeled physiological settings. The results of MMGBSA computations for the complexes are shown in Table 2. Alignment of these derived binding energies with simulation data manifests, displaying Tamoxifen-6GL8's marginally advantageous value (-22.34 ± 2.87 kcal/mol) relative to CPD3-6GL8 (-20.31 ± 3.12 kcal/mol), consistent with its somewhat enhanced overall adherence. Nevertheless, CPD3-6GL8 exhibits slightly diminished structural variability, as evidenced by its slightly higher average RMSD (approximately 0.20 nm *versus* 0.19 nm), indicating comparable positioning but a higher prevalence of hydrogen bonds, suggesting more extensive interfacial connectivity.

Table 2. Free energy of binding obtained using MMGBSA calculations.

Energy component	Average (kcal/mol)		Standard deviation	
	CPD3-6GL8	Tamoxifen-6GL8	CPD3-6GL8	Tamoxifen-6GL8
ΔVDWAΔALS	-32.15	-36.85	3.57	3.16
ΔEEL	-11.4	0.77	4.34	2.85
ΔEGB	27.53	18.82	4.75	2.77
ΔESURF	-4.29	-5.08	0.47	0.45
ΔGGAS	-43.55	-36.08	6.68	3.64
ΔGSOLV	23.24	13.73	4.43	2.75
ΔTOTAL	-20.31	-22.34	3.12	2.87

Concurrently, equivalent RMSF (around 0.1 nm), Rg (approximately 1.45 nm average), and SASA (near 86 nm^2 mean) distributions across both underscore Tamoxifen's edge in affinity likely arise from specific enthalpic factors, including van der Waals (-36.85 kcal/mol) and solvation terms (ΔGSOLV 13.73 kcal/mol), surpassing CPD3's (-32.15 and 23.24 kcal/mol, respectively). In summary, these indicators reveal Tamoxifen's modestly elevated potential for forming a stable complex with the 6GL8 protein under the assessed circumstances.

ADMET prediction analysis

ADMET profiling suggested that CPD3 combines favorable oral absorption with a distribution pattern less indicative of central nervous system exposure than tamoxifen, and it shows fewer mutagenicity and cardiotoxicity alerts in the current prediction panel. Early ADMET evaluation is valuable because permeability, transport, metabolism, and toxicity often influence developability as strongly as target affinity [30]. The ADMET prediction results are shown in Table 3. Regarding absorption, CPD3 showed slightly better predicted aqueous solubility than Tamoxifen (log S -5.136 *vs*. -5.929), while both compounds maintained high intestinal absorption (98.629% and 96.885%, respectively). Caco-2 permeability was favorable for both ligands, with values above the usual high-permeability threshold (1.242 for CPD3; 1.065 for Tamoxifen). Skin permeability was nearly identical, suggesting similarly limited transdermal passage. A notable difference was that CPD3 was predicted not to be a P-glycoprotein substrate, whereas Tamoxifen was, although both were predicted to inhibit P-glycoprotein I and II. This may indicate reduced efflux susceptibility for CPD3, but possible transporter-related interaction risks still require experimental confirmation [31]. Distribution parameters differentiated the compounds more clearly. CPD3 showed a low predicted steady-state volume of distribution (log VDss = -0.493), whereas Tamoxifen had a much higher value (0.830), suggesting broader tissue distribution for the reference drug [32]. Both compounds had low and similar unbound fractions in plasma (Fu 0.097 for CPD3; 0.093 for Tamoxifen), consistent with extensive plasma protein binding. Brain exposure descriptors also favored CPD3 as a more peripheral compound: log BB/log PS values were -0.342/-3.100 for CPD3 *versus* 1.329/-1.473 for Tamoxifen, indicating substantially lower BBB penetration and CNS access for CPD3.

The Boiled-egg model supported this trend. CPD3 fell in the white region but outside the yellow yolk, consistent with high gastrointestinal absorption and limited passive BBB permeation, whereas Tamoxifen was located in the yolk region, indicating greater passive brain entry (Figure 4). However, because the plot showed both compounds as P-glycoprotein substrates despite the tabulated output identifying only Tamoxifen as such, transporter interpretation should rely on the table, while the Boiled-egg plot is best used here to assess GI absorption and BBB region placement [33].

Table 3. Predicted ADMET properties of CPD3 and Tamoxifen

ADMET properties	Unit	CPD3	Tamoxifen
Water solubility	(Log mol/L)	-5.136	-5.929
CaCo2 permeability	(Log Papp in 10-6 cm/s)	1.242	1.065
Intestinal absorption (human)	(% Absorbed)	98.629	96.885
Skin permeability	(Log Kp)	-2.736	-2.737
P-glycoprotein substrate	Yes/No	No	Yes
P-glycoprotein I inhibitor	Yes/No	Yes	Yes
P-glycoprotein II inhibitor	Yes/No	Yes	Yes
VDss	(Log L/kg)	-0.493	0.830
Fraction unbound (human)	(Fu)	0.097	0.093
BBB permeability	(Log BB)	-0.342	1.329
CNS permeability	(Log PS)	-3.100	-1.473
CYP2D6 substrate	Yes/No	No	No
CYP3A4 substrate	Yes/No	Yes	Yes
CYP1A2 inhibitor	Yes/No	No	Yes
CYP2C19 inhibitor	Yes/No	Yes	No
CYP2C9 inhibitor	Yes/No	Yes	No
CYP2D6 inhibitor	Yes/No	No	Yes
CYP3A4 inhibitor	Yes/No	Yes	No
Total clearance	(Log ml/min/kg)	0.456	0.556
Renal OCT2 substrate	Yes/No	No	No
AMES toxicity	Yes/No	No	Yes
Max. tolerated dose (human)	(Log mg/kg/day)	0.257	0.313
hERG I inhibitor	Yes/No	No	Yes
hERG II inhibitor	Yes/No	Yes	Yes
Oral rat acute toxicity (LD50)	(mol/kg)	2.622	2.285
Oral rat chronic toxicity (LOAEL)	(Log mg/kg_bw/day)	1.035	0.41
Hepatotoxicity	Yes/No	No	No
Skin sensation	Yes/No	No	No
Tetrahymena pyriformis toxicity	(Log µg/L)	0.288	0.316
Minnow toxicity	(Log mM)	-0.892	0.600

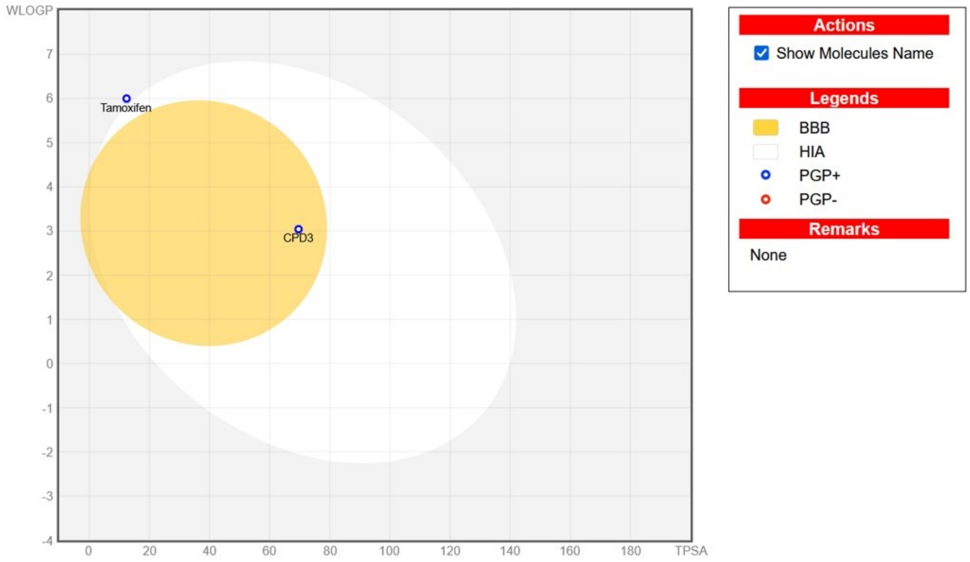

Figure 4. Boiled-egg plot of the selected compounds, generated from Swiss ADME

Metabolically, both compounds were predicted to be CYP3A4 substrates rather than CYP2D6 substrates, suggesting a role for CYP3A4 in clearance. Their inhibition profiles differed. CPD3 was predicted to inhibit CYP2C19, CYP2C9, and CYP3A4, but not CYP1A2 or CYP2D6 [34]. Tamoxifen showed the opposite pattern across several isoforms, inhibiting CYP1A2 and CYP2D6 but not CYP2C19, CYP2C9, or CYP3A4. These results suggest distinct drug-drug interaction risks rather than a clearly safer metabolic profile for either compound.

Excretion differences were modest. Total clearance was slightly lower for CPD3 than for Tamoxifen (0.456 vs. 0.556 log ml/min/kg), suggesting somewhat slower elimination. Neither compound was predicted to be a renal OCT2 substrate [35]. Together with the low unbound fraction, this suggests CPD3 may maintain systemic exposure while distributing less extensively into tissues than Tamoxifen.

The toxicity panel favored CPD3 in several important endpoints. CPD3 was predicted to be Ames-negative, whereas Tamoxifen was Ames-positive, indicating lower mutagenic concern. CPD3 was also negative for hERG I inhibition, while tamoxifen carried a positive hERG I alert; both compounds remained positive for hERG II inhibition. Both were predicted to be non-hepatotoxic and non-sensitizing to skin. Thus, CPD3 appears to have a more favorable early safety profile, although electrophysiological follow-up remains necessary due to the retained hERG II signal [36]. Quantitative toxicity endpoints provided additional detail. Both compounds showed low predicted maximum tolerated doses in humans, below the common threshold. CPD3 also showed slightly better acute and chronic oral toxicity profiles in rats, with a higher LD50 and LOAEL than Tamoxifen [37]. *Tetrahymena pyriformis* toxicity values were comparable for both compounds, whereas Minnow toxicity was less favorable for CPD3, indicating a stronger predicted aquatic toxicity signal.

Overall, CPD3 demonstrated a pharmacokinetic and safety profile supportive of further development as a breast cancer lead. It combined excellent oral absorption, high Caco-2 permeability, strong predicted intestinal uptake, limited BBB penetration, lack of Ames toxicity, and absence of an hERG I alert. However, low solubility, strong plasma binding, CYP inhibition liabilities, persistent hERG II risk, and unfavorable Minnow toxicity remain relevant concerns. Taken together, the ADMET and BOILED-Egg results support CPD3 as a promising compound with improved early safety features over Tamoxifen, while still requiring experimental validation of transporter, metabolic, cardiac, and ecological liabilities.

Quantum chemistry computation using the DFT method

DFT is a powerful quantum-mechanical method used in natural product research to computationally model and predict the electronic structure and properties of molecules. It offers a balance between accuracy and computational cost, making it ideal for studying complex natural products, and is used to investigate properties like chemical reactivity, host-guest interactions, and solubilization mechanisms [39]. Quantum chemistry computations are frequently performed after molecular docking and dynamics simulations to achieve high accuracy in validating and refining the results of classical mechanics methods. In this study, DFT calculations were employed to examine the electronic properties and potential reactivity of CPD3 and Tamoxifen, drawing from the specified descriptors. The derived values encompass energies of the highest occupied molecular orbitals (EHOMO), lowest unoccupied molecular orbitals (ELUMO), energy gap (ΔE), chemical potential (μ), electronegativity (χ), hardness (η), softness (σ), and electrophilicity index (ω). These EHOMO and ELUMO energies offer key insights into electron arrangements, molecular stability, and interaction tendencies within the compounds. EHOMO gauges the ease of electron release, while ELUMO assesses the ability to accept electrons. For CPD3, EHOMO stands at -9.2815 eV, which is lower than Tamoxifen's -8.2093 eV, suggesting that CPD3 is less prone to electron donation and exhibits greater stability against oxidation (Figure 5). Conversely, CPD3's ELUMO of 0.1510 eV is notably below Tamoxifen's 3.2074 eV, indicating CPD3's enhanced aptitude for electron capture. The energy gap (ΔE), calculated as ELUMO less EHOMO, reflects overall durability and chemical responsiveness; smaller gaps correlate with elevated activity and adaptability, whereas larger ones suggest enhanced resilience (Table 4). CPD3's ΔE of 9.4325 eV is smaller compared to Tamoxifen's ΔE of 11.4167 eV, implying that CPD3 has comparatively lower endurance but increased potential for reactions. The ionization potential (IP), defined as -EHOMO, is the energy required to detach an electron; higher values indicate greater oxidation resistance.

Table 4. Quantum descriptors of CPD3 and Tamoxifen.

Molecule	EHOMO (eV)	ELUMO (eV)	ΔE (eV)	μ (eV)	χ (eV)	η (eV)	σ (eV^{-1})	ω (eV)
CPD3	-9.2815	0.1510	9.4325	-4.5653	4.5653	4.7163	0.2120	2.2095
Tamoxifen	-8.2093	3.2074	11.4167	-2.5010	2.5010	5.7084	0.1752	0.5479

EHOMO (eV): highest occupied molecular orbitals; ELUMO (eV): lowest unoccupied molecular orbitals; ΔE (eV): energy gap; μ (eV): chemical potential; χ (eV): electronegativity; η (eV): hardness; σ (eV^{-1}): softness; ω (eV): electrophilicity index.

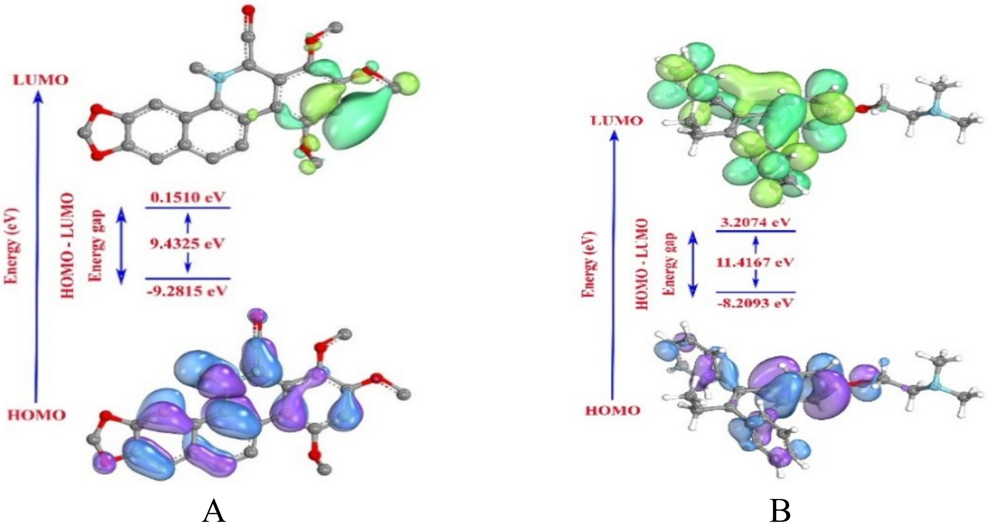

Figure 5. HOMO and LUMO surface diagrams of CPD3 (A) and Tamoxifen (B)

Electron affinity (EA), as measured by -ELUMO, quantifies the ease of electron incorporation; higher values indicate greater electron affinity. Thus, CPD3 shows an IP of 9.2815 eV and EA of -0.1510 eV, *versus* Tamoxifen's IP of 8.2093 eV and EA of -3.2074 eV, highlighting CPD3's superior resistance to electron loss alongside modestly improved electron attraction. Tamoxifen, in contrast, is more amenable to electron release but exhibits weaker electron affinity. Hardness (η), obtained from ΔE/2, evaluates resistance to shifts in electron density, and softness (σ), as 1/η, indicates flexibility in chemical engagements. CPD3 registers hardness of 4.7163 eV and softness of 0.2120 eV^{-1}, compared to Tamoxifen's hardness of 5.7084 eV and softness of 0.1752 eV^{-1}, indicating that CPD3 is more accommodating to electronic adjustments (Figure 4). Electronegativity (χ), determined by (IP + EA)/2, quantifies the pull on electrons in bonds. CPD3's χ at 4.5653 eV exceeds Tamoxifen's 2.5010 eV, revealing CPD3's greater affinity for electrons in shared pairs. Chemical potential (μ), equivalent to -χ, directs the flow of electrons; lower (more negative) values promote intake. Accordingly, CPD3's μ of -4.5653 eV is more negative than Tamoxifen's -2.5010 eV, underscoring CPD3's stronger drive toward electron accumulation. Lastly, the electrophilicity index (ω), defined as $\mu^2/(2\eta)$, quantifies the tendency to attract electrons, with larger values indicating greater electrophilicity. CPD3's ω of 2.2095 eV substantially outpaces Tamoxifen's 0.5479 eV, proposing CPD3 may interact more dynamically as an electrophile with nearby species.

CONCLUSION

This study investigated isoquinoline alkaloids from *H. japonica* as potential breast cancer inhibitors, with a focus on the Bcl-2 protein (6GL8), a key regulator of cell death. CPD3 exhibited stronger docking performance (-7.30 kcal/mol) than Tamoxifen (-7.13 kcal/mol), with 12 interactions, including 1 hydrogen bond and 7 van der Waals interactions. Over 100 ns simulations, the CPD3-6GL8 complex demonstrated solid stability, with a mean RMSD of around 0.20 nm, a radius of gyration (Rg) of approximately 1.45 nm, and approximately 1.8 hydrogen bonds, compared to Tamoxifen's 0.19 nm RMSD and about 1.2 bonds. MMGBSA results indicated stronger binding for CPD3 (-20.31 ± 3.12 kcal/mol) than for Tamoxifen (-22.34 ± 2.87 kcal/mol), supported by van der Waals terms (-32.15 kcal/mol) and solvation (ΔGSOLV 23.24 kcal/mol). ADMET prediction suggested that CPD3 combines excellent intestinal absorption, favorable permeability, limited BBB and CNS penetration, absence of AMES toxicity, and no hERG I inhibition, indicating more favorable early safety and pharmacokinetic profile than Tamoxifen, although potential CYP-mediated drug-drug interactions, hERG II liability, and ecological toxicity concerns remain. DFT analysis revealed CPD3's electronic properties, with EHOMO at -9.2815 eV, ΔE of 9.4325 eV, and ω of 2.2095 eV, compared to Tamoxifen's (-8.2093 eV, 11.4167 eV, and 0.5479 eV). Overall, these outcomes highlight CPD3 as a viable option for breast cancer therapy, meriting additional refinement and testing in cancer research.

REFERENCES

1. G. Colonna, *Cancers*, **17**, 2102 (2025).
2. M. J. Thun, J. O. DeLancey, M. M. Center, A. Jemal, E. M. Ward, *Carcinogenesis*, **31**, 100 (2010).
3. F. Bray, M. Laversanne, H. Sung, J. Ferlay, R. L. Siegel, I. Soerjomataram, A. Jemal, *CA. Cancer J. Clin.*, **74**, 229 (2024).
4. S. D. Nathanson, M. Detmar, T. P. Padera, L. R. Yates, D. R. Welch, T. C. Beadnell, A. D. Scheid, E. D. Wrenn, K. Cheung, *Clin. Exp. Metastasis*, **39**, 117 (2022).
5. E. Carvalho, S. Canberk, F. Schmitt, N. Vale, *Cancers*, **17**, 1102 (2025).
6. A. Kawiak, A. Kostecka, *Cancers*, **14**, 279 (2022).
7. S. Qian, Z. Wei, W. Yang, J. Huang, Y. Yang, J. Wang, *Front. Oncol.*, **12**, 985363 (2022).
8. H. Azmat, J. Faridi, H. M. Habib, U. J. Bugti, A. K. Sheikh, S. K. Riaz, *J. Cancer Res. Ther.*, **18**, S313 (2022).
9. A. Y. Khan, G. Suresh Kumar, *Biophys. Rev.*, **7**, 407 (2015).
10. X. Yang, T. Bu, Y. Ma, X. Yu, Z. Gong, J. Wang, X. Liu, J. Jenis, H. Hu, X. Miao, X. Shang, *Ind. Crops Prod.*, **234**, 121591 (2025).
11. Z. Cao, S. Zhu, Z. Xue, F. Zhang, L. Zhang, Y. Zhang, Y. Guo, G. Zhan, X. Zhang, Z. Guo, *Phytochemistry*, **202**, 113321 (2022).
12. J. B. Murray *et al.*, *ACS Omega*, **4**, 8892 (2019).
13. H. D. Nguyen, *Not. Sci. Biol.*, **17**, 12642 (2025).
14. D. Van Der Spoel, E. Lindahl, B. Hess, G. Groenhof, A. E. Mark, H. J. C. Berendsen, *J. Comput. Chem.*, **26**, 1701 (2005).
15. N. Guex, M. C. Peitsch, *Electrophoresis*, **18**, 2714 (1997).
16. V. Zoete, M. A. Cuendet, A. Grosdidier, O. Michielin, *J. Comput. Chem.*, **32**, 2359 (2011).
17. E. F. Pettersen, T. D. Goddard, C. C. Huang, G. S. Couch, D. M. Greenblatt, E. C. Meng, T. E. Ferrin, *J. Comput. Chem.*, **25**, 1605 (2004).
18. H. D. Nguyen, *Phys. Chem. Res.*, **13**, 783 (2025).
19. F. Neese, *WIREs Comput. Mol. Sci.*, **15**, e70019 (2025).
20. G. Knizia, J. E. M. N. Klein, *Angew. Chemie Int. Ed.*, **54**, 5518 (2015).
21. M. D. Hanwell, D. E. Curtis, D. C. Lonie, T. Vandermeersch, E. Zurek, G. R. Hutchison, *J. Cheminform.*, **4**, 17 (2012).
22. J. Luo, Z. Q. Xue, W. M. Liu, J. L. Wu, Z. Q. Yang, *J. Phys. Chem. A*, **110**, 12005 (2006).
23. R. Das, J.L. Vigneresse, P. K. Chattaraj, *Int. J. Quantum Chem.*, **114**, 1421 (2014).
24. I. Asiamah, S. A. Obiri, W. Tamekloe, F. A. Armah, L. S. Borquaye, *Sci. African*, **20**, e01593 (2023).
25. P. C. Agu, C. A. Afiukwa, O. U. Orji, E. M. Ezeh, I. H. Ofoke, C. O. Ogbu, E. I. Ugwuja, P. M. Aja, *Sci. Rep.*, **13**, 13398 (2023).
26. R. Patil, S. Das, A. Stanley, L. Yadav, A. Sudhakar, A. K. Varma, *PLoS One*, **5**, e12029 (2010).
27. G. Bitencourt-Ferreira, M. Veit-Acosta, W. F. de Azevedo, Van der Waals potential in protein complexes (Docking screens for drug discovery), Springer, New York, 2019.
28. N. T. Issa, E V Badiavas, S. Schürer, *J. Invest. Dermatol.*, **139**, 2400 (2019).
29. A. R. Alanzi, B. A. Alhaidhal, R. M. Aloatibi, *Sci. Rep.*, **15**, 16385 (2025).
30. D. E. Pires, T. L. Blundell, D. B. Ascher, *J. Med. Chem.*, **58**, 4066 (2015).
31. G. Falcón-Cano, C. Molina, M. Á. Cabrera-Pérez, *Pharmaceutics*, **14**, 1998 (2022).
32. M. Gupta, J. Feng, G. Bhisetti, *Molecules*, **29**, 1264 (2024).
33. R. Kato, W. Zeng, V. B. Siramshetty, J. Williams, M. Kabir, N. Hagen, E. C. Padilha, A. Q. Wang, E. A. Mathé, X. Xu, P. Shah, *Front. Pharmacol.*, **14**, 1291246 (2023).
34. J. Lee, J. L. Beers, R. M. Geffert, K. D. Jackson, *Biomolecules*, **14**, 99 (2024).
35. K. Korzekwa, S. Nagar, *Drug Metab. Dispos.*, **51**, 532 (2023).
36. P. Delre, G. J. Lavado, G. Lamanna, M. Saviano, A. Roncaglioni, E. Benfenati, G. F. Mangiatordi, D. Gadaleta, *Front. Pharmacol.*, **13**, 951083 (2022).
37. A. L. Karmaus, K. Mansouri, K. T. To, B. Blake, J. Fitzpatrick, J. Strickland, G. Patlewicz, D. Allen, W. Casey, N. Kleinstreuer, *Toxicol. Sci.*, **188**, 34 (2022).
38. M. E. Valdés-Tresanco, M. S. Valdés-Tresanco, E. Moreno, P. A. Valiente, *J. Phys. Chem. B*, **127**, 944 (2023).
39. H. Guan, H. Sun, X. Zhao, *Int. J. Mol. Sci.*, **26**, (2025).

Bulgarian Chemical Communications, Volume 58, Issue 2 (pp. 154-161) 2026 *DOI: 10.34049/bcc.58.2.5735*

$NiFe_2O_4$@Cellulose-PEG nanocomposite: A novel reusable catalyst for straightforward one-pot synthesis of benzopyran derivatives

S. M. Awari[1], V. V. Vikhe[1], V. K. Vikhe[2], A. G. Gadhave[1], B. K. Uphade[1]*

[1]Department of Chemistry and Research Centre, Padmashri Vikhe Patil College of Arts, Science & Commerce,
Pravaranagar, (Affiliated to Savitribai Phule Pune University, Pune),413713, Dist: Ahilyanagar, Maharashtra, India
[2]Sir Visvesvaraya Institute of Technology, Chincholi, Tal: Sinnar Dist: Nashik, 422101. Maharashtra, India

Received: December 09, 2025; Revised: March 26, 2026

This work presents the effective synthesis, characterization, and catalytic application of a novel $NiFe_2O_4$@Cellulose-PEG nanocomposite. The latter was synthesized by a simple co-precipitation method, and FT-IR, XRD, EDX, and SEM analysis techniques were used to characterize it. As an effective and affordable nanocatalyst, $NiFe_2O_4$@Cellulose-PEG effectively assisted the production of benzopyran derivatives by one-pot condensation of aromatic aldehydes, dimedone, and malononitrile. The yield of benzopyran was determined utilizing a number of reaction parameters, including catalyst quantity, solvent type, temperature, and reaction duration. By using ^1H NMR, ^{13}C NMR and MS studies, some of the synthesized benzopyran derivatives were described. The catalyst was reusable for up to four reaction sessions.

Graphical abstract

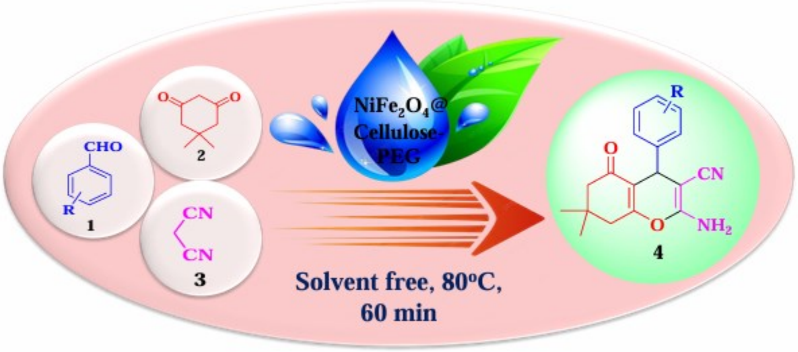

Keywords: $NiFe_2O_4$@Cellulose-PEG, nanocomposite, recyclable catalyst, one-pot multicomponent synthesis, solvent-free, benzopyran.

INTRODUCTION

Research on the synthesis and application of nanomaterials is very intense because of their special physical and chemical characteristics. These materials are significant primarily because of their scientific and technological value. Numerous researchers are drawn to spinel ferrites because of their size, shape, magnetic separation property, reusability, and distinct crystal structure, all of which influence their chemical and physical characteristics. Spinel ferrites and their nanocomposites have grown in popularity in recent years. These materials have several benefits, and their magnetic qualities, which make them easily recovered, allow for recurrent use because of their exceptional catalytic qualities, stability, and reusability. The common formula of spinel ferrite nanoparticles is MFe_2O_4, where M is a transition metal cation [1-4]. Recent years have seen a significant increase in interest in spinel ferrites due to their high chemical and thermal durability, numerous uses in various industries, and superparamagnetic characteristics at the NP scale [5]. Nickel ferrite is one of the most thoroughly investigated spinel ferrites due to its strong magnetic properties and wide variety of uses. Nanosized nickel ferrite possesses favorable properties in addition to the other ferrites that make up a sizable component of magnetic ceramic materials, low-loss materials, soft magnets, and the main parts of high-frequency power transformers. The magnetic characteristics of nickel ferrite are altered by the placement of cations in empty areas [6-8]. This is a crucial element to impress the researchers. Fe^{3+} ions in tetrahedral sites, Fe^{3+} and Ni^{2+} ions in equal amounts at octahedral sites have antiparallel spin magnetic moments, which explains the ferromagnetic nature of this material.

---

* To whom all correspondence should be sent:
Email: *bhagwatuphade@gmail.com*

One of the most adaptable and technologically relevant soft ferrite materials is nickel ferrite which has low conductivity and thus lowers electrical losses. It has high electrical stability, catalytic activity, and is abundant in nature [9-12].

Biopolymer nanocomposites have attracted a lot of interest because of their unique physicochemical properties and small, inexpensive processing size. Like other natural polysaccharides, cellulose is known to be a harmless, biodegradable, and biocompatible polysaccharide. Because of these qualities, cellulose shows promise as a material for medication delivery and biological applications [13-15].

A well-reported technique for synthesis of physiologically active heterocycles is the multicomponent reaction (MCR). The primary benefits of MCRs over traditional multistep protocols are: high efficiency, low cost, experimental simplicity, avoidance of large amounts of waste, and reduction of labor costs, reaction times, and waste production [16-18]. MCRs are one-pot processes in which at least three or more compounds react together to form the target product without the need for intermediate separation and purification. With the use of green or reusable catalysts and solvent-free conditions, it is possible to achieve ideal synthesis based on the green principles through the development of multicomponent strategies [19, 20].

Tetrahydrobenzo[*b*]pyran derivatives are a significant family of medicines and heterocyclic medications. They show numerous biological and pharmacological activities, including anticancer, diuretic, anticoagulant, spasmolytic, antimalarial, antitumor, antidiabetic, and anti-anaphylactic effects [21-25]. The synthesis of tetrahydrobenzo[*b*]pyran heterocycles has been accomplished using a variety of catalysts such as $Ni(NO_3)_2{\cdot}6H_2O$ [26], Fe_3O_4@xanthan gum [27], SiO_2-Pr-SO_3H [28], $NH_4Al(SO_4)_2{\cdot}12H_2O$ (Alum) [29], $ZnFe_2O_4$@alginic acid [30], nano-SiO_2/DBN [31], DAIL@SiO_2 [32],L-proline [33], DABCO [34], CuONPs [35], K_2CO_3[36], sodium benzoate [37], NH_4OAc [38], PPA-SiO_2 [39], and NiO@HNTs-SO_3H [40], each approach having its own advantages and disadvantages. Here, in continuation of our works [41-46], we investigated the catalytic activity of a novel $NiFe_2O_4$@Cellulose-PEG as a heterogeneous nanocatalyst in the synthesis of tetrahydrobenzo [b]pyran derivatives.

EXPERIMENTAL

The reagents and chemicals used in this work were purchased from Merck and used without further purification. Distilled water was used throughout all work. Using thin-layer chromatography, the progress of the organic reaction was tracked. Melting points of all compounds were ascertained in an open capillary tube. A Bruker Avance NEO 500 MHz spectrometer was used to record the NMR spectra in DMSO with TMS as an internal standard.

Synthesis of $NiFe_2O_4$@Cellulose-PEG

$Fe(NO_3)_3{\cdot}6H_2O$ and $Ni(NO_3)_2{\cdot}6H_2O$ were mixed in 100 ml of distilled water at a molar ratio of 2:1 under stirring for 30 min. Next, 1 g of cellulose powder was added to the solution. 20 ml of 5% NaOH solution was added under constant stirring to adjust pH of the solution between 9 to 10. After 2 h, 1 ml of polyethylene glycol was added to the solution and stirred for more 2 h on a magnetic stirrer. The black precipitate obtained was separated using an external magnet and washed several times with deionized water until neutral pH. The prepared $NiFe_2O_4$@Cellulose-PEG nanocomposite was dried in an oven at 70 °C for 24 h and calcined at 400 °C for 2 h [47].

Synthesis of benzopyran derivatives (4a-k) using $NiFe_2O_4$@Cellulose-PEG

A mixture of substituted benzaldehyde **1a-k** (1 mmol), dimedone **2** (1 mmol), malononitrile **3** (1 mmol), and $NiFe_2O_4$@Cellulose-PEG catalyst (40 mg) was added to a 50 mL round-bottom flask. The combination was heated for the duration shown in Scheme 1 at 80°C in an oil bath without use of solvents. TLC was used to track the reaction progress. After the completion of the reaction, 10 ml of ethanol was added to the reaction mixture to extract the $NiFe_2O_4$@Cellulose-PEG catalyst and the solid product was filtered out. The crude product was recrystallized from ethanol. Melting points and spectroscopic information were used to characterize the products and compare them to those documented in the literature.

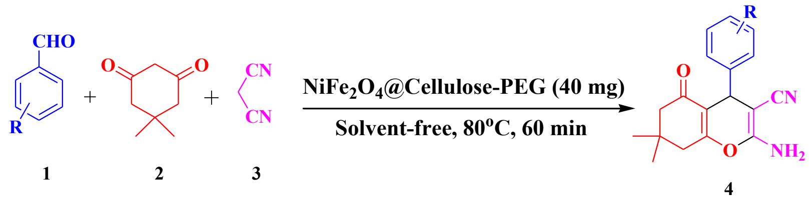

Scheme 1. $NiFe_2O_4$@Cellulose-PEG catalyzed synthesis of tetrahydrobenzo[*b*]pyran derivatives

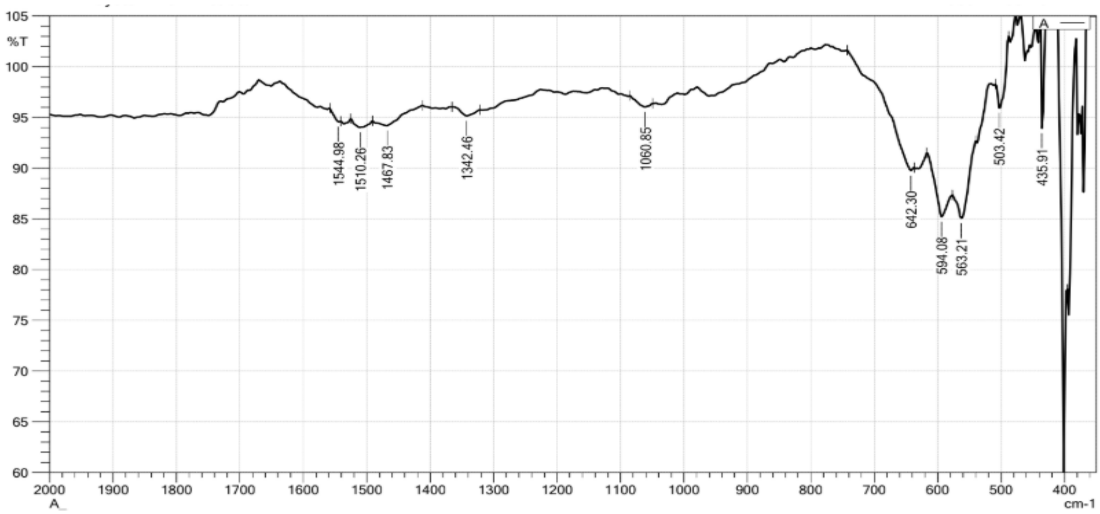

Figure 1. FT-IR spectrum of $NiFe_2O_4$@Cellulose-PEG

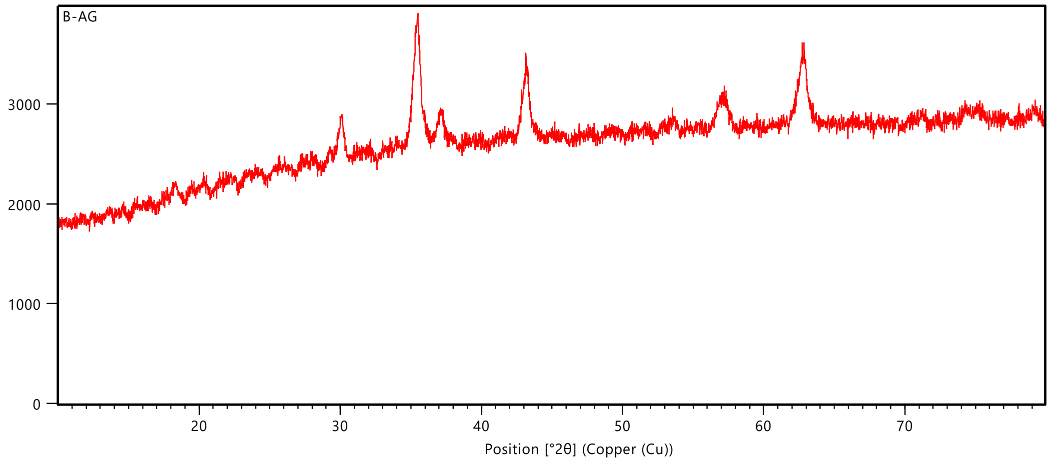

Figure 2. XRD spectrum of $NiFe_2O_4$@Cellulose-PEG

RESULTS AND DISCUSSION

Catalyst characterization

The synthesized nanocatalyst was characterized using a variety of analytical techniques, including Fourier transform infrared (FT-IR) spectroscopy, X-ray powder diffraction (XRD), energy dispersive X-ray spectroscopy (EDX), and field emission scanning electron microscopy (FE-SEM).

FT-IR analysis

The formation of $NiFe_2O_4$@Cellulose-PEG nanocatalyst was confirmed by infrared spectra captured between 400 and 2000 cm^{-1} displayed in Figure 1. The two absorption bands of $NiFe_2O_4$@Cellulose-PEG nanocomposites are visible in the 400-1000 cm^{-1} range. The stretching vibrations of octahedral complexes are associated with the lower absorption band at 435.91 cm^{-1}, while the stretching vibrations of tetrahedral complexes are associated with the higher absorption band at 594.08 cm^{-1}. The absorption band observed at 1510.26 cm^{-1} is due to cellulose doping [48, 49].

XRD analysis

The crystalline structure of the synthesized $NiFe_2O_4$@Cellulose-PEG nanocomposite was confirmed by using the X-ray diffraction (XRD) technique displayed in Figure 2. Diffraction peaks were observed at 2θ values 30.03°, 35.41°, 37.09°, 44.12°, 57.05°, 64.71° (JCPDS Card No. 742081). The sharp and intense peaks indicate a high degree of crystallinity of $NiFe_2O_4$@Cellulose-PEG nanocomposite [50, 51].

EDX analysis

The composition of the synthesized $NiFe_2O_4$@Cellulose-PEG nanocomposite was studied using EDX analysis (see Figure 3). The analysis shows 52.80 wt % and 41.33 at % of iron, 36.88 wt % and 27.34 at % of nickel, 6.44 wt % and 17.52 at % of oxygen, and 3.87 wt % and 14.02 at % of carbon, which supports the formation of $NiFe_2O_4$@Cellulose-PEG nanocomposite.

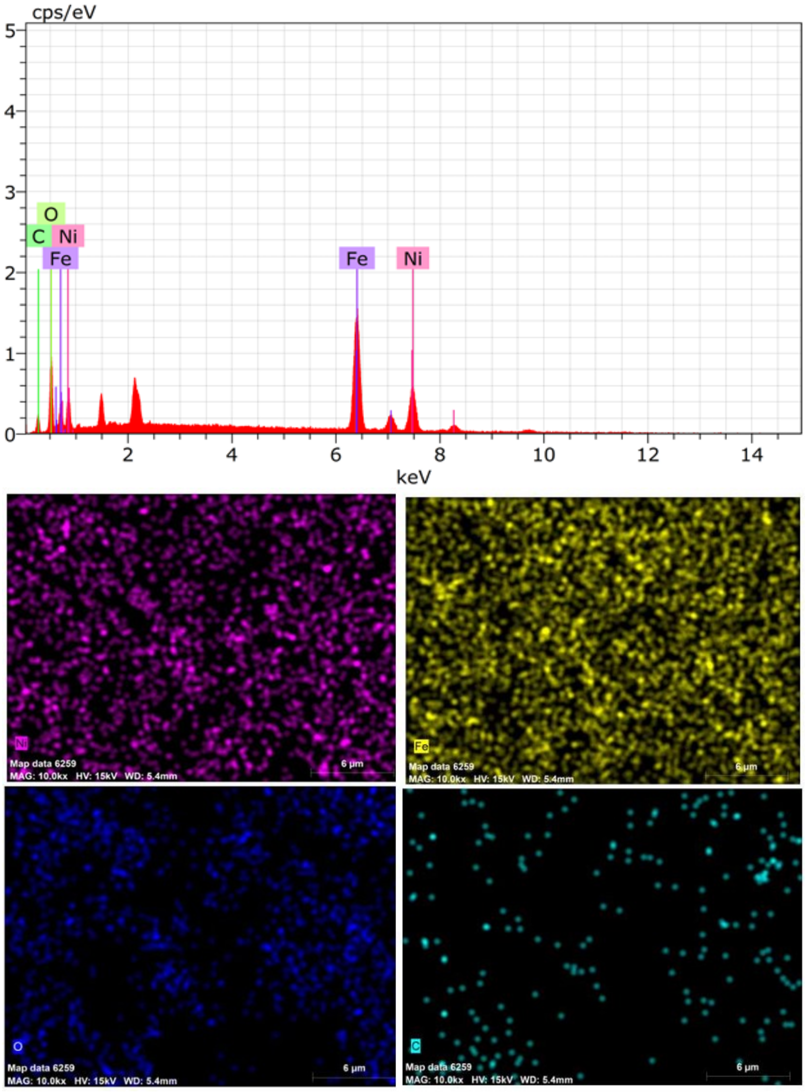

Figure 3. EDX analysis and EDX-MAP images of $NiFe_2O_4$@Cellulose-PEG

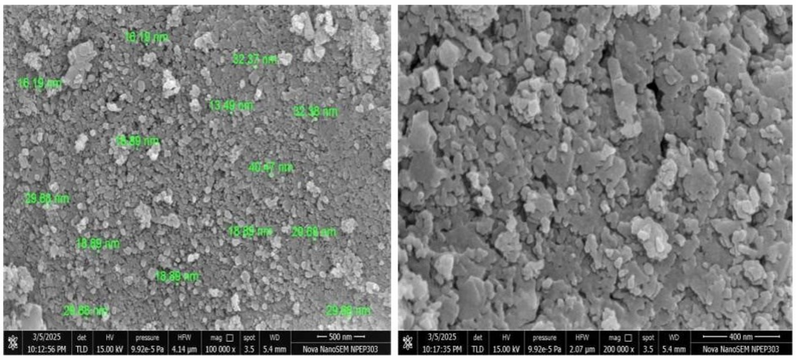

Figure 4. FE-SEM images of $NiFe_2O_4$@Cellulose-PEG

FE-SEM analysis

The surface morphology of the synthesized $NiFe_2O_4$@Cellulose-PEG nanocomposite was investigated using field emission scanning electron microscopy (FE-SEM). The SEM image shown in Figure 4 shows that the particles are uniform and square-shaped, the average particle size is 24.28 nm.

Application of $NiFe_2O_4$@Cellulose-PEG nanocatalyst in the synthesis of benzopyran derivatives

In order to assess the catalytic efficiency of the newly synthesized $NiFe_2O_4$@Cellulose-PEG nanocatalyst, we chose the model reaction between benzaldehyde **1a**, dimedone **2**, and malononitrile **3** for the synthesis of the benzopyran derivative **4a** under eco-friendly conditions. Several reaction parameters, including temperature and solvents, were optimized (see Table 1). The reaction was conducted under reflux in different solvents such as H_2O, EtOH, and aq. EtOH, which led to insufficient product yield. Subsequently, the model reaction was conducted at various temperatures from 80 °C to 100 °C, without the use of solvents. The optimal temperature for the synthesis of benzopyran derivatives was 80°C without the use of any solvents (Table 1, entry 7). The reaction needed less time to finish and produced a larger product yield.

Table 1. Optimization of reaction conditions for the synthesis of benzopyran derivatives using $NiFe_2O_4$@Cellulose-PEG as a catalyst

Entry	Conditions	Temp. (°C)	Time (min)	Yield (%)[a]
1	H_2O	RT	120	No reaction
2	EtOH	RT	120	No reaction
3	H_2O:EtOH	RT	120	No reaction
4	H_2O	Reflux	60	22
5	EtOH	Reflux	60	36
6	H_2O:EtOH	Reflux	60	43
7	Solvent-free	80	60	94
8	Solvent-free	100	60	94
9	Solvent-free	80	30	91

[a]Reaction conditions: benzaldehyde **1a** (1 mmol), dimedone **2** (1 mmol), malononitrile **3** (1 mmol), and $NiFe_2O_4$@Cellulose-PEG catalyst (40 mg).

Spectral data of some tetrahydrobenzo[b]pyran derivatives

2-amino-5,6,7,8-tetrahydro-7,7-dimethyl-4-(4-nitrophenyl)-5-oxo-4H-chromene-3-carbonitrile (4b). IR (KBr, cm^{-1}): 3315, 3176, 2182, 1671, 1416, 1520, 1352, 1218, ^1H NMR (500 MHz, DMSO, δ ppm): 0.98 (*s*, 3H), 1.06 (*s*, 3H), 2.12 (*d*, 1H), 2.24 (*d*, 1H), 2.51 (*s*, 2H), 4.38 (*s*, 1H), 7.16 (*s*, 2H), 7.45 (*d*, 2H), 8.16 (*d*, 2H), ^{13}C NMR (125 MHz, DMSO, δ ppm): 26.8, 28.1, 31.6, 35.5, 39.0, 49.7, 56.9, 111.6, 119.1, 123.5, 128.4, 146.1, 152.1, 158.4, 162.9, 195.5, MS for $C_{18}H_{17}N_3O_4$ (m/z): 340.1[M + H]$^+$.

2-amino-4-(4-chlorophenyl)-5,6,7,8-tetrahydro-7,7-dimethyl-5-oxo-4H-chromene-3-carbonitrile (4e). IR (KBr, cm^{-1}): 3382, 3185, 2188, 1674, 1459, 1216, ^1H NMR (500 MHz, DMSO, δ ppm): 0.95 (*s*, 3H); 1.03 (*s*, 3H), 2.08 (*d*, 1H), 2.22 (*d*, 1H), 2.48 (*s*, 2H), 4.22 (*s*, 1H), 7.05 (*s*, 2H), 7.18 (*d*, 2H), 7.33 (*d*, 2H), ^{13}C NMR (125 MHz, DMSO, δ ppm): 26.7; 28.3, 31.6, 35.6, 39.1, 49.8, 57.8, 112.6, 119.4, 126.2, 129.0, 131.1, 144.6, 158.4, 162.7, 195.5, MS for $C_{18}H_{17}ClN_2O_2$ (m/z): 329.1 [M + H]$^+$.

Further, the effect of catalyst loading on the model reaction was investigated. As shown in Table 2, the maximum yield was obtained with 40 mg of the catalyst (entry 4). The yield and reaction rate were not enhanced by additional catalyst loading (entry 5). A benzopyran derivative was produced with 94% yield using 40 mg of the catalyst at 80°C without the use of solvents.

Table 2. Effect of catalyst loading on the synthesis of benzopyran derivatives under solvent-free conditions at 80°C

Entry	Amount of catalyst (mg)	Reaction time (min)	Yield (%)[a]
1	10	60	69
2	20	60	83
3	30	60	91
4	**40**	**60**	**94**
5	50	60	94
6	60	60	94

[a]Reaction conditions: benzaldehyde **1a** (1 mmol), dimedone **2** (1 mmol), malononitrile **3** (1 mmol), and $NiFe_2O_4$@Cellulose-PEG as a catalyst.

After determining the optimal reaction conditions, we investigated the scope of the suggested methodology by applying several substituted benzaldehydes **1a-k** with dimedone and malononitrile at 80°C under solvent-free conditions in the presence of $NiFe_2O_4$@Cellulose-PEG nanocatalyst. As shown in Table 3, whether the aromatic aldehyde had an electron-donating or electron-withdrawing substituent, the reaction was equally simple and produced the intended benzopyran derivatives in high yields. Physical characteristics were used to describe the products.

The catalytic activity of the $NiFe_2O_4$@Cellulose-PEG nanocatalyst was compared to that of a few other documented catalysts, as shown in Table 4. It can be concluded that the $NiFe_2O_4$@Cellulose-PEG nanocatalyst has superior catalytic efficiency, making it the most efficient catalyst which gives high product yields in a noticeably shorter duration.

Table 3. $NiFe_2O_4$@Cellulose-PEG catalyzed one-pot synthesis of benzopyran derivatives under solvent-free conditions at 80ºC

Entry	Aldehyde	Product	Time (min)	Yield (%)^a	M. P. (°C)	
					Observed	Reported
4a	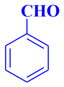	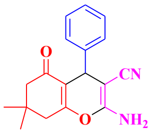	60	94	226-228	226-228
4b	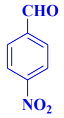	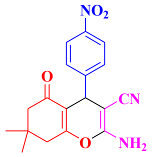	50	94	182-184	186-188
4c	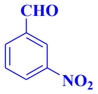	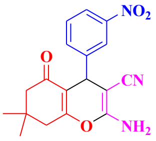	60	91	216-218	212-214
4d	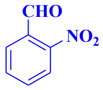	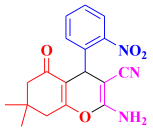	60	90	228-230	224-226
4e	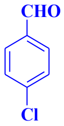	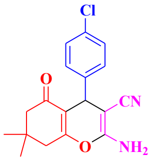	50	94	200-202	198-200
4f	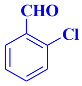	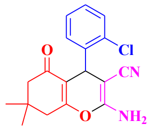	60	88	208-210	210-212
4g	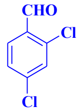	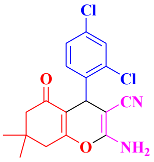	50	90	122-124	118-120
4h	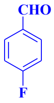	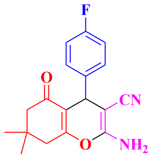	50	93	174-176	178-180
4i	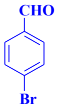	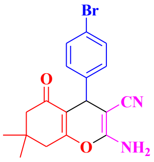	55	92	198-200	202-204
4j	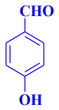	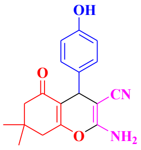	60	90	204-206	208-210
4k	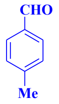	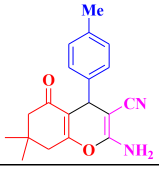	65	92	222-224	218-220

Table 4: Comparison of $NiFe_2O_4$@Cellulose-PEG catalyst with reported catalysts for the synthesis of benzopyran derivatives

Entry	Catalyst	Reaction conditions	Time (min)	Yield (%)	Reference
1	SiO_2-Pr-SO_3H	H_2O/Reflux	8	88	[28]
2	$NH_4Al(SO_4)_2$	EtOH/80ºC	120	92	[29]
3	$ZnFe_2O_4$@alginic acid	EtOH/RT	10	93	[30]
4	nano-SiO_2/DBN	H_2O: EtOH/60ºC	15	93	[31]
5	DAIL@SiO_2	SF/100ºC	120	86	[32]
6	L-Proline	EtOH/Reflux	30	92	[33]
7	DABCO	H_2O/Reflux	120	89	[34]
8	$NiFe_2O_4$@Cellulose-PEG	SF/80ºC	60	94	This work

Catalyst reusability

The model reaction between benzaldehyde **1a** (1 mmol), dimedone **2** (1 mmol), and malononitrile **3** (1 mmol) in the presence of $NiFe_2O_4$@Cellulose-PEG nanocatalyst at optimal reaction conditions was examined to determine the recyclability of the nanocatalyst. Following a successful reaction, hot ethanol was added to the reaction mixture, the nanocatalyst was filtered out, thoroughly washed with distilled water, and then dried for 1 h at 100 °C. The recovered catalyst worked properly up to four cycles (Figure 5).

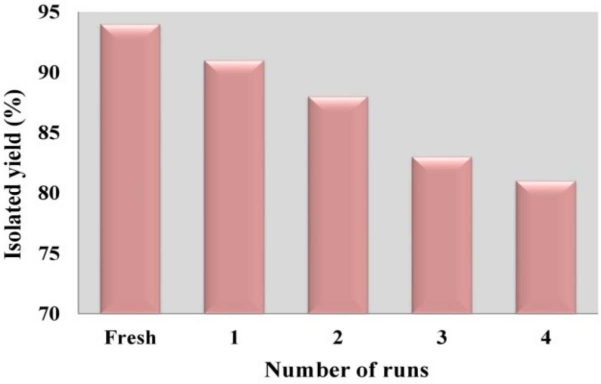

Figure 5. Reusability of $NiFe_2O_4$@Cellulose-PEG nanocatalyst

CONCLUSION

The current study successfully used a simple, economical, and effective method for obtaining $NiFe_2O_4$@Cellulose-PEG nanocatalyst in a solvent-free, one-pot multicomponent reaction of various aromatic aldehydes, dimedone, and malononitrile at 80°C. Characteristics such as straightforward reactions, non-toxic catalysts, straightforward purification, mild reaction conditions, and high product yield are the key components of this green-chemical methodology. The catalyst was recycled and reused without substantially lowering the catalytic activity for four runs.

Disclosure statement: *The authors declare that they have no relevant or material financial interests that relate to the research described in this paper.*

Declaration of funding: *No funding was received.*

Conflict of interest: *The authors declare no conflict of interest, financial or otherwise.*

Acknowledgement: *The authors are thankful to the Management and Principal, P. V. P. College, Pravaranagar for providing laboratory facilities and constant encouragement during the work. The authors are also thankful to the SAIF, Panjab University, Chandigarh, for the spectral analysis.*

REFERENCES

1. S.J. Salih, W.M. Mahmood, *Heliyon*, **9**, 6 (2023).
2. M. Amiri, M. Salavati-Niasari, A. Akbari, *Adv. Colloid Interface Sci*., **265**, 29 (2019).
3. A. Hajalilou, S.A. Mazlan, *Appl. Phys. A*, **122**, 680 (2016).
4. A. Soufi, H. Hajjaoui, W. Boumya, A. Elmouwahidi, E. Baillon-Garcia, M. Abdennouri, N. Barka, *J. Environ. Manage*., **367**, 121971 (2024).
5. A.Q. Malik, H. Singh, A. Kumar, R. Aepuru, D. Kumar, T. Gani Mir, Q. Ain, A.A. Bhat, *ES Energy and Environment*, **19**, 744 (2023).
6. Z.K. Heiba, M.B. Mohamed, L. Arda, N. Dogan, *J. Magn. Magn. Mat*., **391**, 195 (2015).
7. R. Choubey, D. Das, S. Mukherjee, *J. Alloys Compd*., **668**. 33 (2016).
8. D.M. Wu, X.P. Liu, P.Z. Gao, L.T. He, J.W. Li, *Ceram. Int*., **48**, 11228, (2022).
9. U. Ahmad, M. Afzia, F. Shah, B. Ismail, A. Rahim, R.A. Khan, *Mater. Sci. Semicond. Process*., **148**, 106830 (2022).
10. N. Gupta, P. Jain, R. Rana, S. Shrivastava, *Mater. Today Proc*., **4**, 342 (2017).
11. S.P. Dalawai, S. Kumar, M.A. Aly, M.Z. Khan, R. Xing, P.N. Vasambekar, S. Liu, *J. Mater. Sci.: Mater. Electron*., **30**, 7752 (2019).
12. R.S. Rajenimbalkar, V.J. Deshmukh, K.K. Patankar, S.B. Somvanshi, *Sci. Rep*., **14**, 29547 (2024).
13. V. Gopinath, S. Saravanan, A.R. Al-Maleki, M. Ramesh, J. Vadivelu, *Biomed. Pharmacother*., **107**, 96 (2018).
14. I. Benalaya, G. Alves, J. Lopes, L.R. Silva, *Int. J. Mol. Sci*.,**25**, 1322 (2024).

15. S. Sharma, M. Bhende, *Polym. Bull.*, **81**, 12383 (2024).
16. R.C. Cioc, E. Ruijter, R.V. Orru, *Green Chem.*, **16**, 2958 (2014).
17. H.A. Younus, M. Al-Rashida, A. Hameed, M. Uroos, U. Salar, S. Rana, K.M. Khan, *Expert Opin. Ther. Pat.,* **31**, 267 (2021).
18. B.S. Vachan, M. Karuppasamy, P. Vinoth, S.V. Kumar, S. Perumal, V. Sridharan, J.C. Menendez, *Adv. Synth. Catal.*, **362**, 87 (2020).
19. M.B. Gawande, V.D. Bonifacio, R. Luque, P.S. Branco, R.S. Varma, *ChemSusChem*,**7**, 24 (2014).
20. A. Sarkar, S. Santra, S.K. Kundu, A. Hajra, G.V. Zyryanov, O.N. Chupakhin, V.N. Charushin, A. Majee, *Green Chemistry*, **18**, 4475 (2016).
21. M.A. Bodaghifard, M. Solimannejad, S. Asadbegi, S. Dolatabadi Farahani, *Res. Chem. Intermed.*, **42**, 1165 (2016).
22. M. Abaszadeh, M. Seifi, S.Y. Ebrahimipour, *Bull. Chem. Soc. Ethiop.*, **30**, 253 (2016).
23. G.M. Ziarani, A. Abbasi, A. Badiei, Z. Aslani, *J. Chem.*, **8**, 293 (2011).
24. S. Mostafa Habibi-Khorassani, M. Shahraki, E. Mollashahi, S. Shadfar Pourpanah, S. Keshavarz Majdabadi, *Comb. Chem. High Throughput Screen.*, **19**, 865 (2016).
25. H.R. Saadati-Moshtaghin, F.M. Zonoz, *Mater. Chem. Phys.*, **199**, 159 (2017).
26. B. Boumoud, A.A. Yahiaoui, T. Boumoud, A. Debache, *J. Chem. Pharm. Res.*, **4**, 795 (2012).
27. M.S. Esmaeili, M.R. Khodabakhshi, A. Maleki, Z. Varzi, *Polycycl. Aromat. Compd.*, **41**, 1953 (2021).
28. G.M. Ziarani, A. Abbasi, A. Badiei, Z. Aslani, *J. Chem.*, **8**, 293 (2011).
29. A.A. Mohammadi, M.R. Asghariganjeh, A. Hadadzahmatkesh, *Arab. J. Chem.*, **10**, S2213 (2017).
30. A. Maleki, Z. Varzi, F. Hassanzadeh-Afruzi, *Polyhedron*, **171**, 193 (2019).
31. M. Mehravar, B.B. Mirjalili, E. Babaei, A. Bamoniri, *BMC Chem.*, **15**, 34 (2021).
32. Q. Zhang, H. Wei, J. Li, X. Zhao, J. Luo, *Heterocycl. Commun.*, **23**, 411 (2017).
33. P. Kate, V. Pandit, V. Jawale, M. Bachute, *J. Chem. Sci.*, **134**, 4 (2022).
34. D. Tahmassebi, J.A. Bryson, S.I. Binz, *Synth. Commun.*, **41**, 2701 (2011).
35. A. Mulik, P. Hegade, S. Mulik, M. Deshmukh, *Res. Chem. Intermed.*, **45**, 5641 (2019).
36. Z.K. Jaberi, B. Pooladian, *Sci. World J.*, 208796 (2012).
37. H. Ostadzadeh, H. Kiyani, *Polycycl. Aromat. Compd.*, **43**, 9318 (2023).
38. A.M. Zonouz, S. Okhravi, D. Moghani, *Monatsh. Chem.*, **147**, 1819 (2016).
39. A. Davoodnia, S. Allameh, S. Fazli, N. Tavakoli-Hoseini, *Chem. Pap.*, **65**, 714 (2011).
40. V. Vikhe, A. Kshirsagar, B. Uphade, A. Gadhave, *Res. Chem. Intermed.*, **50**, 4199 (2024).
41. V. Vikhe, D. Aute, V. Kadnor, G. Shirole, B. Uphade, A. Gadhave, *Polycycl. Aromat. Compd.*, **45**, 322 (2025).
42. A.K. Mhaske, A.G. Gadhave, A.G. Dholi, B.K. Uphade, *J. Inorg. Organomet. Polym. Mater.*, **34**, 999 (2024).
43. P.D. Ladkat, P.K. Gadekar, V.M. Khedkar, B.K. Uphade, A.G. Gadhave, *ChemistrySelect.*, **10**, e202404836 (2025).
44. A.R. Parhad, D.S. Aute, A.G. Gadhave, B.K. Uphade, *Polycycl. Aromat. Compd.*, **44**, 5261 (2024).
45. A.K. Mhaske, D.V. Vikhe, A.G. Gadhave, B.K. Uphade, *Polycycl. Aromat. Compd.*, **45**, 490 (2025).
46. V.V. Vikhe, A.K. Mhaske, V.K. Vikhe, B.K. Uphade, A.G. Gadhave, *Catal. Surv. Asia*, **29**, 249 (2025).
47. P. Sivakumar, R. Ramesh, A. Ramanand, S. Ponnusamy, C. Muthamizhchelvan, *Mater. Lett.*, **65**, 483 (2011).
48. Z. Li, M. Ye, A. Han, H. Du, *J. Mater. Sci.: Mater. Electron.*, **27**, 1031 (2016).
49. S. Nam, A.D. French, B.D. Condon, M. Concha, *Carbohydr.Polym.*, **135**, 1 (2016).
50. W.E. Pottker, R. Ono, M.A. Cobos, A. Hernando, J.F. Araujo, A.C. Bruno, S.A. Lourenço, E. Longo, F.A. La Porta, *Ceram. Int.*, **44**, 17290 (2018).
51. M. Abushad, M. Arshad, S. Naseem, H. Ahmed, A. Ansari, V.K. Chakradhary, S. Husain, W. Khan, *J. Mol. Struct.*, **1253**, 132205 (2022).

Bulgarian Chemical Communications, Volume 58, Issue 2 (pp. 162-172) 2026 *DOI: 10.34049/bcc.58.2.5741*

Computational modelling of limonoids from *Melia azedarach* as potential inhibitors of leukemia

H. D. Nguyen*

Faculty of Biology, Thai Nguyen University of Education, Thai Nguyen, 24124, Vietnam

Received: December 24, 2025; Revised: March 03, 2026

Leukemia is a systemic hematological malignancy, characterized by dysregulated survival signaling, in which suppression of apoptosis contributes to disease persistence and treatment resistance. In this study, limonoids from *Melia azedarach* were assessed as potential anti-leukemia agents using multi-computational strategies focused on the anti-apoptotic protein Bcl-xL (PDB: 3SPF), with Venetoclax used as a reference ligand for comparative modeling. Docking of eight candidates identified CPD4 as the top binder (-10.35 kcal/mol), surpassing Venetoclax (-9.87 kcal/mol), and revealed a key hydrogen bond with Arg139, alongside extensive hydrophobic/van der Waals contacts in the conserved pocket. Molecular dynamics simulations spanning 100 ns revealed stable complexes, with CPD4 exhibiting a higher backbone RMSD range than Venetoclax while maintaining comparable compactness. MMGBSA analysis yielded favorable binding for both ligands, giving ΔTOTAL values of -19.73 ± 5.33 kcal/mol for CPD4 and -24.48 ± 9.15 kcal/mol for Venetoclax; CPD4 was driven by strong gas-phase interactions (ΔGGAS -43.86 ± 10.49) but incurred a solvation penalty (ΔGSOLV 24.13 ± 6.62). DFT descriptors showed CPD4 with EHOMO -4.3598 eV, ΔE 3.0037 eV, and ω 2.7193 eV, compared with Venetoclax (-9.0405 eV, 4.8522 eV, and 9.0166 eV). Overall, CPD4 emerges as a promising scaffold for targeting Bcl-xL and warrants further optimization and experimental validation in leukemia research.

Keywords: Anti-apoptosis; Bcl-xL; DFT; Leukemia inhibitor; Limonoids; *Melia azedarach*.

INTRODUCTION

Leukemia is a hematological malignancy driven by genetic and epigenetic disruptions in hematopoietic progenitors, most often arising in the bone marrow and resulting in the excessive proliferation of abnormal leukocytes [1]. Unlike many solid tumors that typically form a localized mass before disseminating, leukemic cells are frequently systemic from early stages, which contributes to aggressive clinical behavior and complicates timely diagnosis and durable disease control [2]. Clinically, leukemia is broadly categorized into acute and chronic entities; within the chronic group, chronic myeloid leukemia accounts for approximately 15% of adult cases [3]. Although chemotherapy remains an important therapeutic option, particularly in advanced disease or when targeted regimens are unsuitable, its utility is often constrained by substantial adverse effects such as infection susceptibility, fatigue, and gastrointestinal toxicity. Together with the emergence of treatment resistance, these limitations motivate the search for alternative agents and complementary strategies that can improve efficacy while reducing toxicity burden [4, 5].

A central biological feature supporting malignant persistence is impaired apoptosis, the genetically unnecessary cells to maintain tissue homeostasis [6], programmed mechanism that removes damaged or unnecessary cells to maintain tissue homeostasis [6]. Cancer cells frequently attenuate apoptotic signaling, enabling survival under oncogenic stress and therapeutic pressure, and thereby facilitating uncontrolled expansion. In this context, Bcl-xL (B-cell lymphoma-extra large) is a key anti-apoptotic regulator that suppresses the intrinsic mitochondrial death pathway by limiting cytochrome c release and downstream caspase activation [7, 8]. Its frequent overexpression across cancers has made Bcl-xL an established target for anticancer drug discovery.

Natural products remain a rich source of bioactive scaffolds, and limonoids. Highly oxygenated triterpenoids, abundant in citrus and *Meliaceae* plants, are of particular interest due to reported anticancer, anti-inflammatory, and antiviral activities [9, 10]. Prior studies have identified limonoids from *Melia azedarach*, including pungiolide-type structures, with notable cytotoxicity against multiple human cancer cell lines, including the HL-60 leukemia model [11]. However, the molecular basis of these effects, especially at the level of target-specific recognition and stability, has not been comprehensively examined using modern computational pipelines. Accordingly, this study investigates limonoids from *M. azedarach* as prospective anti-leukemia agents by applying structure-based modelling to characterize their interactions with relevant protein targets, prioritize promising binders within a defined binding region,

---

* To whom all correspondence should be sent: Email*: hungnd@tnue.edu.vn*

and estimate developability-related properties, thereby providing a rationale for subsequent experimental validation *in vitro* and *in vivo*.

MATERIALS AND METHODS

Structural preparation of selected limonoids

The selected limonoids from *M. azedarach* possess significant cytotoxic activity against the HL-60 leukemia cancer cell line [11], including meliarachin C (CPD1), toosendanin (CPD2), 1-*O*-cinnamoyltrichilinin (CPD3), 23-methoxyohchininolide A (CPD4), 3-*O*-deacetyl-4'-demethyl-28-oxosalannin (CPD5), 1-*O*-detigloyl-1-*O*-benzoylohchinolal (CPD6), nimbolinin D (CPD7), meliasenin E (CPD8), which have molecular formulas of $C_{31}H_{40}O_{11}$, $C_{30}H_{38}O_{11}$, $C_{39}H_{46}O_9$, $C_{37}H_{44}O_{10}$, $C_{31}H_{38}O_9$, $C_{36}H_{42}O_{10}$, $C_{36}H_{44}O_9$, $C_{31}H_{48}O_5$, respectively, with molecular weights of 588.2571, 574.2414, 658.3142, 648.2934, 554.2516, 634.2778, 620.2985, and 500.3502 g/mol. Venetoclax, possessing a molecular formula of $C_{45}H_{50}ClN_7O_7S$ and a molecular weight of 867.3181 g/mol, was included as a reference Bcl-xL ligand for comparative docking and simulation analyses (Fig. 1).

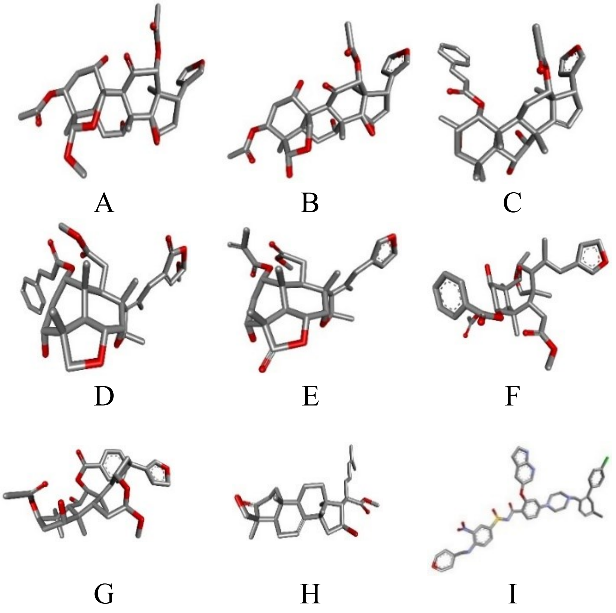

Figure 1. 3D Structures of selected limonoids (A. CPD1; B. CPD2; C. CPD3; D. CPD4; E. CPD5; F. CPD6; G. CPD7; H. CPD8) and the comparative reference Venetoclax (I).

Molecular docking analysis

The three-dimensional structures of the selected limonoids were generated in PDB format using the Biovia Discovery Studio Visualizer 2024 (Dassault Systèmes, San Diego, CA, USA). This process involved adding polar hydrogens, calculating Gasteiger charges, and considering torsional bond flexibility. The structure of the Bcl-xL protein (PDB ID: 3SPF) was retrieved in PDB format from the RCSB Protein Data Bank [12]. Ligand-protein docking simulations were performed using AutoDock Tools, with a grid box spanning 60 points in each x, y, and z dimension at a spacing of 0.375 Å [13]. The binding site coordinates for the Bcl-xL protein were set at x = 32.003 Å, y = 16.833 Å, and z = -18.895 Å. The Lamarckian genetic algorithm was employed to identify low-energy conformations, optimizing the stability of ligand-protein interactions. Following docking, the highest-affinity conformation was evaluated using Biovia Discovery Studio Visualizer 2024 and compared with the docking results obtained for Venetoclax on the same protein to assess similarities in binding interactions.

Molecular dynamics simulation

Molecular dynamics simulations were conducted to examine the highest-affinity docked conformation of the Bcl-xL protein complex (PDB ID: 3SPF) over a period of 100 ns, utilizing GROMACS version 2024.4 [14]. The protein structure was optimized by adding missing atoms and residues, which was accomplished using Swiss-PdbViewer [15]. Ligand force-field parameters were generated through the use of SwissParam [16]. The protein-ligand complex was solvated within a triclinic simulation box using the SPC water model, with 0.15 M NaCl added to maintain an ionic strength of 0.15 M. To ensure structural refinement and charge neutralization, an energy minimization procedure consisting of 50,000 steps was performed. The equilibration process involved a 200 ps NVT ensemble, followed by a 200 ps NPT ensemble, both maintained at 300 K and 1 bar. Three independent production simulations were carried out, each lasting 100 ns with a 2 fs integration step, and the coordinate trajectories were recorded every 10 ns. Analysis of the simulation trajectories was carried out using Grace software, from which key dynamical parameters, including root mean square deviation (RMSD), root mean square fluctuation (RMSF), radius of gyration (Rg), number of hydrogen bonds (Hbonds), and solvent-accessible surface area (SASA), were derived. The stability of the conformations across the simulated complexes was evaluated using UCSF Chimera version 1.13.3 through structural superposition [17].

Molecular mechanics generalised Born surface area (MMGBSA) analysis

Binding free energies for the CPD4-3SPF and Venetoclax-3SPF complexes were computed using the gmx_MMPBSA package, along with the charmm36 force field. The polar solvation energy was determined *via* the generalized Born implicit solvent model, while non-polar contributions were derived from estimations of the solvent-accessible surface area. Data extraction was performed from molecular dynamics trajectories consisting of 125 equally spaced frames, sampled every 80 ps, over an 80 ns duration (ranging from 20 ns to 100 ns). This ensemble-averaging approach allowed for the identification of differences in ligand-protein interaction energetics, thus providing insights into the relative binding affinities and the stability of the complexes during the simulation period [18].

Assay protocol for ADMET prediction

A preliminary assessment of ADMET (Absorption, Distribution, Metabolism, Excretion, Toxicity) properties is essential for predicting pharmacokinetic challenges and safety concerns during the drug discovery process. This approach helps reduce failure rates in later stages and improves the selection of compounds with suitable therapeutic potential. In this study, the pkCSM platform was utilized to predict the ADMET profiles of CPD4 and Venetoclax. This platform employs graph-based molecular descriptors to estimate parameters related to absorption, distribution, metabolism, excretion, and toxicity, facilitating a comprehensive comparison of the key developability features of the compounds under investigation [19].

Quantum chemistry computation using the Density Functional Theory (DFT) method

Molecular geometry optimization for CPD4 and Venetoclax was carried out using the ORCA quantum chemistry package, version 6.1.0 [20]. Initial coordinates were generated in Avogadro [21], and the subsequent visualization of molecular orbitals, along with associated analyses, was performed using IboView version 20211019 [22]. All DFT calculations employed B3LYP/6-31G(d,p) to describe the ground-state electronic structure (electron density and Kohn-Sham orbitals) used to derive frontier-orbital energies and conceptual-DFT descriptors. From the fully optimized molecular structures, key quantum-chemical descriptors were extracted, including the energies of the highest occupied molecular orbital (HOMO) and lowest unoccupied molecular orbital (LUMO), the HOMO-LUMO energy gap (ΔE), chemical potential (μ), electronegativity (χ), global hardness (η), softness (σ), and electrophilicity index (ω). The determination of these reactivity parameters was conducted in accordance with Koopmans' theorem, providing insights into the electronic properties and chemical behavior of the compounds studied [18].

RESULTS AND DISCUSSION

Molecular docking analysis

Molecular docking was employed as an initial structure-based screening approach to estimate the binding propensity of the selected small molecules toward Bcl-xL and to delineate the residue-level determinants underlying ligand recognition. This workflow enables rapid ranking of candidates according to predicted binding free energy surrogates while simultaneously providing interpretable interaction fingerprints, including key pocket-lining residues and hydrogen-bond partners [23]. Accordingly, comparative docking analysis was performed for the selected ligands alongside Venetoclax, a reference Bcl-xL binder, to contextualize candidate binding within a common structural framework before advancing to dynamic stability assessment.

Before ligand docking with protein 3SPF, the binding-pocket residues were defined. Structural inspection of 3SPF in BIOVIA Discovery Studio Visualizer identified key inhibition-associated sites (Fig. 2A). The docking workflow was then validated by redocking the co-crystallized ligand (Fig. 2B), with an RMSD of 1.4637 Å, and the close superimposition with the native pose supported the accuracy of the procedure. An RMSD value below 2 Å is commonly accepted as evidence of a reliable docking protocol [24]. Docked poses were ranked according to the most favorable (lowest) binding energy (kcal/mol).

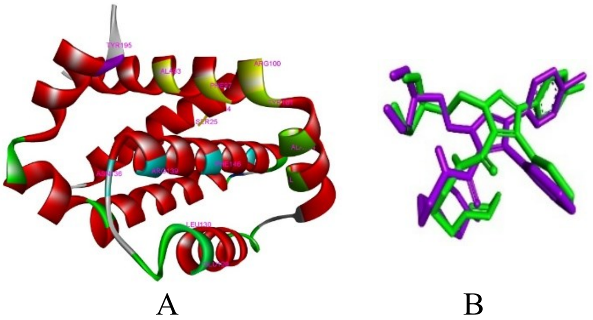

Figure 2. Active sites within the 3SPF protein (A) and superimposition of the docked and native ligands for validation of the molecular docking protocol (violet = native, green = docked) (B).

As summarized in Table 1, docking scores and residue-level contact profiles were evaluated for eight selected ligands within the Bcl-xL binding cavity, with Venetoclax included as a benchmark. Across the candidate set, the interaction field converged on a recurrent pocket architecture dominated by Phe97, Tyr101, Ala104, Phe105, Leu108, Arg139, and Phe146, indicating preferential recognition of a shared binding region. Such complexes are commonly stabilized through a combination of hydrophobic enclosure by aromatic/aliphatic side chains, shape complementarity that optimizes van der Waals contacts, and directional hydrogen bonding that restricts ligand orientation and supports pose persistence within the cavity [25, 26].

Predicted binding energies for CPD1-CPD8 spanned -10.35 to -8.08 kcal/mol, while Venetoclax exhibited a docking score of -9.87 kcal/mol under the same protocol. Within the candidate series, CPD4 produced the most favorable affinity (-10.35 kcal/mol), exceeding the predicted stabilization of Venetoclax. CPD4 occupied the conserved pocket lined by Phe97, Tyr101, Ala104, Phe105, Leu108, Arg139, and Phe146, and additionally involved Asn136, suggesting an expanded polar-contact network relative to several other candidates (Fig. 3A). A hydrogen-bond interaction was annotated with Arg139, consistent with a plausible anchoring role for this residue, while hydrophobic residues (Phe97, Phe105, Leu108, Phe146) provide enclosure. Among the remaining candidates, CPD7 (-9.90 kcal/mol) and CPD5 (-9.78 kcal/mol) approached the reference score. Yet, their contact patterns differed from the most conserved signature: CPD7 engaged a reduced residue subset (Phe97, Ala104, Phe105, Phe146) and formed hydrogen bonds with Val126 and Ser145, whereas CPD5 retained the canonical residue ensemble (Phe97, Tyr101, Ala104, Phe105, Leu108, Arg139, Phe146) with hydrogen bonding to Arg139. By contrast, Venetoclax interacted with a broader region that included Ala93 and Arg100, in addition to the shared core residues. Hydrogen bonding was observed between Arg100 and Gly138, reflecting a distinct anchoring arrangement relative to the selected ligands (Fig. 3B).

Collectively, the docking outcomes indicate that the strongest predicted affinity coincides with the engagement of conserved pocket residues and a defined polar anchor. On this basis, CPD4 was selected for subsequent molecular dynamics simulations, with Venetoclax retained as the comparator to assess the relative stability of the complex, the persistence of key contacts (notably Arg139 for CPD4), and pocket adaptability under explicit-solvent, fully flexible conditions.

Table 1. Interactions between the docked ligands and the protein 3SPF.

Docked ligands	Binding energy (kJ/mol)	Hydrogen bond interaction	Van der Waals interaction	Hydrophobic interaction
CPD1	-8.31	Val126, Arg139	Phe97, Tyr101, Ala104, Val127, Glu129, Asp133, Ala142, Phe146	Phe105, Leu108, Val126, Leu130, Arg139, Ala149
CPD2	-8.08	Val126, Arg139	Phe97, Val127, Glu129, Ala142, Phe146	Tyr101, Ala104, Phe105, Leu108, Val126, Leu130, Ala149
CPD3	-8.44	Arg139	Phe97, Tyr101, Ala104, Leu108, Glu129, Leu130, Gly138	Phe105, Val126, Arg139, Ala142, Phe146
CPD4	-10.35	Arg139	Phe97, Leu108, Val126, Glu129, Leu130, Asp133, Asn136, Ala142, Ser145, Phe146, Ala149	Tyr101, Ala104, Phe105, Arg132
CPD5	-9.78	Arg139	Phe97, Tyr101, Ala104, Asp107, Leu108, Val126, Ser145, Phe146, Ala149	Phe105, Leu130, Arg139, Ala142
CPD6	-8.19	Glu129, Phe146	Phe97, Tyr101, Phe105, Asp107, Leu108, Arg139, Ala142, Ser145, Ala149	Leu130
CPD7	-9.90	Val126, Ser145	Phe97, Phe105, Glu129, Leu130, Ala142, Phe143	Ala104, Phe146, Ala149
CPD8	-8.19	Arg139	Tyr101, Phe105, Leu108, Val126, Glu129, Asp133, Asn136, Phe146	Phe97, Ala104, Leu130, Arg132, Arg139, Ala142
Venetoclax	-9.87	Arg100, Gly138	Glu96, Gln111, Asn136, Ser145, Phe146	Ala193, Phe97, Tyr101, Ala104, Phe105, Leu108, Val126, Leu130, Arg139, Ala142, Tyr195

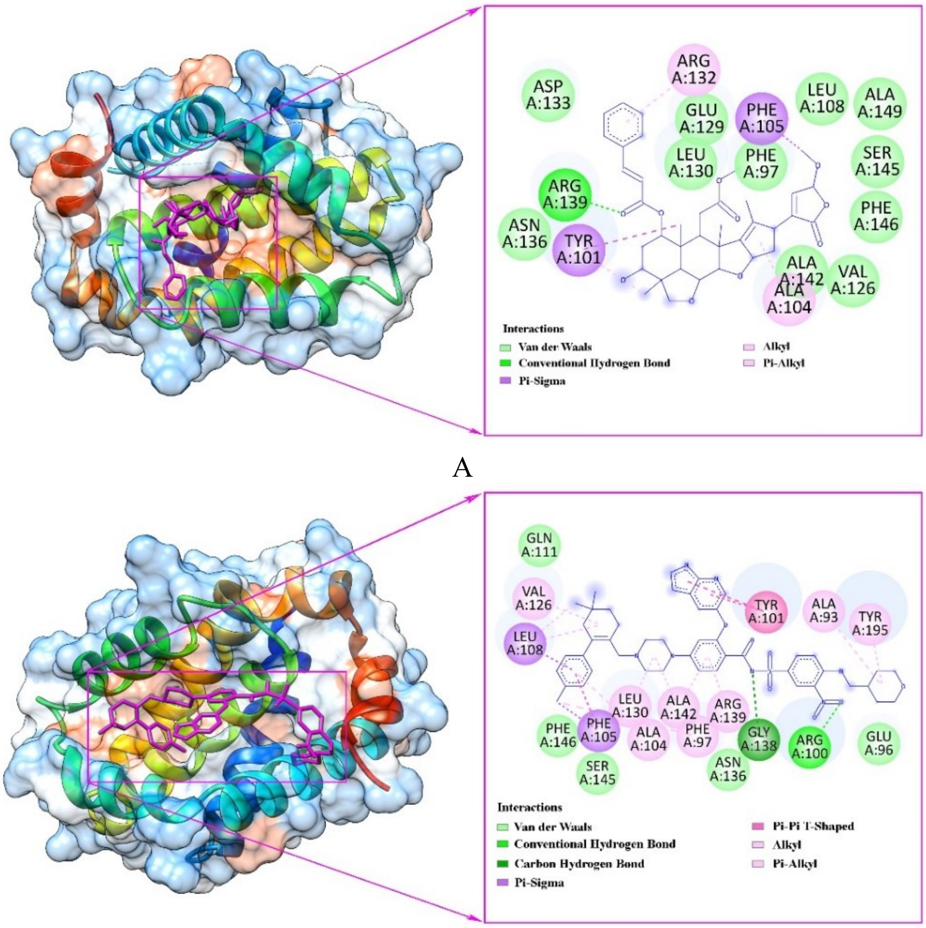

A

B

Figure 3. Molecular docking model and 2D interaction diagram of CPD4 (A) and Venetoclax (B) with 3SPF protein

Notably, the previous study showed that CPD4 exhibited potent cytotoxic activity against HL60 cells with an IC_{50} of 4.9±0.5 µM [11], although it was not the most active compound in the experimental series. Therefore, the present docking results should be interpreted as supporting a putative interaction of CPD4 with the same or an overlapping Bcl-xL binding region used for comparative modeling, rather than as proof that it shares the same experimentally validated mechanism of action as Venetoclax.

Molecular dynamics simulation

To extend the docking observations into a fully flexible, explicitly solvated environment, molecular dynamics simulations were conducted to interrogate the conformational stability and interaction persistence of the two representative predicted bound states. Accordingly, 100-ns trajectories were generated for the CPD4-3SPF and Venetoclax-3SPF complexes, and the resulting ensembles were quantified using RMSD, RMSF, Rg, Hbonds, and SASA to gauge solvent exposure [27]. Consequently, the total energy and potential energy values for the CPD4-3SPF complex were found to be -506,377 kJ/mol and -625,054 kJ/mol, respectively. For the Venetoclax-3SPF complex, the total and potential energy values were -230,784,598 kJ/mol and -287,485 kJ/mol, respectively. The simulation system maintained equilibrium at 300 K.

In Figure 4A, both complexes showed an initial relaxation followed by stable RMSD fluctuations without sustained drift over 100 ns. CPD4-3SPF sampled a higher RMSD range (0.25-0.30 nm, occasionally 0.32 nm), whereas Venetoclax-3SPF remained lower and tighter (0.22-0.25 nm, occasionally 0.26 nm), supporting overall fold stability with slightly reduced global deviation for Venetoclax [28].

RMSF analysis of the Met1-Asn197 segment (Fig. 4B) indicated that the most significant motions were restricted to the extreme N-terminus, peaking at 0.40 nm for CPD4-3SPF and 0.25 nm for Venetoclax-3SPF. Outside this region, fluctuations rapidly decreased and remained low across the rest of the segment (0.04-0.06 nm), with CPD4 showing only slightly higher amplitudes and no evidence of localized destabilization.

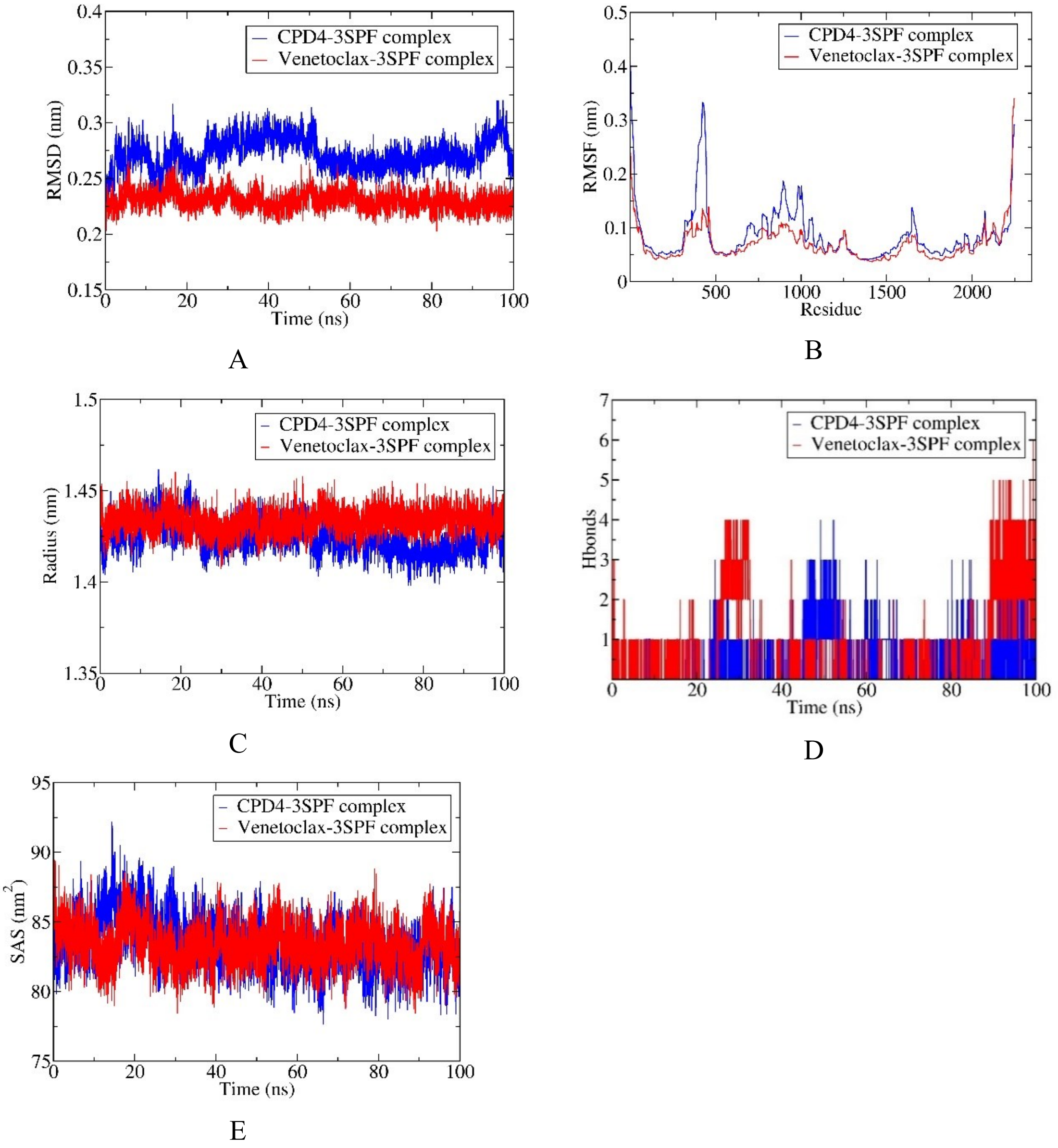

Figure 4. Results of MD simulation for the bindings of CPD4 (blue) and Venetoclax (red) with 3SPF protein. (A) RMSD, (B) RMSF, (C) Rg, (D) Hbonds, (E) SASA

The radius of gyration (Rg) reports mass-weighted compactness. Over the simulation (Fig. 4C), both complexes remained within a narrow Rg range of 1.41-1.46 nm, indicating a stable global structure; CPD4-3SPF tended to slightly lower values, especially later in the trajectory, while Venetoclax-3SPF more often occupied the upper part of the same band.

The intermolecular number of hydrogen bonds summarizes the persistence of polar contacts at the binding interface. In Figure 4D, both complexes were typically dominated by 0-1 hydrogen bond, but CPD4-3SPF showed a mid-trajectory enrichment (45-60 ns) with repeated sampling of 1-3 and brief peaks at 4, whereas Venetoclax-3SPF exhibited stronger episodes around 25-35 ns (up to 4) and 90-100 ns, where counts frequently reached 3-5 and occasionally 6, indicating more frequent high-occupancy polar anchoring for Venetoclax.

SASA, a proxy for overall solvent exposure, remained stable for both complexes over 100 ns (Fig. 4E), with values ranging from 78 to 90 nm² and no sustained trends. CPD4 showed brief early increases but more often occupied the lower end of the shared band later. In contrast, Venetoclax sampled slightly higher values on average, indicating only modest differences in solvent exposure rather than major structural rearrangements [29].

Collectively, the five readouts support the formation of dynamically stable protein scaffolds for both CPD4-3SPF and Venetoclax-3SPF over 100 ns. The CPD4 complex exhibited a higher RMSD band. It enhanced residue-level flexibility in specific internal regions, accompanied by slightly reduced compactness and marginally lower solvent exposure during the later simulation segments. The Venetoclax complex exhibited lower global deviation and displayed more frequent high-count hydrogen-bond episodes, particularly towards the end of the trajectory, consistent with the episodic strengthening of polar contacts while maintaining overall structural stability.

Free binding energy (MMGBSA) analysis

MMGBSA approximates ligand-protein association by combining molecular mechanics interaction energies with an implicit-solvent model, in which polar solvation is treated using the generalized Born method and nonpolar solvation is estimated from solvent-accessible surface area. It is commonly used for relative ligand ranking under a consistent protocol; however, outcomes depend on parameter choices and sampling, and it omits explicit entropy. Therefore, the results should be interpreted comparatively rather than as absolute free energies. As detailed in Table 2, both CPD4 and Venetoclax yield negative mean ΔTOTAL values, supporting a favorable association in the MMGBSA sense. CPD4-3SPF shows ΔTOTAL = -19.73 ± 5.33 kcal/mol, whereas Venetoclax-3SPF is more negative at -24.48 ± 9.15 kcal/mol, indicating a modestly stronger mean binding estimate for Venetoclax in this dataset. The larger dispersion for Venetoclax suggests a broader distribution of sampled binding microstates, consistent with its more variable energetic terms across the trajectory.

Table 2. Free energy of binding obtained using MMGBSA calculations.

Energy component	Average (kcal/mol)		Standard deviation	
	CPD4-3SPF	Venetoclax-3SPF	CPD4-3SPF	Venetoclax-3SPF
ΔVDWAΔALS	-30.40	-42.38	4.45	8.78
ΔEEL	-13.47	76.27	7.69	28.36
ΔEGB	28.18	-52.84	6.93	26.26
ΔESURF	-4.05	-5.53	0.57	1.25
ΔGGAS	-43.86	33.89	10.49	32.24
ΔGSOLV	24.13	-58.36	6.62	25.52
ΔTOTAL	-19.73	-24.48	5.33	9.15

MMGBSA decomposition suggests that CPD4 binding is primarily driven by favorable gas-phase interactions, with ΔVDWAΔALS = -30.40 ± 4.45 kcal/mol and ΔEEL = -13.47 ± 7.69 kcal/mol, resulting in ΔGGAS = -43.86 ± 10.49 kcal/mol. This gain is partly offset by a net solvation penalty (ΔGSOLV = 24.13 ± 6.62 kcal/mol), dominated by polar desolvation (ΔEGB = 28.18 ± 6.93 kcal/mol), while the nonpolar term remains favorable but smaller (ΔESURF = -4.05 ± 0.57 kcal/mol). Venetoclax shows the opposite balance: despite strong van der Waals stabilization (ΔVDWAΔALS = -42.38 ± 8.78 kcal/mol), its electrostatics are unfavorable on average (ΔEEL = 76.27 ± 28.36 kcal/mol), giving a positive ΔGGAS of 33.89 ± 32.24 kcal/mol that is overcompensated by highly favorable solvation (ΔGSOLV = -58.36 ± 25.52 kcal/mol), mainly driven by ΔEGB = -52.84 ± 26.26 kcal/mol and supported by ΔESURF = -5.53 ± 1.25 kcal/mol. Overall, CPD4 appears more contact-driven but desolvation-limited, whereas Venetoclax achieves a slightly more favorable net ΔTOTAL through solvation compensation and shows greater energetic variability across the trajectory.

Table 3. Predicted ADMET properties of CPD4 and Venetoclax

ADMET properties	Unit	CPD4	Venetoclax
Water solubility	(Log mol/L)	-4.542	-3.037
Caco2 permeability	(Log Papp in 10^{-6} cm/s)	0.876	0.847
Intestinal absorption (human)	(% Absorbed)	97.76	100
Skin permeability	(Log Kp)	-2.755	-2.735
P-glycoprotein substrate	Yes/No	No	Yes
P-glycoprotein I inhibitor	Yes/No	Yes	Yes
P-glycoprotein II inhibitor	Yes/No	Yes	Yes
VDss	(Log L/kg)	-0.469	-0.329
Fraction unbound (human)	(Fu)	0	0.169
BBB permeability	(Log BB)	-1.362	-1.747
CNS permeability	(Log PS)	-2.721	-3.119
CYP2D6 substrate	Yes/No	No	No
CYP3A4 substrate	Yes/No	Yes	Yes
CYP1A2 inhibitor	Yes/No	No	No
CYP2C19 inhibitor	Yes/No	No	No
CYP2C9 inhibitor	Yes/No	No	No
CYP2D6 inhibitor	Yes/No	No	No
CYP3A4 inhibitor	Yes/No	Yes	Yes
Total clearance	(Log ml/min/kg)	0.137	-0.096
Renal OCT2 substrate	Yes/No	No	No
AMES toxicity	Yes/No	No	No
Max. tolerated dose (human)	(Log mg/kg/day)	-0.208	0.278
hERG I inhibitor	Yes/No	No	No
hERG II inhibitor	Yes/No	No	Yes
Oral rat acute toxicity (LD50)	(mol/kg)	2.291	2.604
Oral rat chronic toxicity (LOAEL)	(Log mg/kg_ bw/day)	1.03	1.924
Hepatotoxicity	Yes/No	No	Yes
Skin sensation	Yes/No	No	No
Tetrahymena pyriformis toxicity	(Log µg/L)	0.285	0.285
Minnow toxicity	(Log mM)	0.442	-0.481

ADMET prediction analysis

In silico ADMET profiling was used to compare the predicted pharmacokinetic behavior and safety-relevant flags of CPD4 with those of Venetoclax, with descriptors grouped into absorption, distribution, metabolism, excretion, and toxicity (Table 3). This side-by-side comparison provides an early indication of potential developability trade-offs that may complement the docking and molecular dynamics prioritization.

For absorption, CPD4 shows lower predicted water solubility than Venetoclax (-4.542 *vs* -3.037 log mol/L), indicating a greater dissolution constraint. By contrast, Caco-2 permeability is similar (0.876 *vs* 0.847 log Papp), and both retain very high intestinal absorption (97.76% *vs* 100%) with comparable skin permeability (-2.755 *vs* -2.735 log Kp) [30]. Both ligands exhibit low VDss (-0.469 for CPD4 and -0.329 log L/kg for Venetoclax), but binding differs markedly, with Fu = 0 for CPD4 versus 0.169 for Venetoclax. CPD4 also shows higher predicted BBB/CNS permeability (log BB -1.362 *vs* -1.747; log PS -2.721 *vs* -3.119), although both indicate limited overall penetration [31]. For metabolism, the two compounds share a similar pattern. Neither is predicted to be a CYP2D6 substrate, while both are classified as CYP3A4 substrates. Inhibition liabilities across the screened CYP isoforms are largely absent except for CYP3A4, for which both CPD4 and Venetoclax are predicted inhibitors, suggesting a comparable potential for CYP3A4-related interaction risk in this specific output [32]. CPD4 shows a higher predicted total clearance than Venetoclax (0.137 vs -0.096 log ml/min/kg). Neither compound is predicted to be a renal OCT2 substrate, indicating that it is not designated as an OCT2 substrate in the current panel. For toxicity, both compounds are AMES-negative and are not predicted to inhibit hERG I; however, Venetoclax is flagged as a hERG II inhibitor, while CPD4 is not. CPD4 shows a lower predicted maximum tolerated dose (-0.208 *vs* 0.278 log mg/kg/day) and lower LD50 and LOAEL values (2.291 *vs* 2.604 mol/kg; 1.03 *vs* 1.924 log mg/kg_bw/day), whereas hepatotoxicity is predicted only for Venetoclax; skin sensitization is negative for both, *Tetrahymena pyriformis* toxicity is identical (0.285 log µg/L), and Minnow toxicity differs (0.442 *vs* -0.481 log mM). Overall, CPD4 is predicted to have high absorption with similar Caco-2 permeability but lower solubility and Fu, while lacking P-gp substrate status and the hERG II flag seen for Venetoclax. Venetoclax is more soluble and less protein-bound, but is predicted to be a P-gp substrate with hERG II inhibition and hepatotoxicity alerts, despite a higher tolerated dose and more favorable rodent toxicity indices. The Boiled-egg model was additionally applied (Fig. 5). CPD4 was positioned in the white region but outside the yellow yolk, supporting high GI absorption and low BBB permeation, whereas Venetoclax was out of range and therefore not displayed in the plot.

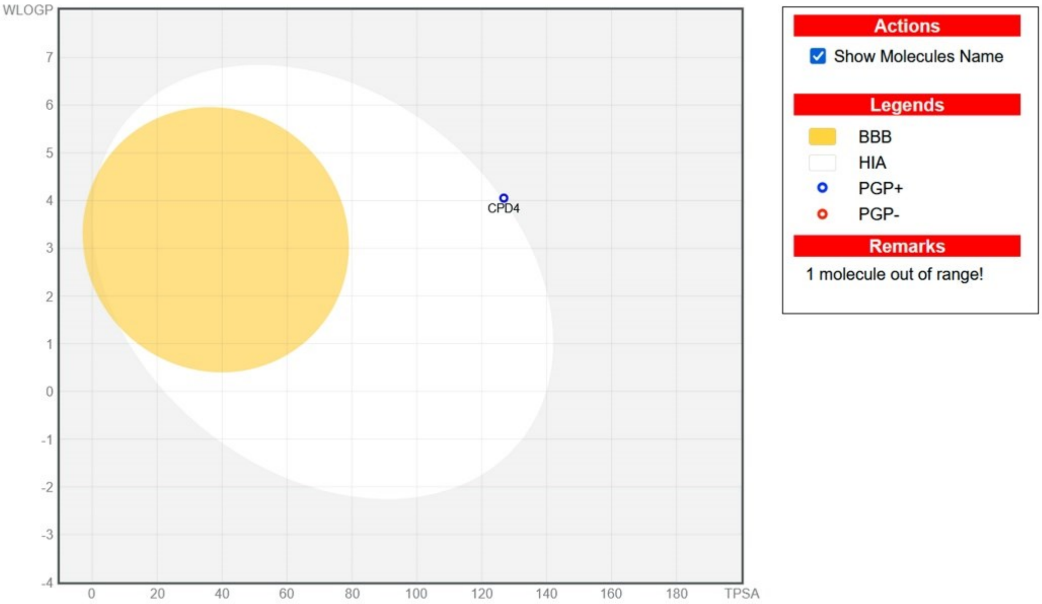

1 molecule out of range!

Figure 5. Boiled-egg plot of the selected compounds, generated from Swiss ADME

Table 4. Quantum descriptors of CPD4 and Venetoclax.

Molecule	EHOMO (eV)	ELUMO (eV)	ΔE (eV)	μ (eV)	χ (eV)	η (eV)	σ (eV^{-1})	ω (eV)
CPD4	-4.3598	-1.3561	3.0037	-2.8580	2.8580	1.5019	0.6658	2.7193
Venetoclax	-9.0405	-4.1883	4.8522	-6.6144	6.6144	2.4261	0.4122	9.0166

EHOMO (eV): highest occupied molecular orbitals; ELUMO (eV): lowest unoccupied molecular orbitals; ΔE (eV): energy gap; μ (eV): chemical potential; χ (eV): electronegativity; η (eV): hardness; σ (eV^{-1}): softness; ω (eV): electrophilicity index.

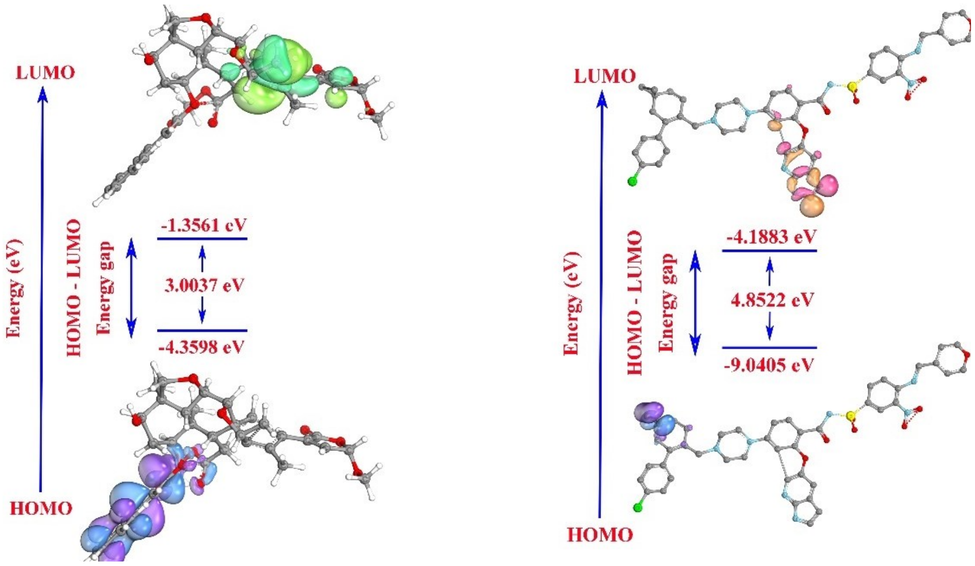

A B

Figure 6. HOMO and LUMO surface diagrams of CPD4 (A) and Venetoclax (B)

Quantum chemistry computation using the DFT method

DFT calculations were performed to complement the docking, molecular dynamics, and MMGBSA analyses by characterizing the electronic structure of CPD4 in comparison with the reference compound Venetoclax. CPD4 exhibits EHOMO (eV) = -4.3598, whereas Venetoclax shows a substantially lower value (-9.0405). Within the usual frontier-orbital interpretation, the less damaging EHOMO for CPD4 is consistent with a comparatively greater propensity to donate electron density relative to Venetoclax under the same theoretical level (Table 4). For the acceptor channel, CPD4 has ELUMO (eV) = -1.3561, while Venetoclax presents -4.1883, indicating that Venetoclax possesses a lower-lying acceptor orbital in this calculation. The combined consequence is a markedly smaller ΔE (eV): energy gap for CPD4 (3.0037) than for Venetoclax (4.8522) (Fig. 6). A reduced gap is commonly associated with increased electronic responsiveness and easier polarization, whereas a larger gap is typically interpreted as greater intrinsic electronic stability.

Frontier-orbital and global conceptual-DFT descriptors provide a qualitative link between electronic structure and noncovalent recognition. A smaller HOMO-LUMO gap (ΔE) generally implies higher electronic polarizability/softness and easier charge redistribution upon environmental perturbation, which can facilitate adaptation to the electrostatic field of the binding pocket and strengthen polarization-driven contributions to binding. In contrast, a larger ΔE is often associated with higher intrinsic electronic stability and lower responsiveness. The electrophilicity index (ω) reflects the tendency to accept electron density; ligands with higher ω typically display a stronger electron-accepting character and may engage more favorably in interactions where electron density donation from the protein stabilizes the complex. These descriptors help rationalize the observed differences in electrostatic and solvation terms in MMGBSA and complement the molecular docking and molecular dynamics simulations results as an electronic-structure perspective rather than a direct quantitative predictor of potency [33], [34].

Global descriptors further distinguish the ligands: Venetoclax has a more negative μ (-6.6144 *vs* -2.8580 eV) and higher χ (6.6144 *vs* 2.8580 eV), indicating stronger electron-attracting character, together with higher η (2.4261 *vs* 1.5019 eV) and lower σ (0.4122 *vs* 0.6658 eV^{-1}), consistent with greater resistance to charge redistribution than CPD4. This separation is reinforced by the electrophilicity index, where ω is significantly higher for Venetoclax (9.0166 eV) than for CPD4 (2.7193 eV), supporting a more electrophilic signature that may relate to the distinct electrostatic-solvation balance observed in the MMGBSA analysis.

CONCLUSION

This study performed computational modelling of limonoids from *M. azedarach* as potential inhibitors of leukemia, focusing on the Bcl-xL protein (3SPF). CPD4 showed the best docking score compared with Venetoclax, forming a hydrogen bond with Arg139 and extensive hydrophobic and van der Waals interactions within the conserved pocket. During 100 ns molecular dynamics, both complexes remained stable; CPD4 sampled a higher RMSD range than Venetoclax while maintaining similar compactness, and hydrogen-bond counts were generally low but more frequently elevated for Venetoclax late in the trajectory. MMGBSA supported favorable binding for both ligands, with ΔTOTAL = -19.73 ± 5.33 kcal/mol for CPD4 and -24.48 ± 9.15 kcal/mol for Venetoclax, where CPD4 was driven by gas-phase interactions (ΔGGAS -43.86 ± 10.49) but penalized by solvation (ΔGSOLV 24.13 ± 6.62). DFT descriptors indicated that CPD4 is more polarizable, showing EHOMO = -4.3598 eV, ΔE = 3.0037 eV, and ω = 2.7193 eV, whereas Venetoclax displayed EHOMO = -9.0405 eV, ΔE = 4.8522 eV, and a higher ω = 9.0166 eV. Overall, the integrated results position CPD4 as a promising computational hit for further optimization and experimental evaluation as a potential Bcl-xL-interacting scaffold in leukemia research. However, the present computational results do not establish that the studied limonoids share the same mechanism of action as Venetoclax, but instead support a possible interaction with the same or an overlapping Bcl-xL pocket region.

REFERENCES

1. S. Ishaq, S. Afzal, S. A. Usmani, I. Wajid, A. Aziz, R. Tahir, A. Ahmad, A. Ullah, *Crit. Rev. Oncol. Hematol.*, **215**, 104909 (2025).
2. S. Shimony, M. Stahl, R. M. Stone, *Am. J. Hematol.*, **98**, 502 (2023).
3. L. Kalinkova, A. Sevcikova, V. Stevurkova, I. Fridrichova, S. Ciernikova, *Int. J. Mol. Sci.*, **24**, 633 (2023).
4. S. Ingole, N. Vasdev, M. Tekade, T. Gupta, B. Pawar, M. Mhatre, A. G. Prasad, R. K. Tekade, Toxic effects of cancer therapies (Public health and toxicology issues in drug research), Academic Press, Boston, 2024.
5. S. K. Jha, N. Singh, O. R. Shanker, I. Antil, J. S. Baghel, V. Huddar, R. Tripathi, *Front. Nat. Prod.*, **4**, 1635197 (2025).
6. J. Plati, O. Bucur, R. Khosravi-Far, *Integr. Biol.*, **3**, 279 (2011).
7. M. Morales-Martínez, M. I. Vega, *Int. J. Mol. Sci.*, **23**, 2193 (2022).
8. P. Ryzhov, Y. Tian, Y. Yao, A. A. Bobkov, W. Im, F. M. Marassi, *Biophys. J.*, **119**, 1324 (2020).
9. Y. S. Shi, Y. Zhang, H. T. Li, C. H. Wu, H. R. El-Seedi, W. K. Ye, Z. W. Wang, C. B. Li, X. F. Zhang, G. Y. Kai, *J. Funct. Foods*, **75**, 104213 (2020).
10. A. Roy, S. Saraf, *Biol. Pharm. Bull.*, **29**, 191 (2006).
11. T. Akihisa, X. Pan, Y. Nakamura, T. Kikuchi, N. Takahashi, M. Matsumoto, E. Ogihara, M. Fukatsu, K. Koike, H. Tokuda, *Phytochemistry*, **89**, 59 (2013).
12. H. Zhou, J. Chen, J. L. Meagher, C. Y. Yang, A. Aguilar, L. Liu, L. Bai, X. Cong, Q. Cai, X. Fang, J. A. Stuckey, S. Wang, *J. Med. Chem.*, **55**, 4664 (2012).
13. G. M. Morris, R. Huey, W. Lindstrom, M. F. Sanner, R. K. Belew, D. S. Goodsell, A. J. Olson, *J. Comput. Chem.*, **30**, 2785 (2009).
14. D. Van Der Spoel, E. Lindahl, B. Hess, G. Groenhof, A. E. Mark, H. J. Berendsen, *J. Comput. Chem.*, **26**, 1701 (2005).
15. N. Guex, M. C. Peitsch, *Electrophoresis*, **18**, 2714 (1997).
16. V. Zoete, M. A. Cuendet, A. Grosdidier, O. Michielin, *J. Comput. Chem.*, **32**, 2359 (2011).
17. E. F. Pettersen, T. D. Goddard, C. C. Huang, G. S. Couch, D. M. Greenblatt, E. C. Meng, T. E. Ferrin, *J. Comput. Chem.*, **25**, 1605 (2004).
18. H. D. Nguyen, *Phys. Chem. Res.*, **13**, 783 (2025).
19. D. E. Pires, T. L. Blundell, D. B. Ascher, *J. Med. Chem.*, **58**, 4066 (2015).
20. F. Neese, *WIREs Comput. Mol. Sci.*, **15**, e70019 (2025).
21. M. D. Hanwell, D. E. Curtis, D. C. Lonie, T. Vandermeersch, E. Zurek, G. R. Hutchison, *J. Cheminform.*, **4**, 17 (2012).
22. G. Knizia, *J. Chem. Theory Comput.*, **9**, 4834 (2013).
23. S. Singh, Q. Bani Baker, D. B. Singh, Molecular docking and molecular dynamics simulation (Bioinformatics), Academic Press, Boston, 2022.
24. D. Ramírez, J. Caballero, *Molecules*, **23**, 1038 (2018).
25. G. Bitencourt-Ferreira, M. Veit-Acosta, W. F. de Azevedo, Hydrogen bonds in protein-ligand complexes (Docking screens for drug discovery), Springer, New York, 2019.
26. G. Bitencourt-Ferreira, M. Veit-Acosta, W. F. de Azevedo, Van der Waals potential in protein complexes (Docking screens for drug discovery), Springer, New York, 2019.
27. Z. Jin, Z. Wei, *Compr. Rev. Food Sci. Food Saf.*, **23**, e13280 (2024).
28. H. Rajput, G. Choudhary, H. Siddiqui, A. Ghosh, M. Prajapat, A. Prakash, B. Medhi, *Indian J. Pharmacol.*, **57**, 308 (2025).
29. H. O. Tekin, G. ALMisned, S. A. M. Issa, E. S. Kasikci, M. Arooj, A. Ene, M. S. Al-Buriahi, M. Konuk, H. M. H. Zakaly, *Front. Phys.*, **10**, 838725

(2022).

30. A. K. Madan, H. Dureja, Prediction of pharmacokinetic parameters (Computational toxicology), Humana Press, Totowa, 2012.
31. P. Sucharitha, K. Ramesh Reddy, S. V Satyanarayana, T. Garg, Absorption, distribution, metabolism, excretion, and toxicity assessment of drugs using computational tools (Computational approaches for novel therapeutic and diagnostic designing to mitigate SARS-CoV-2 infection), Academic Press, Boston, 2022.
32. F. P. Guengerich, *Toxicol. Res.*, **37**, 1 (2021).
33. F. Basha, F. L. A. Khan, S. Muthu, M. Raja, *Comput. Theor. Chem.*, **1198**, 113169 (2021).
34. Y. Huang, C. Rong, R. Zhang, S. Liu, *J. Mol. Model.*, **23**, 3 (2016).

Bulgarian Chemical Communications, Volume 58, Issue 2 (pp. 173-182) 2026 *DOI: 10.34049/bcc.58.2.5738*

Optimization and performance evaluation of hydroxyapatite–magnesium oxide coatings on UHMWPE for improved tribological and antibacterial behavior in orthopaedic applications

A. Samraj Selvaraj[1]*, A. Sanmugam[1], A. Muniyappan[2]

[1] *Department of Applied Chemistry, Sri Venkateswara College of Engineering, Sriperumbudur, Tamil Nadu, 602117 India*
[2] *Department of Mechanical Engineering, Sri Venkateswara College of Engineering, Sriperumbudur, Tamil Nadu, 602117 India*

Received: December 01, 2025; Revised: April 21, 2026

Ultra-high molecular weight polyethylene (UHMWPE) remains the leading bearing material for joint prostheses, favored for its excellent biocompatibility and mechanical characteristics. However, wear-induced osteolysis remains a significant challenge. This study delves into the development and characterization of hydroxyapatite (HA) and magnesium oxide (MgO) coatings, both singly and in combination, applied to the surface of UHMWPE to enhance its tribological and antibacterial properties. Systematically varied key parameters of the dip-coating process were: immersion speed (IS), dwell time (DT), and withdrawal speed (WS). Through ANOVA analysis, the optimal input conditions for the dip-coating procedure were identified. The performance was subsequently assessed using a pin-on-disc tribometer under dry sliding conditions. This experimental study results indicate that UHMWPE coated with HA-MgO dual layers exhibited a marked reduction in the coefficient of friction (COF) and specific wear rate compared to both uncoated and singly coated UHMWPE samples. Additionally, the antibacterial effectiveness against *Escherichia coli* was significantly enhanced, as evidenced by the larger zones of inhibition on HA-MgO-coated surfaces. These findings highlight the potential of HA-MgO composite coatings to provide multifunctional enhancements for UHMWPE orthopaedic implants, thereby promoting implant longevity and reducing the risk of postoperative infection.

Keywords: Hydroxyapatite, magnesium oxide, dip-coating, pin-on-disc, antibacterial assay, *E. coli* bacteria.

INTRODUCTION

Ultra-high molecular weight polyethylene (UHMWPE) has been integral to orthopaedic implants since the 1960s, primarily due to its high toughness, excellent wear resistance, and biocompatibility. It remains the material of choice for bearing surfaces in total joint arthroplasties, particularly in hip and knee replacements, as evidenced by its dominance in the field [1]. Advances in UHMWPE processing have aimed to mitigate issues such as oxidative degradation and wear particle-induced osteolysis — two major contributors to implant failure. Despite its widespread application, UHMWPE's surface characteristics lead to significant challenges. The effects of γ-ray sterilization and endogenous oxidation can severely diminish its mechanical properties and accelerate wear rates. Oxidized UHMWPE is known to elicit heightened granulocyte activity compared to its unoxidized counterparts, potentially resulting in increased inflammation and expedited implant failure [2]. Furthermore, oxidative processes can induce granulocyte apoptosis, directly affecting the integrity of the implant-tissue interface [3]. The hydrophobic nature of UHMWPE also presents limitations in lubrication by synovial fluid, exacerbating wear issues when compared to the lubrication properties of natural cartilage [4]. To address these challenges, various modifications to both the surface and bulk properties of UHMWPE have been proposed [5]. Crosslinking *via* ionizing radiation enhances durability but can also generate free radicals that contribute to long-term oxidative degradation [6]. The incorporation of vitamin E (α-tocopherol) as an antioxidant has shown promise in mitigating oxidation through diffusion or blending techniques, effectively enhancing oxidative resistance and reducing bacterial adhesion without compromising wear behavior [7]. Moreover, researchers are exploring graftable reactive antioxidants that chemically bond with the polymer matrix during the radiation crosslinking process, thereby improving oxidative stability with minimal additional processing [8]. Surface engineering has emerged as a critical focus, employing methods such as plasma immersion ion implantation and laser surface modification to

---

* To whom all correspondence should be sent:
E-mail: *allwin.samraj@gmail.com*

enhance wear resistance and biocompatibility through alterations in surface chemistry and microstructure [9, 10]. Ion implantation, in particular, promotes wear resistance by forming nitrogen-carbon crosslinks while preserving the integrity of the surface [11]. Additionally, the combination of ion-implanted UHMWPE with thermally oxidized Ti6Al4V counterfaces has significantly improved tribological performance, enhancing mechanical stability and wear resistance [12]. Porous surface modifications also present opportunities for controlled drug release from acetabular liners, addressing infection prophylaxis while maintaining mechanical integrity — heralding a new era of multifunctional implants [13]. Researchers are exploring surface modifications using bioactive ceramic coatings, specifically hydroxyapatite (HA) and magnesium oxide (MgO), to enhance the bioactivity and osseointegration of ultra-high molecular weight polyethylene (UHMWPE), which exhibits poor integration with bone. Hydroxyapatite, a calcium phosphate analogous to bone mineral, has garnered attention in orthopaedic applications due to its ability to promote cell adhesion and proliferation. Numerous studies indicate that HA coatings on implants significantly enhance osseointegration and osteoconductivity. For example, titanium implants with HA coatings demonstrate improved cell viability and mineralization, particularly when supplemented with natural extracts or dopants [14]. Additionally, dip-coating magnesium alloys with HA not only provides corrosion protection but also maintains cellular compatibility while fostering osteogenesis [15]. Magnesium oxide (MgO), a relatively under-researched bioactive ceramic, shows potential due to its antibacterial properties and ability to modulate cellular responses. When incorporated in HA, magnesium significantly enhances implant performance. Mg-doped HA coatings have been shown to facilitate osseointegration and mechanical fixation in osteoporotic bone models [16] while also mitigating corrosion and inflammatory responses in magnesium alloy substrates [17]. Investigations into HA/Mg composite coatings on stainless steel highlight their superior biocompatibility and bioactivity, particularly when the degradation rate of Mg is controlled to optimize osteogenic outcomes [18]. The synergistic effect of HA and MgO coatings markedly improves both integration and longevity of orthopaedic implants. Composite or bilayer coatings that incorporate HA alongside Mg or MgO not only enhance corrosion resistance and cellular viability but also promote superior bone tissue regeneration compared to single-layer coatings. Research combining HA with magnesium-based polymers has demonstrated that the HA/Mg interface diminishes ion release, slows degradation, and fosters osteoblast proliferation [19]. Notably, double-layer HA coatings with Mg have been found to prevent substrate corrosion and reinforce mechanical strength [20]. Dip-coating has emerged as a cost-effective and efficient technique for applying HA and MgO coatings to orthopaedic materials, ensuring uniform application and strong adhesion. Comparative studies have shown that dip-coating outperforms spin coating in terms of protecting magnesium alloys from corrosion and eliciting cellular responses [21]. Furthermore, dip-coating allows for precise control over coating thickness and uniformity, which minimizes defects such as cracks and delamination [22]. Overall, the application of dip-coated HA and MgO has significant potential for enhancing the longevity and performance of implants by reducing corrosion and wear debris while improving osseointegration. For instance, bioresorbable magnesium implants coated with HA/Mg composites exhibit reduced ion release and enhanced tissue compatibility over time, signaling improved durability and functional efficacy [23].

EXPERIMENTAL

Materials

UHMWPE is a commonly used material in orthopaedic implants, particularly in total joint arthroplasty, due to its excellent wear resistance, low coefficient of friction, biocompatibility, and mechanical toughness. Table 1 presents the material properties of UHMWPE as a biomaterial. In accordance with ASTM G99 standards, the pin specimens were created into cylindrical or spherical shapes from purchased rod material. The specimens were carefully machined to dimensions of 28 mm in length and 10 mm in diameter using wire-cut electrical discharge machining (EDM).

Table 1. Mechanical properties of UHMWPE

Property	Typical value
Density	970 kg/m^3
Tensile strength	20 – 40 MPa
Young's modulus	500 –1500 MPa
Compressive yield strength	38 Mpa
Impact strength	80–160 kJ/m^2 (Izod)
Hardness	Shore D ~62–66
Poisson's ratio	0.33

Figure 1(a) shows the machined UHMWPE pin specimen. The disc serves as the counter body in the setup, while the pin specimens are typically traversed across its surface. For our application involving the interaction of a polymer with metal, a metal spacer composed of 316L stainless steel is used. This material has a density of 8000 kg/m^3, demonstrating favorable mechanical strength along with excellent corrosion resistance. It is a widely used material in biomedical applications, including implants and components for body modification. Figure 1(b) shows an illustration of the disc employed in the pin-on-disc experimental study.

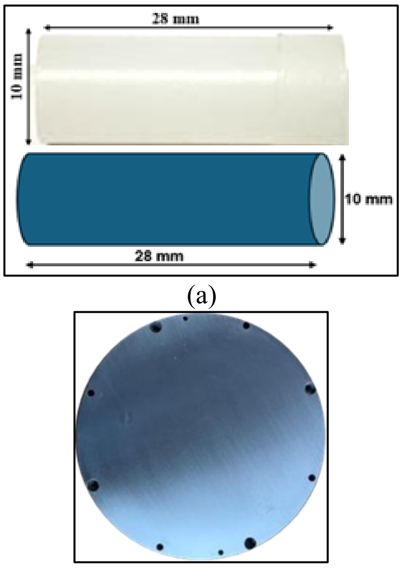

(a)

(b)

Figure 1. (a) UHMWPE pin specimen; (b) 316L SS counterpart disc.

Dip-coating process

Hydroxyapatite is typically synthesized *via* wet chemical methods, where calcium nitrate and diammonium hydrogen phosphate are reacted under controlled pH and temperature conditions to precipitate HA particles. These particles are then calcined and suspended in a solvent medium like ethanol or distilled water for coating applications [24]. For MgO, the sol–gel route is commonly used, starting from magnesium alkoxide or nitrate, followed by hydrolysis and drying to form MgO nanoparticles. These are also suspended in a suitable solvent to prepare a stable dip-coating solution [25]. The dip-coating process involves immersing the UHMWPE pins in the prepared suspension of coating material and withdrawing them at a constant speed. This process has been successfully used in several studies to deposit HA and MgO layers on various biomaterials [24, 26]. The following steps are carried out to do the dip-coating process using different coating materials, such as hydroxyapatite and magnesium oxide. First, UHMWPE surfaces are cleaned with ethanol to remove contaminants. The specimen is then immersed in the HA solution at a controlled speed, dipped into the HA solution for a specified dwell time, and withdrawn from the HA solution. After each dip, the specimen is dried at room temperature for up to 60 min to allow solvent evaporation and partial curing [27, 28]. Each specimen typically undergoes five dip cycles per material to achieve optimal surface coverage and adhesion. This repetition builds up a sufficient coating layer while avoiding defects like cracks or peeling [24]. Figure 2 illustrates the dip-coating process for the UHMWPE_HA, UHMWPE_MgO and UHMWPE_HA_MgO specimens. The second coating material, magnesium oxide, is applied in the same manner as the previous steps for HA. Finally, for the composite coatings of hydroxyapatite and magnesium oxide, the order of dipping is critical. Studies recommend coating first with HA to promote osteointegration, followed by MgO to enhance antibacterial and mechanical properties [25, 29]. Table 2 clearly indicates the mass difference after the dip-coating; this increase in mass is due to the coated material added to the substrate.

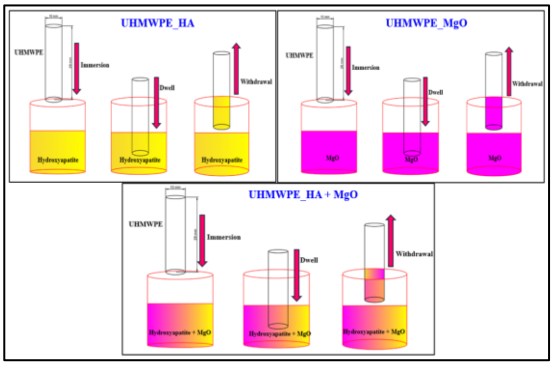

Figure 2. Dip-coating process

Table 2. Mass and hardness values after coating

Specimen type	Mass before coating (g)	Mass after coating (g)	Hardness value HV
UHMWPE	1.963	1.963	7.6
UHMWPE_HA	1.963	2.075	23.5
UHMWPE_MgO	1.960	2.096	25.1
UHMWPE_HA_MgO	1.961	2.135	36.4

Pin-on-disc tribometer

Tribological testing was performed using a pin-on-disc tribometer, shown in Figure 3, following the ASTM G99 standard for wear assessment. In this setup, the pin specimen, oriented vertically, was pressed against a horizontally rotating 316L stainless steel disc. A constant normal load of 100 N was applied throughout the experiment [30], and frictional forces were continuously monitored *via* a load cell. The experimental parameters were standardized to simulate extreme contact conditions relevant to biomedical and engineering applications employing UHMWPE-based materials, specifically: sliding speed of 2.1 m/s [31], test duration of 10 min, conducted at room temperature under dry sliding conditions.

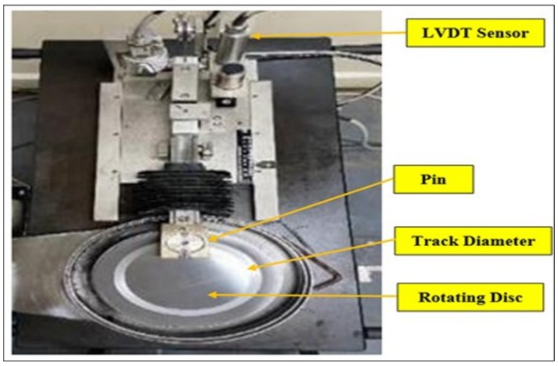

Figure 3. Pin-on-disc tribometer

The specific wear rate of the pin specimens was calculated using the following relations:

$$W = \frac{\Delta V}{F \times L} \tag{1}$$

$$L = v \times t \tag{2}$$

$$\mu = \frac{F_f}{F} \tag{3}$$

where, W - specific wear rate (mm^3/N-m); ΔV - volume loss (mm^3); F - applied normal load (N); L - sliding distance (m); υ - sliding velocity (m/s); t - time period (s); F_f - frictional force.

Table 3 presents the results of the wear test conducted on different UHMWPE-based specimens. It compares the mass of each specimen before and after the wear test, with the corresponding mass loss calculated. Pure UHMWPE showed the highest mass loss (0.201 g), indicating the lowest wear resistance. The incorporation of hydroxyapatite (HA) and magnesium oxide (MgO) significantly reduced the wear loss. Among the composites, UHMWPE reinforced with both HA and MgO exhibited the least mass loss (0.084 g), suggesting that the combined reinforcement enhances wear resistance more effectively than individual fillers.

Table 3. Mass of the specimen before and after the wear test

Specimen type	Mass before wear test (g)	Mass after wear test (g)
UHMWPE	1.963	1.762
UHMWPE_HA	2.071	1.978
UHMWPE_MgO	2.096	2.004
UHMWPE_HA_MgO	2.135	2.054

ANOVA

Table 4. Analysis of variance

Source	DF	SS	MS	F	p-value
Immersion speed	2	0.00165	0.00083	136.34	<0.001
Dwell time	2	0.00040	0.00020	32.67	<0.001
Withdrawal speed	2	0.00044	0.00022	36.43	<0.001
Material	2	0.06758	0.03379	11107.1	<0.001
Immersion × saterial	4	0.00155	0.00039	6.37	<0.001
Dwell × saterial	4	0.00142	0.00036	5.83	<0.001
Withdrawal × saterial	4	0.00038	0.00009	1.48	0.224
Immersion × dwell	4	0.00067	0.00017	2.77	0.038
Immersion × withdrawal	4	0.00007	0.00002	0.27	0.893
Dwell × withdrawal	4	0.00015	0.00004	0.61	0.660
Error	54	0.00033	0.00001	–	–
Total	82	0.07463	–	–	–

Table 4 reveals that immersion speed, dwell time, withdrawal speed, and material type exert statistically significant effects on the response variable ($p < 0.001$ for all factors). Among these, the material exhibits the most dominant influence, with an exceptionally high F-value (11107.1), indicating that the choice of material plays a critical role in governing performance. Immersion speed (F = 136.34), withdrawal speed (F = 36.43), and dwell time (F = 32.67) also contribute significantly, though to a lesser degree. Interaction effects, particularly immersion × material and dwell × material, are also significant ($p < 0.001$), suggesting that the material properties strongly mediate the impact of processing parameters. Conversely, interactions such as withdrawal × material, immersion × withdrawal, and dwell × withdrawal show no significant influence ($p > 0.05$), highlighting that not all parameter combinations are critical. Overall, these results emphasize that optimizing material selection, along with immersion and dwell conditions, is essential for improving system performance, whereas withdrawal-related effects are comparatively less influential.

Antibacterial assay

To evaluate the antibacterial activity of UHMWPE, UHMWPE_HA, UHMWPE_MgO, and UHMWPE_HA_MgO specimens against *E. coli* the zone of inhibition (ZOI) method was used. Figure 4 shows the detailed experimental procedure for the antibacterial assay.

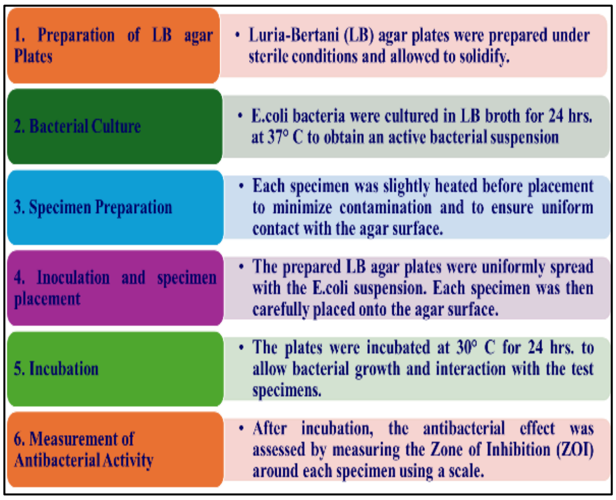

1. Preparation of LB agar Plates
- Luria-Bertani (LB) agar plates were prepared under sterile conditions and allowed to solidify.

2. Bacterial Culture
- E.coli bacteria were cultured in LB broth for 24 hrs. at 37° C to obtain an active bacterial suspension

3. Specimen Preparation
- Each specimen was slightly heated before placement to minimize contamination and to ensure uniform contact with the agar surface.

4. Inoculation and specimen placement
- The prepared LB agar plates were uniformly spread with the E.coli suspension. Each specimen was then carefully placed onto the agar surface.

5. Incubation
- The plates were incubated at 30° C for 24 hrs. to allow bacterial growth and interaction with the test specimens.

6. Measurement of Antibacterial Activity
- After incubation, the antibacterial effect was assessed by measuring the Zone of Inhibition (ZOI) around each specimen using a scale.

Figure 4. Experimental procedure of antibacterial assay

RESULTS AND DISCUSSION

Main effects of process parameters

Figure 5 shows the main effects plots which demonstrate that immersion speed, dwell time, and withdrawal speed significantly influence both the friction coefficient and the wear rate.

Immersion speed: For both friction coefficient and wear rate, the lowest values were observed at an immersion speed of 7.5 mm/s. At lower speeds (5.0 mm/s), higher friction (0.220) and wear (0.00444 mm³/N-m) were recorded, while further increasing the speed to 10.0 mm/s again elevated both properties. This indicates that moderate immersion speeds promote optimal coating uniformity and adhesion, whereas excessively low or high speeds lead to non-uniform films and poorer tribological performance.

Dwell time: The results show that a dwell time of 30 s consistently minimized friction (0.218) and wear (0.00425 mm³/N-m). Shorter (10 s) and longer (50 s) dwell times resulted in higher values for both responses. This suggests that 30 s is the optimal time window to allow solvent exchange and coating stabilization, whereas insufficient or excessive dwell periods may cause structural instabilities or thickness variations.

Withdrawal speed: Withdrawal speed of 3.5 mm/s yielded the lowest friction (0.218) and wear (0.00428 mm³/N-m), while both slower (2.0 mm/s) and faster (5.0 mm/s) speeds increased these values. This confirms that intermediate withdrawal speeds ensure smooth drainage and film uniformity, while extremes result in uneven coating layers.

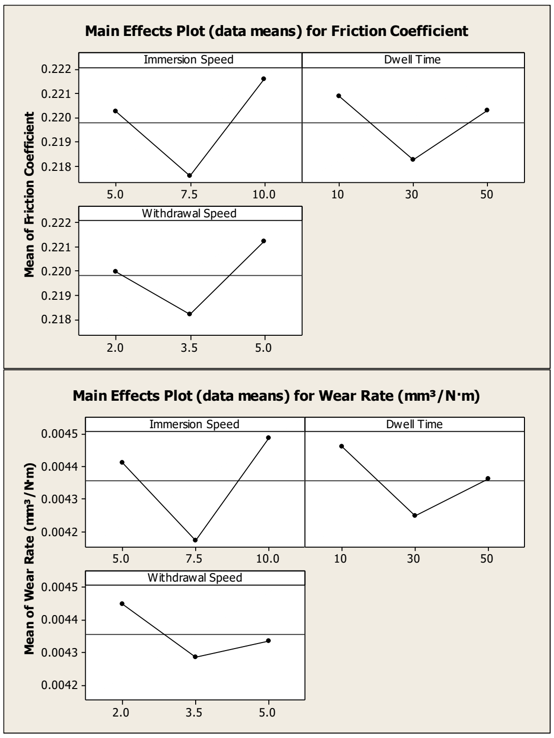

Figure 5. Main effects plot for friction and wear rate

Interaction effects of process parameters

Figure 6 illustrates the interaction plots which provide deeper insights into the coupled effects of the parameters.

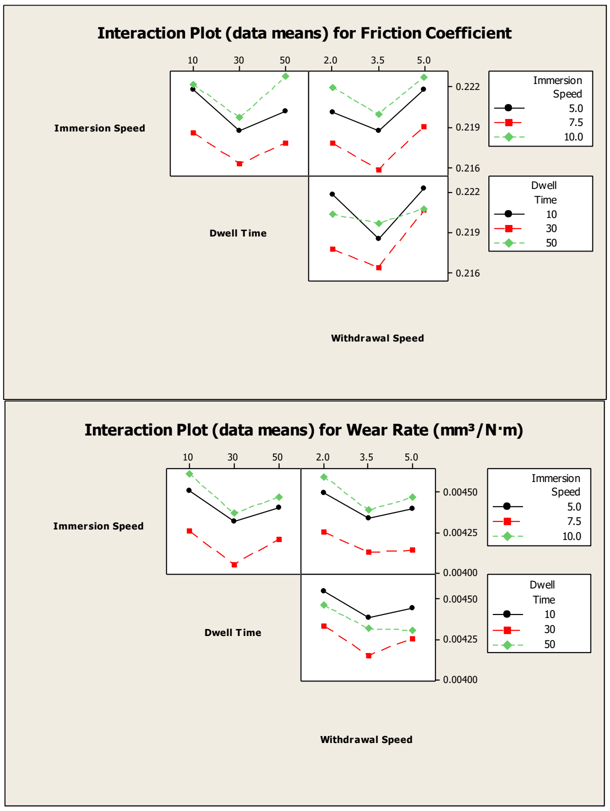

Figure 6. Interaction plot for friction and wear rate

Immersion speed × dwell time: Across immersion speeds, the lowest friction and wear were consistently achieved at a dwell time of 30 s. The benefit of this dwell period was most pronounced at an immersion speed of 7.5 mm/s, highlighting the importance of parameter synergy. At higher immersion speeds (10 mm/s), dwell time had a reduced effect, suggesting less control over coating uniformity.

Withdrawal speed × dwell time: optimal withdrawal speed of 3.5 mm/s and dwell time of 30 s consistently gave the lowest values for both friction and wear. However, at higher withdrawal speeds (5.0 mm/s), differences among dwell times diminished, indicating that excessive withdrawal speed can overshadow the influence of dwell optimization.

Immersion speed × withdrawal speed: For all immersion speeds, the withdrawal speed of 3.5 mm/s resulted in the lowest friction and wear, with the strongest reduction observed at 7.5 mm/s immersion speed. This again confirms the synergistic effect of intermediate immersion and withdrawal rates in producing more stable, uniform coatings.

The results highlight that tribological performance strongly depends on careful optimization of process parameters. Both friction coefficient and wear rate followed similar trends, with intermediate levels of immersion speed, dwell time, and withdrawal speed providing the most favorable outcomes. Mechanistically, these trends may be explained by the dynamics of film formation during dip-coating. At intermediate speeds, the coating layer is more uniform, minimizing asperities that contribute to friction and wear. Likewise, the dwell time of 30 s appears to strike a balance between solvent exchange and coating stabilization, avoiding incomplete deposition at short times and instability at longer times. The optimal combination of parameters is shown in Table 5. This combination consistently produced the lowest friction coefficient (0.218) and wear rate (0.00425 mm³/N-m). Importantly, the alignment of optimal conditions for both properties underscores the robustness of this parameter set in achieving durable, low-friction coatings.

Table 5. Optimum process parameters

Parameter	Optimum value
Immersion speed (IS)	7.5 m/s
Dwell time (DT)	30 s
Withdrawal speed (WS)	3.5 m/s

Effect of process parameters on friction coefficient

Figure 7 shows the variation of the friction coefficient with (a) immersion speed, (b) dwell time, and (c) withdrawal speed for HA, MgO, and HA+MgO coatings. The results show that HA coatings consistently exhibited the highest friction, while HA+MgO coatings achieved the lowest values. In all cases, intermediate processing parameters (7.5 mm/s immersion speed, 30 s dwell time, and 3.5 mm/s withdrawal speed) minimized the friction coefficient, highlighting the importance of parameter optimization for achieving uniform and adherent coatings.

Influence of deposition parameters on wear resistance

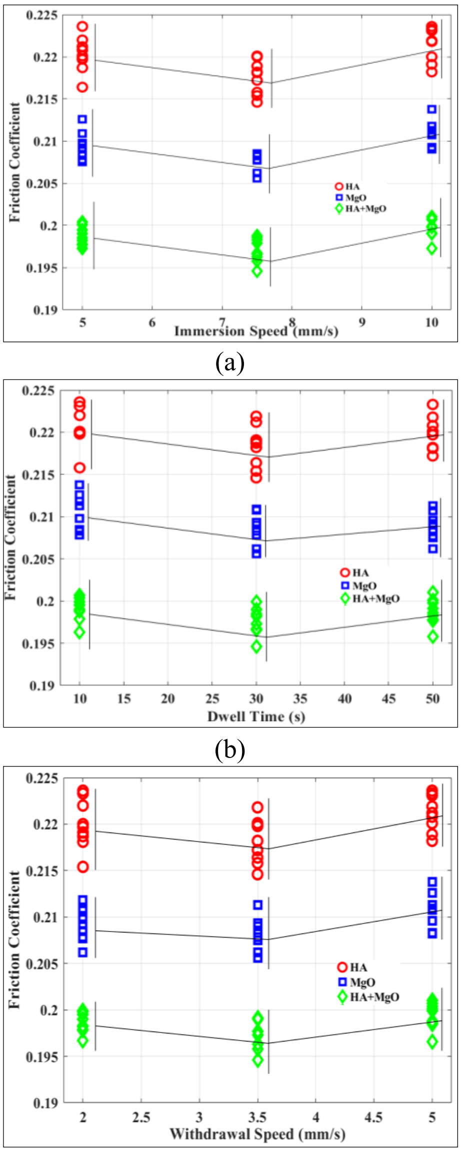

(a)

(b)

(c)

Figure 7. (a) Friction *versus* immersion speed, (b) Friction *versus* dwell time, (c) Friction *versus* withdrawal speed.

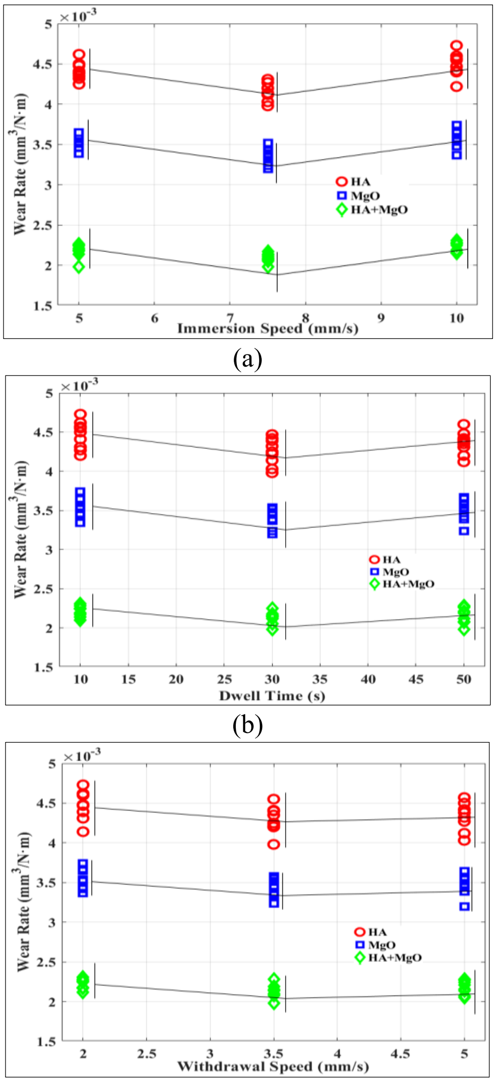

(a)

(b)

(c)

Figure 8. (a) Wear *versus* immersion speed, (b) Wear *versus* dwell time, (c) Wear *versus* withdrawal speed.

Elemental composition analysis (EDX)

The elemental composition of uncoated UHMWPE and its surface-modified variants was analyzed using energy dispersive X-ray spectroscopy (EDX), with the results illustrated in Figure 9. The EDX spectrum of the base UHMWPE, depicted in Figure 9(a), reveals a predominance of carbon (C) at 92.85 wt.% and oxygen (O) at 5.72 wt.%, characteristic of its polyolefin structure. Minor trace elements detected include titanium (Ti) (0.84 wt.%) and calcium (Ca) (0.59 wt.%), likely originating from environmental interactions or processing residues. Figure 9(b) illustrates the elemental profile of UHMWPE coated with hydroxyapatite (HA), showing substantial alterations in composition. The carbon content diminishes to 32.1 wt.%, whereas oxygen (38.25 wt.%), phosphorus (P, 9.82 wt.%), and calcium (18.4 wt.%) significantly increase, aligning with the hydroxyapatite's composition ($Ca_{10}(PO_4)_6(OH)_2$). This shift confirms the successful deposition of HA onto the UHMWPE surface, with minor peaks of residual sodium (Na) and titanium (Ti) suggesting the influence of processing artefacts. In Figure 9(c), the EDX analysis of the UHMWPE surface coated with magnesium oxide (MgO) reveals a prominent magnesium (Mg) peak at 11.9 wt.%, along with an elevated oxygen content of 25.8 wt.%, indicating effective incorporation of MgO. The carbon content remains substantial (61.5 wt.%) due to the underlying UHMWPE structure, while trace amounts of silicon (Si) and calcium (Ca) may reflect slight cross-contamination or impurities from the synthesis. Figure 9(d) presents the EDX results for the hybrid-coated UHMWPE surface, demonstrating a successful co-deposition of HA and MgO.

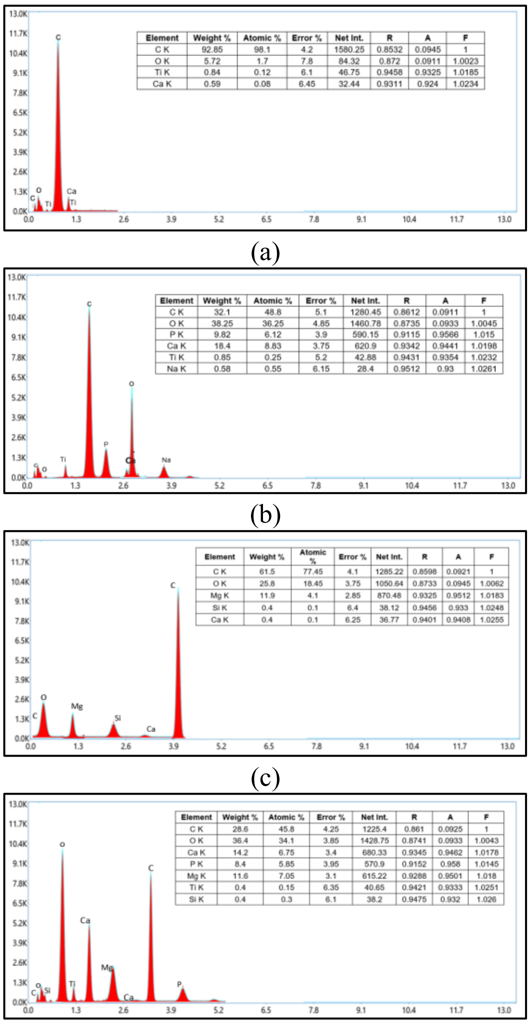

Element	Weight %	Atomic %	Error %	Net Int.	R	A	F
C K	92.85	98.1	4.2	1580.25	0.8532	0.0945	1
O K	5.72	1.7	7.8	84.32	0.872	0.0911	1.0023
Ti K	0.84	0.12	6.1	46.75	0.9458	0.9325	1.0185
Ca K	0.59	0.08	6.45	32.44	0.9311	0.924	1.0234

(a)

Element	Weight %	Atomic %	Error %	Net Int.	R	A	F
C K	32.1	48.8	5.1	1280.45	0.8612	0.0911	1
O K	38.25	36.25	4.85	1460.78	0.8735	0.0933	1.0045
P K	9.82	6.12	3.9	590.15	0.9115	0.9566	1.015
Ca K	18.4	8.83	3.75	620.9	0.9342	0.9441	1.0198
Ti K	0.85	0.25	5.2	42.88	0.9431	0.9354	1.0232
Na K	0.58	0.55	6.15	28.4	0.9512	0.93	1.0261

(b)

Element	Weight %	Atomic %	Error %	Net Int.	R	A	F
C K	61.5	77.45	4.1	1285.22	0.8598	0.0921	1
O K	25.8	18.45	3.75	1050.64	0.8733	0.0945	1.0062
Mg K	11.9	4.1	2.85	870.48	0.9325	0.9512	1.0183
Si K	0.4	0.1	6.4	38.12	0.9456	0.933	1.0248
Ca K	0.4	0.1	6.25	36.77	0.9401	0.9408	1.0255

(c)

Element	Weight %	Atomic %	Error %	Net Int.	R	A	F
C K	28.6	45.8	4.25	1225.4	0.861	0.0925	1
O K	36.4	34.1	3.85	1428.75	0.8741	0.0933	1.0043
Ca K	14.2	6.75	3.4	680.33	0.9345	0.9462	1.0178
P K	8.4	5.85	3.95	570.9	0.9152	0.958	1.0145
Mg K	11.6	7.05	3.1	615.22	0.9288	0.9501	1.018
Ti K	0.4	0.15	6.35	40.65	0.9421	0.9333	1.0251
Si K	0.4	0.3	6.1	38.2	0.9475	0.932	1.026

(d)

Figure 9. Element composition of (a) UHMWPE; (b) HA coated; (c) MgO coated; (d) Hybrid coated HA and MgO.

Elemental analysis shows significant levels of oxygen (36.4 wt.%), calcium (14.2 wt.%), magnesium (11.6 wt.%), and phosphorus (8.4 wt.%), with the carbon content further reduced to 28.6 wt.%, indicative of effective surface coverage. Titanium and silicon are also detected in minor quantities. The EDX findings unequivocally confirm that the surface coatings were successfully deposited on the UHMWPE substrates. The elemental distributions for each sample correspond well with the targeted HA and MgO materials, validating the coating process. The HA-coated surface enhances bioactive elements such as calcium and phosphorus, promoting osteoconductivity and bone integration.

Conversely, the MgO coating introduces magnesium, recognized for its antibacterial properties and its contribution to improved tribological performance through enhanced wear resistance. The synergistic benefits of the dual HA-MgO coating position it as an outstanding candidate for orthopaedic applications, combining bioactivity with antimicrobial functionality.

Tribological behavior of unreinforced UHMWPE and its composites

The tribological behavior of unreinforced UHMWPE and its composites with hydroxyapatite (HA), magnesium oxide (MgO), and hybrid HA–MgO fillers was systematically evaluated in terms of coefficient of friction (COF) and specific wear rate. The variation of COF with sliding distance (Figure 10) shows that unreinforced UHMWPE exhibits the highest and most unstable COF values, fluctuating around 0.23–0.25 throughout the sliding distance. The incorporation of HA slightly reduces the COF (0.21–0.23) while MgO reinforcement demonstrates a more significant improvement, lowering the COF to 0.20. The hybrid composite (UHMWPE_HA_MgO) exhibited the most stable and lowest COF (0.18–0.19), indicating the synergistic effect of HA and MgO in enhancing load-bearing capacity and reducing interfacial shear during sliding.

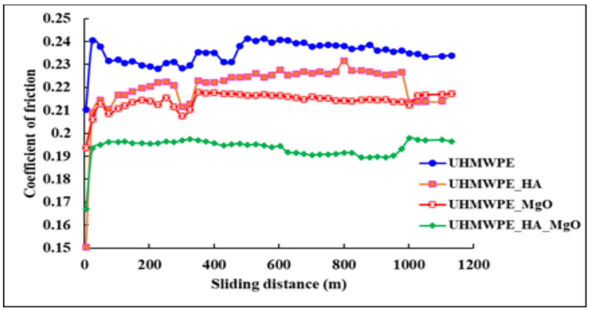

Figure 10. Coefficient of friction *versus* sliding distance

The average COF comparison (Figure 11) further supports this trend, with UHMWPE showing the highest value (0.26), followed by UHMWPE_HA (0.22), UHMWPE_MgO (0.20), and UHMWPE_HA_MgO (0.18). This reduction in COF can be attributed to the improved hardness and load-sharing capability provided by the HA and MgO fillers which reduce polymer chain deformation under load. The hybrid combination likely contributes to improved surface stability by balancing hardness with toughness and dispersion strengthening. At the start of sliding, the contact occurs between fresh, relatively rough asperities of the coating and counterface, leading to higher real contact stress and increased adhesive interaction, which temporarily raises the COF. Additionally, there is no established transfer film or tribolayer at this stage, further contributing to the higher friction value. As the sliding distance increases, surface asperities undergo micro-smoothing and a stable tribolayer (transfer film) forms at the interface. This reduces direct asperity interaction and promotes smoother sliding, resulting in a lower and more stable COF.

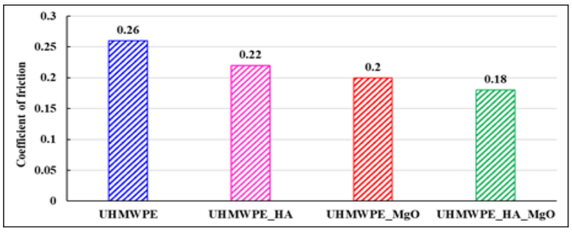

Figure 11. Average coefficient of friction

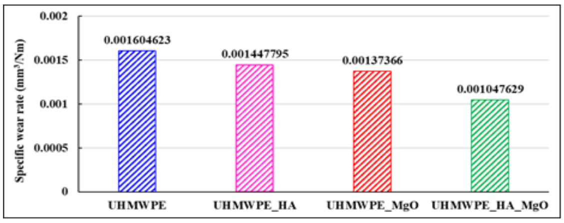

Figure 12. Specific wear rate of UHMWPE and its composite specimens

The specific wear rate analysis (Figure 12) shows a similar trend. Pure UHMWPE has the highest wear rate (1.6046 × 10^{-3} mm^3/Nm), indicating poor resistance to material loss under sliding conditions. The addition of HA decreases the wear rate to 1.4478 × 10^{-3} mm^3/Nm while MgO reinforcement further reduces it to 1.3737 × 10^{-3} mm^3/Nm. The hybrid composite again demonstrates the best performance, with the lowest wear rate of 1.0476 × 10^{-3} mm^3/Nm, representing a 34% improvement compared to pure UHMWPE. This superior wear resistance can be ascribed to improved interfacial bonding and enhanced microstructural stability imparted by the hybrid reinforcement. Overall, the results confirm that reinforcement of UHMWPE with ceramic fillers significantly enhances tribological performance.

While both HA and MgO individually improve friction and wear resistance, the synergistic hybrid reinforcement (HA + MgO) provides the most stable and lowest COF as well as the highest resistance to wear, making UHMWPE_HA_MgO the most promising material among those studied.

Zone of inhibition

Figure 13 shows the antibacterial activity of different UHMWPE composites evaluated using the agar diffusion method against *E. coli* after 24 h of incubation at 30 °C. The results clearly demonstrate that surface modification of UHMWPE with magnesium oxide enhances its antibacterial properties. MgO nanoparticles are known to generate reactive oxygen species and release Mg^{2+} ions, both of which disrupt bacterial cell membranes and inhibit growth.

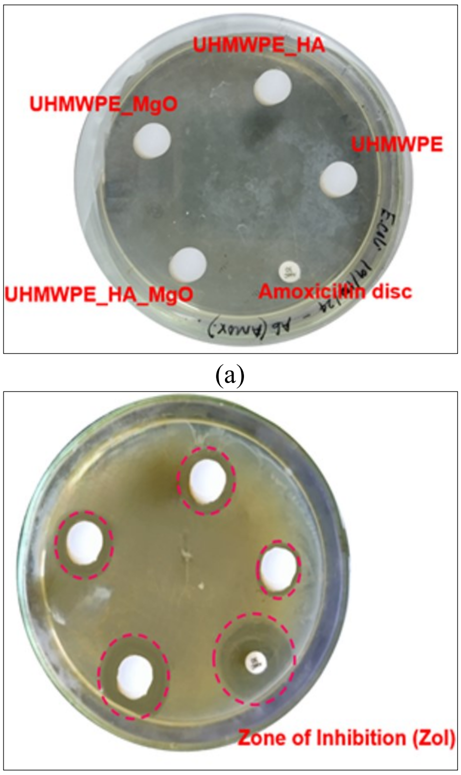

(a)

(b)

Figure 13. (a) Before incubation; (b) After 24 h of incubation.

The ZOI observed around UHMWPE_MgO supports this antibacterial mechanism. In contrast, UHMWPE_HA did not exhibit antibacterial activity. Hydroxyapatite is bioactive and osteoconductive, making it useful for bone integration, but it lacks inherent antimicrobial properties. Interestingly, when MgO and HA were combined (UHMWPE_HA_MgO), antibacterial activity was present but appeared weaker compared to MgO alone. This suggests that while HA contributes to biocompatibility, it may reduce the effective surface availability or reactivity of MgO, leading to a smaller ZOI. The unmodified UHMWPE showed no inhibitory effect, which aligns with its known bioinert nature. This confirms that antibacterial enhancement is directly linked to surface modification with MgO. The amoxicillin disc served as a positive control, showing a strong ZOI and validating the bacterial strain's susceptibility to antibiotics. Table 6 shows that magnesium oxide appears to be the key component imparting antibacterial functionality to UHMWPE while hydroxyapatite mainly contributes to bioactivity but does not enhance antimicrobial performance.

Table 6. ZOI for different UHMWPE samples after 24 h at 30 °C

Sample	Zone of inhibition	Antibacterial activity
UHMWPE	None	No activity
UHMWPE_HA	None	No activity
UHMWPE_MgO	Medium	Strong activity
UHMWPE_HA_MgO	Small	Moderate activity
Amoxicillin disc	Large	Very strong activity

Overall, statistical and performance mapping analyses confirmed that coating composition and dwell time were the most influential factors for antibacterial performance, whereas coating composition and intermediate process parameters (immersion and withdrawal speeds) were most significant for tribological enhancement.

CONCLUSION

This study successfully demonstrated that surface modification of UHMWPE using hydroxyapatite (HA), magnesium oxide (MgO), and their hybrid HA–MgO composite *via* dip-coating can significantly enhance the material's functional performance for orthopaedic applications. The experimental results showed that:

(i) *Tribological performance*: The HA–MgO composite coating consistently achieved the lowest coefficient of friction (~0.18–0.19) and the highest wear resistance, representing a ~34% improvement compared to uncoated UHMWPE. This indicates a strong synergistic effect, with HA contributing to hardness and osteoconductivity while MgO improved toughness and load-bearing capacity.

(ii) *Process optimization*: Dip-coating parameters were found to be critical. Intermediate conditions — immersion speed of 7.5 mm/s, dwell time of 30 s, and withdrawal speed of 3.5 mm/s — produced the most uniform coatings, minimizing friction and wear while ensuring coating stability.

(iii) *Antibacterial activity*: MgO was identified as the key contributor to antibacterial functionality, producing strong inhibition against *E. coli*. While HA alone did not exhibit antimicrobial effects, the HA–MgO hybrid provided moderate antibacterial activity alongside improved biocompatibility, suggesting a balanced multifunctional surface.

(iv) *Trade-offs in performance*: Performance maps revealed that while moderate process parameters favored wear and friction reduction, longer dwell times were advantageous for antibacterial performance. The identified compromise — immersion speeds of 7–8 mm/s, withdrawal speeds of 3–4 mm/s, and dwell times of 35–40 s offer a practical balance for maximizing overall implant performance.

In conclusion, the HA–MgO dual-layer coating emerges as the most promising modification strategy, offering superior wear resistance, stable frictional behavior, and enhanced antibacterial protection compared to uncoated or singly coated UHMWPE. These findings highlight the potential of HA–MgO hybrid coatings to extend implant longevity, reduce the risk of postoperative infection, and improve patient outcomes in orthopaedic applications. Future work should explore *in vivo* evaluations and long-term biological responses to validate these multifunctional benefits under physiological conditions.

REFERENCES

1. C. Cucinelli, *Proc. Electr. Insul. Conf. Electr. Manuf. Expo.*, 424 (2005).
2. F. Renò, M. Sabbatini, M. Cannas, *J. Mater. Sci.: Mater. Med.*, **14**, 241 (2003).
3. F. Renò, F. Lombardi, M. Cannas, *Biomaterials*, **24**, 2895 (2003).
4. S. P. James, R. K. Oldinski, M. Zhang, H. Schwartz, UHMWPE Biomaterials Handbook, 2009, p. 259.
5. S. V. Dorozhkin, *J. Compos. Sci.*, **7**, 273 (2023).
6. J. He, Y. Wang, Y. Qian, J. Guo, J. Lu, W. Yang, *Polymers*, **16**, 3431 (2024).
7. P. Bistolfi, G. Bracco, V. Banche, M. Allizond, A. Boffano, E. M. B. Cimino, A. Del Prever, M. Cuffini, *Orthop. Proc.*, **96** (B), 83 (2014).
8. S. Jefferies, H. Al-Malaika, H. Sheena, *Polym. Degrad. Stab.*, **183**, 109462 (2021).
9. H. Dong, T. Bell, C. Blawert, B. L. Mordike, *J. Mater. Sci. Lett.*, **19**, 1147 (2000).
10. R. Riveiro, J. Soto, R. Del Val, M. Comesaña, F. Boutinguiza, F. Quintero, J. Pou Lusquiños, *Appl. Surf. Sci.*, **302**, 236 (2014).
11. J. Chen, F. Zhu, H. Pan, J. Cao, D. Zhu, H. Xu, Q. Cai, J. Shen, L. Chen, Z. He, *Nucl. Instrum. Methods Phys. Res., Sect. B,* **169**, 26 (2000).
12. W. Shi, H. Dong, *J. Shanghai Univ.* (Engl. Ed.), **9**, 164 (2005).
13. R. Manoj Kumar, P. Gupta, S. K. Sharma, A. Mittal, M. Shekhar, V. Kumar, B. V. Manoj Kumar, P. Roy, D. Lahiri, *Mater. Sci. Eng. C*, **77**, 649 (2017).
14. S. Prabakaran, K. Rohini, *J. Aust. Ceram. Soc.*, **61**, 755 (2025).
15. Y. Husak, O. Solodovnyk, A. Yanovska, Y. Kozik, I. Liubchak, V. Ivchenko, O. Mishchenko, Y. Zinchenko, V. Kuznetsov, M. Pogorielov, *Coatings*, **8** (2018).
16. X. Li, Y. Li, Y. Liao, J. Li, L. Zhang, J. Hu, *Int. J. Oral Maxillofac. Implants*, **29**, 196 (2014).
17. M. Razavi, M. Fathi, O. Savabi, D. Vashaee, L. Tayebi, *Mater. Sci. Eng. C,* **48**, 21 (2015).
18. R. Rezaei, B. Golenji, F. Alipour, M. M. Hadavi, I. Mobasherpour, *Ceram. Int.*, **46**, 25374 (2020).
19. M. M. Bardizadeh, N. Aboudzadeh, A. Khavandi, A. Eivani, *J. Mater. Res. Technol.*, **29**, 2483 (2024).
20. Y. Xu, T. Wang, Y. Guo, G. Li, J. Lian, *Langmuir*, **36**, 13937 (2020).
21. D.-T. Tran, F.-H. Chen, G.-L. Wu, P. C. O. Ching, M.-L. Yeh, *ACS Biomater. Sci. Eng.*, **9**, 705 (2023).
22. S. Ardhy Gunawarman, J. Affi, Y. Yetri, *IOP Conf. Ser.: Mater. Sci. Eng.*, **1041**, 012057 (2021).
23. R. Rojaee, M. Fathi, K. Raeissi, *Mater. Sci. Eng. C,* **33**, 3817 (2013).
24. V. Morales-Nieto, C. H. Navarro, K. J. Moreno, A. Arizmendi-Morquecho, A. Chávez-Valdez, S. García-Miranda, J. F. Louvier-Hernández, *Prog. Org. Coat.*, **76**, 204 (2013).
25. E. Lin, S. S. Kure-Chu, J. Liu, P. Wang, N. Kurita, X. Li, *ECS Meet. Abstr.*, **MA2024-02**, 1578 (2024).
26. G. Çelebi Efe, E. Yenilmez, *Surf. Eng.*, **38**, 417 (2022).
27. J. Jin, X. Chen, S. Zhou, *Mater. Technol.*, **37**, 503 (2022).
28. X. Zhang, X.-W. Li, J.-G. Li, X.-D. Sun, *ACS Appl. Mater. Interfaces*, **6**, 513 (2014).
29. M. L. Dittler, I. Unalan, A. Grünewald, A. M. Beltrán, C. A. Grillo, R. Destch, M. C. Gonzalez, A. R. Boccaccini, *Colloids Surf. B: Biointerfaces*, **182**, 110346 (2019).
30. G. Bergmann, A. Bender, F. Graichen, J. Dymke, A. Rohlmann, A. Trepczynski, M. O. Heller, I. Kutzner, *PLoS One,* **9** (2014).
31. R. Liu, D. Qian, Y. Chen, J. Zou, S. Zheng, B. Bai, Z. Lin, Y. Zhang, Y. Chen, *Sports Biomech.* (2021).

Selected papers presented at the 12th National Conference of Chemistry, September 2025, Sofia, Bulgaria

Bulgarian Chemical Communications, Volume 58, Issue 2 (pp. 185-188) 2026 DOI: 10.34049/bcc.58.2.NCC01

Kinetic study of softwood cooking for bleached pulp production

S. Petrin*, S. Kuzeva, I. Gavrilov, G. Radeva, P. Mileva-Petrova, I. Valchev

University of Chemical Technology and Metallurgy, 8 St. Kl. Ohridski Blvd., 1756 Sofia, Bulgaria

Received: November 30, 2025; Accepted: March 01, 2026

The partition of softwood pulp production worldwide is constantly decreasing. New plants are not being built, but are only being modernized, increasing their capacity. The timber harvesting of softwood in Bulgaria is significant, and after the closure of the Stamboliyski plant of Mondi, large quantities of wood remained available. This has led to interest in starting the production of softwood bleached pulp in Bulgaria, which is a marketable product and an indispensable raw material.

Industrial wood chips of softwood were cooked in the laboratory and the effect of the parameters: active alkali charge and duration of the cooking time were investigated. Total pulp yield, screening pulp yield, knots, residual alkali in the black liquor and Kappa number of the obtained pulp were determined. The optimal parameters of the active alkali charge and the duration of the process of producing pulp with the required Kappa number for bleaching were established. Based on the results of the cooking, the bleachability of the pulp and the possibility of obtaining high-quality bleached softwood pulp were determined.

Keywords: softwood, cooking, kinetics, bleachability, bleached pulp

INTRODUCTION

Wood is the main raw material used in pulp and paper production and represents the most significant cost component in pulp production. Consequently, the quality and price of wood have become critical factors in modern pulp production operations. The suitability of wood for pulp production varies not only between species, it also depends on the cutting location, growing conditions and age of the tree. The kinetics of Kraft pulping have been extensively studied and documented since the late 1950s [1]. There are numerous studies in the scientific literature examining individual softwood and hardwood species [2–5]. However, comparing results from different periods is often challenging, as analytical techniques, tools and interpretation methodologies have evolved over time. Since differences in cooking behavior between some species – especially softwoods – can be minor, it is often advantageous to rely on results obtained in a single laboratory using well-defined procedures. This complicates broad comparative evaluations of multiple types based on different literature sources [1].

The two main methods for producing chemical pulp are alkaline processes, such as the Kraft process, and acidic processes, such as the sulfite process. Historically, both wood and non-wood fibrous materials have been processed primarily by chemical pulping techniques. World production statistics show that the majority of chemical pulp is produced today by the Kraft process. Although the latter process yields stronger fibers, this method is increasingly affected by environmental regulations regarding emissions of total reduced sulfur (TRS) compounds, sulfur dioxide, suspended solids, and wastewater pollutants. In contrast, sulfite pulp production is continuously declining due to environmental concerns and the lower mechanical properties of the resulting pulp [6].

The Kraft process continues to be the leading method for producing paper pulp. Although softwood has long been the primary raw material in Northern Europe, recent years have seen growing interest in the use of hardwoods [7].

Alkaline pulping is generally divided into three distinct phases, each characterized by unique kinetic behavior. In the initial phase, delignification proceeds rapidly, accompanied by significant carbohydrate degradation [8]. The subsequent bulk delignification phase, characterized by slow reaction rates, is responsible for the removal of most of the lignin and shows higher selectivity – meaning that lignin is removed more efficiently than carbohydrates. During the residual delignification phase, all reaction rates decrease significantly, including those associated with carbohydrate degradation, resulting in reduced selectivity [9]. Therefore, to maximize carbohydrate yield, it is preferable to terminate the cooking process before

---

* To whom all correspondence should be sent:
Email: *stpetrin@uctm.edu*

residual delignification begins. The chemical reactions underlying delignification are very complex and remain only partially understood [10].

The parameters applied during Kraft cooking have a decisive influence on the subsequent bleaching step, shaping the total consumption of bleaching reagents, the environmental footprint of the wastewater, the stability of the whiteness and the mechanical properties of the resulting pulp. While extended delignification during cooking usually reduces the demand for bleaching chemicals, supports increased closure of bleaching plants and increases the calorific value of the black liquor, achieving deep delignification without concomitant carbohydrate degradation remains a significant technical limitation. As a result, significant amounts of chemicals are usually required in the bleaching sequence to compensate for the residual lignin content [12].

It is well-established that different types of alkaline pulps exhibit different bleaching profiles, usually quantified as the amount of bleaching chemicals required to achieve the target whiteness. Numerous studies have attempted to correlate the structural characteristics of residual lignin with pulp bleachability. Many studies have shown that residual lignin enriched with specific structural motifs exhibits increased reactivity to chlorine dioxide [13].

The demand for bio-based packaging materials has increased in recent years due to the shift away from plastics. In 2023, global paperboard production is estimated to be approximately 55 million metric tons per year, with the United States accounting for 29% of this total, or nearly 14 million tons. Global production is projected to increase to 66 million metric tons by 2032. The Kraft process continues to be the predominant method of producing the fibers used in paperboard production [14].

The aim of the present study is to investigate the possibility of obtaining softwood pulp for bleaching under low sulfidity cooking and to establish the kinetic dependences of the process and the optimal active alkali charges.

MATERIALS AND METHODS

The experiments were carried out using industrial softwood chip. Wood chips were hand-sorted to remove knots and bark, and 100 g of absolutely dry chips were cooked in 2 L stainless steel laboratory autoclaves rotating at constant rate in a polyglycol heating bath. The liquor-to-wood ratio during cooking was 3.5:1, the sulfidity was 7.4% and the active alkali charge varied from 22% to 24% as NaOH. Cooking started at 80°C followed by heating to a maximum temperature of 172°C with a reaction time of 50 to 130 min at this temperature. Kappa number and residual active alkali were measured according to SCAN standards (SCAN-C 1:77 and SCAN-N 33:94).

RESULTS AND DISCUSSION

The results of the investigation of the influence of the duration of Kraft cooking and the active alkali (AA) charge on the Kappa number of softwood pulp are presented in Fig. 1. It is established that extending the duration of the cooking has a positive effect on the delignification process, but at AA charge of 22%, pulp with a Kappa number between 50 and 90 units is obtained. This means that only unbleached pulp for kraft paper or kraftliner can be produced under these conditions. At an AA charge of 23%, a Kappa number between 30 and 35 units is achieved, while the reaction time is from 110 to 130 min. These Kappa number values are considered optimal for standard softwood pulping for bleaching. 24% of AA leads to a much faster and extended delignification, as the optimal Kappa number can be achieved in just 70 min of reaction time (Fig. 1). It was found that a reaction time of 110 – 130 min leads to a Kappa number between 24 and 28 units. These Kappa numbers are typical for modified Kraft pulping methods of softwood, which are characterized by an impregnation stage with a solution with very high sulfide content, followed by main pulping at an optimal alkali concentration until the end of the process at relatively lower temperature.

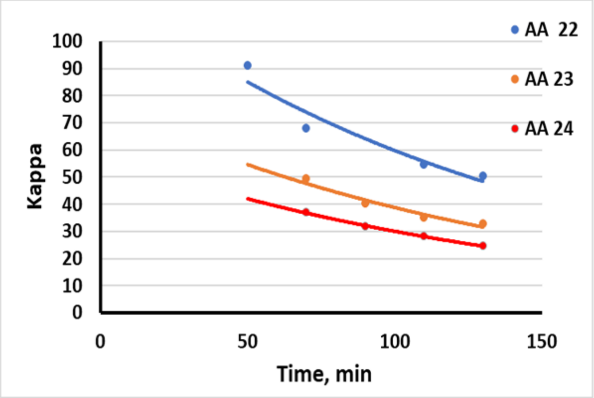

Fig. 1. Effect of the reaction time and active alkali charge on Kappa number

At a higher active alkali charge we have an increased content of residual alkali (Fig. 2), but the screening pulp yield remains practically the same. This is explained by the significant reduction of the duration of the pulping to the same Kappa number (Fig. 3).

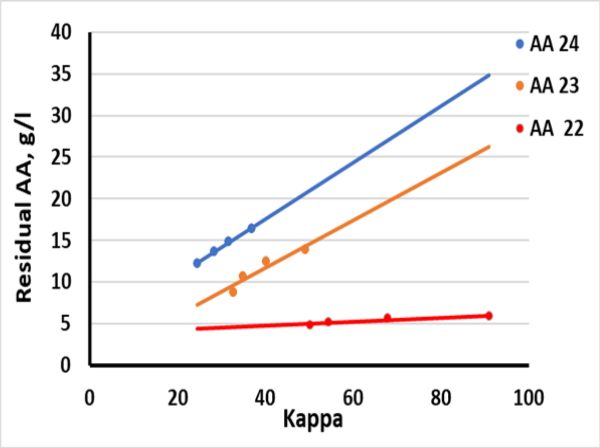

Fig. 2. Correlation between residual alkali and Kappa number

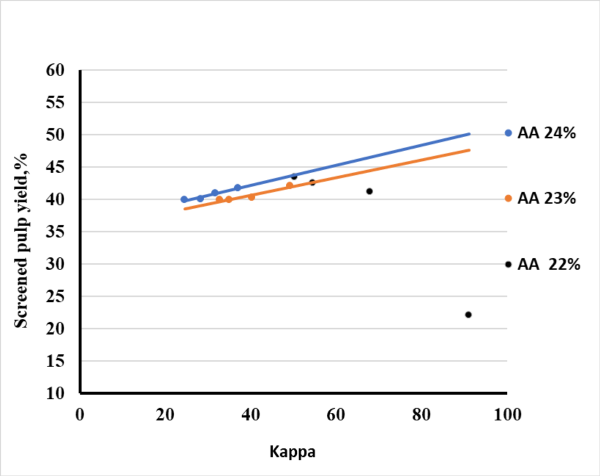

Fig. 3. Correlation between pulp screening yield and Kappa number

As a result, cellulose degradation is reduced, and the pulp yield remains relatively high (Table 1). The well-known advantage of fast pulping regime in terms of process selectivity and pulp yield is confirmed by these results.

It should be noted that owing to the very low sulfidity of the cooking liquor, which is close to natron pulping, all yield values are below the optimum (Table 1).

The general relationships between the pulp parameters after the cooking process with an AA charge of 24%, presented in Fig. 4, show that under these conditions, softwood pulp with a low Kappa number can be obtained. This will improve the efficiency of the bleaching process and reduce the need of expensive chemicals but will also slightly reduce the pulp yield.

Table 1. Effect of alkali charge on pulp yield

Active alkali charge as NaOH - 22% and sulfidity as Na_2S – 7.4%					
Time, min	50	70	90	110	120
Screened pulp yield, %	22.1	41.2	-	42.5	43.4
Screening reject, %	-	3.8	-	2.3	1.2
Total yield, %	-	45.0	-	44,8	44.6
Active alkali charge as NaOH - 23% and sulfidity as Na_2S – 7.4%					
Time, min	50	70	90	110	120
Screened pulp yield, %	-	42.1	40.2	39.9	39.7
Screening reject, %	-	0.4	1.3	0.3	0.3
Total yield, %	-	42.5	41.5	40.2	39.9
Active alkali charge as NaOH - 24% and sulfidity as Na_2S – 7.4%					
Time, min	50	70	90	110	120
Screened pulp yield, %	-	41.7	40.9	40.0	39.9
Screening reject, %	-	0.3	0.2	0.1	0.0
Total yield, %	-	42.0	41.1	40.1	39.9

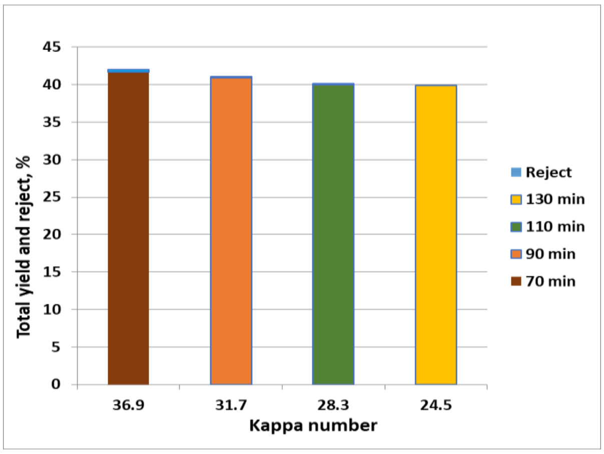

Fig. 4. Relationships between pulp parameters after 24% AA cooking

CONCLUSIONS

The results of this investigation show that at conditions of "Svilocell" EAD – Svishtov low sulfidity cooking of softwood, the active alkali charge of 23 % is optimal for obtaining a pulp for bleaching. It is established that at active alkaline charge of 24%, pulp with a lower Kappa number is obtained, which will increase the efficiency of the bleaching process. At the same time, the pulp screening yield remains practically unchanged, due to both significant reduction in cooking reaction time and improvement in its selectivity. By softwood cooking with an active charge of less than 23%, unbleached pulp with a Kappa number of more than 50 units is obtained, which can be used in the production of kraft paper or kraftliner.

REFERENCES

1. M. Margarido, O. Anjos, P. Dénilson da Silva, M. Gérard, Evaluation of kraft cooking behavior for six different softwoods species, in: ABTCP-TAPPI-Congresso e Exposição Internacional de Celulose e Papel, **43**, São Paulo, (2010).
2. L. Yang, S. Liu, *I&EC Research*, **44**(18), 7078 (2005).
3. N. V. Polowski, E. C. Vasco de Toledo, R. M. Filho, *IFAC Proceedings*, **39** (2), 291 (2006).
4. O. Fearon, S. Kuitunen, K. Ruuttunen, V. Alopaeus, T. Vuorinen, *I&EC Research,* **59** (29), 12977 (2020), DOI: 10.1021/acs.iecr.0c02110.
5. O. Fearon, V. Nykänen, S. Kuitunen, K. Ruuttunen, R. Alen, V. Alopaeus, *AIChE Journal,* **66,** e16252 (2020), https://doi.org/10.1002/aic.16252
6. W. Sridach, *J. Sci. Technol.*, **17**, 105 (2010).
7. N. Andersson, D. Wilson, U. Germgard, *NPPRJ,* **18**, 200 (2003).
8. K. Nieminen, H. Sixta, *Holzforschung*, **66** (7), 791 (2012), https://doi.org/10.1515/hf-2011-0122
9. A. Teder, *Pulp and Paper Chemistry and Technology*, **2**, 149 (2007), ISBN 978-3-11-021341-6
10. H. Sixta, A. Potthast, A. Krotschek, *Handbook of Paper and Board*, 109, (2008) ISBN 3-527-30997-7
11. J. Franco, F. Urdaneta, Y. Cordoba, L. Meza, I. Urdaneta, H. Jameel, W. Gonzalez, *Ind. Crops and Products,* **232**, 121252 (2025), ISSN 0926-6690, https://doi.org/10.1016/j.indcrop.2025.121252.
12. G. Gellerstedt, V. Al-Dajani, *Holzforschung,* **54** (6), 609 (2000),
13. X. S. Choai, J. Zhu, J. Li, *J. Pulp Paper Sci.,* **27** (5), 165 (2001).
14. J. Franco, F. Urdaneta, Y. Cordoba, L. Meza, I. Urdaneta, H. Jameel, W. Gonzalez, *Ind. Crops and Products*, **232**, 121252 (2025), https://doi.org/10.1016/j.indcrop.2025.121252

Bulgarian Chemical Communications, Volume 58, Issue 2 (pp. 189-192) 2026 DOI: 10.34049/bcc.58.2.NCC02

Temperature-time and concentration dependences of mild dilute acid hydrolysis

I. Gavrilov*, S. Petrin, P. Mileva-Petrova, G. Radeva, I. Valchev

University of Chemical Technology and Metallurgy, 8 St. Kl. Ohridski Blvd., 1756 Sofia, Bulgaria

Received: December 04, 2025; Revised: March 05, 2026

Microcrystalline cellulose (MCC) is a powder-like multifunctional product with wide-spread and diverse applications. It is also a suitable raw material in the manufacture of microfibrillated cellulose. The commonly used MCC products have an average particle size of 40 - 60 µm. Products with a size of more than 100 µm are much more expensive, due to the difficulty in achieving the required degree of polymerization.

The results of this study show that for MCC production with a degree of polymerization less than 350 units, the hydrolysis temperature of the bleached hardwood pulp with dilute sulfuric acid should be 130°C and higher. At a hydrolysis temperature of 120°C and sulfuric acid content up to 2%, only modified cellulose is obtained. Under these conditions, the yield remains high with a minimum amount of dissolved xylose.

Keywords: mild acid hydrolysis, kinetics, degree of polymerization, microcrystalline cellulose

INTRODUCTION

Microcrystalline cellulose (MCC) is a multifunctional product with wide-spread and diverse applications (food, pharmaceutical and cosmetic industries). It is partially depolymerized cellulose which according to the European Pharmacopoeia has a degree of polymerization less than 350 [1, 2].

Microcrystalline cellulose is mainly produced from wood pulp and purified cotton linters. In industrial applications, only bleached dissolving pulp, obtained from raw materials such as softwood, hardwood, cotton, or straw, is utilized**.** The main advantage of dissolved pulp is its high purity while the disadvantage is its high price.

Toshkov *et al*. developed a method using 1% sulfuric acid solution as hydrolyzing medium and obtained a high yield, lowering the aggregation by optimization of the pulping process [3]. The classic process for MCC production, pioneered by Battista [4] is acid hydrolysis in a 2.5 normal solution of hydrochloric acid, followed by mechanical treatment. According to the Aalto Cell™ process, microcrystalline cellulose can be effectively produced from paper-grade pulp by sulfuric acid hydrolysis at a consistency of at least 8% and temperature of at least 80 °C, and the manufacturing process can be integrated into a kraft pulp mill [5].

A method for producing bleached microcrystalline cellulose from unbleached cellulose has also been developed, with the main advantage of efficient bleaching with significant saving of chemicals [6]. Our research group has been working for several years in the field of obtaining MCC from bleached paper-grade pulp. Technology has been developed for obtaining MCC by hydrolysis with dilute sulfuric acid in two stages, which allows the production of microcrystalline cellulose with high brightness, good particle uniformity and a desirable degree of polymerization, from hardwood bleached kraft pulp [7]. Cleaning effects and increasing pulp brightness have been established in the initial step of acid hydrolysis due to the dissolution of the residual chromophores absorbed on xylan, and in the second hydrolysis stage - due to the removal of the absorbed humins.

The commonly used MCC products have an average particle size of 40-60 µm. The highest particle size of available MCC products is 250 µm. Products with a size of more than 100 µm are much more expensive, due to the difficulty in achieving the required degree of polymerization.

MCC is a suitable raw material in the manufacture of microfibrillated cellulose (MFC) as well [8, 9]. Considerable strength improvements have been gained by adding MFC to paper, composite structures, or other structures [10, 11]

Dilute acid hydrolysis of lignocellulosic materials and cellulose depends on temperature, time, and concentration, which is essential in optimizing microcrystalline cellulose production. At low acid concentrations and moderate temperature conditions, hydrolysis proceeds through a complex mechanism determined by the structural characteristics of the feedstock, including crystallinity, accessibility, and distribution of amorphous regions. Previous studies on dilute acid hydrolysis of hardwood and bleached pulp have

---

* To whom all correspondence should be sent:
Email: *igavrilov@uctm.edu*

shown that the process follows well-defined kinetic steps, reflecting the transition from rapidly hydrolyzed amorphous domains to more stable crystalline structures. In our previous studies, including those focused on the topochemical mechanisms of enzymatic and acid hydrolysis, we have highlighted the importance of the spatial distribution of reactive sites on the fiber surface and the influence of structural heterogeneity on the reaction kinetics. Our studies on dilute acid hydrolysis of bleached pulp for the production of microcrystalline cellulose and microfibrillated cellulose (MFC) confirm that temperature regimes, processing time and acid concentration strongly influence the reaction rate and the quality of the final product [12-14].

The aim of the present study is to investigate the temperature-time and concentration dependences of mild dilute acid hydrolysis of bleached pulp to microcrystalline cellulose and to modified pulp for microfibrillated cellulose.

EXPERIMENTAL

The experimental studies were carried out with bleached hardwood kraft pulp delivered by "Svilocel" AD, Bulgaria, which has been previously disintegrated and dehydrated.

The sulfuric acid hydrolysis was carried out in 1L stainless laboratory autoclaves at the following conditions: mass concentration of pulp 12.5%, charge with different acid percentages (1% and 1.5%), different temperatures (120°C and 130°C) and reaction times from 40 to 120 min. The process was stopped by cooling the autoclaves.

The obtained cellulose was washed and filtered through a filter with a pore size of 2 – 3 µm. The filtrate was analyzed by a Dionex HPLC system according to NREL Technical Report (NREL/TP-510-42623).

The degree of polymerization of cellulose was determined according to the SCAN-CM 15:88 standard, Mark-Hownik equation, and to the Japanese Pharmacopoeia standard used by JRS Pharma.

RESULTS AND DISCUSSION

The degree of polymerization (DP) is a main characteristic of microcrystalline cellulose (MCC). It is well known that DP decreases during the acid hydrolysis, which is basically associated with cellulose chain breakage. On the other hand, the extraction of the low-molecular xylan leads to a slight DP increase.

The kinetic studies of acid hydrolysis at temperatures of 120°C and 130°C and sulfuric acid charges of 1% and 1.5% show that in the time interval of 40 - 120 min, the degree of cellulose polymerization is in the range 295 – 611, as for DP lower than 350, temperature of 130° is required (Fig. 1).

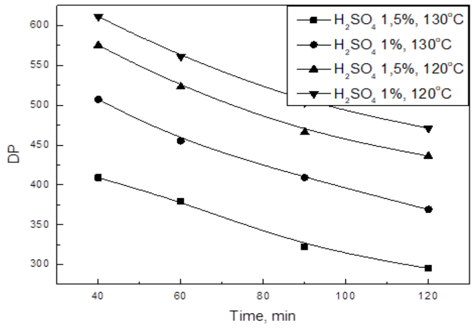

Figure 1. DP of MCC at different sulfuric acid charges *versus* temperature and time.

The degree of hydrolysis depends not only on temperature and time, but also on acid concentration. Under the experimental conditions, the yield of modified cellulose remains high [12]. The obtained results are presented in Table 1.

Table 1. Yields of modified cellulose at different temperatures and acid charges

Time, min	Yields of modified cellulose, %			
	T=120°C	T=120°C	T=130°C	T=130°C
	H_2SO_4 1%	H_2SO_4 1.5%	H_2SO_4 1%	H_2SO_4 1.5%
40	>99.0	>98.5	>98.5	>98.0
60	>98.5	>98.0	97.3	97.0
90	>98.0	97.3	96.7	96.5
120	>97.5	97.0	96.5	96.0

Dilute acid hydrolysis generates xylose during the process (Fig. 2). This could be related to the high pentosans content of the bleached pulp.

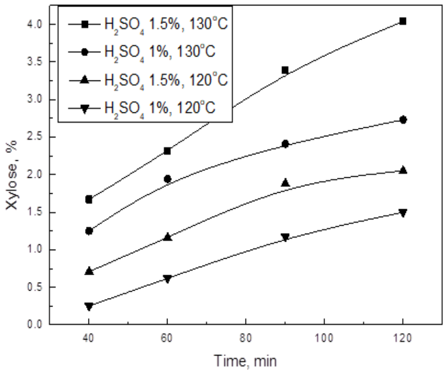

Figure 2. Xylose extraction at different temperatures and reaction times

As seen from Fig. 3, the yield of glucose increases much slower compared to that of xylose, indicating that this parameter is not determining for the hydrolysis process.

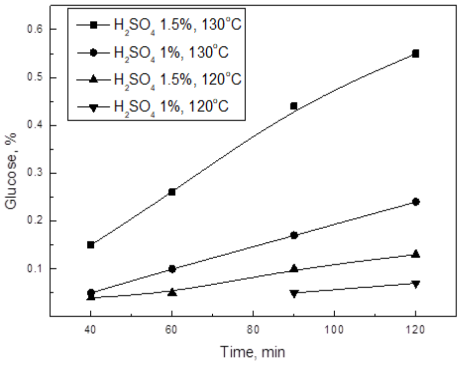

Figure 3. Glucose yield at different sulfuric acid charges, temperatures and time.

The kinetics of the process is investigated by the dimensionless quantity α which is determined as the relative change of DP and is calculated in correspondence with Equation (1):

$$\alpha = \frac{(1100-DP)}{1100} \qquad (1)$$

where 1100 is the initial value of pulp DP.

Kinetic curves of the process of depolymerization are presented in Fig. 4.

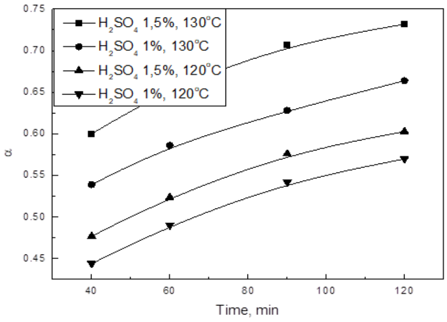

Figure 4. Kinetic curves of the hydrolysis process at different sulfuric acid charges and temperatures.

The applicability of different kinetic equations referring to different heterogeneous processes is verified (see Table 2). The kinetic investigation of the process of cellulose depolymerization shows that the modified Prout-Tompkins equation describes most precisely the heterogeneous process of dissolution of cellulose amorphous domains.

The modified Prout – Tompkins equation is used to describe the kinetics of solid decomposition of the fibrous structure of the pulp [13, 14]. The equation is presented in the following form:

$$\frac{\alpha}{(1-\alpha)} = (k.t)^{\chi} \qquad (2)$$

where k is apparent rate constant, χ is power factor which takes values ($0<\chi<1$) characteristic for the system.

All kinetic curves are linearized in coordinates $ln\frac{\alpha}{(1-\alpha)}$ *vs.* lnt according to the logarithmic form of Equation (2).

$$ln\frac{\alpha}{1-\alpha} = \chi \ln k + \chi lnt \qquad (3)$$

The dependences obtained are presented in Figure 5.

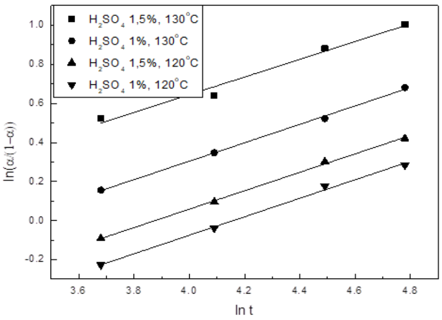

Figure 5. Linearization of Prout – Tompkins equation.

The value of the power coefficient χ is approximately equal to 0.47. The values of the apparent rate constant k are calculated and presented in Table 3.

Table 2. Comparison between correlation coefficient values obtained in the description of the process by different kinetic equations

Equation	R^2			
	120°C		130°C	
	H_2SO_4-1%	H_2SO_4-1.5%	H_2SO_4-1%	H_2SO_4-1.5%
Power kinetic equation $\ln(1-\alpha) = -kt$	0.99344	0.98758	0.99443	0.98224
Exponential kinetic equation $\alpha = k + a^{-1}.lnt$	0.99665	0.99254	0.99882	0.9903
Modified Prout – Tompkins equation $\frac{\alpha}{(1-\alpha)} = (k.t)^{\chi}$	0.99471	0.99809	0.99767	0.99136

Table 3. Values of the apparent rate constant *k*

Experimental conditions	Rate constant $k \times 10^{-2}$, min^{-1}
H_2SO_4 1.5%, 130ºC	8.3
H_2SO_4 1%, 130ºC	3.4
H_2SO_4 1.5%, 120ºC	2.0
H_2SO_4 1%, 120ºC	1.5

As can be seen from Table 3, the highest value of the rate constant is obtained at acid concentration of 1.5% and temperature of 130˚C, which affects the yield of MCC.

CONCLUSIONS

The degree of hydrolysis depolymerization of bleached hardwood pulp depends not only on temperature and time, but also on sulfuric acid concentration.

Under the studied conditions, the amounts of dissolved substances remain minimal while the yield of modified cellulose remains high.

The kinetic investigation of dilute sulfuric acid hydrolysis of bleached hardwood kraft pulp aiming microcrystalline cellulose production shows that the modified topochemical Prout – Tompkins equation describes the process of the pulp depolymerization. The temperature – time dependence obtained can be used for control and simulation of the process of depolymerization of pulp to microcrystalline cellulose.

Acknowledgement: *This research is supported by the Bulgarian Ministry of Education and Science under the National Program "Young Scientists and Postdoctoral Students-2".*

REFERENCES

1. European Pharmacopoeia (Ph. Eur.), **8.0**, 1824 (2013).
2. M. Krstic, Z. Maksimovic, S. Ibric, T. Bakic, J. Prodanovic, S. Razic, *Cellulose Chem. Tehnol*., **52**, 577 (2018), http://www.cellulosechemtechnol.ro/pdf/CCT7-8(2018)/Contents.pdf
3. T. S. Toshkov, N. R. Gospodinov, E. P. Vidimski, U.S. Patent 3,954,727 (1976), https://patents.google.com/patent/US3954727
4. A. O. Battista, P. A. Smith, U.S. Patent 2,978, 446 (1961), https://patents.google.com/patent/US2978446A
5. O. Dahl, K. Vanhatalo, K. Parviainen, U.S. Patent 9,469,695 B2 (2016), https://patents.google.com/patent/US9469695B2/
6. I. Valchev, K. Dachev, N. Yavorov, Patent № 67533/15.06.2023 B1, https://portal.bpo.bg/web/guest/bpo_online/-/bpo/patent-search
7. I. V. Valchev, K. B. D, E. P. Vidimsky, S. A. Petrin, N. A. Yavorov, EP 3710487B1, Applicant Svilosa AD, 23.10.2024, Bulletin 2024/43. https://patents.google.com/patent/EP3710487B1/en
8. K. Vanhatalo, T. Lundin, A. Koskimäki, M. Lillandt, O. Dahl, *J. Mater. Sci.,* **51**(12), 6019 (2016).
9. A. Lähdeniemi, A. Knuts, O. Dahl, *BioResources,* **19**(4), 9375 (2024).
10. Ø. Eriksen, K. Syverud, Ø. Gregersen, *NPPRJ,* **23**, 299 (2008).
11. T. Taipale, M. Österberg, A. Nykänen, J. Ruokolainen, J. Laine, *Cellulose,* **17**, 1005 (2010).
12. I. Gavrilov, P. Mileva-Petrova, S. Petrin, I. Valchev, G. Radeva, *XXVI International Symposium in the Field of Pulp, Paper, Packaging and Graphics* (2025), DOI: 10.46793/CPAG25.011G
13. I. Valchev, N. Yavorov, S. Petrin, *Holzforschung,* **70,** 1147 (2016).
14. N. Yavorov, I. Valchev, G. Radeva, D. Todorova, *Carbohydr. Res.,* **488,** 107910 (2020).

Bulgarian Chemical Communications, Volume 58 Issue 2 (pp. 193-199) 2026 DOI: 10.34049/bcc.58.2.NCC03

Quantum chemical insights into porous s-triazine and tri-s-triazine carbon nitrides

J. N. Petkova[1,2], I. Mijakov[1], E. P. Simeonova[1], G. K. Madjarova[1,2]

[1]*Laboratory of Quantum and Computational Chemistry, Faculty of Chemistry and Pharmacy, Sofia University "St. Kliment Ohridski", Sofia, Bulgaria*

[2]*National Centre of Excellence Mechatronics and Clean Technologies, Sofia University "St. Kliment Ohridski", Sofia, Bulgaria*

Received: November 05, 2025; Revised: January 06, 2026

Density functional theory calculations are performed to investigate a series of carbon nitride models based on s-triazine and tri-s-triazine units. Single-pore structures, varying in nanopore shape and size, are extended to form highly porous nanosheets. The structures, electron density distributions, HOMO-LUMO energy gaps are analyzed and compared. Slightly pronounced edge effects indicate possible competition between nanopores during the interactions with gas molecules. This study is an initial step in the quantum chemical investigation of carbon nitride structures for gas mixture separation applications.

Keywords: carbon nitrides, density functional theory, gas separation membranes

INTRODUCTION

Graphene-type carbon nitrides are a class of organic microporous materials that have attracted increasing interest within the scientific community due to their narrow bandwidth, thermal stability, easy synthesis and easy functioning [1-23]. These materials have a wide range of potential applications, including photocatalysis [4], photovoltaic cells [5], sensors [6] and lithium-ion batteries [7]. The naturally stable nanopores make these materials promising candidates for atom-thick membranes for an inexpensive, energy-efficient gas mixture purification and separation. The geometry and electronic structure of the material are crucial factors for all these applications.

Carbon nitrides consist of layers of covalently bonded sp^2-hybridized carbon and nitrogen atoms, primarily based on heptazine and s-triazine units and feature well-defined nanopores [8]. Poly (triazine-imide) (PTI) is an example of s-triazine-based carbon nitride. PTI compounds have a layered 2D π-conjugated planar structure, with triazine fragments linked by imide groups and weak Van der Waals interactions between the individual layers. Another example of carbon nitride, based on s-triazine rings, is g-C_3N_3 material. Unlike PTI, the ring fragments in the g-C_3N_3 are directly linked through covalent bond between carbon atoms. A 2D π-conjugated plane is also formed, but the shape and the size of the pores are differing from those of the PTI.

Another class of graphite-like carbon nitrides are with stoichiometry C_3N_4. g-C_3N_4 exists in two types: one based on triazine unit (TGCN) and another based on heptazine fragments (HGCN). TGCN contains three triazine fragments linked by amine groups, resulting in much smaller nanopores in comparison to PTI and C_3N_3. The most studied theoretically and experimentally carbon nitride is HGCN with three heptazine units. Two forms of HGCN are identified – amorphous and crystalline [9]. The amorphous form shows weaker photocatalytic activity, but is characterized by a smaller band gap width. Kang and co-authors propose a method for synthesis of amorphous form with a band gap energy of 1.9 eV. Quantum chemical calculations indicated that the folded form of HGCN has lower energy than the planar structure due to the reduction of repulsion between the lone pairs of nitrogen atoms [10].

Different theoretical and experimental approaches are used to study the application of the PTI, C_3N_3, TGCN and HGCN carbon nitrides as gas separation membranes [11-17] and as photocatalysis [18, 19]. The adsorption properties, selectivity and permeability are evaluated. The electronic structure and band gap are discussed. However, to the best of our knowledge, there is no systematic investigation conducted under consistent conditions, models, and computational parameters on different types of carbon nitride. Such a study would allow a comparison of the carbon nitride characteristics and provide a basis for developing a model to obtain materials with the desired properties.

---

* To whom all correspondence should be sent:
Email: *fhjp@chem.uni-sofia.bg*

The current quantum chemical study aims to systematically evaluate and compare the structures and electronic properties of four distinct carbon nitrides - PTI, C_3N_3, TGCN and HGCN, with a particular emphasis on the nanopore characteristics. Geometry, electron density distribution, and the HOMO-LUMO gap - characteristics related to the sieving, adsorption, and permeability capacities of the nanopores - are discussed. The influence of the model size was also assessed and analyzed. These findings provide a foundation for investigating the potential of PTI, C_3N_3, TGCN and HGCN as atom-thick membranes for gas mixtures separation.

Computational details

Four types of carbon nitrides were investigated in the study (Figure 1). Three of them – PTI, C_3N_3 and TGCN - are based on s-triazine units. In PTI and TGCN, the s-triazine units are linked *via* nitrogen groups, whereas in C_3N_3, the s-triazine fragments are directly bound through carbon–carbon bonds between the rings. The results for the triazine-based carbon nitrides were compared with those for HGCN, where tri-s-triazine units are linked by amine groups. The four carbon nitrides contain nanopores of varying shapes and sizes: C_3N_3 has spherical pores, PTI and TGCN feature triangular pores, and HGCN has hexagonal pores. Nanopore size was determined by measuring the maximum distance between atoms in the pore's interior (Figure 1). The smallest is the nanopore of TGCN (~2.6 Å), followed by PTI (~ 4.05 Å), HGCN (~ 4.90 – 5.00 Å), and the largest one is in C_3N_3 (~ 5.47 Å).

All calculations were performed with the B3LYP hybrid functional with added three-parameter empirical correction (GD3) [20]. The 6-31G** basis set was used. The electron density distribution was estimated by Natural Population Analysis (NPA), which is a component of the Natural Bond Orbital (NBO) analysis method [21]. The calculations were carried out with Gaussian software [22].

RESULTS AND DISCUSSION

Structure of PTI, C_3N_3, TGCN and HGCN

In PTI, the nanopores are formed from six s-triazine fragments that are linked by nitrogen groups. The interior of the nanopores is defined by the presence of alternating sp^2- carbon and sp^2-, sp^3-nitrogen atoms (Figure 1). The nitrogen groups play a key role in determining the triangular shape of the nanopore, with hydrogen atoms oriented towards the interior. The distance between these hydrogen atoms is approximately 4.05 Å (Figure 1). The lengths of the C-N bonds in the s-triazine rings are in the range of 1.329 to 1.353 Å. The longest bonds are those with the nitrogen linker (1.379÷1.380 Å). Both the model featuring a single nanopore and the 2D nanosheet with ten pores (*10*-PTI) have a fully planar structure, with pores of identical size (Figure 2). The enlargement of the model does not result in any significant structural changes.

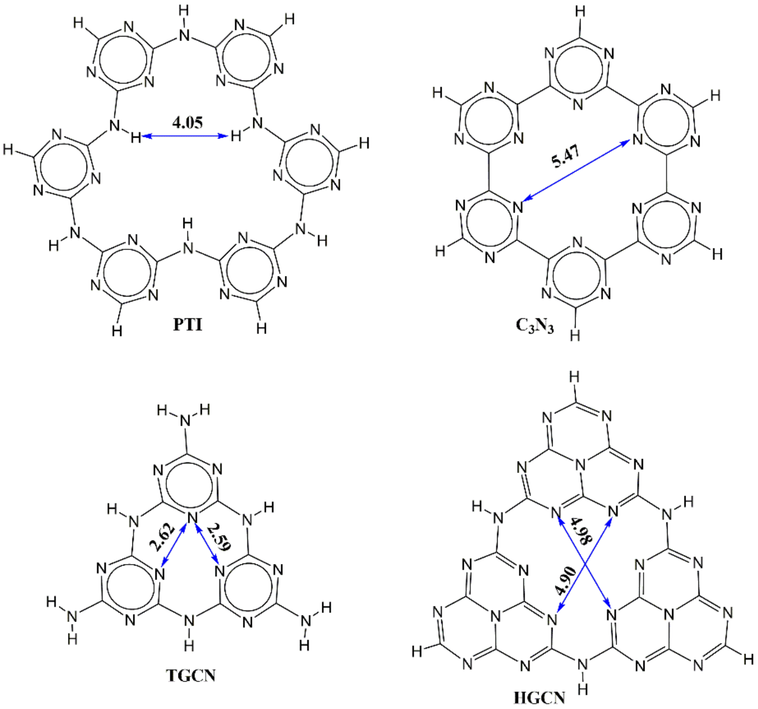

Figure 1. Chemical structures of PTI, C_3N_3, TGCN and HGCN containing a single nanopore. The sizes of the nanopores are indicated.

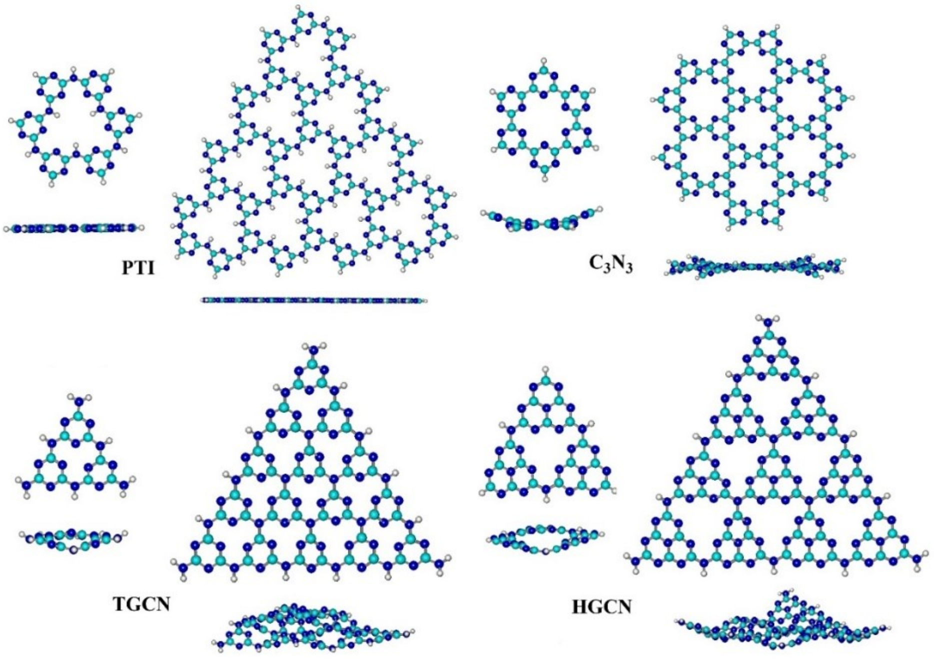

Figure 2. Front and side views of the smallest and largest structures of the modelled carbon nitrides (C green, N – blue, H - grey). Structure optimization is performed with B3LYP-D3/6-31G**.

In contrast to PTI, C_3N_3 is constructed from s-triazine rings directly linked by C-C bonds (Figure 1). As a result, the molecule is not quite planar. A distortion occurs due to the slight rotations (about 20°) around four of the C–C bonds in the pore. This causes two of the opposing triazine rings to tilt upwards, while the other four tilt downwards (Figure. 2). The pore size, defined by circumscribed circle formed by the imine nitrogen atoms in the interior of the nanopore, is with diameter (the longest distance measured between each pair of opposite nitrogen) of 5.47 Å (Figure 1). The carbon-nitrogen bond lengths vary between 1.335 and 1.339 Å, the length of the carbon-carbon bond is about 1.504-1.506 Å. The 2D nanosheet of C_3N_3 with seven pores (*7*-C_3N_3) is characterized by folding at the outer pores and flattening of the inner pores. The deformation in the periphery of the nanosheet is about 13÷23° (similar to the distortion in the single C_3N_3 pore) while the inner pore remains relatively planar, with an out-of-plane deviation of about 2.5÷3°.

The optimized structure of the single-pore model of TGCN is presented in Figure 2. The interior of the nanopore is defined by three imine nitrogen atoms, one from each ring. To minimize repulsion between the lone electron pairs of these nitrogen atoms, the three-ring framework becomes distorted, resulting in a nonplanar stable structure for TGCN (Figure 2). Two of the three nitrogen atoms lie in the same plane, separated by 2.59 Å, while the third nitrogen atom is displaced from this plane by 39° at a distance of 2.62 Å. The pore adopts a nonplanar, open-ring geometry (Figure 2). In the 2D TGCN nanosheet containing ten nanopores (*10*-TGCN), this bent structure is preserved (Figure 2). The central nanopore is characterized with additional distortion compared to the single-pore model and shows slightly greater deformation than the other pores in the nanosheet. The dihedral angle between the two nitrogen atoms, that remain coplanar in the smallest model, is ~18° (5 - 13° in different cavities). The other dihedral angles describing the mutual nonplanarity of the nitrogen atoms are 40° and -57° (30° - 55° across the different pores). The three nitrogens from the pore lie in distinct symmetry planes, with interatomic distance of approximately ~2.5 - 2.8 Å, slightly longer than those in the single-pore TGCN model.

The single-pore HGCN structure is composed of three tri-s-triazine fragments linked by amino groups (Figure 1). HGCN has a bent geometry similar to this of TGCN. One of the heptazine fragments deviates with 43° from the plane formed by the other, indicating a slightly larger distortion compared to TGCN. HGCN forms an open nanopore similar in shape to that of TGCN, but with a larger size. The maximum distance between nitrogen atoms from opposite rings is ~4.98 Å. The bent geometry becomes more pronounced in the larger HGCN model with six pores (*6*-HGCN), with dihedral angles reaching 50°- 60°. The 2D HGCN nanosheet forms a highly curved layer, analogous to the amorphous form of graphite-like C_3N_4 [23].

Electron density distribution and HOMO-LUMO gap

The electron density distribution in the carbon nitride models is analyzed using the NBO scheme (Figure S1). Particular attention is given to the atomic charges within the nanopore, as these atoms play a major role in gas capture processes. The effect of model size on the charge distribution is also evaluated. All carbon nitride nanopores are composed of alternating negatively charged nitrogen atoms and positively charged carbon atoms. Although the total charge of the nanopores in different carbon nitride models is positive, the interior of each nanopore is negatively charged due to the presence of nitrogen atoms and groups (Figure 3).

Among the studied carbon nitride models, C_3N_3 is the only one with no linker groups between the triazine rings. As a result, C_3N_3 is the carbon nitride with the weakest nucleophilic and electrophilic character of the nitrogens and carbons, respectively. The charges of these atoms from the nanopore are -0.423 and ~0.413 (Figure 3). Therefore, it is expected that the C_3N_3 nanopore will exhibit less selective adsorption among the studied carbon nitrides. The total charge of the nanopore, calculated as the sum of all atomic charges within the pore, is 2.408. The addition of nitrogen groups as a linker group between s-triazine units in PTI leads to an increase in both nucleophilic and electrophilic character of the atoms within the rings. Nitrogen and carbon atoms forming the nanopore are with charges of -0.549 and ~0.625, respectively. The amino groups introduce additional negatively charged centres, with an average group charge of about -0.143. The excess of electron density at these groups is significantly lower than of the other nitrogen atoms. The total nanopore charge in PTI is 3.361, making PTI the model with the highest positive total nanopore charge among the studied systems.

The carbon nitride model with the smallest size of the nanopore, TGCN, possesses the lowest total charge of the nanopore of ~1.665. The carbon atoms in TGCN have a slightly stronger electrophilic character in comparison to those of PTI, while the amino groups are stronger nucleophilic centres with a group charge of about -0.177. The charges of the imine nitrogen atoms forming the nanopore are comparable to those in PTI. This outlines PTI and TGCN as nanopores with centers that provide the strongest adsorption of molecules such as CO_2 and CO, and are expected to have the highest selectivity towards these gases among all the studied structures. In comparison, the HGCN shows a lower excess of electron density on both types of nitrogen centers within the nanopore compared to PTI and TGCN. The total charge of the pore is 2.314.

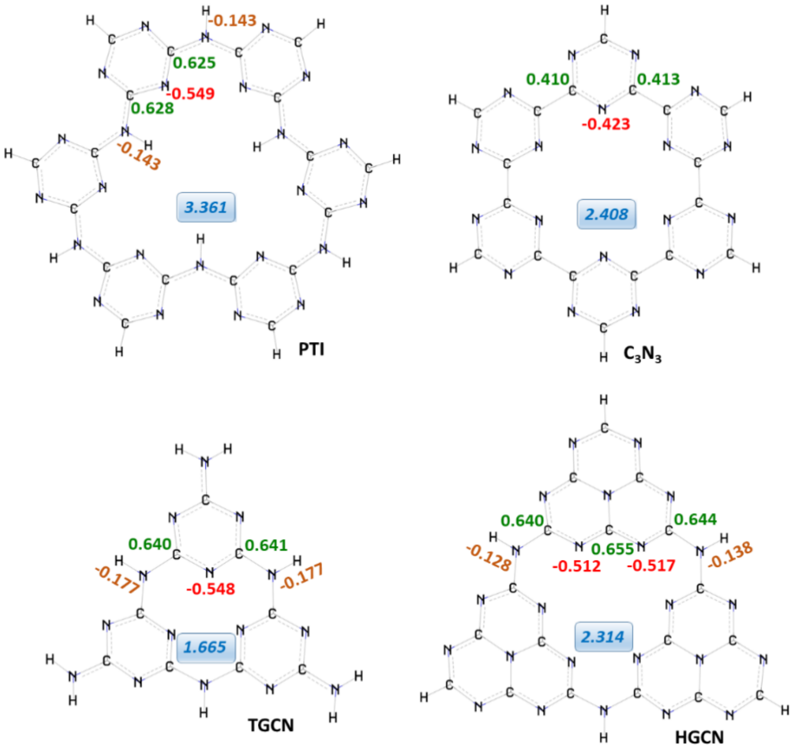

Figure 3. Representative atomic charges of the atoms forming the nanopores in PTI and C_3N_3 (first row); and in TGCN and HGCN nanopore (second row). The charges of carbon atoms are shown in green; of nitrogen atoms in red; total charges of the N-H groups in orange. The total charge of the nanopore is indicated in the blue box.

The trends observed in the charge distribution of the PTI are preserved in the larger model containing ten nanopores (Figure S2). A slight strengthening of the nucleophilic character of the imine nitrogen atoms (atomic charge is -0.565) and the electrophilic character of carbon atoms (atomic charge is 0.637) is observed from the rings participating in more than one cavity. The edge effects are weakly pronounced, manifesting as a minor increase in the absolute charge values of atoms located at the periphery. The central region of the nanosheet displays a slightly higher electron density, suggesting that this part of the layer may be more reactive. Increasing the model size does not affect the total charge of the linking –NH groups. The total charge of the peripheral pores is about 3.380, while the central nanopore is slightly more positive with value of 3.396.

The largest C_3N_3 model (Figure S3) is characterized with a highly homogeneous distribution of the atomic charges within the internal pore. The nitrogen atoms carry of -0.414, while the carbon atoms are charged at 0.414. The excess electron density on the nitrogen atoms is reduced, while the charge of the carbon atoms remains unchanged compared to the smaller C_3N_3 model. The nitrogen atoms at the periphery are the most negatively charged, ranging from -0.454 to -0.457. The total charge of the peripheral nanopores is about 2.462 while the charge of the central nanopore is 2.484.

Similar to the C_3N_3 models, the nucleophilic strength of the imine nitrogens and the electrophilic character of the carbons in the central nanopore decrease from TGCN single-pore model to the nanosheet (Figure S4). There is also a slight disproportionation in the charges of the three imine nitrogens in the central pore: two have charges of -0.518 and -0.512, while the third one has a charge of -0.507. The positive charge on some of the carbons increases to about 0.666. The nitrogens linking three rings reveal a notable excess of electron density, with charges ranging from -0.455 to -0.461, comparable to other nitrogen types in the structure. As a result, the total charge of the central cavity is 1.013, while the charges of the peripheral ones/cavities are around 1.480.

The enlargement of the HGCN (Figure S5) model results in the conversion of the linking -NH groups into nitrogen centres that connect three ring fragments. This structural change leads to an increase in the electron density at these centres, transforming them into much stronger nucleophiles. The larger number of the neighboring nanopores corresponds to a total charge of 1.752 ÷ 1.770, which is significantly smaller than the total charge of 2.314 in the single HGCN nanopore model.

Among the single-pore models, C_3N_3 presents the weakest charge separation between atoms in the nanopore interior, with the smallest absolute charge values. Therefore, it is considered as a slightly less reactive structure in the gas capture process. The addition of -NH linker groups enhance the nucleophilic and electrophilic characters of the atoms in the nanopore of PTI, TGCN, and HGCN. While these three models exhibit relatively similar values of the atomic electron density, TGCN displays the largest absolute charges, suggesting that it is the most reactive structure of the four carbon nitride models. The total nanopore charge decreases in the following order: PTI, C_3N_3, HGCN, TGCN. The charge distribution trends observed in the single-pore models are largely preserved as the model size increases. The most pronounced changes occur in TGCN and HGCN, where nanosheet formation reduces the total nanopore charge due to electron density localization at the linking nitrogen centers. The weak edge effects in all systems suggest potential competition between neighboring nanopores during gas adsorption and separation. Negatively charged nitrogen atoms, especially in the PTI and TGCN nanopores, strongly attract polar and quadrupolar gases such as CO and CO_2, resulting in enhanced adsorption and selectivity in comparison to H_2 and CH_4. H_2 can easily permeate due to its small size and weak interactions with the nanopores.

The dipole moments of the studied carbon nitride models are also considered. PTI and C_3N_3, both in their smaller and larger structures, have no permanent dipole moment. Among the single-pore models, TGCN possesses the largest dipole moment of 1.49 D, followed by HGCN with 0.50 D. The dipole moment values increase significantly as the models enlarge: *10*-TGCN with ten nanopores, doubles its value to 3.03 D, while 6-HGCN with six nanopores increases approximately five times, reaching 5.46 D.

The magnitude of the intrinsic dipole moment in these structures could influence adsorption and selectivity, as well as the transport properties through the nanopores. This could affect their applications as gas separation membranes and photocatalysts.

The energy differences (ΔE, eV) between the lowest unoccupied molecular orbital (LUMO) and the highest occupied molecular orbital (HOMO) for all carbon nitride models are summarized in Table 1. The largest HOMO-LUMO gap is found for PTI (5.24 eV), followed by TGCN (5.01 eV).

Table 1. HOMO-LUMO gap (ΔE in eV) of carbon nitride models, calculated with B3LYP-D3/6-31G**.

	PTI	*10*-PTI	C_3N_3	*7*-C_3N_3	TGCN	*10*-TGCN	HGCN	*6*-HGCN
Δ E, eV	5.24	5.21	3.94	3.79	5.01	4.49	3.65	3.54

Slightly smaller and comparable values are obtained for C_3N_3 and HGCN, 3.94 eV and 3.65 eV, respectively. Enlargement of the structural models does not lead to a meaningful reduction in the energy gap between the two frontier orbitals. C_3N_3 and HGCN with the smaller energy difference, display promising potential for photocatalytic applications, as their band gap can be tuned to enhance light absorption and overall photocatalytic efficiency.

The interaction of these materials with gas molecules can influence the energy levels of the frontier molecular orbitals (HOMO and LUMO), thereby affecting their adsorption properties and selectivity. The large band gap values, particularly for PTI and HGCN, are associated with high chemical stability and low reactivity [24], important characteristics for application of the models as gas separation membranes.

CONCLUSION

A series of carbon nitride models based on s-triazine (PTI, C_3N_3, TGCN) and tri-s-triazine units (HGCN) were studied using density functional theory. The potential of structures with varying nanopore shape and size for use as one-atom thick gas separation membranes was evaluated. Both the smallest single-pore models and the highly porous 2D nanosheets were considered. Increasing the size of the carbon nitride models does not lead to significant structural variations: the PTI nanosheet remains planar and the folding in HGCN is preserved. Edge effects become slightly more pronounced in TGCN, where differences between the central pore and the peripheral ones are observed. As the number of the building units increases, the C_3N_3 nanosheet tends to adopt a more planar structure. Enlargement of the structures is not associated with major redistribution of the electron density, although, a slight increase in the total charge was observed for the central nanopores in the PTI and C_3N_3 nanosheets and a reduction was found for TGCN, and more notable, for HGCN. The relatively similar charge distribution among the nanopores in the nanosheets suggests possible competition between pores during the gas capturing process. The enlargement of the models does not affect the HOMO-LUMO energy difference, indicating good chemical stability of the structures. The studied structural and electronic characteristics of the carbon nitride models are an initial step toward exploring their potential as one atom-thick membranes.

Supporting information: *The following data are provided as Supporting information: atomic charges of the single and multiple-pore models of PTI, C_3N_3, TGCN, HGCN (Figures S1 to S5).*

Acknowledgement: *This work was supported by Project BG16RFPR002-1.014-0006 "National Centre of Excellence Mechatronics and Clean Technologies", co-funded by the European Union, under "Research Innovation and Digitalization for Smart Transformation" program 2021-2027.*

REFERENCES

1. S. Wang, L. Wang, H. Cong, R. Wang, J. Yang, X. Li, Y. Zhao, H. Wang, *J. Environ. Chem. Eng.*, **10**, 108189 (2022).
2. T. Ashirov, J. S. Siena, M. Zhang, A. O. Yazaydin, M. Antonietti, A. Coskun, *Nat. Commun.* **13**, 7299 (2022).
3. S. Hua, D. Qu, L. An, W. Jiang, Y. Wen, X. Wang, Z. Sun, *Appl. Catal. B – Environ*, **240**, 253 (2019).
4. K. Schwinghammer, M. B. Mesch, V. Duppel, C. Ziegler, J. Senker, B. V. Lotsch, *J. Am. Chem Soc.* **136**, 1730 (2014).
5. M. Wu, Q. Wang, Q. Sun, P. Jena, *J. Phys. Chem. C*, **117**, 6055 (2013).
6. X.-L. Zhang, C. Zheng, S. S. Guo, J. Li, H. H. Yang, G. Chen, *Anal. Chem.*, **86**, 3426 (2014).
7. M. Wu, Q. Wang, Q. Sun, P. Jena, *J. Phys. Chem. C.*, **117**, 6055 (2013).
8. G. Dong, Y. Zhang, Q. Pan, J. Qiu, *J. Photochem. Photobiol. C: Photochem. Rev.*, **20**, 33 (2014).
9. Y. Kang, Y. Yang, L. C. Yin, H. M. Cheng, *Adv. Mater.* **27**, 4572 (2015).
10. J. Sehnert, K. Baerwinkel, J. Senker, *J. Phys. Chem.*, **111**, 10671 (2007).
11. Y. Wang, Q. Yang, C. Zhong, J. Li, *J. Phys. Chem. C*, **120**, 28782 (2016).
12. Z. Ma, X. Zhao, Q. Tang, *Int. J. Hydrogen Energy*, **39**, 5037 (2014).
13. B. Zhu, S. Wageh, A. A. Al-Ghamdi, S. Yang, Z. Tian, J. Yu, *Catal. Today*, **335**, 117 (2019).
14. M. T. Vahdat, D. Campi, N. Colonna, N. Marzari, K. V. Agrawal, *J. Phys. Chem. C*, **125**, 18896 (2021).
15. S. W. de Silva, A. Du, W. Senadeera, Y. Gu, *J. Membr. Sci.*, **528**, 201 (2017).
16. Y. Zhou, Y. Wu, H. Wu, J. Xue, H. Wang, *Nat. Commun.*, **13**, 5852 (2022).
17. Y. Ji, H. Dong, H. Lin, L. Zhang, T. Hou, Y. Li, *RSC Adv.*, **6**, 52377 (2016).
18. P. Li, F. Wang, S. Wei, X. Li, Y. Zhou, *Phys. Chem. Chem. Phys.*, **19**, 4405 (2017).
19. J. Wang, Z. Guan, J. Huang, Q. Li, J. Yang, *J. Mater. Chem. A*, **2**, 7960 (2014).

20. S. Grimme, J. Antony, S. Ehrlich, H. Krieg, *J. Chem. Phys.*, **132**, 154104 (2010).
21. A. E. Reed, L. A. Curtiss, F. Weinhold, *Chem. Rev.*, **88**, 899 (1988).
22. M. J. Frisch, G. W. Trucks, H. B. Schlegel, G. E. Scuseria, M. A. Robb, J. R. Cheeseman, G. Scalmani, V. Barone, G. A. Petersson, H. Nakatsuji, X. Li, M. Caricato, A. V. Marenich, J. Bloino, B. G. Janesko, R. Gomperts, B. Mennucci, H. P. Hratchian, J. V. Ortiz, A. F. Izmaylov, J. L. Sonnenberg, D. Williams-Young, F. Ding, F. Lipparini, F. Egidi, J. Goings, B. Peng, A. Petrone, T. Henderson, D. Ranasinghe, V. G. Zakrzewski, J. Gao, N. Rega, G. Zheng, W. Liang, M. Hada, M. Ehara, K. Toyota, R. Fukuda, J. Hasegawa, M. Ishida, T. Nakajima, Y. Honda, O. Kitao, H. Nakai, T. Vreven, K. Throssell, J. A. Montgomery, Jr., J. E. Peralta, F. Ogliaro, M. J. Bearpark, J. J. Heyd, E. N. Brothers, K. N. Kudin, V. N. Staroverov, T. A. Keith, R. Kobayashi, J. Normand, K. Raghavachari, A. P. Rendell, J. C. Burant, S. S. Iyengar, J. Tomasi, M. Cossi, J. M. Millam, M. Klene, C. Adamo, R. Cammi, J. W. Ochterski, R. L. Martin, K. Morokuma, O. Farkas, J. B. Foresman, D. J. Fox, Gaussian, Inc., Wallingford, CT, Gaussian 16, Revision B.01, 2016.
23. J. Sehnert, K. Baerwinkel, J. Senker, *J. Phys. Chem. B*, **111**, 10671 (2007).
24. U. Khan, R. A. Khera, N. Anjum, R. A. Shehzad, S. Iqbal, K. Ayub, J. Iqbal, *RSC Adv.,* **11***,* 7779 (2021).

Bulgarian Chemical Communications, Volume 58, Issue 2 (pp. 200-208) 2026 DOI: 10.34049/bcc.58.2.NCC04

Computational evaluation of COX-1 binding by EPA, DHA, and AA using blind and flexible docking approaches

R. Stancheva[1*], I. Iliev[2], A. Merdzhanova[1], S. Georgieva[2]

[1]*Department of Chemistry, Faculty of Pharmacy, Medical University of Varna, Bulgaria*
[2]*Department of Pharmaceutical Chemistry, Faculty of Pharmacy, Medical University of Varna, Bulgaria*

Received: October 22, 2025; Revised: March 16, 2026

Omega-3 polyunsaturated fatty acids (PUFAs), including eicosapentaenoic acid (EPA) and docosahexaenoic acid (DHA), are associated with anti-inflammatory effects, but their molecular interactions with cyclooxygenase-1 (COX-1) remain incompletely understood. This study employed blind and flexible molecular docking simulations using AutoDock 4.2 to assess the binding of EPA, DHA, and arachidonic acid (AA) to COX-1 (PDB ID: 6Y3C). In rigid blind docking, DHA exhibited the strongest predicted affinity (−7.83 kcal/mol, Ki = 1.82 μM), followed by EPA (−7.21 kcal/mol, Ki = 5.21 μM) and AA (−6.11 kcal/mol, Ki = 33.11 μM), although none of the ligands engaged the catalytic residues, and high RMSD values indicated broad conformational sampling. Flexible docking, allowing selected active site residues (ARG120, TYR355, LEU384, TYR385, ILE523) to move, repositioned all ligands within the catalytic pocket, yielding improved binding energies (ΔG = −9.09 kcal/mol for AA, −9.03 kcal/mol for EPA, and −8.73 kcal/mol for DHA) and nanomolar inhibition constants. EPA closely reproduced the AA binding pose (RMSD = 3.90 Å), while DHA adopted a distinct but favorable orientation (RMSD = 5.37 Å). Both ω-3 PUFAs formed hydrogen and hydrophobic interactions with key residues (ARG120, TYR355, TYR385, SER530), consistent with competitive engagement of the catalytic site. These results indicate that EPA and DHA can stably interact with COX-1, supporting a mechanistic basis for their anti-inflammatory properties, and underscore the importance of receptor flexibility in accurately modeling enzyme-ligand interactions. Further studies, including molecular dynamics simulations and experimental validation, are warranted to confirm these findings and elucidate the mechanistic basis of ω-3 fatty acids' anti-inflammatory effects.

Keywords: Omega-3 fatty acids, Cyclooxygenase-1 (COX-1), Blind rigid-body docking, AutoDock 4.2, Anti-inflammatory potential, Flexible docking

INTRODUCTION

Cyclooxygenase-1 (COX-1) is a constitutively expressed enzyme that plays an important role in the biosynthesis of prostaglandins from arachidonic acid (AA), thereby contributing to a variety of physiological processes such as gastric protection, platelet aggregation, and renal function [1-3]. COX-1 is one of three isoforms – alongside COX-2 and COX-3 – each of which exhibits distinct expression patterns and biological roles [1, 2].

Structurally, COX-1 exists as a homodimer, and each monomer contains a large globular catalytic domain with an active site shaped as an inverted L-channel composed mainly of hydrophobic residues [3-5]. This active site can be subdivided into proximal, central, and distal pockets which cooperate to stabilize and position AA during catalysis [4, 5]. One of the key residues governing ligand selectivity in COX-1 is isoleucine at position 523, distinguishing it from COX-2, where valine at this site confers greater flexibility and substrate access [1, 6]. This structural divergence has been exploited in the development of selective COX-2 inhibitors and underscores the pharmacological significance of understanding COX-1-ligand interactions [1, 2].

In recent years, the anti-inflammatory potential of omega-3 polyunsaturated fatty acids (PUFAs) – particularly eicosapentaenoic acid (EPA) and docosahexaenoic acid (DHA) – has attracted considerable scientific attention. These long-chain fatty acids are essential components of cell membranes and serve as precursors for a variety of bioactive lipid mediators that modulate inflammatory responses, neuroprotection, and immune regulation [7-10]. Unlike AA which gives rise to pro-inflammatory eicosanoids, EPA and DHA are generally associated with the production of less inflammatory or even anti-inflammatory derivatives [8, 9]. For example, DHA has been implicated in promoting neurite growth and maintaining cognitive function, while EPA-derived lipid mediators exhibit reduced potency in eliciting inflammation compared to their AA-derived counterparts [7, 9].

The metabolic pathways of these fatty acids are tightly interconnected. AA is synthesized from linoleic acid, while EPA and DHA are derived from α-linolenic acid through desaturation and elongation,

---

[*] To whom all correspondence should be sent:
Email: *rositsa.stancheva@mu-varna.bg*

although conversion rates in humans are low, making dietary intake crucial [9, 10]. Retroconversion of DHA can also produce EPA and docosapentaenoic acid (DPA), adding another layer of metabolic interplay [10]. Of particular interest are electrophilic fatty acid oxo-derivatives, a novel class of endogenous anti-inflammatory molecules derived from EPA, DHA, and DPA, which can activate PPARγ and inhibit pro-inflammatory cytokines [7]. These findings highlight the relevance of omega-3 fatty acids as modulators of inflammation.

Despite the growing body of literature supporting the anti-inflammatory potential of omega-3 fatty acids, questions remain regarding their direct competitive behavior with AA at the active site of COX-1 [11]. While many studies have investigated downstream metabolic effects and systemic outcomes, comparatively fewer have addressed the molecular details of how long-chain polyunsaturated fatty acids interact with COX-1 at the binding-site level. Previous experimental work has largely focused on prostaglandin production and substrate availability, without evidence for altered COX-1 or COX-2 expression [12]. In parallel, recent biochemical and structural studies have demonstrated that cyclooxygenase enzymes possess both catalytic and allosteric sites capable of accommodating fatty acids and small-molecule ligands [13].

To address this gap, computational approaches such as molecular docking offer valuable tools for elucidating ligand-enzyme interactions at the atomic level. Docking techniques predict the binding affinity and pose of a ligand within the active site of a target protein, and are widely used in early-stage drug discovery and mechanistic studies [14]. Among the various strategies, rigid-body docking is computationally efficient and assumes that both the ligand and the receptor remain static during interaction [15-17]. A subtype of this method, blind docking, involves scanning of the entire protein surface without predefined binding-site information, allowing for unbiased identification of potential ligand-accessible pockets [18-20]. Although blind docking is more computationally intensive, it is particularly useful when the ligand's binding site is unknown or when allosteric interactions are being considered [14, 18].

However, flexible docking approaches provide a more realistic representation of biological binding by allowing conformational adjustments in selected amino acid residues or even in the entire active site during ligand accommodation [21]. This dynamic treatment of the receptor enables better modeling of induced-fit effects and can reveal binding modes inaccessible to rigid-body docking. Consequently, flexible docking is often employed as a refinement step following initial rigid or blind docking analyses, improving the accuracy of predicted binding poses and interaction energies [22].

This study employs blind rigid-body and flexible docking to computationally evaluate and compare the binding of AA, EPA, and DHA to the active site of COX-1. By applying AutoDock-based protocols, the aim is to assess whether omega-3 fatty acids can effectively compete with AA for enzymatic binding and to what extent their binding affinities and predicted interaction profiles provide molecular-level insight into potential competitive interactions with arachidonic acid at COX-1. The results may offer mechanistic insights into how EPA and DHA interact with COX-1 at the molecular level and contribute to a deeper understanding of their anti-inflammatory potential through interference with arachidonic acid metabolism.

MATERIALS AND METHODS

Three ligands – eicosapentaenoic acid (EPA), docosahexaenoic acid (DHA), and arachidonic acid (AA) – were selected for molecular docking based on their established involvement in inflammatory signaling pathways. The 3D structures of all compounds were retrieved from the PubChem database [23] in SDF format. Each ligand is imported into Avogadro [24], where geometry optimization is performed using the "Optimize Geometry" function to obtain low-energy conformations. The optimized structures were then saved in MOL2 format and subsequently loaded into AutoDock Tools [21]. Polar hydrogens were added, Gasteiger charges were assigned, rotatable bonds were detected, and the ligands were saved in PDBQT format for docking.

The crystal structure of cyclooxygenase-1 (COX-1) was obtained from the RCSB Protein Data Bank (PDB ID: 6Y3C) [25, 26]. 6Y3C represents the only available experimentally resolved structure of human COX-1. Other human cyclooxygenase structures deposited in the PDB correspond to the COX-2 isoform, while the majority of COX-1 structures originate from ovine sources. Accordingly, 6Y3C was selected to ensure human isoform specificity and to avoid species-dependent structural variations in the cyclooxygenase channel. Initial preprocessing was conducted using UCSF ChimeraX [27], where all non-standard residues were removed. The protein was then imported into AutoDock Tools, where water molecules were deleted, missing atoms were verified and corrected and polar hydrogen atoms were added. Kollman charges were assigned, atom types were set according to the AD4 specification, and the protein was saved in PDBQT format.

Molecular docking simulations were carried out using AutoDock 4.2 with the Lamarckian Genetic Algorithm. Two complementary docking strategies were applied for each ligand – blind rigid-body docking and flexible docking – to ensure both global and localized exploration of potential binding modes. In the blind docking protocol, a large grid box encompassing the entire enzyme surface was defined to allow unrestricted ligand exploration. Each ligand-protein pair was subjected to 100 independent docking runs, with a population size of 150, a mutation rate of 0.02, a crossover rate of 0.8, and a maximum of 25,000,000 energy evaluations per run. The best binding pose for each ligand was selected based on the lowest predicted binding free energy (ΔG). Since the docking was performed with a rigid protein structure and a blind search across the entire macromolecular surface, the generation of dispersed conformational clusters and higher RMSD values was anticipated. For this reason, RMSD-based convergence was not used as a strict selection criterion for pose selection in blind docking.

The purpose of blind docking in this study was to assess the global binding preferences of AA, EPA, and DHA across the entire COX-1 surface in an unbiased manner. This approach allows evaluation of whether the canonical cyclooxygenase channel is energetically favored relative to other hydrophobic regions of the enzyme prior to focused docking simulations. For the flexible docking simulations, a focused grid centered at coordinates x = –31.521, y = –45.301, z = 5.179, with grid spacing 0.375 Å, was applied to target the enzyme's catalytic site. The same algorithmic parameters and number of docking runs (100) were maintained to ensure comparability. The following residues were defined as flexible to account for induced-fit effects: ARG120, TYR355, LEU384, TYR385, ILE523, and SER530. The population size for the flexible docking runs was increased to 300 to enhance conformational sampling within the active site.

To validate the docking protocol, the co-crystallized molecule present in the human COX-1 crystal structure (PDB ID: 6Y3C), FLC (citrate ion), was extracted and re-docked into a focused grid centered on its crystallographic position within the protein. It should be noted that the co-crystallized molecule labeled FLC in the 6Y3C structure corresponds to citrate ion, present as three copies originating from the crystallization buffer. These ions do not occupy the enzyme's canonical cyclooxygenase channel and are not considered biologically relevant ligands for COX-1. Nevertheless, 6Y3C was retained as the receptor model, as it represents the only experimentally resolved crystal structure of human COX-1 in the Protein Data Bank. The use of FLC in the re-docking validation was limited to geometric pose reproduction, assessing the protocol's ability to recover the crystallographic placement of the molecule within the protein matrix, irrespective of its biological role.

Re-docking was carried out using AutoDock 4.2 with a focused grid centered on the crystallographic position of the citrate ion (grid spacing 0.375 Å), employing the same Lamarckian Genetic Algorithm parameters as used in the flexible docking simulations, with validation based on geometric pose reproduction. The top-ranked docked pose was compared to the experimental crystallographic pose by calculating the heavy-atom RMSD. The validation was based on pose reproduction rather than a detailed interaction analysis, as the primary objective was to assess the geometric reliability of the docking protocol. The resulting RMSD of 1.739 Å confirms the geometric reliability of the AutoDock 4.2 setup and parameterization, demonstrating the consistency of the docking algorithm in recovering crystallographic poses and supporting its application for the subsequent focused docking of AA, EPA, and DHA within the catalytic site. Protocol validation was thus based solely on geometric pose reproduction of FLC, independently of its biological relevance. For all subsequent comparative analyses, arachidonic acid (AA) – the endogenous substrate of COX-1 – served as the primary biological reference ligand.

Inhibition constants (Ki) were estimated by AutoDock 4.2 from predicted binding free energies using its built-in thermodynamic conversion ($\Delta G = RT \ln Ki$, where $R = 1.987\times10^{-3}$ kcal/mol·K and T = 298 K). The resulting Ki values are theoretical estimates used for relative comparison. AA was used as a reference ligand for comparative analysis to evaluate the biological relevance and spatial accuracy of docking results. Comparative analyses included spatial overlap and relative orientation of docked EPA and DHA poses with respect to the docked AA reference within the COX-1 catalytic channel.

For comparative analysis of ligand positioning within the COX-1 catalytic pocket, the reference configuration was defined as the top-ranked docked pose of arachidonic acid (AA) obtained from the flexible docking protocol. All ligand-protein complexes were first aligned based on the COX-1 backbone to ensure a common structural reference frame.

Post-docking analyses were performed using UCSF ChimeraX and Discovery Studio Visualizer [28] to examine ligand-protein interactions, including hydrogen bonding, hydrophobic contacts, and steric complementarity. The spatial orientation of each ligand was analyzed with respect to catalytically relevant residues of COX-1, particularly LEU117, ARG120, PHE205, VAL344, TYR385, and SER530. Interaction profiles were used to assess whether omega-3 fatty acids form stable complexes in proximity to, or overlapping with, the enzyme's functional site.

RESULTS AND DISCUSSION

Both blind and flexible docking simulations were performed to assess the binding characteristics of DHA, EPA, and AA toward COX-1. Blind docking was used to identify potential surface-accessible binding sites, while flexible docking was employed to refine ligand placement within the catalytic pocket by allowing conformational mobility of selected residues.

Blind rigid-body docking results

Molecular docking simulations revealed that both omega-3 fatty acids exhibit stronger binding affinities to COX-1 compared to AA. DHA showed the most favorable binding profile, with a predicted binding energy (ΔG) of −7.83 kcal/mol and an estimated inhibition constant (Ki) of 1.82 μM. EPA followed with a ΔG of −7.21 kcal/mol and Ki of 5.21 μM. In contrast, AA showed the weakest interaction, with a ΔG of −6.11 kcal/mol and a significantly higher Ki of 33.11 μM. Intermolecular energy values further supported this trend, with DHA exhibiting the most stabilizing interactions (−12.30 kcal/mol), followed by EPA (−11.38 kcal/mol) and AA (−10.59 kcal/mol). These results suggest that DHA and EPA may form more stable complexes with COX-1 than the endogenous substrate AA, which is consistent with their proposed anti-inflammatory potential. A complete summary of the docking results, including electrostatic, internal, and torsional energy components, is presented in Table 1.

The predicted binding free energy (ΔG) serves as a thermodynamic estimate of how strongly a ligand interacts with its target under simulated conditions. More negative ΔG values typically indicate the formation of energetically favorable and stable ligand-receptor complexes, which may correlate with the higher inhibitory potential in biochemical systems [22]. In this context, the relatively low ΔG values observed for the omega-3 fatty acids suggest that they are capable of establishing stable interactions with COX-1, possibly outcompeting the natural substrate arachidonic acid. The estimated inhibition constants reinforce this interpretation, as lower Ki values are indicative of stronger binding affinity and greater likelihood of effective enzyme modulation. When Ki falls within the low micromolar range – as is this case – it is generally considered biologically relevant and compatible with physiological ligand concentrations [29, 30]. These findings support the hypothesis that omega-3 fatty acids may act as competitive modulators of COX-1-mediated inflammatory signaling.

To gain further insight into the nature of these interactions, the ligand-protein binding profiles were examined in detail. DHA forms three hydrogen bonds – with CYS41, GLN44, and HIS43 – alongside extensive hydrophobic contacts involving CYS36, CYS47, PRO40, PRO153, PRO156, LEU152, and ARG469. EPA, while forming only a single hydrogen bond with CYS47, engages in multiple alkyl interactions with residues such as CYS36, CYS41, PRO153, and PRO156. Arachidonic acid similarly forms a hydrogen bond with CYS41 and hydrophobic interactions with CYS47, PRO153, ILE46, LEU152, and PRO125.

Despite some overlap in the interacting residues – particularly CYS41, CYS47, and PRO153 – all three ligands bind outside the canonical catalytic pocket of COX-1, which includes ARG120, TYR385, SER530, and neighboring residues critical for substrate binding and enzymatic activity [31]. This observation is consistent with the rigid-body docking approach employed, which does not account for protein flexibility or induced fit effects that may be required for productive orientation within the active site.

Blind docking revealed multiple energetically favorable binding regions outside the canonical catalytic channel, motivating subsequent focused flexible docking to directly probe ligand behavior within the enzymatic pocket.

Nevertheless, the broader and more diverse interaction network formed by DHA, including multiple hydrogen bonds and stabilizing hydrophobic contacts, suggests a more extensive and potentially favorable surface interaction pattern compared to EPA and AA. EPA shows a similar, albeit less extensive, interaction pattern, while AA displays the least complex interaction profile. These differences further support the view that omega-3 fatty acids may occupy functionally relevant surface regions of COX-1 and interact with COX-1 through non-classical surface binding modes. The ligand-protein interaction profiles for DHA, EPA, and AA are shown in Figure 1.

Table 1. Summary of blind docking results for DHA, EPA, and AA with COX-1.

Ligand	Binding energy ΔG, kcal/mol	Ki, µM	Intermolecular energy, kcal/mol	Electrostatic energy, kcal/mol	Torsional free energy, kcal/mol	Internal energy, kcal/mol
DHA	−7.83	1.82	−12.30	−0.20	4.47	−1.35
EPA	−7.21	5.21	−11.38	−0.16	4.18	−1.18
AA	−6.11	33.11	−10.59	−0.19	4.47	−0.96

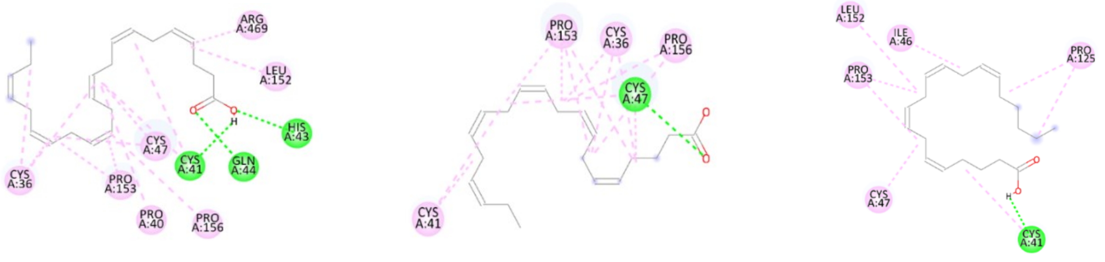

DHA **EPA** **AA**

Interactions:

🟩 *Covalent hydrogen bond* ■ *Alkyl*

Figure 1. Two-dimensional interaction diagrams from blind docking of docosahexaenoic acid (DHA), eicosapentaenoic acid (EPA), and arachidonic acid (AA) bound to COX-1, illustrating conventional hydrogen bonds (green) and alkyl interactions (pink).

Although none of the three ligands directly engages catalytically essential residues, their consistent interaction with overlapping peripheral residues suggests a common binding surface on COX-1. The absence of active-site contacts is likely a consequence of the rigid-body docking approach, which does not account for protein flexibility or induced fit. However, given the stronger binding energies of DHA and EPA compared to AA, along with their spatial overlap in surface-binding regions, it is plausible to hypothesize that omega-3 fatty acids may have the potential to access the catalytic site under more physiologically relevant, dynamic conditions.

The interpretation of these findings should be considered in light of the methodological limitations inherent to rigid-body docking. This approach treats the protein as a fixed structure, which limits the exploration of induced-fit phenomena and may lead to underestimation of ligand accessibility to conformationally adaptive binding sites. Additionally, solvent effects and entropic contributions were not explicitly modeled, which may further influence the accuracy of the predicted affinities. The elevated RMSD values observed during clustering reflect the exploratory nature of blind docking across the enzyme's entire surface and were not used as a strict convergence criterion in pose selection.

Despite these limitations, blind rigid-body docking was employed in this study as a suitable first-line computational strategy to identify potential binding regions and estimate the relative affinity of ligands toward the target protein. This method is widely used for preliminary screening due to its efficiency, simplicity, and ability to generate hypotheses for further validation.

To overcome the limitations described above, flexible docking protocols were subsequently applied in the present study to allow structural adaptation of the active site. This approach enables evaluation of whether AA, DHA and EPA can access the catalytic pocket under conditions that better account for induced-fit effects.

Docking protocol validation

Re-docking of the co-crystallized molecule FLC (citrate ion) into COX-1 resulted in a close reproduction of the experimental binding pose, with RMSD of 1.739 Å between the crystallographic pose of FLC and the top-ranked re-docked conformation.

These results support the geometric reliability of the docking setup and justify its application for subsequent comparative docking analyses.

Flexible docking results

To further refine the docking analysis, flexible docking was performed to account for the conformational adaptability of amino acid residues within the COX-1 active site. In contrast to the blind docking approach, flexible docking enables selected residues in the binding pocket to move during the simulation, providing a more realistic representation of enzyme-ligand interactions.

The results of flexible docking, presented in Table 2, show binding energies consistent with those obtained from blind docking, but with generally more favorable (lower) energy values, reflecting improved accommodation of the ligands within the active site. Among the tested compounds, AA exhibits a binding energy of –9.24 kcal/mol, confirming its strong affinity toward the COX-1 catalytic pocket. In comparison, EPA and DHA display binding energies of –8.67 kcal/mol and –8.53 kcal/mol, respectively.

These results suggest that both ω-3 fatty acids can adopt binding poses within the catalytic pocket that overlap with key substrate-interacting regions, indicating a potential for competitive interactions at the molecular level. The observed RMSD values reflect the conformational spread of docked poses within the catalytic site. AA and EPA show relatively lower values (RMSD = 3.715 Å and 3.901 Å, respectively), indicating more convergent clustering, whereas DHA shows a larger deviation (RMSD = 5.368 Å), consistent with its greater conformational freedom. Despite this difference in conformational spread, all three ligands achieve substantially improved binding energies under the flexible protocol (nanomolar-range Ki), with AA and EPA showing the most favorable ΔG.

Table 2. Summary of flexible docking results for DHA, EPA, and AA with COX-1.

Parameter	**DHA**	**EPA**	**AA**
RMSD of docked conformations (clustering), Å	5.368	3.901	3.715
Estimated free energy of binding (ΔG), kcal/mol	-8.73	-9.03	-9.09
Estimated inhibition constant (Ki, 298.15 K), nM (nanomolar)	398.60	239.03	216.87
Final intermolecular energy, kcal/mol	-13.20	-13.21	-13.57
• *Ligand–fixed receptor, kcal/mol*	-11.36	-8.63	-8.66
– *vdW + H-bond + desolvation, kcal/mol*	-11.32	-8.62	-8.66
– *Electrostatic, kcal/mol*	-0.04	-0.01	+0.01
• *Ligand–flexible residues, kcal/mol*	-1.84	-4.58	-4.91
– *vdW + H-bond + desolvation, kcal/mol*	-1.85	-4.42	-4.87
– *Electrostatic, kcal/mol*	+0.00	-0.16	-0.04
Final total internal energy, kcal/mol	-15.19	-12.92	-12.72
• *Ligand internal energy, kcal/mol*	-1.40	-0.86	-0.67
• *Ligand–fixed receptor, kcal/mol*	-13.54	-11.68	-11.96
• *Ligand–flexible residues, kcal/mol*	-0.25	-0.38	-0.09
Torsional free energy, kcal/mol	+4.47	+4.18	+4.47
Unbound system energy, kcal/mol	-15.19	-12.92	-12.72

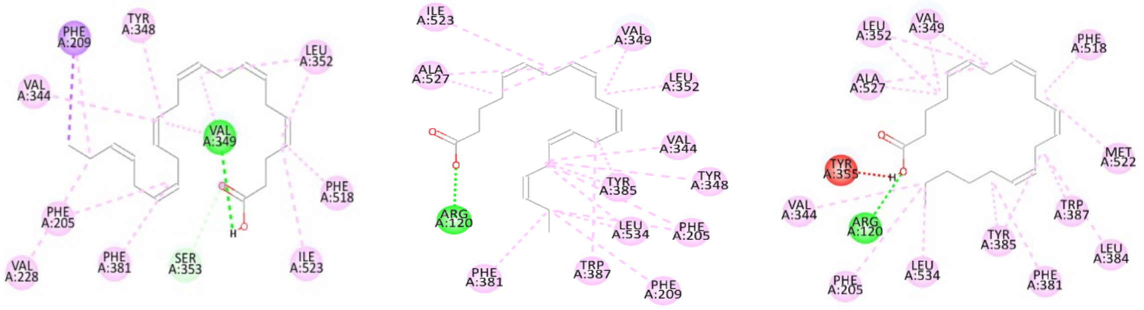

DHA **EPA** **AA**

Interactions:

🟩 Conventional hydrogen bond ⬜ Carbon hydrogen bond ⬜ Alkyl and pi-alkyl
🟪 Pi-sigma 🟥 Unfavorable donor-donor

Figure 2. Two-dimensional interaction diagrams from flexible docking of docosahexaenoic acid (DHA), eicosapentaenoic acid (EPA), and arachidonic acid (AA) bound to COX-1, illustrating conventional hydrogen bonds (green) and alkyl interactions (pink).

The larger RMSD for DHA likely reflects its greater conformational freedom (longer, more unsaturated chain) and may correspond to an alternative but still energetically favorable binding mode. Collectively, the flexible docking results support the notion that ω-3 fatty acids can access and be accommodated by the COX-1 catalytic region under receptor flexibility, although the exact orientation and contacts differ among ligands.

In the flexible docking simulations, all three ligands localized within the hydrophobic channel leading to the cyclooxygenase catalytic site of COX-1, establishing key contacts with residues known to participate in substrate anchoring and catalysis. The ligand-protein interaction profiles for DHA, EPA, and AA are shown in Figure 2. The inclusion of receptor flexibility allows the side chains of several residues to adjust their conformations, resulting in tighter fitting and improved complementarity between the ligands and the binding pocket compared to rigid-body docking.

In the flexible docking simulations, AA, EPA, and DHA all localized within the COX-1 catalytic channel, maintaining interactions with residues critical for substrate anchoring and catalysis. AA, used as the reference substrate, forms the characteristic hydrogen bonds between its carboxylate terminus and ARG120 and TYR355, while engaging the hydrophobic residues PHE205, VAL344, LEU534, TYR385, PHE381, LEU384, TRP387, MET522, PHE518, VAL349, LEU352 and ALA527. EPA adopts a nearly identical pose, preserving the hydrogen bond with ARG120 and forming additional alkyl interactions with PHE209, TYR348 and ILE523. In contrast, DHA exhibits a more extended conformation due to its higher degree of unsaturation. It retained a stable hydrogen bond but with VAL349, formed compensatory polar contacts with SER353, and established hydrophobic interactions with PHE381, PHE205, VAL228, VAL344, PHE209, TYR348, LEU352, PHE518 and ILE523. Despite its greater torsional flexibility and higher RMSD, DHA remains anchored through conserved interactions with VAL349 and SER353, confirming its compatibility with the catalytic environment and supporting the view that ω-3 fatty acids can competitively engage the COX-1 active site in a manner comparable to arachidonic acid.

These results indicate that both EPA and DHA can occupy the COX-1 catalytic site, with EPA closely mimicking the reference substrate AA and DHA adopting an alternative yet stable orientation. The observed hydrogen bonding and hydrophobic contacts with key residues support a potential competitive mechanism, although the distinct conformations of DHA highlight the influence of chain flexibility on binding dynamics. Considering the limitations of docking simulations, including neglect of solvent effects and entropic contributions, further studies using molecular dynamics and experimental validation are necessary to confirm these interactions and clarify their functional relevance in COX-1 modulation.

Comparative analysis

Comparison between blind and flexible docking outcomes reveals a clear progression from surface-level association to catalytically relevant binding. In the blind docking simulations, all three fatty acids occupied similar peripheral regions on the COX-1 surface rather than the canonical catalytic pocket. This spatial overlap suggests that the molecules share comparable physicochemical properties governing initial enzyme recognition and surface adhesion. However, the absence of interactions with the key residues ARG120, TYR385, and SER530 indicated that these poses likely represent preliminary, non-productive associations.

When receptor flexibility was introduced, the binding profiles changed substantially. The flexible docking protocol allowed rearrangement of side chains surrounding the active site, enabling all three ligands to access the catalytic channel. Importantly, the binding energies inverted their relative order: while AA exhibited the weakest binding in the rigid-body scenario, it became the most strongly bound ligand under flexible conditions ($\Delta G = -9.09$ kcal/mol), followed closely by EPA (−9.03 kcal/mol) and DHA (−8.73 kcal/mol). This reversal highlights the influence of local conformational adaptation on ligand accommodation and suggests that rigid docking may underestimate true binding affinity for flexible active sites such as COX-1.

The RMSD values (3.7–5.4 Å) reflect the conformational spread of docked poses within the catalytic groove, with AA and EPA showing more convergent clustering and DHA exhibiting greater conformational variability consistent with its longer, more unsaturated chain. The consistent anchoring of the carboxylate group to ARG120 and, in some cases, TYR355 and SER530, confirms productive alignment along the catalytic axis. The energetic improvement of approximately 1-2 kcal/mol for EPA and DHA relative to their rigid-body poses reflects enhanced hydrophobic packing and steric complementarity within the enzyme cavity.

The observed similarities in binding positions and interaction energies among arachidonic, eicosapentaenoic, and docosahexaenoic acids can be rationalized by their close structural and electronic resemblance, which inherently dictates a comparable pattern of molecular recognition within the COX-1 binding region. Their shared amphiphilic character – defined by a polar carboxylate head and a flexible hydrophobic tail – promotes analogous anchoring near ARG120 and alignment toward the catalytic TYR385–SER530 dyad. These consistent binding profiles across blind and flexible docking simulations reinforce the notion that all three fatty acids may engage the enzyme through similar physicochemical mechanisms, despite differences in flexibility and unsaturation degree. Nevertheless, the computational results presented here serve primarily as predictive evidence and require further validation through biochemical and kinetic assays to confirm the physiological relevance of these interactions.

CONCLUSION

The combined results of blind and flexible docking analyses provide complementary insights into the molecular recognition of COX-1 by arachidonic acid and the omega-3 fatty acids eicosapentaenoic acid and docosahexaenoic acid. While blind docking simulations identify peripheral surface-binding regions shared among all three ligands, flexible docking reveals their capacity to occupy the catalytic channel when receptor mobility is permitted. The restoration of key interactions with ARG120, TYR355, and SER530 under flexible conditions demonstrates that both EPA and DHA can adopt conformations comparable to the native substrate and potentially compete for access to the active site.

Energetically, the small differences in binding free energy (ΔG ≈ 1–2 kcal/mol) between the ligands suggest similar affinities toward the catalytic pocket, reflecting their shared amphiphilic architecture and structural homology. The comparable binding orientations and overlapping interaction networks observed for the three fatty acids support the hypothesis that omega-3 compounds may modulate COX-1 activity through competitive mechanisms.

These findings contribute to the growing body of evidence that omega-3 fatty acids possess intrinsic potential to interfere with arachidonic acid metabolism, thereby influencing prostaglandin biosynthesis and inflammatory signaling. However, as docking simulations represent theoretical approximations of molecular interactions, further *in vitro* and *in vivo* studies such as enzyme inhibition assays, kinetic evaluations, and structural analyses are required to validate the predicted binding modes and clarify the physiological implications of these interactions.

REFERENCES

1. K. K. Reddy, V. K. Vidya Rajan, A. Gupta, P. Aparoy, P. Reddanna, *BMC Res. Notes*, **8**, 152 (2015). https://doi.org/10.1186/s13104-015-1101-4
2. R. K. Vishwakarma, D. S. Negi, *International Journal of Pharmaceutical Sciences and Research*, **11** (8), 3544 (2020).
3. S. Wan, P. V. Coveney, *Journal of Computational Chemistry*, **30** (7), 1038 (2009). https://doi.org/10.1002/jcc.21130
4. C. A. Rouzer, L. J. Marnett, *Chem Rev.*, **120** (15), 7592 (2020). http://doi.org/10.1021/acs.chemrev.0c00215
5. A. J. Vecchio, D. M. Simmons, M. G. Malkowski, *Journal of Biological Chemistry*, **285** (29), 22152 (2010). http://doi.org/10.1074/jbc.m110.119867
6. L.L.C. Schrödinger, Docking and Scoring. https://www.schrodinger.com/life-science/learn/white-papers/docking-and-scoring/
7. S. C. Dyall, *Front. Aging Neurosci.*, **7** (52), (2015). http://doi.org/10.3389/fnagi.2015.00052
8. U. N. Das, *Current Pharmaceutical Biotechnology*, **7** (6), 467 (2006). https://doi.org/10.2174/138920106779116856
9. M. J. Calvo, M. S. Martínez, W. Torres, M. Chávez-Castillo, E. Luzardo, N. Villasmil, J. Salazar, M. Velasco, V. Bermúdez, *Vessel Plus*, **1**, 116 (2017). http://dx.doi.org/10.20517/2574-1209.2017.14
10. Y. Zhang, Y. Liu, J. Sun, W. Zhang, Z. Guo, Q. Ma, *MedComm*, **4** (5), e363 (2023). https://doi.org/10.1002/mco2.363
11. L. Dong, H. Zou, C. Yuan, Y. H. Hong, D. V. Kuklev, W. L. Smith, *J. Biol. Chem.*, **291** (8), 4069 (2016). http://doi.org/10.1074/jbc.M115.698001
12. A. S. Roman, J. Schreher, A. P. Mackenzie, P. W. Nathanielsz, *Am. J. Obstet. Gynecol.*, **195** (6), 1693 (2006). http://doi.org/10.1016/j.ajog.2006.04.009
13. W. L. Smith, M. G. Malkowski, *J. Biol. Chem.*, **294** (5), 1697 (2019).
14. P. C. Agu, C. A. Afiukwa, O. U. Orji, E. M. Ezeh, I. H. Ofoke, C. O. Ogbu, E. I. Ugwuja, P. M. Aja, *Scientific Reports,* **13**, 13398 (2023). https://doi.org/10.1038/s41598-023-40160-2
15. P. H. M. Torres, A. C. R. Sodero, P. Jofily, F. P. Silva-Jr, *Int. J. Mol. Sci.,* **20** (18), 4574 (2019). http://doi.org/10.3390/ijms20184574
16. I. A. Guedes, C. S. de Magalhães, L. E. Dardenne, *Biophysical Reviews*, **6**, 75 (2014). https://doi.org/10.1007/s12551-013-0130-2
17. E. Mateev, B. Angelov, M. Kondeva-Burdina, I. Valkova, M. Georgieva, A. Zlatkov, *Farmacia*, **70** (6), 1126 (2022). http://doi.org/10.31925/farmacia.2022.2.21
18. C. Hetényi, D. van der Spoel, *Protein Science*, **20** (5), 880 (2011) https://doi.org/10.1002/pro.618
19. C. Hetényi, D. van der Spoel, *FEBS Letters*, **580** (5), 1447 (2006)
20. E. Mateev, M. Kondeva-Burdina, M. Georgieva, A. Mateeva, I. Valkova, V. Tzankova, A. Zlatkov, *Sci.*

Pharm., **92** (2), 18 (2024). https://doi.org/10.3390/scipharm92020018

21. G. M. Morris, R. Huey, W. Lindstrom, M. F. Sanner, R. K. Belew, D. S. Goodsell, A. J. Olson, *Journal of Computational Chemistry*, **30** (16), 2785 (2009). https://doi.org/10.1002/jcc.21256
22. L. G. Ferreira, R. N. Dos Santos, O. Glaucius, A. D. Andricopulo, *Molecules,* **20** (7), 13384 (2015). https://doi.org/10.3390/molecules200713384
23. S. Kim, J. Chen, T. Cheng, A. Gindulyte, J. He, S. He, Q. Li, B. A. Shoemaker, P. A. Thiessen, B. Yu, L. Zaslavsky, J. Zhang, E. E. Bolton, *Nucleic Acids Research*, **49** (D1), D1388 (2021). https://doi.org/10.1093/nar/gkaa971
24. M. D. Hanwell, D. E. Curtis, D. C. Lonie, T. Vandermeersch, E. Zurek, G. R. Hutchison, *Journal of Cheminformatics*, **4**, 17 (2012). https://doi.org/10.1186/1758-2946-4-17
25. S. K. Burley, C. Bhikadiya, C. Bi, S. Bittrich, L. Chen, G. V. Crichlow, C. H. Christie, K. Dalenberg, L. Di Costanzo, J. M. Duarte, S. Dutta, Z. Feng, S. Ganesan, D. S. Goodsell, S. Ghosh, R. K. Green, V. Guranović, D. Guzenko, B. P. Hudson, C. L. Lawson, Y. Liang, R. Lowe, H. Namkoong, E. Peisach, I. Persikova, C. Randle, A. Rose, Y. Rose, A. Sali, J. Segura, M. Sekharan, C. Shao, Y.-P. Tao, M. Voigt, J. D. Westbrook, J. Y. Young, C. Zardecki, M. Zhuravleva, *Nucleic Acids Research*, **49** (D1), D437 (2021). https://doi.org/10.1093/nar/gkaa1038
26. M. Miciaccia, B. D. Belviso, M. Iaselli, G. Cingolani, S. Ferorelli, M. Cappellari, P. Loguercio Polosa, M. G. Perrone, R. Caliandro, A. Scilimati, *Scientific Reports,* **11**, 4312, (2021). https://doi.org/10.1038/s41598-021-83438-z
27. E. F. Pettersen, T. D. Goddard, C. C. Huang, E. C. Meng, G. S. Couch, T. I. Croll, J. H. Morris, T. E. Ferrin, *Protein Science,* **30** (1), 70 (2021). https://doi.org/10.1002/pro.3943
28. Dassault Systèmes BIOVIA, Discovery Studio Visualizer, Version 21.1.0. San Diego: Dassault Systèmes BIOVIA Corp., 2020. Available at: https://discover.3ds.com/discovery-studio-visualizer-download
29. A. C. Rufer, *Drug Discovery Today*, **26** (4), 875 (2021). https://doi.org/10.1016/j.drudis.2021.01.006
30. S. F. Sousa, P. A. Fernandes, M. J. Ramos, *Proteins: Structure, Function, and Bioinformatics*, **65** (1), 15 (2006). https://doi.org/10.1002/prot.21082
31. H. Zou, C. Yuan, L. Dong, R. S. Sidhu, Y. H. Hong, D. V. Kuklev, W. L. Smith, *Journal of Lipid Research*, **53** (7), 1336 (2012). https://doi.org/10.1194/jlr.M026856

Bulgarian Chemical Communications, Volume 58, Issue 2 (pp. 209-217) 2026 DOI: 10.34049/bcc.58.2.NCC05

Computational evaluation of bexarotene alkyl esters through DFT and molecular docking

N. A. Toshev[1*], I. R. Iliev[2], N. V. Agova[2], A. Abdollahi[3], S. F. Georgieva[2]

[1]*Medical University of Plovdiv, Faculty of Pharmacy, Department of Bioorganic Chemistry, 15A Vasil Aprilov Blvd., 4002 Plovdiv, Bulgaria*

[2]*Medical University Varna, Faculty of Pharmacy, Department of Pharmaceutical Chemistry, 84 Tsar Osvoboditel Blvd., 9000 Varna, Bulgaria*

[3]*Medical University of Plovdiv, Faculty of Medicine, 15A Vasil Aprilov Blvd., 4002 Plovdiv, Bulgaria*

Received: November 01, 2025; Revised: January 08, 2026

Bexarotene (Bex), a selective RXRα agonist approved by the U.S. Food and Drug Administration (FDA) for cancer treatment, is limited by poor aqueous solubility and suboptimal pharmacokinetic behavior. Structural modification *via* esterification with short-chain alcohols has been explored as a strategy to improve these properties. Methyl, ethyl, propyl, and butyl esters of Bex have been previously synthesized and characterized and they are commonly considered as potential prodrugs. However, existing data suggest that some of these derivatives may exhibit intrinsic biological activity or to hydrolysis, indicating a more complex pharmacodynamic profile. To further evaluate the suitability of esterification as a modification strategy, a comprehensive computational study was undertaken. Density Functional Theory (DFT) calculations at the B3LYP/6-311++G(d,p) level with implicit solvation (PCM) were employed to investigate the electronic properties of the esters, including descriptors such as HOMO–LUMO energy gap (ΔE), ionization potential (IP), electron affinity (EA), chemical hardness (η), chemical potential (μ), electronegativity (χ), electrophilicity index (ω), and maximum charge transfer index (ΔN max). Additionally, molecular docking simulations targeting the RXRα ligand-binding domain (PDB ID: 1FBY) were conducted to explore the binding potential and interaction profiles of the ester derivatives. The results provide insight into the molecular basis of receptor engagement and support a critical assessment of alkyl esterification as a rational strategy for enhancing the therapeutic profile of Bex. This theoretical framework offers a foundation for future design of bexarotene-based analogues and provides a conceptual basis for extending this approach beyond simple alkyl esters to include aryl derivatives.

Keywords: Bexarotene; alkyl esters; Density Functional Theory; molecular docking; RXRα; electronic descriptors

INTRODUCTION

Bexarotene (Bex) is a synthetic retinoid that selectively activates retinoid X receptors (RXRs) α, β, and γ, which act as transcription factors regulating genes involved in cellular differentiation, proliferation, apoptosis, and insulin sensitivity [1-3]. RXRs also form heterodimers with other nuclear receptors, contributing to their diverse biological functions [4-9]. The structural formula of Bex is shown in Fig. 1.

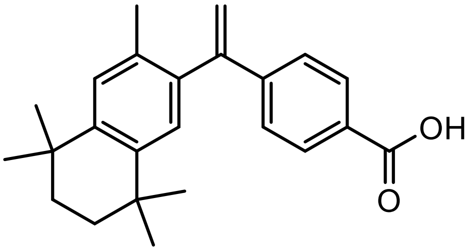

Figure 1. Structural formula of Bex.

Clinically, Bex is approved by the U.S. Food and Drug Administration (FDA) for the treatment of cutaneous T-cell lymphoma (CTCL) [4, 5, 9]. However, its therapeutic application is limited by poor aqueous solubility and suboptimal pharmacokinetic profile, both of which restrict its bioavailability and efficacy [9]. To overcome these limitations, various short-chain alkyl esters of Bex – methyl, ethyl, propyl, and butyl – have been synthesized and characterized.

The derivatives are frequently considered as potential prodrugs due to their ability to overcome the limitations associated with bexarotene. By modifying the chemical structure, these derivatives aim to improve pharmacokinetic properties, ultimately facilitating better absorption and target delivery in the treatment of the target receptors [10]. For the purpose of this study, they are denoted as E1 (methyl ester), E2 (ethyl ester), E3 (propyl ester), and E4 (butyl ester) throughout the text. The chemical structures of Bex alkyl esters are shown in Fig. 2.

---

* To whom all correspondence should be sent:
Email: *nikolay.toshev@mu-plovdiv.bg*

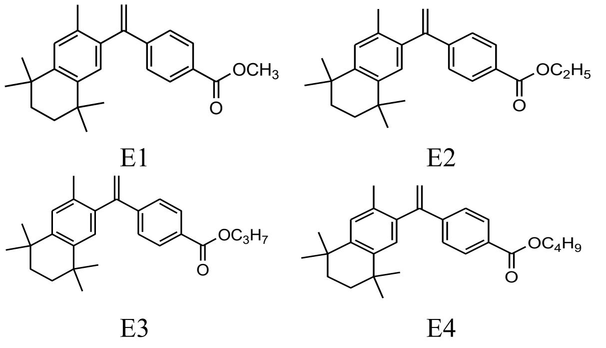

E1 E2 E3 E4

Figure 2. Chemical structures of Bex esters: E1 (methyl ester), E2 (ethyl ester), E3 (propyl ester), and E4 (butyl ester).

Although Bex has been extensively studied as a selective RXRα agonist, less is known about how esterification affects its electronic structure and receptor-binding potential. Understanding how alkyl substitution influences molecular reactivity and interaction with RXRα could support rational optimization of Bex derivatives.

Esterification is a well-established strategy for prodrugs that is often used to modify the lipophilicity, permeability, and pharmacokinetic behavior of bioactive compounds, including retinoids like bexarotene. While alkyl esters (such as methyl and butyl esters) are typically designed to undergo rapid enzymatic hydrolysis to release the parent drug, increasing evidence suggests that some ester derivatives can retain receptor affinity or exhibit measurable biological effects even before they are metabolized. These findings indicate that esterification does not always lead to pharmacologically inactive intermediates and may result in altered or additional pharmacodynamics properties. Therefore, computational approaches can be valuable tools for systematically assessing how esterification impacts molecular interactions and biological activity [11, 12].

In this study, we employed Density Functional Theory (DFT) and molecular docking analyses to investigate the relationship between electronic descriptors (HOMO–LUMO energy gap, electrophilicity index, dipole moment, etc.) and receptor affinity across the ester series. The aim was to determine whether computationally derived descriptors can predict biological performance and identify electronically favorable and pharmacologically relevant candidates for future development.

EXPERIMENTAL

Computational methodology -DFT study

The molecular orbitals Highest Occupied Molecular Orbital (HOMO) and Lowest Unoccupied Molecular Orbital (LUMO) were calculated using quantum chemistry methodology. All calculations were performed with the Gaussian 16 Rev. A.03 [13]. The combination between the B3LYP functional [14-16] and the 6-311++g (d, p) [17] basis set was chosen based on previous studies on carboxylic acids [18, 19]. The structures of the studied molecules were first optimized in the gas phase, and subsequently in water. All structures were optimized to a local minimum of potential energy, and no imaginary frequencies were found. PCM calculations in water ($\varepsilon = 78$) were applied to account for the effects of the solvation. The structures were visualized with the ChemCraft version 1.8.3 [20]. Global reactivity parameters that are derived from HOMO and LUMO energies provide additional interpretation of the results. Furthermore, data obtained from HOMO energies shed light on the molecule's capacity to act as an electron donor, while LUMO elucidates the potential as an electron acceptor. In this study, such descriptors as ionization potential ($IP = -E_{HOMO}$), electron affinity ($EA = -E_{LUMO}$), chemical potential ($\mu = 1/2\ (E_{LUMO} + E_{HOMO})$), Mulliken electronegativity ($\chi = -\mu$), chemical hardness ($\eta = ½\ (E_{LUMO} - E_{HOMO})$), softness ($\zeta = 1/\eta$), electrophilicity index ($\omega = \mu^2/2\eta$), and maximum charge transfer index (ΔN max) were calculated at the B3LYP/6-311+g(d,p) basis set for Bex and its alkyl esters in water.

Computational methodology - docking study

Ligand dataset preparation. Bex and its ester derivatives were selected as ligands for molecular docking with the human retinoid X receptor alpha (RXRα). The 3D structure of Bex was retrieved from the PubChem database [21]. The methyl and ethyl esters of Bex were obtained from the literature where they have been previously synthesized and characterized, while the propyl and butyl esters were generated in-house and structurally confirmed [10]. All ester derivatives were generated and converted into 3D structures using OpenBabel [22], followed by geometry optimization in Avogadro [23] with the MMFF94 force field. The optimized structures were saved in MOL2 format and further processed in AutoDock Tools [24], where polar hydrogens were added, Gasteiger charges were assigned, torsional degrees of freedom were defined, and ligands were saved in the PDBQT format for docking.

Reference ligand. 9-cis Retinoic acid, the natural ligand of RXRα, was included as a reference for validation of the docking protocol. Its 3D structure was obtained from the PubChem database (CID:

5282379), prepared using the same workflow as described for Bex and its esters.

Target protein preparation. The crystallographic structure of the human RXRα ligand-binding domain bound to 9-cis retinoic acid (PDB ID: 1FBY) [25] was retrieved from the RCSB Protein Data Bank [26]. Preprocessing was performed using UCSF ChimeraX [27], where chain B was removed due to its high structural similarity to chain A. All water molecules and non-standard residues were deleted. The protein was then imported into AutoDock Tools, where missing atoms were checked and repaired, polar hydrogens were added, Kollman charges were assigned, and atom types were set to AD4 specifications. The processed protein was saved in the PDBQT format for docking.

Flexible docking setup. To account for induced fit effects in the binding pocket, selected residues reported to be involved in ligand accommodation and stabilization within RXRα were defined as flexible: Phe313, Arg316, Ala271, Ala272, His435, Ile268, Ile345, Cys269, Ala327, Val342, and Cys432. The receptor side chains of these residues were allowed to rotate during docking, while the remaining protein was kept rigid.

Molecular docking protocol

Flexible docking simulations were carried out using AutoDock 4.2 with the Lamarckian Genetic Algorithm (LGA). The grid box was centered at coordinates x = 16.23, y = 27.27, z = 49.33 with dimensions of 60 × 60 × 60 points and a grid spacing of 0.375 Å, encompassing the entire ligand-binding pocket. Each docking run consisted of 100 independent LGA runs, with a population size of 300, a maximum of 25 000 000 energy evaluations, a mutation rate of 0.02, and a crossover rate of 0.8. Docked conformations were clustered using a root-mean-square deviation (RMSD) tolerance of 2.0 Å, and the lowest binding energy (ΔG) within the most populated cluster was selected as the representative binding pose.

Virtual screening analysis

Ligand–receptor interactions were examined in UCSF ChimeraX to evaluate binding orientation, hydrogen bonding, and hydrophobic contacts relative to the RXRα ligand-binding pocket. Two-dimensional interaction diagrams were generated using BIOVIA Discovery Studio Visualizer (Dassault Systèmes, San Diego, CA, USA) [28] to provide residue-level interpretation of binding interactions. Docking of 9-cis retinoic acid to RXRα served as internal validation of the docking protocol.

RESULTS AND DISCISSION

Density Functional Theory study

The optimized geometries of Bex and its alkyl esters, namely, the methyl (E1), ethyl (E2), propyl (E3), and butyl (E4) esters, are shown in Fig. 3.

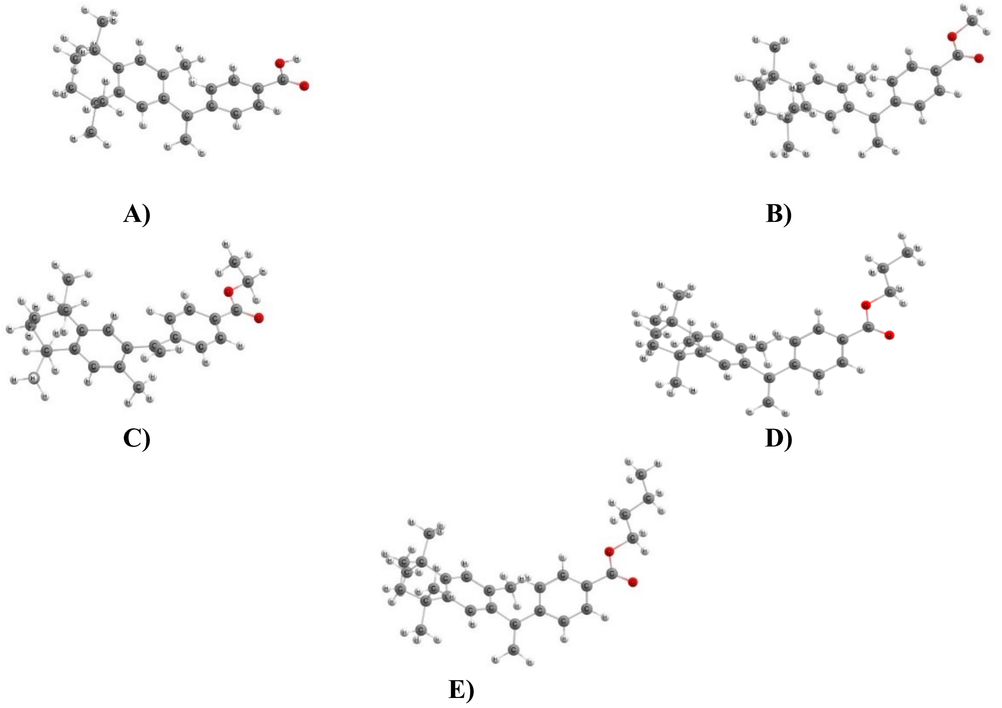

A) B) C) D) E)

Figure 3. B3LYP/6-311++g (d, p) optimized structures in water of: A) Bex, B) Bex methyl ester (E1), C) Bex ethyl ester (E2), D) Bex propyl ester (E3), E) Bex butyl ester (E4).

Table 1. Energies (in eV) of the HOMO and LUMO, energy gap ΔE, ionization potential (IP), electron affinity (EA), electronegativity (χ), chemical potential (μ), chemical hardness (η), chemical potential (μ), electrophilicity index (ω), maximum charge transfer index (ΔN max), and dipole moment (D) calculated using the B3LYP/6-311+g (d, p) basis set for Bex and its alkyl esters in water.

	E_{HOMO}	E_{LUMO}	ΔE	IP	EA	χ	η	μ	ζ	ω	ΔN max	Dipole moment
Bexarotene	-6.36	-2.12	4.24	6.36	2.12	4.24	2.12	-4.24	0.47	4.24	2.00	3.99
Methyl ester (E1)	-6.35	-2.02	4.32	6.35	2.02	4.32	2.16	-4.19	0.46	4.05	1.94	3.77
Ethyl ester (E2)	-6.34	-2.01	4.34	6.34	2.01	4.34	2.17	-4.18	0.46	4.02	1.93	3.87
Propyl ester (E3)	-6.34	-2.01	4.34	6.34	2.01	4.34	2.17	-4.17	0.46	4.02	1.93	3.96
Butyl ester (E4)	-6.34	-2.00	4.34	6.34	2.00	4.34	2.17	-4.17	0.46	4.01	1.92	3.87

HOMO and LUMO analysis. The frontier molecular orbital (HOMO and LUMO) analysis of Bex and its alkyl esters provides useful information about the electronic structure and reactivity. Moreover, the energy gap between HOMO and LUMO sheds light on chemical reactivity and kinetic stability. The smaller the gap, the greater the decrease in kinetic stability, and higher chemical reactivity, as opposed to a higher gap, whereby the molecules have higher kinetic stability and lower chemical reactivity [29]. The HOMO and LUMO data for Bex and its alkyl esters are shown in Table 1.

Bex exhibits the highest occupied molecular orbital (HOMO) energy of -6.36 eV and the lowest unoccupied molecular orbital (LUMO) -2.12 eV, having an energy gap of 4.24 eV. In comparison, the ester derivatives show slight upward shifts in both HOMO and LUMO energies. The methyl ester has a HOMO -6.35 eV and a LUMO around 2.03 eV, thus yielding a gap of 4.32 eV. Similar energy gap was calculated for ethyl ester (4.34 eV), propyl ester (4.34 eV), and butyl ester (4.34 eV). As a result, the substitution of the -COOH group with -COOR increases the frontier energy orbital energies and slightly widens the HOMO-LUMO gap. Notably, the increase in the gap is most pronounced from the acid to the methyl ester (0.08 eV), while further increases in the length of the chain from methyl to butyl give around 0.02 eV. As a result, increasing the carbon chain through its inductive effect, does not significantly influence reactivity and stability. From a reactivity standpoint, Bex is expected to have higher reactivity compared to esters, esters having greater kinetic stability. In the context of drug molecules or candidates, a reduced band gap means that Bex has an enhanced ability to interact with biological targets compared to the ester derivatives. These findings align with prior studies conducted that, with an analogous series of compounds, suggest molecules with the smallest HOMO-LUMO gap tend to exhibit the highest activity or reactivity. In the context of drug candidates, reduced energy gaps correlate with increased biological and pharmacological activity; these molecules can more easily undergo charge-transfer reactions or bind to biological targets [30].

DFT descriptors analysis.

Bex showed the highest ionization potential (6.36 eV) and electronegativity (4.24 eV), demonstrating greater electronic stability compared to its esters. The alkyl esters exhibit slightly reduced ionization potential (6.34-6.35 eV) and electron affinity (2.02-2.00 eV). Moreover, the ionization potential (IP) and electron affinity (EA) values computed from HOMO and LUMO energies use Koopmans' theorem, which operates on fixed geometries and excludes structural relaxation after electron addition or removal. This approximation is widely used in DFT studies for rapid descriptor analysis; however, geometry relaxation may be missed. For this purpose, we ran an additional DFT calculation for the Bex to evaluate this effect. The adiabatic IP and EA were 6.05 eV and 2.56 eV, respectively, from the total energy differences between Bex, cationic, and anionic species. Compared to the Koopmans-based values (IP=6.36 eV, EA=2.12 eV), the differences were small: ΔIP= 0.31 eV and ΔEA= 0.44 eV. These results suggest that relaxation effects, while present, do not significantly alter the electronic effects. Thus, Koopmans-derived values represent a good approximation for this system, although full relaxation for all derivatives may improve descriptor precision. Bex has the lowest hardness of the series (η=2.12 eV); while esters are slightly higher in the series (η=2.17 eV), contrary to the hardness, the softness of the esters is higher than that of Bex. As a result, these differences, albeit subtle, underline the fact that the free acid is the "softest", whereas the addition of alkyl substituents makes the molecules more rigid. Chemically, a softer molecule is more reactive, especially in polarizable interactions, while a harder molecule is more resistant to change [31]. Note that all these compounds have relatively high hardness (around 2 eV), which is a typical value for large conjugated organic molecules. From the perspective of chemical potential, which is negative to electronegativity, Bex is the most electrophilic, having negative chemical potential (-4.24 eV). The overall electronic stability is not significantly altered by esterification, supporting the idea that these modifications could be pharmacokinetically beneficial without severely affecting electronic potential.

The electrophilicity index (ω) describes a molecule's capacity to accept electron density and is linked with increased reactivity toward biological nucleophiles [31]. Weak electrophiles have an electrophilicity index $\omega < 0.8$ eV; moderate electrophiles have $0.8 < \omega < 1.5$; and strong electrophiles exhibit $\omega > 1.5$ eV [32]. Bex showed the highest value (4.24 eV), indicating a greater tendency to accept electrons compared to its ester derivatives. For the esters, the values were almost equal (4.01 – 4.05 eV), revealing that no remarkable change in electrophilicity index character is caused by esterification. This stability demonstrates that ester derivatives continue to exhibit enhanced reactivity towards biological nucleophilic targets. However, their stability suggests that they may be less reactive in biological pathways until they are metabolized.

The maximum charge transfer index (ΔN max) slightly decreased from Bex (2.00) to its butyl ester, indicating a small decrease in electron-donating capacity upon esterification. As a result of alkyl substitution, charge transfer potential is lowered, but all derivatives retain sufficient ability to engage in donor-acceptor interactions with biomolecular targets.

In terms of dipole moment, Bex demonstrated the largest dipole moment (3.99 D), showing a greater potential for solvation and polar reactions. The esters exhibited similar dipole moments (3.78-3.96 D), with propyl ester (3.96 D) closely matching with the parent molecule. This consistency confirms that polarity is well preserved during esterification, which is beneficial for maintaining solubility and interaction with polar residues in the RXRα binding site.

Overall, the DFT results indicate that esterification of Bex slightly increases the HOMO–LUMO gap without significantly altering its core electronic distribution. The large conjugated π-system common to all molecules dominates their electronic behavior, while ester substitution exerts only a minor local effect on frontier orbital energies and global reactivity parameters. This preservation of electronic features suggests that the alkyl esters may retain comparable electron density distribution and reactivity patterns to the parent compound, which is consistent with their potential to participate in similar molecular interactions or undergo metabolic conversion to Bex. This study used DFT calculations with the PCM implicit solvent model, which calculates solvent effects but does not account for individual hydrogen bonding interactions between the studied molecules and water. Note that this limitation may slightly affect the accuracy of descriptors, especially for more polar compounds. Modeling explicit water interactions enhances accuracy, but it is computationally demanding.

Molecular docking study

System preparation and method validation. The protein structure of the human RXRα ligand-binding domain (PDB ID: 1FBY) was prepared for docking by retaining only chain A, while chain B was removed due to its structural identity. Since both chains share an identical ligand-binding site, excluding chain B avoided redundancy and reduced computational complexity.

A set of key residues within the binding pocket was treated as flexible during docking to allow for more accurate modeling of ligand–receptor interactions. These included Phe313, Arg316, Ala271, Ala272, His435, Ile268, Ile345, Cys269, Ala327, Val342, and Cys432 which have been identified from the crystal structure and supported by literature data as critical for ligand recognition and stabilization [25].

To validate the docking protocol, a redocking experiment was performed using the reference ligand 9-cis retinoic acid, which is co-crystallized with 1FBY. The redocked pose yielded an RMSD of 3.14 Å compared to the crystallographic conformation, indicating acceptable reproducibility of the method.

Docking energy results. A summary of the docking outcomes for Bex, its ester derivatives, and the reference ligand 9-cis retinoic acid is presented in Table 2. The table reports the calculated binding free energy (ΔG), estimated inhibition constant (Ki), intermolecular energies, and torsional penalties for each ligand.

When comparing the docking results, all Bex esters exhibited stronger predicted binding affinities than the parent compound. Among them, the ethyl ester derivative showed the most favorable

Table 2. Docking results for Bex, its ester derivatives, and 9-cis retinoic acid with RXRα (PDB ID: 1FBY).

Parameter	Ref.	Bex	E1	E2	E3	E4
RMSD from reference structure, Å	3.14	55.112	54.656	54.595	54.703	59.276
Estimated free energy of binding (ΔG), kcal/mol	-10.64	-12.45	-13.25	-13.66	-13.40	-10.86
Estimated inhibition constant (Ki, 298.15 K)	15.96 nM	746.19 pM	194.74 pM	96.53 pM	149.85 pM	10.91 nM
Final intermolecular energy, kcal/mol	-12.43	-13.64	-14.44	-15.15	-15.19	-12.95
Ligand–fixed receptor, kcal/mol	-7.22	-5.06	-7.40	-7.99	-7.62	-7.88
- vdW+H-bond+desolvation, kcal/mol	-7.13	-4.94	-7.39	-7.96	-7.- 63	-7.88
- Electrostatic, kcal/mol	-0.09	-0.12	-0.01	-0.03	+0.02	0.00
Ligand–flexible residues, kcal/mol	-5.21	-8.58	-7.04	-7.16	-7.58	-5.07
- vdW+H-bond+desolvation, kcal/mol	-5.15	-7.89	-6.86	-7.00	-7.52	-5.07
- Electrostatic, kcal/mol	-0.05	-0.70	-0.18	-0.17	-0.06	0.00
Final total internal energy, kcal/mol	-8.98	-5.11	-10.53	-10.85	-9.70	-6.74
Ligand internal energy, kcal/mol	-1.18	-0.83	-0.84	-0.99	-0.94	-1.10
Ligand–fixed receptor, kcal/mol	-6.79	-3.59	-8.56	-8.43	-7.33	-6.28
Ligand–flexible residues, kcal/mol	-1.01	-0.70	-1.13	-1.42	-1.43	+0.64
Torsional free energy, kcal/mol	+1.79	+1.19	+1.19	+1.49	+1.79	+2.09
Unbound system energy, kcal/mol	-8.98	-5.11	-10.53	-10.85	-9.70	-6.74

interaction profile, with a binding free energy of -13.66 kcal/mol and the lowest inhibition constant (Ki = 96.53 pM), surpassing both Bex and the reference ligand 9-cis retinoic acid.

A clear trend was observed: increasing the length of the alkyl chain enhances hydrophobic interactions within the binding pocket, leading to more favorable intermolecular energies. However, this effect is counterbalanced by a progressive rise in the torsional free energy penalty, particularly for the longer-chain propyl and butyl esters. This indicates a trade-off between stability and conformational flexibility, with the ethyl ester providing the optimal balance.

The RMSD values for Bex and its ester derivatives were considerably higher than for 9-cis-retinoic acid, which can be attributed to the greater structural complexity and conformational flexibility of the polyaromatic framework of these molecules. Unlike the relatively rigid single-ring structure of the reference ligand, the extended and branched skeletons of Bex analogues allow multiple low-energy conformations, resulting in broader RMSD distributions during docking.

Interaction analysis (2D complexes)

The main intermolecular interactions between RXRα and all ligands were visualized using 2D interaction diagrams generated with Discovery Studio Visualizer, as shown in Figure 4. The docking poses revealed a consistent set of interactions between Bex and its ester derivatives with the RXRα binding pocket. Several key residues were identified as crucial for ligand stabilization:

- Hydrophobic and π-alkyl contacts: Phe313, Leu309, Ile268, Val342, Cys269, and Cys432 contributed significantly to the hydrophobic stabilization of the ligand.
- Hydrogen bonds: observed predominantly with Arg316 and Ala327, which were particularly evident in the methyl and ethyl ester derivatives, strengthening their binding affinity.
- π–Sulfur interactions: involving Cys269 and Cys432, further stabilized the aromatic core of the ligands and reinforced their orientation within the binding cavity.

A comparative analysis of the derivatives highlighted distinct patterns:

- Methyl and ethyl esters displayed enhanced hydrogen bonding capacity along with well-positioned hydrophobic interactions, resulting in superior binding profiles.
- Propyl and butyl esters demonstrated stronger hydrophobic contacts due to their extended alkyl chains, but this was counterpoised by a higher torsional energy penalty, reflecting reduced conformational efficiency.

When compared with the reference ligand 9-cis retinoic acid, both Bex and its esters demonstrated more extensive hydrophobic contacts. Although 9-cis retinoic acid engaged in hydrogen bonding, its overall weaker hydrophobic interactions accounted for the less favorable binding free energy and higher inhibition constant (Ki = 15.96 nM).

SAR analysis

The docking results provide valuable insights into the structure–activity relationship (SAR) of Bex and its ester derivatives. The carboxyl group of the parent compound enables strong ionic and hydrogen-bonding interactions; however, upon esterification, this capacity is reduced. Instead, the ester derivatives benefit from enhanced hydrophobic contacts within the binding cavity, leading to lower binding free energies (ΔG).

Increasing the length of the alkyl chain further strengthens hydrophobic interactions, which is reflected in the improved binding affinities of the methyl, ethyl, and propyl esters compared to the parent ligand. Nevertheless, this effect appears to have a limit: the butyl ester did not exceed the ethyl derivative, suggesting that excessive chain elongation introduces steric strain and higher torsional penalties, diminishing the overall benefit. Taken together, the results confirm that small to medium-sized ester substitutions are optimal for improving the binding affinity of Bex analogues toward RXRα, balancing hydrophobic stabilization with conformational flexibility.

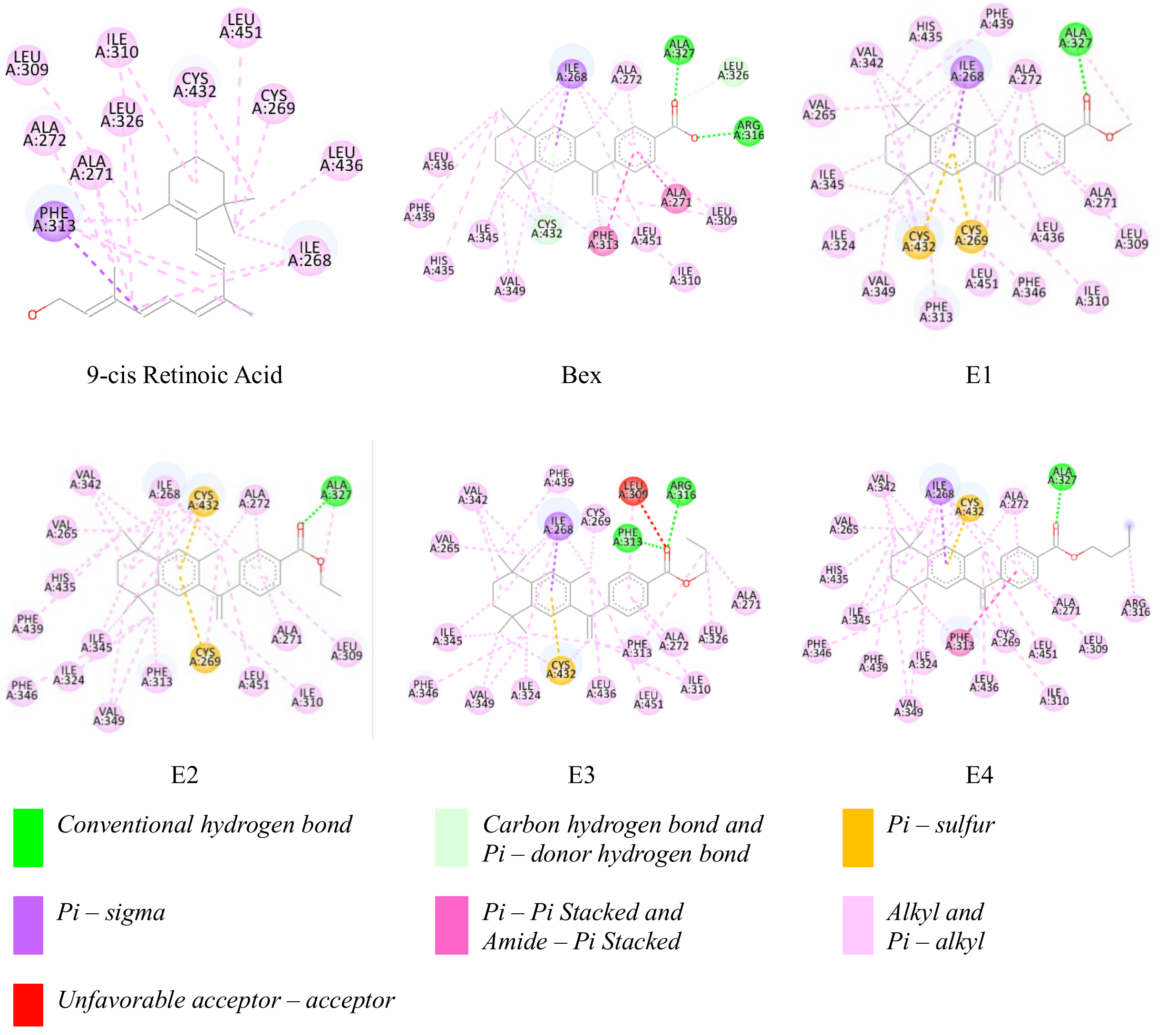

9-cis Retinoic Acid

Bex

E1

E2

E3

E4

Figure 4. Two-dimensional interaction diagrams of the RXRα–ligand complexes showing key amino acid contacts for 9-cis retinoic acid (Ref), Bexarotene, and its methyl (E1), ethyl (E2), propyl (E3), and butyl (E4) esters. Hydrophobic interactions, hydrogen bonds, and π–sulfur contacts are indicated by standard color codes and symbols as generated by Discovery Studio Visualizer.

Biological interpretation

The markedly lower inhibition constants (Ki) observed for the ester derivatives—within the picomolar range – compared to the nanomolar affinity of 9-cis retinoic acid highlight their potential as highly potent RXRα ligands.

These findings suggest that Bex esters may serve as alternative RXRα agonists with improved binding capabilities relative to both the parent compound and the endogenous reference ligand. Their enhanced hydrophobic stabilization within the receptor's binding pocket supports the hypothesis of stronger and more sustained receptor activation.

Furthermore, the ester derivatives may function as prodrugs, undergoing metabolic hydrolysis to regenerate the active carboxylic acid form of Bex *in vivo* [10]. This dual mechanism – direct receptor engagement by the ester and potential conversion to the acid – could provide therapeutic advantages, such as modulated pharmacokinetics and improved bioavailability.

CONCLUSION

Based on density functional theory and docking calculations, a systematic theoretical study of Bex and its alkyl esters has been carried out. Esterification of Bex leads to increased HOMO-LUMO energy gaps (4.32-4.34 eV), indicating decreased electronic reactivity of the esters compared to Bex. Nevertheless, this shows that esterification does not produce a significant effect on the electronic properties or the overall electron density distribution of esters. The dipole moments were consistent throughout the series, with Bex having a slightly higher polarity (3.99 D) compared to its methyl (3.78 D) and ethyl (3.87 D) esters. Among the derivatives, the ethyl ester displayed a dipole moment, chemical softness, and ionization energy, closely aligning to Bex. Despite lower reactivity, docking studies revealed enhanced RXRα binding for all esters, especially the ethyl ester, which exhibited the strongest binding affinity (-13.66 kcal/mol, Ki=96.53 pM). These results indicate that improved binding is related not only to polarity or electrophilicity index, but also to favorable hydrophobic interactions and optimal ligand flexibility. The moderate electrophilicity index (4.02 eV), along with preserved polarity and improved docking performance, highlights ethyl ester as a promising lead compound. Note that the large conjugated system that is common for all studied molecules is predominant in the electronic structure compared to the possible carboxylic group modification, thus affecting the behavior of these molecules in a biological context. The combined DFT study and docking analyses suggest that Bex ethyl ester may offer improved receptor engagement, supporting its potential as an optimized RXRα ligand that retains essential electronic features of the parent molecule while exhibiting physicochemical properties consistent with possible metabolic interconversion to Bex. However, these computational predictions require experimental validation, and further *in vitro* RXR binding assays will be essential to confirm the observed trends and assess their biological significance.

Acknowledgement: *The research that led to these results was carried out using the infrastructure purchased under the national Roadmap for RI financially coordinated by the MES of the Republic of Bulgaria (grant № D01-98/26.06.2025). The computation was performed by shared resource with GAUSSIAN 16 by project KP-06-N59/7(project leader Vassil Delchev).*

REFERENCES

1. K. Tomita, K. Nakashima, E. Yamaguchi, A. Itoh, K. Tsutsumiuchi, M. Inoue, *Mol. Pharmacol.*, **107** (8), 100057 (2025).
2. F. Lalloyer, C. Fiévet, S. Lestavel, G. Torpier, J. van der Veen, V. Touche, S. Bultel, A. Tailleux, *Arterioscler. Thromb. Vasc. Biol.*, **26** (12), 2731 (2006).
3. M. Certo, Y. Endo, K. Ohta, S. Sakurada, G. Bagetta, D. Amantea, *Pharmacol. Res.*, **102**, 298 (2015).
4. L. T. Farol, K. B. Hymes, *Expert Rev. Anticancer Ther.*, **4** (2), 180 (2004).
5. L. Qu, X. Tang, *Cancer Chemother. Pharmacol.*, **65** (2), 201 (2010).
6. H. Cao, R. Bissinger, A. T. Umbach, M. Gawaz, F. Lang, *Cell. Physiol. Biochem.*, **42** (2), 838 (2017).
7. T. W. Hermann, W.-C. Yen, P. Tooker, B. Fan, K. Roegner, A. Negro-Vilar, W. W. Lamph, R. P. Bissonnette, *Lung Cancer*, **50** (1), 9 (2005).
8. C. Hacioglu, F. Kar, S. Kacar, V. Sahinturk, G. Kanbak*Med. Oncol.*, **38**, 31 (2021).
9. A. Mahajan, L. Singh, G. Singh, R. K. Dhawan, M. Kaur, P. K. Malhi, K. Thakur, L. Kaur, An evidence-based review on bexarotene, *Tumor Discov.*, **2** (2), 0436 (2023).
10. I. Iliev, S. Georgieva, *Bulg. Chem. Commun.*, **56** (Spec. Issue D1), 77 (2024).
11. J. B. Lee, A. Zgair, J. Malec, T. H. Kim, M. G. Kim, J. Ali, C. Qin, W. Feng, M. Chiang, X. Gao, G. Voronin, A. E. Garces, C. L. Lau, T.-H. Chan, A. Hume, T. M. McIntosh, F. Soukarieh, M. Al-Hayali, E. Cipolla, H. M. Collins, D. M. Heery, B. S. Shin, S. D. Yoo, L. Kagan, M. J. Stocks, T. D. Bradshaw, P. M. Fischer, P. Gershkovich, *Journal of Controlled Release*, **286**, 10 (2018).
12. K. Beaumont, R. Webster, I. Gardner, K. Dack*Current Drug Metabolism*, **4** (6), 461 (2003)

13. M. J. Frisch, G. W. Trucks, H. B. Schlegel, G. E. Scuseria, M. A. Robb, J. R. Cheeseman, G. Scalmani, V. Barone, G. A. Petersson, H. Nakatsuji, X. Li, M. Caricato, A. V. Marenich, J. Bloino, B. G. Janesko, R. Gomperts, B. Mennucci, H. P. Hratchian, J. V. Ortiz, A. F. Izmaylov, J. L. Sonnenberg, D. Williams, F. Ding, F. Lipparini, F. Egidi, J. Goings, B. Peng, A. Petrone, T. Henderson, D. Ranasinghe, V. G. Zakrzewski, J. Gao, N. Rega, G. Zheng, W. Liang, M. Hada, M. Ehara, K. Toyota, R. Fukuda, J. Hasegawa, M. Ishida, T. Nakajima, Y. Honda, O. Kitao, H. Nakai, T. Vreven, K. Throssell, J. A. Montgomery Jr., J. E. Peralta, F. Ogliaro, M. J. Bearpark, J. J. Heyd, E. N. Brothers, K. N. Kudin, V. N. Staroverov, T. A. Keith, R. Kobayashi, J. Normand, K. Raghavachari, A. P. Rendell, J. C. Burant, S. S. Iyengar, J. Tomasi, M. Cossi, J. M. Millam, M. Klene, C. Adamo, R. Cammi, J. W. Ochterski, R. L. Martin, K. Morokuma, O. Farkas, J. B. Foresman, D. J. Fox, Gaussian 16 Rev. C.01, Gaussian, Inc., Wallingford CT, 2016.
14. A. D. Becke, *J. Chem. Phys.*, **98**, 5648 (1993).
15. A. D. Becke, *J. Chem. Phys.*, **104**, 1040 (1996).
16. C. Lee, W. Yang, R. G. Parr, *Phys. Rev. B*, **37**, 785 (1988).
17. R. Krishnan, J. S. Binkley, R. Seeger, J. A. Pople, Self-consistent molecular orbital methods. XX. A basis set for correlated wave functions, *J. Chem. Phys.*, **72**, 650 (1980).
18. M. Karabacak, Z. Cinar, M. Kurt, S. Sudha, N. Sundaraganesan, *Spectrochim. Acta A Mol. Biomol. Spectrosc.*, **85** (1), 179 (2012).
19. T. Kaweetirawatt, Y. Kokita, S. Iwai, M. Sumimoto, K. Hori, *Chem. Phys. Lett.*, **547**, 97 (2012).
20. Chemcraft—graphical software for visualization of quantum chemistry computations, Version 1.8 (Build 682), Chemcraft, 2010.
21. National Center for Biotechnology Information (NCBI), U.S. National Library of Medicine, available at: https://www.ncbi.nlm.nih.gov/
22. N. M. O'Boyle, M. Banck, C. A. James, C. Morley, T. Vandermeersch, G. R. Hutchison, *J. Cheminform.*, **3**, 33 (2011).
23. M. D. Hanwell, D. E. Curtis, D. C. Lonie, T. Vandermeersch, E. Zurek, G. R. Hutchison, *J. Cheminform.*, **4**, 17 (2012).
24. G. M. Morris, R. Huey, W. Lindstrom, M. F. Sanner, R. K. Belew, D. S. Goodsell, A. J. Olson, *J. Comput. Chem.*, **30**, 2785 (2009).
25. P. F. Egea, A. Mitschler, N. Rochel, M. Ruff, P. Chambon, D. Moras, *EMBO J.*, **19**, 2592 (2000).
26. RCSB Protein Data Bank (RCSB PDB), U.S. National Library of Medicine, available at: https://www.rcsb.org/
27. R. J. Read, E. F. Pettersen, A. J. McCoy, T. I. Croll, T. C. Terwilliger, B. K. Poon, E. C. Meng, D. Liebschner, P. D. Adams, *Acta Crystallogr. D: Struct. Biol.*, **80**, 588 (2024).
28. U. Baroroh, Z. S. Muscifa, W. Destiarani, F. G. Rohmatullah, M. Yusuf, *J. Comput. Biol.*, **2**, 22 (2023).
29. K. Fukui, S*cience*, **218**, 747 (1982).
30. S. K. Misra, G. Ghoshal, M. R. Gartia, Z. Wu, A. K. De, M. Ye, C. R. Bromfield, E. M. Williams, K. Singh, K. V. Tangella, *ACS Nano*, **9**, 10695 (2015).
31. R. G. Parr, R. G. Pearson, *J. Am. Chem. Soc.*, **105**, 7512 (1983).
32. L. R. Domingo, M. J. Aurell, P. Pérez, R. Contreras, *Tetrahedron*, **58**, 4417 (2002).

Bulgarian Chemical Communications, Volume 58, Issue 2 (pp. 218-225) 2026 DOI: 10.34049/bcc.58.2.NCC06

Deposition of zinc nanoparticles on woolen substrates in footwear

D. I. Zheleva*, D. S. Angelova

Department Textile, Leather and Fuels, University of Chemical Technology and Metallurgy, Sofia, Bulgaria

Received: December 23, 2025; Revised: March 04, 2026

In footwear, especially winter footwear, lining and insoles are made of woolen materials. Owing to to their organic origin and exposure to moisture and temperature, these materials are susceptible to microbial attack. It is known that ZnO nanoparticles exhibit excellent antibacterial activity.

In our study, several methods were applied to deposit zinc nanoparticles on the surface of wool substrates. The particles were synthesized *in situ* on a film of cross-linked collagen hydrogel. The wool samples were modified using three different methods, varying the sequence of component addition and reaction conditions to achieve uniform distribution and dispersion of the synthesized particles. In one method, ultrasonication was applied.

Microscopic analyses showed that ultrasonic treatment of the samples improves the distribution of zinc particles on the surface and within the substrate. It was found that for the physico-mechanical properties, a change in color fastness is observed compared to the control sample, i.e., darkening of the surface. In terms of vapor-air properties, the best results were again registered for the ultrasonically treated samples, in which an increase in water vapor absorption and a slight decrease in the vapor permeability coefficient were observed. The obtained experimental data are promising for antibacterial activity; however, for a more comprehensive characterization of the obtained composites, antimicrobial studies are necessary.

Keywords: wool, antibacterial modification, ZnO nanoparticles, footwear

INTRODUCTION

Footwear is a complex composite consisting of many different in nature details that must be connected, providing the shoe with reliability, durability, comfort, and elasticity. Of great importance is the choice of materials for the footwear, especially for the inner details. Insoles and lining details, especially in winter footwear, are often made of woolen materials. Prolonged wearing of shoes creates prerequisites for bacterial and fungal diseases. To protect the foot from microbial attack, it is also extremely important that the materials have undergone a certain antibacterial treatment.

The unique properties of wool include its complex morphology with multilayered cuticle and cortex, the keratin proteins in wool, which contribute to its chemical resistance, strength, moisture permeability, and porosity. Its diverse functional groups facilitate various binding mechanisms, making it suitable for nanoparticle functionalization and enabling the production of fabrics with antimicrobial, self-cleaning, and UV-protective properties. Additionally, as a protein fiber, wool contains active groups such as amide, disulfide, and carboxyl, which can reduce metal salts to form nanoparticles [1].

The treatment of wool with metal salt solutions gives rise to metal ions interaction. The attained wool properties depend on the type of interacting metal ions, the conditions of treatment, and the metal salt concentration. The free carboxyl groups of wool are considered to be the binding sites over a wide range of pH values. Several reactions of metal ions with wool effectively improved its antibacterial properties, flame resistance, shrinkage, abrasion, wrinkle recovery, dye ability, deodorizing [2].

ZnO is widely used as an antimicrobial agent. The antibacterial mechanisms of ZnO NPs are as follows: integrated cell destruction due to direct contact of ZnO with the cell wall, release of antimicrobial ions, mainly Zn^{2+} ions, ROS formation, and photoconductivity [3].

The surface layer of wool fibers has a scale structure that provides good insulation and hygroscopic properties. However, this structure also makes wool prone to absorbing moisture in humid environments, creating ideal conditions for mold and bacteria growth. Functional finishing of wool fabrics currently emphasizes on antimicrobial treatment, with Ag nano-ions, chitosan, lysozyme, and natural dyes being the most commonly applied agents to achieve antimicrobial effects [4].

Several physical and chemical methods including microwave-assisted, sol–gel, and hydrothermal methods have been established to prepare nano-ZnO.

---

* To whom all correspondence should be sent:
Email: *darinajeleva@abv.bg*

Zinc acetate, zinc sulfate, and zinc nitrate are the most common precursors used as a Zn source. The sol–gel consequential precipitates are usually requiring post-heat treatment to induce crystallization that frequently gives rise to particle agglomeration and grain growth. In contrast, ultrasound has been established as an accomplished and environmentally friendly technique for synthesis of novel materials at low temperature and short time. The effect of ultrasound in enhancing the kinetics of chemical reactions is related to the creation of highly reactive free radicals such as O^-, OH^-, HO_2^- due to the temporary cavitation bubble collapse caused by the ultrasound wave [5].

In situ synthesis of nano-ZnO is an alternative pathway towards durable finishing. The durability of the incorporated properties can also be improved by adding suitable chemicals, which will form covalent or ionic bonds between the host substrate (textiles) and the used NPs. This study employs a novel *in situ* approach to synthesize ZnO nanoparticles by utilizing wool, silane, and a capping agent [6]. These agents help binding ZnO nanoparticles more strongly to the wool surface.

Functional coatings aim to enhance the properties and performance of textile substrates, as well as to introduce new textile functions. To this end, different classical and contemporary organic, organic-inorganic hybrid, and inorganic compounds are used in application processes. Among the latter compounds, ZnO has already been established as a chemical agent for textile functionalization because of its unique physical and chemical properties, environmental friendliness, biocompatibility, and low price [7].

For improvement of the mechanical properties of medical textiles, polyethylene wax emulsion is added to nano-ZnO. It is an agent that forms a flexible film on the fabric surface, making the fabric soft with a smooth coating and improving its mechanical properties. Excellent and encouraging results have been found for antibacterial activity [8].

Amidoxime-functionalized wool fibers loaded with nano-ZnO were successfully prepared by *in situ* coprecipitation and radiation-induced copolymerization. Wool-AO@ZnO showed excellent antimicrobial properties to aerobic bacteria, anaerobic bacteria, and fungi [9].

The padding method has been used for the treatment of dyed cotton and wool fabrics with ZnO, TiO_2 and CuO to impart functional properties such as antimicrobial, self-cleaning, and UV blocking properties [10].

Antimicrobial finishing prevents microbial attack on wool and prolongs its useful life. There are different ways to prevent the attachment of microorganisms to fiber surface, using aromatic halogen compounds, organometallic salts, quaternary ammonium salts, iodophors, phenols, urea and its related compounds (i.e., formaldehyde derivatives), amines and silver nanoparticles. Natural products such as chitin derivatives and their protonated amino groups on the glucose ring are also used. The goal of these studies [11] is to develop an approach to imparting bioactive features to wool macromolecules by incorporating functional groups such as carboxylic groups, into fibers before the treatment with appropriate antibiotics. Carboxylic groups were incorporated into wool fabric by grafting acrylic acid chemically initiated with hydrogen peroxide and metallic ions (e.g., Cu^{2+}) and post-treatment with two antibiotics: neomycin (Ne) and tetracycline hydrochloride (Te) to obtain antibacterial fibers active to Gram-positive and Gram-negative microorganisms (*Staphylococcus aureus*, *Escherichia coli* and *Pseudomonas aeruginosa*). This was confirmed by measuring the zones of inhibition of wool fabric treated with the abovementioned antibiotics under various conditions. Higher temperature enhanced sorption rate to wool grafted with acrylic acid. There is a correlation between the sorption percentage and size of inhibition zone, depending on the type of added antibiotics [11].

In our previous studies, we synthesized and applied TiO_2 nanoparticles in coatings for leather materials [12]. Based on these investigations, in the present study, we decided to develop formulations for the synthesis and application of ZnO nanoparticles on wool substrates in a similar manner. Consequently, the present study aims to develop methods for modifying wool fabrics with ZnO for use in shoe linings by improving the functional properties and potentially provide antibacterial protection capabilities. For the first time, an *in situ* method was applied for depositing zinc oxide particles in a cross-linked gelatin hydrogel coating on a wool substrate. This method aims to improve the fixation of particles in the wool fabric. An ultrasonic approach was also applied to improve the dispersion and the uniform distribution of particles.

METHODS AND ANALYSES

Materials

Wool samples from a local upholstery materials producer - industrial wool, 100% wool felt sheet with specifications of 3.3 mm thickness and 250 g/mm^3 density were used. Square samples, each measuring 50×50 mm in dimensions and weighing approximately 2.6 g, were carefully prepared. The chemical reagents employed in the study consisted of zinc nitrate hexahydrate ($Zn(NO_3)_2 \cdot 6H_2O$, CAS: 10196-18-6), sodium hydroxide (NaOH, Sigma-Aldrich, Darmstadt, Germany), a 25% aqueous solution of glutaraldehyde (Sigma-Aldrich, Darmstadt, Germany), and gelatin (CAS: 9000-70-8, Merck KGaA, Darmstadt, Germany). Distilled water was used as the solvent for all prepared solutions.

Methods for preparation of composite materials

ZnO nanoparticles were deposited and fixed to the wool substrate using a cross-linked gelatin hydrogel. The ZnO particles were synthesized *in situ* and deposited on the gelatin film. Modification of wool samples was performed with glutaraldehyde - cross-linked gelatin. The synthesis of ZnO nanoparticles was carried out by varying the components and processing conditions (Fig. 1).

The processing of the first sample PW ZnO_1 involved initial pre-treatment of the wool with 2% oxalic acid ($H_2C_2O_4$) followed by immersion in a 5% gelatin solution and final cross-linking with 1,5% glutaraldehyde. The next stage of the processing was with a solution of zinc nitrate hexahydrate (0.1M) and sodium hydroxide (1M), followed by heat treatment and dehydration. The complete processing sequence included: 30 min treatment at room temperature, 24 h conditioning at 23°C, heat treatment for 30 min at 85°C, 5 min treatment at 55°C, dehydration in a dryer for 2 h at 85°C and final drying phase of 96 h at room temperature.

Fot the second sample PW ZnO_2 a comparable methodology was used, starting with immersion of the wool sample in a gelatin solution, followed by treatments with $Zn(NO_3)_2 \cdot 6H_2O$, glutaraldehyde, and NaOH. The heat treatment and dehydration steps were the same as in the previous method.

The third sample PW ZnO_3 was treated in an ultrasonic bath. The wool samples were first immersed in a gelatin solution, then in the mixed solution of $Zn(NO_3)_2 \cdot 6H_2O$ and NaOH, followed by addition of glutaraldehyde.

ANALYSES

Analyses of specimen thickness, air permeability, absorption, abrasion resistance, microscopic observations, and photoluminescence were performed in the study to characterize the deposition of zinc oxide particles on wool fibers and study their influence on permeability and physico-mechanical responses of wool fibers after such modification.

Thickness and weight

The ASTM D1777 standard test was used to measure the thickness of a textile sample. A digital gauge was used for this test [13].

Vapor absorption and water vapor permeability

Equipment used for evaluating water vapor permeability was SATRA STM 473, England. Water vapor absorption and water vapor permeability were calculated by formulas 1 and 2, respectively [14, 15]:

$$W_1 = \frac{m_2 - m_1}{a} \quad (1)$$

where: W_1 – water vapor absorption [mg/cm^2]; m_1 - initial mass [g]; m_2 – mass after testing [g]; a - test surface [cm^2].

$$W_3 = \frac{m_2 - m_1}{a.t} \quad (2)$$

where: W_3 – water vapor permeability [$mg/cm^2.h$]; m_1 - initial mass [g]; m_2 – mass after testing [g]; a - test surface [cm^2]; t - test time [h].

Water absorption insoles [16]

$$W_A = (M_P - M_0)/A$$

where: W_A– absorption [g/m^2]; M_P –final mass [g]; M_0 –initial mass [g]; A - area [m^2].

Water desorption insoles [16]

$$W_p = \frac{M_F - M_R}{M_F - M_0} \times 100$$

where: W_p – desorption [%]; M_F –final mass [g]; M_R – mass after conditioning for 24 h [g].

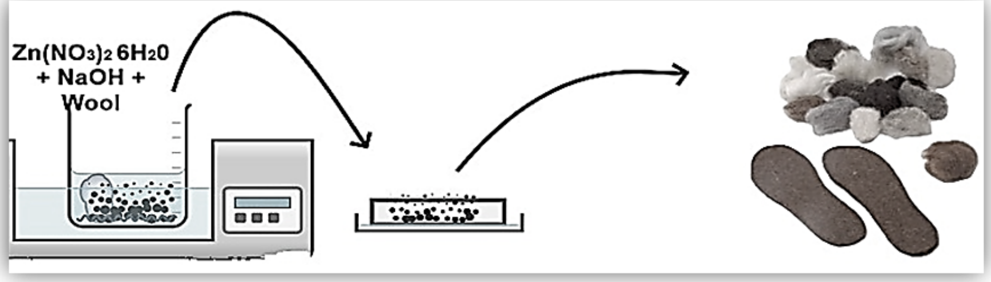

Fig. 1. Preparation of wool samples with ZnO coatings

Abrasion resistance

A test method was used to determine the abrasion resistance of insoles irrespective of the material. After 400 cycles of friction with the accompanying fabric, a visual evaluation was made against the uneraded material of the test specimen [17].

Color coordinates and color difference

The color changes of the samples, the intermediate values of L*, a* and b* and the color differences (E*) were determined using a reflectance spectrophotometer (UVA/VIS/NIR Lambda 750S Perkin Elmer, in the wavelength range λ=800 ÷ 340 nm) with a D 65 light source and a 10° viewing angle. Chromatogram of all colors visible to the human eye on an x/y grid and assigning a numerical value allows us to make uniform measurements and comparisons between colors. All measurements and calculations were made according to CIELAB: 1973.

Equipment used to assess the degree of damage and color transfer on the surface of the material during mild dry or wet abrasion was Satra STM 421. Grey scales corresponding to ISO 105-A02 and ISO 105-A03, respectively, were used to assess the color changes and the degree of staining, according to method B, EN ISO 17700 [18].

Microscopic and fluorescence analyses

Samples were observed using an inverted microscope Metaval (Carl Zeiss, Germany) operated in the dark-field mode with Planachromat-HD objectives (at magnification from 5× to 50×) and halogen light illumination (12V, 50W). A microfluorimeter was adapted to the microscope for fluorescence spectroscopy studies.

UVA – VIS - NIR transmittance spectral analyses

A spectrophotometer (UVA/VIS/NIR Lambda 750S, Perkin Elmer, USA) was used to perform the analysis which covered the wavelength range from λ 2000 to 250 nm.

RESULTS AND DISCUSSION

Thickness and weight

The results of the thickness ($\bar{t}$) and mass (m_2) measurements of the wool samples before and after coating are shown in Table 1. The values are presented as mean ± instrumental error.

Thickness and mass measurements before and after coating showed that ZnO-based layers were successfully deposited on the wool samples. While all samples showed an increase in mass and thickness, the effect was most pronounced for PW ZnO_2.

Table 1. Thickness and weight of the tested wool samples

Sample name	m_1, g	m_2, g	$\bar{t}$, mm
Zero sample	2.6 ± 0.1	2.6 ± 0.1	3.32 ± 0.12
PW ZnO_1	2.6 ± 0.1	3.2 ± 0.1	3.72 ± 0.12
PW ZnO_2	2.6 ± 0.1	3.5 ± 0.1	3.75 ± 0.13
PW ZnO_3	2.6 ± 0.1	3.1 ± 0.1	3.74 ± 0.13

For sample PW ZnO_3 the coating was the thinnest, which could be due to a more uniform and finer deposition. Such modifications are of particular importance, as they provide information on improved surface coverage and possible enhancement of functional properties, including UV protection, antibacterial activity, etc.

Water absorption, desorption, and abrasion resistance

Table 2 shows the experimental data on water absorption, desorption and abrasion resistance of the modified samples. The values are presented as mean ± instrumental error.

The samples PW ZnO_2 and PW ZnO_3 show the best results, for PW ZnO_2 probably due to the NaOH-induced partial hydrolysis of the wool cuticle, which increased hydrophilicity and absorption, and for PW ZnO_3 due to the ultrasonic modification with nanoparticles, maintaining the integrity of the fibers and causing moderate absorption.

A change in water absorption and water release properties was observed. It was found that the treatment using ultrasound did not significantly affect the newly obtained characteristics. All three methods also meet the requirements for use in safety shoes. The best water absorption was observed in PW ZnO_2. From the visual assessment of abrasion resistance, it followed that there is no decrease in the quality of the materials.

The analyses showed that all tested samples exceeded the requirements of the ISO 20345 standard for water absorption, confirming the presence of hydrophilic properties. The wool samples modified with ZnO showed higher values than the zero sample, and the sample PW ZnO_2 reached the maximum absorption (156.9 mg/cm^2), indicating that the inclusion of ZnO improves moisture retention through increased surface polarity and interactions between nanoparticles and fibers [19]. While all samples in Table 2 met the permeability requirement, the zero sample showed the highest release (130.6%). In contrast, the samples treated with ZnO showed slightly lower permeability values (lowest in PW ZnO_1 at 89.7%), probably due to the stronger binding of water in the modified fiber matrix. The abrasion resistance remained unchanged, demonstrating that the ZnO modification preserves the structural integrity under friction.

Color coordinates and color difference

The analysis of the color coordinates reveals distinct differences between the zero sample and the three PW ZnO specimens (see Table 3). PW ZnO_1 shows moderate darkening (L*= 79.52), slight shift toward red and increase in the yellow component, resulting in a visible color difference. PW ZnO_2 exhibits the strongest deviation, with substantial decrease in brightness, pronounced change in the red-yellow range and high color difference (ΔE=17.92). PW ZnO_3 occupies an intermediate position with a color difference of ΔE=11.75.

These analyses confirm that ZnO modifies the surface and the optical properties of the material, which may serve as an indicator of functional effects such as antibacterial activity and coating durability. The observed deviations from the zero sample indicate a modification of the optical properties, which, from a physical perspective, is directly related to the interaction of the material with light and its potential antibacterial activity. Surface modifications in the presence of ZnO promote the formation of reactive oxygen species and the discharge of Zn^{2+} ions, resulting in damage to bacterial cells [20].

Morphological analysis

Figure 2 presents microscopic images of the wool specimens treated with ZnO-NPs. It is observed that the changes in the surface depend on the treatment method used.

The micrographs clearly show the applied coating of cross-linked gelatin hydrogel containing ZnO. In the modified sample PW ZnO_1, the nanoparticles are finely dispersed and evenly distributed on the surface of the film. The distribution of ZnO nanoparticles is even more uniform and compact in PW ZnO_2, but is located in the film. The use of ultrasonication (in sample PW ZnO_3) allows the particles to penetrate the micropores of the fibers, resulting in a more stable film structure. These observations confirm that the ZnO particles are effectively incorporated into the wool fibers and suggest a potential for improved functional properties and antibacterial effectiveness.

Table. 2. Water absorption, permeability and abrasion resistance of analyzed wool samples

Sample	W_A, mg/cm^2	ISO 20345 requirements	W_p, %	ISO 20345 requirements	Abrasion resistance	ISO 20345 requirements
Zero sample	120.9 ± 4.3	> 70	130.6 ± 2.3	> 80	no defects	without visual defects
PW ZnO_1	137.7 ± 4.7	> 70	89.7 ± 1.3	> 80	no defects	
PW ZnO_2	156.9 ± 5.6	> 70	98.2 ± 1.5	> 80	no defects	
PW ZnO_3	152.8 ± 5.4	> 70	97.2 ± 1.4	> 80	no defects	

Table 3. Color coordinates and color difference of the tested wool samples

Sample name	Measurement conditions	Color coordinates			Color difference
		L*	a*	b*	Δ Eab
Zero sample	Illuminator D65 Viewing angle 100	83.06	0.84	9.87	-
PW ZnO_1		79.52	2.18	17.47	8.49
PW ZnO_2		70.81	8.48	20.49	17.92
PW ZnO_3		76.03	6.25	17.58	11.75

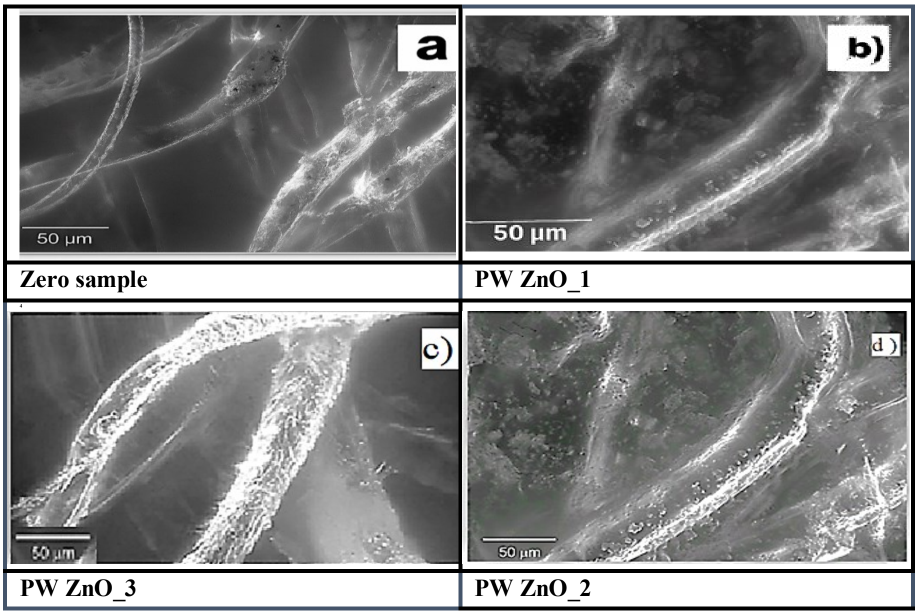

Zero sample | **PW ZnO_1** | **PW ZnO_3** | **PW ZnO_2**

Fig. 2. Microscopic images of wool samples (optical microscope, ×50): a) Zero sample; b) PW ZnO_1; c) PW ZnO_3; d) PW ZnO_2

Fluorescence analysis

The fluorescence analysis of the three wool samples revealed clear differences in their optical properties (Figs. 3, 4). The zero sample of untreated wool exhibited only weak autofluorescence typical of keratin. PW ZnO_1 showed enhanced intensity and a distinct peak around 540 nm due to alkaline hydrolysis of the cuticle, which increases hydrophilicity and creates active binding sites for nanoparticles. The best results were observed for PW ZnO_3 (under ultrasound) - the most intense and uniform fluorescence indicating good nanoparticle dispersion and stable adhesion to the fibers [21, 22].

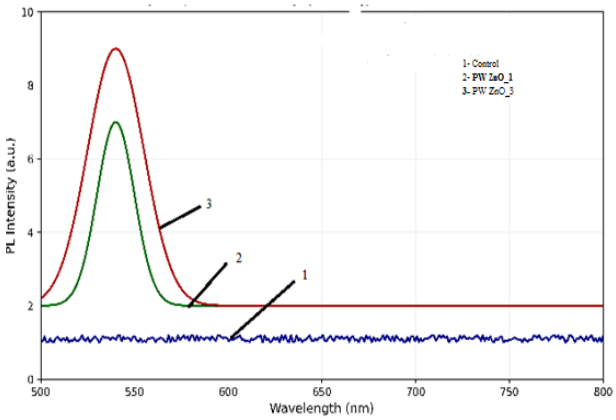

Fig. 3. Fluorescence analysis of wool samples treated with ZnO nanoparticles

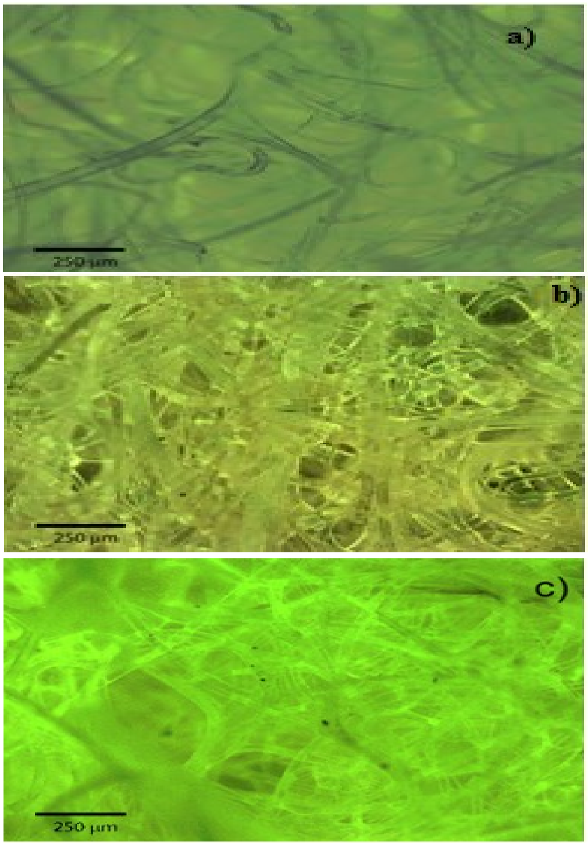

Fig. 4. Fluorescence images of the studied samples: a) Control; b) PW ZnO_1; c) PW ZnO_3

These data confirm that the combined chemical and physical modification of wool samples significantly improve the functionalization of wool fibers and the promotion of nanostructuring.

UV-Vis analysis

UV-Vis analysis was used to identify electronic transitions and bonding interactions between ZnO nanoparticles, gelatin, glutaraldehyde, and wool keratin, demonstrating how chemical modifications alter the optical properties of the fibres and reflect the strength and type of bonds formed [23]. Previous studies on cotton fabrics using similar modifications with gelatin-glutaraldehyde and ZnO nanoparticles have shown improved UV protection and antibacterial activity [24].

On Fig. 5 the characteristic UV peak for PW ZnO_2 at 423 nm corresponds to the absorption band of ZnO. NaOH hydrolyzes the wool cuticle, thereby exposing carboxyl groups that coordinately bind to Zn^{2+}, increasing the hydrophilicity and absorption compared to the control sample [23, 24]. The main peaks in the near-infrared region (1183 - 150 nm) for PW ZnO_1 are associated with ZnO stabilized by gelatin cross-linked with glutaraldehyde. In PW ZnO_3, the peaks at 441 nm indicate improved dispersion of ZnO nanoparticles.

CONCLUSION

Modification of woolen materials was carried out with a view to their application as lining details of footwear. A finish coating was successfully obtained by modifying woolen samples with cross-linked gelatin containing *in situ* synthesized ZnO particles. Microscopic studies showed that ZnO-NPs were impregnated into the structure of the gelatin hydrogel and were distributed into small film-forming structures. Hygienic parameters such as water adsorption and water permeability were also preserved and even improved in some of the samples. The obtained experimental data are promising for antibacterial activity, but for a more complete characterization of the obtained composites, antimicrobial studies are necessary.

Acknowledgement: *The study was performed under Contract NIS-№ 403-31, UCTM, Project „Antibacterial treatment of materials used in footwear".*

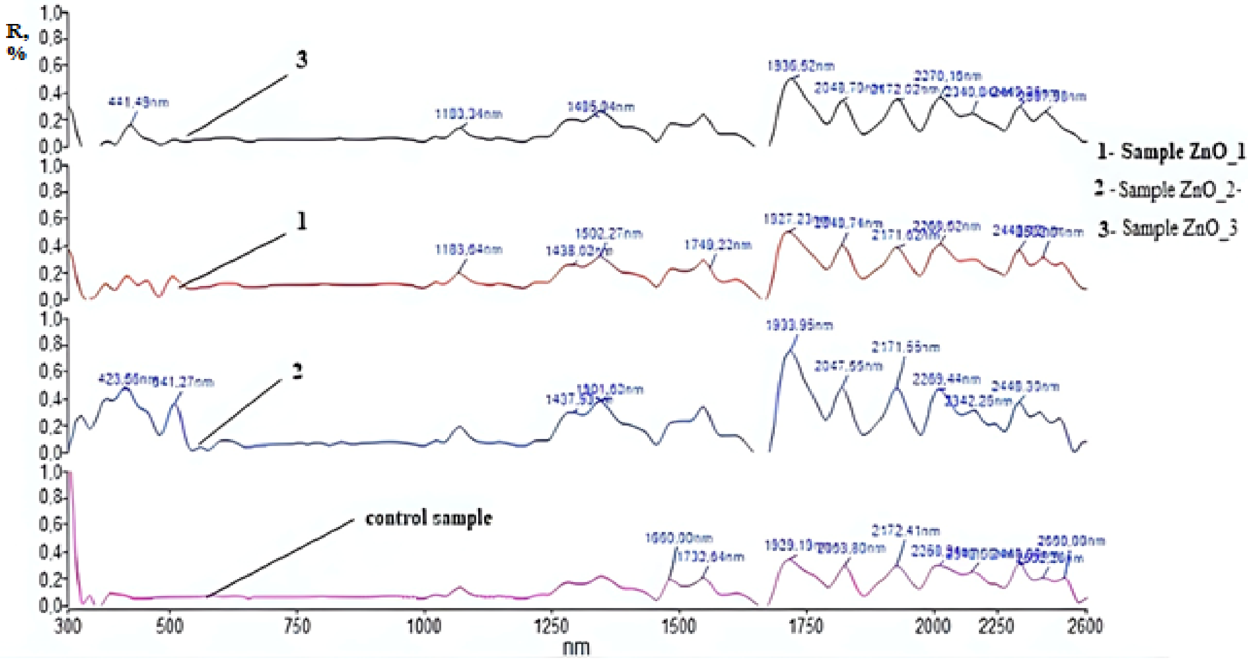

Fig. 5. UV-Vis spectra of wool samples: Control; PW ZnO_1; PW ZnO_2; and PW ZnO_3

REFERENCES

1. A. Behzadnia, M. Montazer, M. M. Rad, M. Rastgoo, *Heliyon,* **10**, e36522 (2024), https://doi.org/10.1016/j.heliyon.2024.e36522
2. M. Salama, A. Bendak, M. Muller, *Industria Textilă*, **62,** 320 (2011).
3. R. M.-Nodoushan, S. Shekarriz, Z. Shariatinia, A.Heydari, M. Montazer, *International Journal of Biological Macromolecules,* **242**, 124916 (2023)
4. X. Meng, Q. Nan, Q. Zeng, J. Zhang, S. Liu, L. Tan, Z. Zheng, X. Wang, G. Li, *Applied Surface Science,* **680**, 161341 (2025). https://doi.org/10.1016/j.apsusc.2024.161341
5. A. Behzadniaa, M. Montazer, M. M. Rad, J*ournal of Photochemistry and Photobiology B: Biology*, **149,** 103 (2015), http://dx.doi.org/10.1016/j.jphotobiol.2015.05.006
6. S. Ghosh, P. Goswami, S. Rana, *Surfaces and Interfaces*, **51**, 104630 (2024), https://doi.org/10.1016/j.surfin.2024.104630
7. A. Verbic, M. Gorjanc, B. Simoncic, *Coatings*, **9**, 550 (2019).
8. I.S. Tania, M. Ali, *Polymers*, **13,** 2701 (2021), https://doi.org/10.3390/polym13162701
9. H. Ma, F. Zhang, Q. Li, G. Chen, S. Hub, H. Cheng. *RSC Adv*., **9,** 18406 **(**2019).
10. H. Kafafy, A. A. Shahin, H. M. Mashaly, H. M. Helmy, A. Zaher, *Egypt. J. Chem*., **64** (9), 5255 (2021).
11. S. H. Abdel-Fattah, E. M. El-Khatib, *Research Journal of Textile and Apparel RJTA,* **16** (3) 42 (2012).
12. D. S. Angelova, D. Zheleva, Y. Gocheva, E. Krumova, *ICAMS 2024, Bucharest, Romania (Proceedings of the 10th International Conference on Advanced Materials and Systems),* 17 (2024), doi:10.2478/9788367405805-002
13. БДС EN ISO 2589, *Leather - Physical and mechanical tests - Determination of thickness,* https://bds-bg.org/bg/project/show/bds:proj:99774
14. БДС EN ISO 17229, *Leather - Physical and mechanical tests - Determination of water vapour absorption,* https://bds-bg.org/bg/project/show/bds:proj:99776
15. БДС EN ISO 20344, *Personal protective equipment - Test methods for footwear*, https://bds-bg.org/bg/project/show/bds:proj:107986
16. ISO 22649: 2016, *Test methods for insoles and insocks: Water absorption and desorption.*
17. ISO 20868: 2001, *Footwear - Test methods for insoles - Abrasion resistance.*
18. БДС EN ISO 22700, *Leather - Measuring the colour and colour difference of finished leather*, https://bds-bg.org/bg/project/show/bds:proj:105687
19. C. L. Huang, *Coatings*, **10** (8), 781 (2020), https://doi.org/10.3390/coatings10080781
20. V. Zhagan, O. Isaieva, O. Selyshchev, T. Selyshchev, M. Belyaev, A. Yukhymchuk, V.O. Valakh, M. Zahn, *Journal of Nanoparticle Research,* **24,** 269 (2022).
21. A. Galdámez-Martinez, G. Santana, F. Güell, P.R Martínez-Alanis, A. Dutt, *Nanomaterials*, **10** (5), 857 (2020).
22. T. Imana, A. Mohammad, A. Mahmuda, *Journal of Engineered Fibers and Fabrics*, **17**, 1-11 (2022).
23. M. Munir, M. Ashraf, H. A. Abid, A. Javid, S. Riaz, H. Khanzada, A. Rehman, K. Iqbal, *Journal of Coatings Technology and Research,* **19**, 467 (2021).
24. D. Zheleva, M. Koleva, D. Angelova, D. Grabcheva, P. Todorov, *ICAMS 2022, Bucharest, Romania (Proceedings of the 9th International Conference on Advanced Materials and Systems)*, (2022), DOI: 10.24264/icams-2022.II.29

Bulgarian Chemical Communications, Volume 58, Issue 2 (pp. 226-232) 2026 DOI: 10.34049/bcc.58.2.NCC07

Chelation reaction *vs.* isotope exchange for production of effective receptor-targeted radiopharmaceuticals

G. V. Simeonova[1], T. P. Trifonova[1, 2]

[1]*UMHAT "St. Marina"– Varna, Clinic of Nuclear Medicine, Varna, Bulgaria*
[2]*Medical University – Varna, Department of Nuclear Medicine, Metabolic Therapy and Radiotherapy, Varna, Bulgaria*

Received: November 01, 2025; Revised: December 12, 2025

Peptide-based pharmaceuticals have applications in both diagnostic imaging and targeted therapy. Various prostate-specific membrane antigens (PSMA) are of considerable interest in the development of specific markers for the diagnosis and treatment of prostate cancer (PCa).

The aim of the present study was to compare the methods for the production of two diagnostic radiopharmaceuticals based on PSMA – [^{68}Ga]PSMA-11 and [^{18}F]SiPSMA-14. The syntheses of the indicated products differ in the modification of the starting peptide precursor, the duration and the mechanism of the process. Two methods for radiochemical synthesis were applied – chelation reaction and isotope exchange reaction. The peptide precursor PSMA was labelled with two different positron-emitting radionuclides ^{68}Ga and ^{18}F, obtained from a ^{68}Ge/^{68}Ga generator and a cyclotron, respectively. An automated synthesis procedure was applied to ensure safe and efficient production of the radiopharmaceuticals. The radiochemical yield, chemical and radiochemical purity, and radionuclide identity of both radiopharmaceuticals were determined according to the requirements of the European Pharmacopoeia.

In conclusion, [^{18}F]SiPSMA-14 is a new PET radiotracer for radiopharmaceutical science, recently introduced into clinical practice for the evaluation of PCa patients. The isotope exchange reaction was adapted and used for the first time in Bulgaria. The production of [^{18}F]SiPSMA-14 is a faster process and occurs under milder reaction conditions compared to the production of [^{68}Ga]PSMA-11. The high yield of [^{18}F]SiPSMA-14 and the better nuclear characteristics of ^{18}F are essential. An additional advantage of the production of [^{18}F]SiPSMA-14 is the availability of an in-house cyclotron in the clinic.

Keywords: radiopharmaceuticals, PSMA, ^{68}Ga, ^{18}F, prostate cancer

Abbreviations:

[^{68}Ga]PSMA-11 – Prostate-specific membrane antigen labelled with ^{68}Ga
[^{18}F]SiPSMA-14 – Prostate-specific membrane antigen labelled with ^{18}F
PCa – Prostate cancer
PET – Positron emission tomography
CT – Computed tomography
SPECT – Single-photon emission computed tomography
HBED-CC – Hydroxy-5-(carboxyethyl)benzyl ethylenediamine diacetic acid
NOTA – Triazacyclononane-triacetic acid (bifunctional chelator)
HEPES – Hydroxyethyl piperazineethanesulfonic acid
HPLC – High performance liquid chromatography
TLC – Thin-layer chromatography
TFA – Trifluoroacetic acid
SPE – Solid phase extraction
QMA cartridge - Quaternary methyl ammonium
HLB cartridge - Hydrophilic-lipophilic balanced sorbent

INTRODUCTION

Prostate cancer is one of the most common malignancies in men. With the development of molecular imaging diagnostics, PSMA (prostate-specific membrane antigen) has become established as a key marker for the detection, monitoring and targeted therapy of the disease due to its high tumor expression [1-3]. PSMA is found on the surface of prostate cancer cells at all stages of the disease. Therefore, this protein is considered the best target antigen [4, 5], although its low expression is also found in the salivary glands, kidneys and in the endothelium of most solid tumors [6]. Initially, PSMA antibodies [7] or their fragments were used as radionuclide carriers in nuclear medicine for the treatment of prostate cancer [8, 9]. In recent years, various new radiopharmaceuticals based on PSMA ligands have been introduced into clinical practice

---

* To whom all correspondence should be sent:
Email: *gerimm@abv.bg*

for PET or SPECT imaging and therapy [3, 10, 11]. ^{68}Ga and ^{18}F-labelled PSMA ligands are commonly used for PET diagnostics [12], as they provide high image contrast [13].

The radionuclide ^{18}F is a positron emitter with a half-life of 109 min. It is mainly produced in a cyclotron by proton bombardment of ^{18}O-enriched water. The rapid initiation of the ^{18}O(p,n)^{18}F reaction permits the production of large quantities of ^{18}F using cyclotrons with average energies up to 20 MeV. A major advantage of this method of production is the lack of competing nuclear reactions [14]. The radionuclide ^{68}Ga is also a positron emitter with a half-life of 68 min. It can be produced in a cyclotron by proton bombardment of a liquid target containing a solution of [^{68}Zn]Zn(NO$_3$)$_2$ [15]. However, for the purpose of routine radiopharmaceutical synthesis of ^{68}Ga-labelled radiopharmaceuticals, a ^{68}Ge/^{68}Ga generator system is primarily used. The ^{68}Ga radionuclide is obtained by a standard hydrochloric acid elution method. The availability of a ^{68}Ge/^{68}Ga generator facilitates the on-site production of ^{68}Ga-labelled radiopharmaceuticals [16].

Some PSMA PET agents are labelled by chelating with ^{68}Ga, while others are directly labelled with ^{18}F [17]. The most commonly developed PSMA radiotracers are labelled with gallium-68, e.g., [^{68}Ga]PSMA-11 and [^{68}Ga]PSMA-617 [18]. One advantage of Ga-labelled compounds is that they include a chelate that can also be used to bind isotopes such as ^{177}Lu or ^{225}Ac in the production of therapeutics, thus constituting a true theragnostic agent [17, 19]. Although the most commonly used PSMA PET radioligands are currently labelled with ^{68}Ga, this is associated with a number of disadvantages compared with fluorine-18 labelled ones. The short half-life and relatively low available radioactivity of gallium-68 limits both the transport of ^{68}Ga-labelled PET compounds to other PET centers and delays imaging [18]. Furthermore, ^{68}Ge/^{68}Ga generators are associated with logistical limitations such as long delivery duration due to shortage of commercially available approved generators; moreover, high activity yields cannot be obtained due to capacity limitations of available generators [20]. Gallium-68 produced by a generator is readily available for radiolabelling using lyophilized precursor formulations, but production capacity is limited to 2–4 patient doses depending on the lifetime of the generator. A significant disadvantage of using ^{68}Ga-radiolabelled PSMA synthetic peptides is the reduced number of patients that can be imaged with PET/CT at one time. Such a limitation is due to the relatively low amount of ^{68}Ga available after each elution and the decrease in generator activity over time [21, 22]. On the other hand, cyclotron-produced fluorine-18 can be obtained with significantly higher activity, allowing for more doses to patients and a higher dose activity [18, 23, 24]. The longer half-life of ^{18}F allows for the delivery of final radiopharmaceuticals to off-site PET centers that are no more than 4 hours away from the cyclotron-equipped manufacturing facility [25]. This has led to a rapid and significant increase in the development of ^{18}F-labelled PSMA ligands [18]. Several ^{18}F-labelled PSMA targeting radiotracers have been introduced and increasingly used in clinical practice [21, 22].

One of the ^{18}F-labelled radiopharmaceuticals used is [^{18}F]PSMA-1007, the initial synthesis of which consists of the production of an activated ^{18}F-labelled prosthetic group, which is subsequently coupled to the unprotected precursor, followed by HPLC-purification of the product (total 1.5%-6.0% decay-corrected yield, 45 min) [26, 27]. The implementation of multi-step and time-consuming radiofluorination procedures is particularly detrimental for the radiolabelling of large biomolecules, which require mild conditions and a one-step labelling procedure [18, 28]. A one-step procedure was later presented that can produce [^{18}F]PSMA-1007 with improved radiochemical yield (25%-80%) in less than 55 min [29]. Other alternative ^{18}F-labelling strategies were developed. A new technique for introducing fluorine-18 to a biomolecule is through metal-based radiochemistry. Ga^{3+} and Al^{3+} are trivalent metals with similar ionic radii, and the fluoride-aluminum (AlF^{2+}) complex is associated with strong bond formation and high *in vivo* stability. This suggests that AlF^{2+} can form stable complexes with hexadentate ligands such as NOTA or HBED-CC [18, 30]. This radiofluorination method is efficient, simple, rapid, and can be performed in aqueous media, eliminating the need for azeotropic drying [31].

To avoid the complex multi-step process of C – F bond formation, the labelling can be performed by another efficient radiofluorination method based on isotope exchange using a silicon fluoride (SiFA) acceptor building block. This reaction proceeds rapidly with high yield and high molar activity and is resistant to hydrolysis due to the surrounding sterically demanding substituents [5, 18, 32]. Kinetic analysis of the isoenergetic substitution of ^{19}F with the positron isotope ^{18}F in the SiFA moiety revealed a low energy barrier of only 15.7 kcal/mol [33]. This explains the rapid isotopic exchange reaction from ^{19}F to ^{18}F at room temperature within 5 min, giving [^{18}F]SiFA-conjugated compounds with high yields

(40%) and high molar activity. Furthermore, the lack of by-products allows for simple cartridge-based purification, resulting in a total synthesis time of 30 min [34-36]. The introduction of radiohybrid ligands containing both a SiFA building block and a chelator allows labelling of the biomolecule with both a diagnostic (e.g., fluorine-18 or gallium-68) and a therapeutic (e.g., lutetium-177) radioisotope [32, 37].

The aim of the present study was to compare the methods for the production of two diagnostic radiopharmaceuticals based on PSMA – [^{68}Ga]PSMA-11 and [^{18}F]SiPSMA-14. The presented synthesis methods were not developed in our clinic, but were introduced as standardized procedures for the production of the indicated radiopharmaceuticals. Syntheses were performed according to the manufacturer's synthesis instructions (Scintomics, Fürstenfeldbruck, Germany). The novelty is the application of the isotope exchange reaction as a convenient method for labelling the PSMA molecule with ^{18}F in one step, without the risk of destroying the peptide structure. In addition, the aim was to point out the advantages not only of this production method, but also of the radionuclide ^{18}F itself. In the presence of an in-house cyclotron, it is more convenient and preferable to produce the ^{18}F-labelled radiopharmaceutical [^{18}F]SiPSMA-14.

EXPERIMENTAL

Materials and equipment

For the production of both radiopharmaceuticals [^{68}Ga]PSMA-11 and [^{18}F]SiPSMA-14, standardized automated synthesis procedures with a Scintomics GRP radiochemical synthesis module were applied. Disposable synthesis cards for synthesis of [^{68}Ga]PSMA-11, appropriate peptides and reagent kits supplied by ABX Advanced Biochemical Compounds (Radeberg, Germany) were used. All solvents and reagents (ethanol 70%, ethanol/water 1/1, water for injections, 1.5 M hydroxyethyl-piperazineethanesulfonic acid (HEPES) buffer, 5 M NaCl, phosphate buffered saline (PBS) (pH=7.4) were sterile and ultrapure. In addition to the above reagents, lyophilized peptide precursor PSMA-11 (10 µg) was used for the synthesis, and 4 ml of 0.05 M HCl was used for elution of ^{68}Ga from the ^{68}Ge/^{68}Ga generator.

The kit for the production of [^{18}F]SiPSMA-14 included: 10 ml of anhydrous acetonitrile (>99.9%), 250 µl of dimethyl sulfoxide anhydrous (DMSO, >99.9%), 3 ml of ethanol/water 1/1, 2 ml of anhydrous acetonitrile (for dissolving the eluent, >99.9%), 38 ml of 0.1 M citrate buffer (pH=5.0), lyophilized eluent cocktail, 100 µl of 1M oxalic acid and lyophilized peptide precursor SiPSMA-14 (150 nmol/vial). All solvents and reagents for synthesis of [^{18}F]SiPSMA-14 were sterile and ultrapure or HPLC grade from Huayi isotopes, China.

- *Production of [^{68}Ga]PSMA-11*

The synthesis of this radiopharmaceutical was based on the chelation reaction between ^{68}Ga and the peptide precursor PSMA-11. The complexation of the radionuclide gallium-68 was achieved by the bifunctional acyclic chelator HBED-CC, which is a hexadentate chelator. For the production of [^{68}Ga]PSMA-11, the radionuclide ^{68}Ga was obtained *via* a ^{68}Ge/^{68}Ga generator (1850 MBq, ITM Isotope Technologies Munich SE, Germany) by elution with 0.05M HCl, as a part of the automated procedure.

After elution of ^{68}Ga from the ^{68}Ge/^{68}Ga generator in the form of [^{68}Ga]Cl$_3$, it entered the synthesis cassette, then was captured in a PSH cartridge. NaCl solution was used for elution of ^{68}Ga^{3+}. The radiolabelling was carried out at a temperature of 95°C followed by purification of the product on a C18 cartridge. Subsequently, the product was eluted with 3 ml of ethanol/water in a sterile vial and diluted with PBS (pH 7.4). The entire synthesis procedure lasted 30 min. The procedure for preparing the radiopharmaceutical [^{68}Ga]PSMA-11 is standard and adapted from literature data [16, 40]. The structure of the ^{68}Ga-labelled radiopharmaceutical is presented in Figure 1.

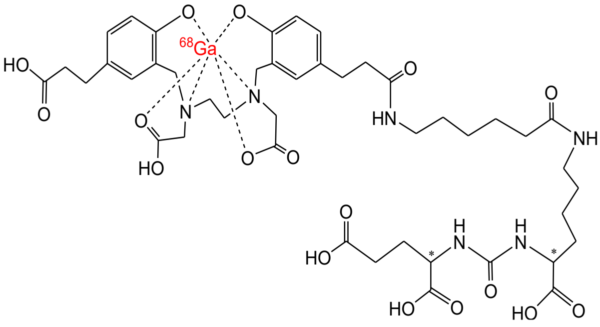

Figure 1. Structure of [^{68}Ga]PSMA-11

Automated production of [^{68}Ga]PSMA-11 using a synthesis module reduces radiation exposure to operators, allows for high reproducibility, and compliance with local health requirements, regulatory standards, and good manufacturing practice (GMP) standards [15, 38, 39].

- *Production of [^{18}F]SiPSMA-14*

The synthesis of [^{18}F]SiPSMA-14 was based on the ^{19}F/^{18}F isotope exchange reaction, without modifying the drug molecule itself. For this purpose, the radionuclide ^{18}F was produced in a liquid target using a medical cyclotron with a proton energy of 7.5 MeV (ABT Molecular Imaging BG-75) by irradiating a standard volume of 280 µL of ^{18}O-enriched water, [^{18}O]H_2O (≥98% purity; Taiyo-Nippon Sanso Corporation, Japan). Two consecutive bombardment cycles of 45 min each were carried out at an average target current of 4 µA, after which the resulting ^{18}F was transferred to the automated radiosynthesis module. After ^{18}F entered the synthesis card, the production of [^{18}F]SiPSMA-14 included the following steps: fluoride fixation; drying of the quaternary methyl ammonium (QMA) cartridge with CH_3CN anhydride; elution of the QMA with an eluent cocktail (K222/KOH in CH_3CN anhydride); labelling of the peptide; dilution of the reaction mixture with citrate buffer; solid phase extraction (SPE) of the product in the HLB cartridge; SPE purge; SPE elution; sterile filtration of the product using a sterile 0.2 µm filter; dilution of the product with citrate buffer (pH = 5.0) [41]. The labelling reaction was carried out at room temperature for 17 min. There was no need for HPLC purification as in direct ^{18}F labelling of substrates. The synthesis was performed according to the manufacturer's synthesis instructions (Scintomics, Fürstenfeldbruck, Germany). The structure of the ^{18}F-labelled radiopharmaceutical is presented in Figure 2.

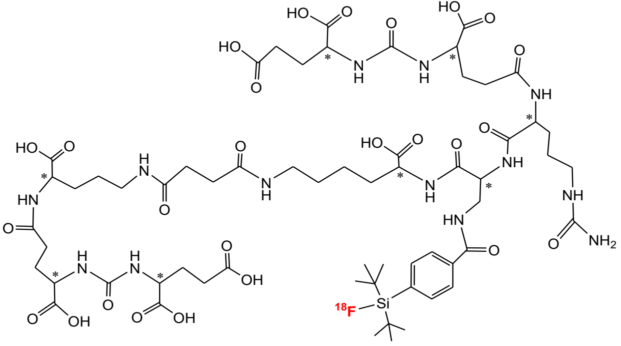

Figure 2. Structure of [^{18}F]SiPSMA-14

Quality control of [^{68}Ga]PSMA-11 and [^{18}F]SiPSMA-14 products

To release both radiopharmaceuticals for clinical use, appropriate quality control measures were taken, according to the European Pharmacopoeia (Ph. Eur.) [42-44].

The radionuclides ^{18}F and ^{68}Ga were identified by determining the physical half-life ($t_{1/2}$) of each radionuclide, measuring five activity values over a 15-min interval using an ISOMED 2010 dose calibrator. A Digital Spectrum Analyzer DSA-1000 gamma spectrometer with a germanium detector was used to determine the radionuclide purity. The physicochemical characterization of the two final products was performed by radiochemical identification and determination of radiochemical purity, chemical purity, pH measurement and analysis of solvent residues. In addition, a test for endotoxin determination was performed using the Endosafe PTS Charles River apparatus.

Routinely, radiochemical purity is determined by radio-TLC, which is a fast and cheap method (Scan–Ram PET/SPECT radio TLC-scanner, using Laura software, version V5.0.974.SP6). Paper chromatography plates (iTLC-SG, Agilent Technologies) were used as stationary phase, and a mixture of methanol and 0.1 M ammonium acetate in a ratio of 1/1 was used as mobile phase. The radiochemical purity was confirmed by radio-HPLC (HPLC–system SCI8100 Plus, software YL-Clarity, version 8.7), using a Meteoric Core C18 BIO chromatographic column (100 mm × 3.0 mm). The mobile phase used included the following two components: phase A (0.1 % TFA in water) and phase B (0.1 % TFA in acetonitrile). The analysis was performed using a gradient method with the following parameters: 0–0.5 min: 95% phase A and 5% phase B; 0.5–10 min: phase A 95% → 60% and phase B 5% → 40%; 10–11 min phase A 60% → 95% and phase B 40% → 5%; 11–16 min phase A 95% and phase B 5%. The mobile phase flow rate was 0.6 ml/min. The radio-HPLC system was equipped with a UV/VIS detector SCI8120 (YL9120) and a radioactivity detector SN:6967 operating at a wavelength of 280 nm.

RESULTS AND DISCUSSION

For clinical purposes, [^{68}Ga]PSMA-11 and [^{18}F]SiPSMA-14 were successfully prepared with good radiochemical yield and high radiochemical purity. Both products were qualitatively characterized and met the requirements of the European Pharmacopoeia. The two procedures differed in the modification of the precursor used, the type of reaction, the duration of the process and the reaction conditions. For the analysis of the results, a sample of 24 syntheses was taken for each of the produced radiopharmaceuticals, on the basis of which the average radioactivity of the final product obtained and the average radiochemical yield were calculated. A summary of the data is presented in Table 1.

The data from the [^{68}Ga]PSMA-11 syntheses were taken from the initial stage of the ^{68}Ge/^{68}Ga generator operation, when its activity and production capacity were at their highest. The theoretically expected initial activity of the eluted ^{68}Ga at that time was between 1620 – 1680 MBq.

Table 1. Comparative data for [^{68}Ga]PSMA-11 and [^{18}F]SiPSMA-14

Indicator	[^{68}Ga]PSMA-11 (sample of 24 syntheses)	[^{18}F]SiPSMA-14 (sample of 24 syntheses)
Average activity of the final product	855.9 ± 12.6 MBq	1821.6 ± 17.3 MBq
Specific activity of the final product	50.4 ± 5.6 MBq/mL	107.2 ± 7.9 MBq/mL
Average radiochemical yield	52.2 ± 11.3%	68.6 ± 12.4%
Labelling temperature [°C]	95°C	22°C
Labelling time [min]	30	17
Purification	SPE – PS-H$^+$, C18	SPE – QMA, HLB
Radiochemical purity	> 98%	> 99%
Number of patients injected	72	100

The synthesis of [^{68}Ga]PSMA-11 was performed in 30 min and resulted in a product volume of 17-18 ml, an average radiochemical yield of 52.2 ±11.3% (non-decay corrected), specific activity of 50.4 ± 5.6 MBq/mL and radiochemical purity greater than 98%. During the study period, the ^{68}Ga-labelled radiopharmaceutical was obtained with an activity ranging between 680.6 and 916.4 MBq, the mean activity value being 855.9 ± 12.6 MBq. After successful quality control tests, the product was distributed to three patients.

Regarding the other product, the initial activity of ^{18}F produced after two consecutive bombardment cycles was in the range between 2000 and 2950 MBq, depending on the state of the ion source and the target in the cyclotron. The synthesis of [^{18}F]SiPSMA-14 was performed in 17 min and resulted in a product volume of 17-18 ml, average radiochemical yield of 68.6 ± 12.4% (non-decay corrected), specific activity of 107.2 ± 7.9 MBq/ml and radiochemical purity greater than 99%. The resulting activity of the final product [^{18}F]SiPSMA-14 varied between 1100 and 2353 MBq, with a mean value of 1821.6 ± 17.3 MBq. The activity of the ^{18}F-labelled radiopharmaceutical produced was sufficient to perform imaging studies on up to five patients, allowed for a longer injection interval between patients, and enabled later scanning.

CONCLUSIONS

In the activities of the Clinic of Nuclear Medicine, Varna since 2019, the radiopharmaceutical [^{68}Ga]PSMA-11 has been used for the diagnosis of prostate cancer, and in 2023 [^{18}F]SiPSMA-14 was introduced as an alternative radiopharmaceutical. For the first time, the isotope exchange reaction was used as a convenient method for labelling the PSMA molecule with ^{18}F. [^{18}F]SiPSMA-14 has great advantages compared to [^{68}Ga]PSMA-11 in terms of both the radionuclide ^{18}F and the synthesis method. The radionuclide ^{18}F was produced on site in the clinic with the in-house cyclotron with a significantly higher initial activity compared to that of ^{68}Ga obtained from a ^{68}Ge/^{68}Ga generator. ^{18}F has a longer half-life and lower average positron energy, which allows for PET images with higher resolution and longer scanning time to be obtained. The process of obtaining [^{18}F]SiPSMA-14 by isotope exchange has the following advantages: (1) it leads to the formation of an *in-vivo* stable ^{18}F-Si bond; (2) it proceeds faster at room temperature, which is gentler to the peptide molecule PSMA; (3) no by-products are expected, so there is no need for additional purification. [^{18}F]SiPSMA-14 is obtained with a higher radiochemical yield, higher molar activity and better selectivity compared to [^{68}Ga]PSMA-11. The synthesis also allows the obtained product to be administered to more patients. When an in-house cyclotron is available, it is more expedient and preferable to produce and use the ^{18}F-labelled radiopharmaceutical [^{18}F]SiPSMA-14. This approach provides an opportunity to overcome the difficulties associated with the production, high cost and logistic issues related to the use of ^{68}Ge/^{68}Ga generators.

REFERENCES

1. M. Dyankova, PhD Thesis, MU, Varna, 2022.
2. A. Afshar-Oromieh, U. Haberkorn, M. Eder, M. Eisenhut, C.M. Zechman, *Eur. J. Nucl. Med. Mol. Imag.*, **39 (6)**, 1085 (2012).
3. E. Mena, M.L. Lindenberg, J.H. Shih, S. Adler, S. Harmon, E. Bergvall, D. Citrin, W. Dahut, A.T. Ton, Y. McKinney, J. Weaver, P. Eclarinal, A. Forest, G. Afari, S. Bhattacharyya, R.C. Mease, M.J. Merino, P. Pinto, B.J. Wood, P. Jacobs, M.G. Pomper, P.L. Choyke, B. Turkbey, *Eur. J. Nucl. Med. Mol. Imaging*, **45**, 4 (2018).
4. K.S. Ajish Kumar, A. Mathur, *Eur. J. Med. Chem. Reports*, **3**, 100014 (2021).

5. S. Huang, S. Ong, D. McKenzie, A. Mirabelli, D. C. Chen, Th. Chengodu, D. G. Murphy, M. S. Hofman, N. Lawrentschuk, M. Perera, *Prostate Cancer Prostatic Dis.*, **27**(4), 654 (2024).
6. S. Blok, C. Wängler, P. Bartenstein, K. Jurkschat, R. Schirrmacher, S. Lindner. *EJNMMI Radiopharm. Chem.*, **8**(1), 25 (2023).
7. B. J. B. Nelson, J. D. Andersson, F. Wuest, S. Spreckelmeyer. *EJNMMI Radiopharm. Chem.,* **7**(1), 27 (2022).
8. D.M. Schuster, P.A. Taleghani, P.T. Nieh, V.A. Master, R. Amzat, B. Savir-Baruch, R.K. Halkar, T. Fox, A.O. Osunkoya, C.S. Moreno, J.A. Nye, W. Yu, B. Fei, Z. Wang, Z. Chen, M.M. Goodman, *Am. J. Nucl. Med. Mol. Imag.*, **3**, 85 (2013).
9. S. Wilkinson, G. Chodak, *J. Urol*., **172(1)**, 133 (2004).
10. A. Afshar-Oromieh, C.M. Zechmann, A. Malcher, M. Eder, M. Eisenhut, H.G. Linhart, T. Holland-Letz, B.A. Hadaschik, F.L. Giesel, J. Debus, U. Haberkorn, *Eur. J. Nucl. Med. Mol. Imag.,* **41(1)**, 11 (2014).
11. P.J.L. de Visschere, C. Standaert, J. Fütterer, G.M. Villeirs, V. Panebianco, J. Walz, T. Maurer, B.A. Hadaschik, F.E. Lecouvet, G. Giannarini, S. Fanti*,* *Eur. Urol. Oncol*., **2**, 47 (2019).
12. S. Sheikhbahaei, R.A. Werner, L.B. Solnes, K.J. Pienta, M.G. Pomper, M.A. Gorin, S.P. Rowe, *Semin. Nucl. Med*., **49**, 255 (2019).
13. N. Mottet, P. Cornford, R.C.N. van den Bergh, E. Briers, M. De Santis, S. Fanti, N. Fossati, G. Gandaglia, S. Gillessen, N. Grivas, J. Grummet, A.M. Henry, T. H. van der Kwast, T.B. Lam, M. Lardas, M. Liew, M.D. Mason, L. Moris, D. E. Oprea-Lager, H.G. van der Poel, O. Rouvière, I.G. Schoots, D. Tilki,T. Wiegel, P.M. Willemse, P; Cornford, *EAU, Edn. presented at the EAU Annual Congress Amsterdam*, ISBN 978-94-92671-07-3 (2021).
14. IAEA (International Atomic Energy Agency) TECDOC SERIES - N°1968, Vienna (2021).
15. M.E. Rodnick, C. Sollert, D. Stark, M. Clark, A. Katsifis, B.G Hockley, D.C. Parr, J. Frigell, B.D. Henderson, M. Abghari-Gerst, M.R. Piert, M.J. Fulham, S. Eberl, K. Gagnon, P.J.H. Scott, *EJNMMI Radiopharm. Chem*., **5(1)**, 25 (2020).
16. R. Nanabala, M.K. Anees, A. Sasikumar, A. Joy, M.R. Pillai. *Nucl. Med. Biol.* **43(8)**, 463 (2016).
17. E. Mena, L.M. Lindenberg, P.L. Choyke, *Semin. Nucl. Med*., **49**, 326 (2019).
18. S. Piron, J. Verhoeven, C. Vanhove, F. De Vos, *Nucl. Med. Biol*., **106**, 29 (2022).
19. F. Dietlein, C. Kobe, S. Neubauer, M. Schmidt, S. Stockter, T. Fischer, K. Schomäcker, A. Heidenreich, B.D. Zlatopolskiy, B. Neumaier, A. Drzezga, M. Dietlein*, J. Nucl. Med*., **58(6)**, 947 (2017).
20. S. Naka, T. Watabe, K. Kurimoto, M. Uemura, F. Soeda, O.C. Neels, K. Kopka, M. Tatsumi, H. Kato, N. Nonomura, E. Shimosegawa, J. Cardinale, F. L. Giesel, J. Hatazawa, *EJNMMI Radiopharm. Chem*. **5(1)**, 18, (2020).
21. C. Zippel, S.C. Ronski, S. Bohnet-Joschko, F.L. Giesel, K. Kopka, *Pharmaceuticals (Basel),* **13(1)**, 12 (2020).
22. R.A. Werner, T. Derlin, C. Lapa, S. Sheikbahaei, T. Higuchi, F.L. Giesel, S. Behr, A. Drzezga, H. Kimura, A.K. Buck, F.M. Bengel, M.G. Pomper, M.A. Gorin, S.P. Rowe, *Theranostics*, **10(1)**, 1 (2020).
23. M. Conti, L. Eriksson, *EJNMMI Phys.,* **3(1)**, 8 (2016).
24. C. Kesch, C. Kratochwil, W. Mier, K. Kopka, F.L. Giesel, *J. Nucl. Med*., **58(5)**, 687 (2017).
25. O. Shammi, B. Nebeling, H. Grievink, E. Mishani. *J. Label. Compd. Radiopharm*., **62**, 252 (2019).
26. H.J. Wester, M. Schottelius, *Semin. Nucl. Med*., **49(4)**, 302 (2019).
27. J. Cardinale, M. Schäfer, M. Benešová, U. Bauder-Wüst, K. Leotta, M. Eder, O. C. Neels, U. Haberkorn, F. L. Giesel, K. Kopka, *J. Nucl. Med*., **58(3)**, 425 (2017).
28. J.L. Zeng, J. Wang, J.A. Ma, *Bioconjug. Chem.*, **26(6)**, 1000 (2015).
29. J. Cardinale, R. Martin, Y. Remde, M. Schäfer, A. Hienzsch, S. Hübner, A-M. Zerges, H. Marx, R. Hesse, K. Weber, R. Smits, A. Hoepping, M. Müller, O.C. Neels, K. Kopka, *Pharmaceuticals (Basel)*, **10(4)**, 77 (2017).
30. N. Malik, B. Baur, G. Winter, S.N. Reske, A.J. Beer, C. Solbach, *Mol. Imaging Biol. US*, *Springer*, **17(6)**, 777 (2015).
31. W.J. McBride, R.M. Sharkey, D.M. Goldenberg, *EJNMMI Res. Springer*, **3(1)**, 36 (2013).
32. A. Wurzer, D. Di Carlo, A. Schmidt, R. Beck, M. Eiber, M. Schwaiger. *J. Nucl. Med*., **61(5)**, 735 (2020).
33. A.P. Kostikov, L. Iovkova, J. Chin, E. Schirrmacher, B. Wängler, C. Wängler, K. Jurkschat, G. Cosa, R. Schirrmacher. *J. Fluor. Chem*., **132**, 27 (2011).
34. S. Niedermoser, J. Chin, C. Wängler, A. Kostikov, V. Bernard-Gauthier, N. Vogler, J.-P. Soucy, A.J. McEwan, R. Schirrmacher, B. Wängler, *J. Nucl. Med.,* **56(7)**, 1100 (2015).
35. S. Lindner, C. Michler, S. Leidner, C. Rensch, C. Wängler, R. Schirrmacher, P. Bartenstein, B. Wängler, *Bioconjug. Chem.,* **25,** 738 (2014).
36. C. Wängler, S. Niedermoser, J. Chin, K. Orchowski, E. Schirrmacher, K. Jurkschat, L. Iovkova-Berends, A.P. Kostikov, R. Schirrmacher, B. Wängler, *Nat. Protoc*., **7**, 1946 (2012).
37. A. Wurzer, M. Parzinger, M. Konrad, R. Beck, T. Günther, V. Felber, S. Färber, D. Di Carlo, H.-J. Wester, *EJNMMI Res*., **10(1)**, 149 (2020).
38. L.L. Fuscaldi, D.V. Sobral, A.C.R. Durante, F.F. Mendonça, A. Cláudia, C. Miranda, M.L. da Cunha, L. Malavolta, J. Mejia, M.F. de Barboza, *Pharmac. (Basel)*, **14(5)**, 385 (2021).
39. I. Velikyan, *Molecules,* **20(7)**, 12913 (2015).
40. Y. Wang, G. Shao, J. Wu, C. Cui, S. Zang, F. Qiu, R. Jia, Z. Wang, F. Wang, *Contrast Media & Mol. Im.,* (2018).

41. J. Miksch, E. Yousefzadeh-Nowshahr, D. Hardiansyah, G. Glatting, C. Solbach, C. Bolenz, F. Zengerling, T. Wiegel, M. Beer, V. Prasad, H. J. Wester, A. J. Beer, W. Thaiss, *Nuclear Medicine*, **64(5)**, 285 (2025).
42. Gallium [^{68}Ga]PSMA-11 injection, monograph 3044, Ph. Eur. Suppl. 10.4. Strasbourg, France, Council of Europe.
43. PSMA-1007[^{18}F] injection, monograph 3116, Ph. Eur. Suppl. 10.5. Strasbourg, France, Council of Europe.
44. [^{68}Ga] Gallium edotreotide solution for injection, monograph 2482, Ph. Eur. Suppl. 10.6. Strasbourg, France, Council of Europe.

Instructions about Preparation of Manuscripts

General remarks: Manuscripts are submitted in English by e-mail. The text must be prepared in A4 format sheets using Times New Roman font size 11, normal character spacing. The manuscript should not exceed 15 pages (about 3500 words), including photographs, tables, drawings, formulae, etc. Authors are requested to use margins of 2 cm on all sides.

Manuscripts should be subdivided into labelled sections, e.g. INTRODUCTION, EXPERIMENTAL, RESULTS AND DISCUSSION, etc. **The title page** comprises headline, author(s)' names and affiliations, abstract and key words. Attention is drawn to the following:

a) **The title** of the manuscript should reflect concisely the purpose and findings of the work. Abbreviations, symbols, chemical formulae, references and footnotes should be avoided. If indispensable, abbreviations and formulae should be given in parentheses immediately after the respective full form.

b) **The author(s)'** first and middle name initials and family name in full should be given, followed by the address (or addresses) of the contributing laboratory (laboratories). **The affiliation** of the author(s) should be listed in detail (no abbreviations!). The author to whom correspondence and/or inquiries should be sent should be indicated by an asterisk (*) with e-mail address.

The abstract should be self-explanatory and intelligible without any references to the text and containing up to 250 words. It should be followed by keywords (up to six).

References should be numbered sequentially in the order, in which they are cited in the text. The numbers in the text should be enclosed in brackets [2], [5, 6], [9−12], etc., set on the text line. References are to be listed in numerical order on a separate sheet. All references are to be given in Latin letters. The names of the authors are given without inversion. Titles of journals must be abbreviated according to Chemical Abstracts and given in italics, the volume is typed in bold, the initial page is given and the year in parentheses. Attention is drawn to the following conventions: a) The names of all authors of a certain publications should be given. The use of "et al." in the list of references is not acceptable; b) Only the initials of the first and middle names should be given. In the manuscripts, the reference to author(s) of cited works should be made without giving initials, e.g. "Bush and Smith [7] pioneered...". If the reference carries the names of three or more authors it should be quoted as "Bush et al. [7]", if Bush is the first author, or as "Bush and co-workers [7]", if Bush is the senior author.

Footnotes should be reduced to a minimum. Each footnote should be typed double-spaced at the bottom of the page, on which its subject is first mentioned. **Tables** are numbered with Arabic numerals on the left-hand top. Each table should be referred to in the text. Column headings should be as short as possible but they must define units unambiguously. The units are to be separated from the preceding symbols by a comma or brackets. Note: The following format should be used when figures, equations, etc. are referred to the text (followed by the respective numbers): Fig., Eqns., Table, Scheme.

Schemes and figures. Each manuscript should contain or be accompanied by the respective illustrative material, as well as by the respective figure captions in a separate file. As far as presentation of units is concerned, SI units are to be used. However, some non-SI units are also acceptable, such as °C, ml, l, etc. Avoid using more than 6 (12 for review articles) figures in the manuscript. Since most of the illustrative materials are to be presented as 8-cm wide pictures, attention should be paid that all axis titles, numerals, legend(s) and texts are legible.

The authors are required to submit the text with a list of three individuals and their e-mail addresses that can be considered by the Editors as potential reviewers. Please note that the reviewers should be outside the authors' own institution or organization. The Editorial Board of the journal is not obliged to accept these proposals.

The authors are asked to submit **the** final text (after the manuscript has been accepted for publication) in electronic form by e-mail. The main text, list of references, tables and figure captions should be saved in separate files (as *.rtf or *.doc) with clearly identifiable file names. It is essential that the name and version of the word-processing program and the format of the text files is clearly indicated. It is recommended that the pictures are presented in *.tif, *.jpg, *.cdr or *.bmp format. The equations are written using "Equation Editor" and chemical reaction schemes are written using ISIS Draw or ChemDraw programme.

EXAMPLES FOR PRESENTATION OF REFERENCES

REFERENCES

1. D. S. Newsome, Catal. Rev.–Sci. Eng., 21, 275 (1980).
2. C.-H. Lin, C.-Y. Hsu, J. Chem. Soc. Chem. Commun., 1479 (1992).
3. R. G. Parr, W. Yang, Density Functional Theory of Atoms and Molecules, Oxford Univ. Press, New York, 1989.
4. V. Ponec, G. C. Bond, Catalysis by Metals and Alloys (Stud. Surf. Sci. Catal., vol. 95), Elsevier, Amsterdam, 1995.
5. G. Kadinov, S. Todorova, A. Palazov, in: New Frontiers in Catalysis (Proc. 10th Int. Congr. Catal., Budapest (1992), L. Guczi, F. Solymosi, P. Tetenyi (eds.), Akademiai Kiado, Budapest, 1993, Part C, p. 2817.
6. G. L. C. Maire, F. Garin, in: Catalysis. Science and Technology, J. R. Anderson, M. Boudart (eds.), vol. 6, Springer Verlag, Berlin, 1984, p. 161.
7. D. Pocknell, GB Patent 2 207 355 (1949).
8. G. Angelov, PhD Thesis, UCTM, Sofia, 2001, pp. 121-126.
9. JCPDS International Center for Diffraction Data, Power Diffraction File, Swarthmore, PA, 1991.
10. CA 127, 184 762q (1998).
11. P. Hou, H. Wise, J. Catal., in press.
12. M. Sinev, private communication.
13. http://www.chemweb.com/alchem/articles/1051611477211.html.

Texts with references which do not match these requirements will not be considered for publication!!!

CONTENTS

Selected papers presented at the 12th National Conference of Chemistry, September 2025, Sofia, Bulgaria